NRL Report 7462

Proceedings of the Conference on

Antennas and Transionospheric Propagation

as related to

ELF/VLF Downlink Satellite Communications

June 8 - 10, 1970

Naval Research Laboratory
Washington, D.C.

LOREN S. BEARCE

Conference Chairman

November 27, 1972

NAVAL RESEARCH LABORATORY
Washington, D.C.

PREFACE

An initial conference on Antennas and Transionospheric Propagation as related to ELF/VLF Downlink Satellite Communications was held at the Naval Research Laboratory (NRL) on 8-10 June 1970 under the sponsorship of the Naval Air Systems Command and NRL for the purpose of providing a forum for interested people to review pertinent physical principles and data, recent theoretical and experimental results, and current thinking; to stimulate and focus attention on appropriate new activity for further studies; and to allow participants an opportunity to present and discuss recommendations for pertinent experimentation, related instrumentation, and studies considered to be most timely and meaningful for implementation in the '70's.

Contained here are the agenda and abstracts and/or papers for most of the formal presentations.

CONTENTS

ACKNOWLEDGEMENTS

The cooperation of the Technical Information Division (Codes 2630 and 2650), Public Works Division (Code 2527), and the Security Branch (Code 1220) of the Naval Research Laboratory for essential services in connection with this conference is gratefully acknowledged. In particular, the helpful services and support of Mr. J.P. Leiphart, Mr. and Mrs. Dennis J. Baker, Mr. Albert E. Showalter, Mr. Arthur J. Ziffer, Mr. Emil E. Kohler, and Mr. Robert A. LeFande in making the conference effective were appreciated. In addition, we wish to acknowledge the excellent cooperation given by the various Session Chairmen including Dr. Lewis B. Wetzel, Dr. William R. Faust, Dr. William S. Ament, Dr. Robert L. Smith, Dr. William E. Blair, Dr. Janis Galejs, and Dr. Tudor W. Johnston.

Loren S. Bearce
Conference Chairman

ATTENDANCE LIST

Mr. Edwin L. Althouse
Naval Research Laboratory
Washington, D.C.

Dr. William S. Ament
Naval Research Laboratory
Washington, D.C.

Dr. M. P. Bachynski
RCA Victor Research Laboratories
Montreal, Quebec

Mr. Dennis J. Baker
Naval Research Laboratory
Washington, D.C.

Dr. Keith G. Balmain
University of Toronto
Toronto, Ontario

Mr. Loren S. Bearce
Naval Research Laboratory
Washington, D.C.

Dr. Alan Berman
Naval Research Laboratory
Washington, D.C.

Dr. William E. Blair
Stanford Research Institute
Menlo Park, California

Mr. John Boning
RCA: Astro-Electronics Division
Princeton, New Jersey

Mr. Peter K. Carlston
Computer Sciences Corporation
Falls Church, Virginia

Mr. David P. Cauffman
University of Iowa
Iowa City, Iowa

Dr. Hollis C. Chen
Ohio University
Athens, Ohio

Mr. Richard W. Cole, Jr.
Naval Research Laboratory
Washington, D.C.

Dr. F. W. Crawford
Stanford University
Stanford, California

Dr. David R. Criswell
Houston, Texas

Mr. Ronald D. Croghan
Westinghouse Georesearch Laboratory
Boulder, Colorado

Dr. John R. Davis
Naval Research Laboratory
Washington, D.C.

Dr. Franco Einaudi
Cooperative Institute for Research
in Environmental Sciences
University of Colorado
Boulder, Colorado

Dr. William R. Faust
Naval Research Laboratory
Washington, D.C.

Mr. Louis H. A. Feher
Naval Research Laboratory
Washington, D.C.

Dr. L. B. Felsen
Polytechnic Institute of Brooklyn
Farmingdale, New York

Dr. Edward C. Field, Jr.
The Rand Corporation
Santa Monica, California

Dr. Janis Galejs
Sylvania Electronic Systems
Needham Heights, Massachusetts

Mr. Howard Gates
Naval Research Laboratory
Washington, D.C.

Mr. Charles Good
Naval Air Systems Command
Washington, D.C.

Mr. David Guerrino
Naval Research Laboratory
Washington, D.C.

Mr. John L. Heckscher
Air Force Cambridge Research Laboratory
Bedford, Massachusetts

CMDR George A. Heffernan
Office of Naval Research
Washington, D.C.

Dr. Yuji Inoue
University of Pittsburgh
Pittsburgh, Pennsylvania

Dr. J. Ralph Johler
ESSA Research Laboratories
Boulder, Colorado

Mr. Charles Y. Johnson
Naval Research Laboratory
Washington, D.C.

Lt. Pierce Johnson
University of Missouri
Rolla, Missouri

Dr. Tudor W. Johnston
University of Houston
Houston, Texas

Dr. R. Michael Jones
ESSA Research Laboratories
Boulder, Colorado

Mr. Martin Katzin
Electromagnetic Research Corporation
College Park, Maryland

Dr. Francis J. Kelly
Naval Research Laboratory
Washington, D.C.

Mr. Harold Killen
Houston, Texas

Mr. Emil E. Kohler
Naval Research Laboratory
Washington, D.C.

Dr. Harry C. Koons
The Aerospace Corporation
Los Angeles, California

Mr. Robert A. LeFande
Naval Research Laboratory
Washington, D.C.

Mr. J. Plumer Leiphart
Naval Research Laboratory
Washington, D.C.

Dr. Donald A. McPherson
The Aerospace Corporation
Los Angeles, California

CMDR William Michael
Naval Air Systems Command
Washington, D.C.

Dr. E. K. Miller
M. B. Associates
San Ramon, California

Dr. Raj Mittra
University of Illinois
Urbana, Illinois

Mr. Richard Newman
Naval Electronics Systems Command
Washington, D.C.

Dr. Frank Palmer
Communications Research Center
Ottawa, Ontario

Dr. Richard A. Pappert
Naval Electronics Laboratory Center
San Diego, California

Dr. Lee W. Parker
Mt. Auburn Research Associates
Cambridge, Massachusetts

Mr. Anthony Pisano
Naval Air Systems Command
Washington, D.C.

Mr. P. Rodriquez
University of Iowa
Iowa City, Iowa

Mr. Samuel Russell
RCA: Astro-Electronics Division
Princeton, New Jersey

Dr. F. L. Scarf
TRW Systems Group
Redondo Beach, California

Mr. D. Lynn Shaeffer
University of Pittsburgh
Pittsburgh, Pennsylvania

Mr. Bertram Sheffield
RCA: Astro-Electronics Division
Princeton, New Jersey

Dr. I. P. Shkarofsky
RCA Victor Research Laboratory
Montreal, Quebec

Dr. Robert L. Smith
Stanford University
Stanford, California

Mr. Lou Snider
Naval Air Systems Command
Washington, D.C.

Dr. Kenneth Stone
General Dynamics/Convair
San Diego, California

Mr. Iwao Sugai
Computer Sciences Corporation
Falls Church, Virginia

Dr. S. Y. K. Tam
RCA Victor Research Laboratories
Montreal, Quebec

Mr. T. N. C. Wang
Stanford Research Institute
Menlo Park, California

Dr. Herschel Weil
University of Michigan
Ann Arbor, Michigan

Dr. Lewis B. Wetzel
Naval Research Laboratory
Washington, D.C.

Dr. Eldon C. Whipple, Jr.
ESSA Research Laboratories
Boulder, Colorado

Mr. Charles E. Young
Naval Research Laboratory
Washington, D.C.

AGENDA FOR

Conference on ANTENNAS AND TRANSIONOSPHERIC PROPAGATION
as related to ELF/VLF DOWNLINK SATELLITE COMMUNICATIONS

MONDAY MORNING SESSION - 9:00 A.M. - 8 June 1970

Session Chairman: Dr. Lewis B. Wetzel, Supt.,
Communications Sciences Division - NRL

Opening Remarks - L. Wetzel

Welcome - Dr. Alan Berman, Director of Research, NRL

Some Considerations Related to the Feasibility of ELF/VLF Downlink Satellite Communications - L.S. Bearce - Naval Research Laboratory

The Complex Refractive Indexes for a Two-Component Warm Plasma - D.J. Baker - Naval Research Laboratory

Collisional Damping of Electrostatic Whistlers - I.P. Shkarofsky - RCA Victor Research Laboratories

Procedures for Estimating Radiation Resistances of Antenna in Magnetoplasmas - W.S. Ament - Naval Research Laboratory

The Electromagnetic Fields of an Electric Dipole in a Compressible Magnetoplasma - W.E. Blair and T.N.C. Wang - Stanford Research Institute

MONDAY AFTERNOON SESSION - 1:30 P.M. - 8 June 1970

Session Chairman: Dr. Wm. R. Faust, Associate Director of Research - Electronics - NRL

Antenna Impedance in the Ionosphere - H. Weil - University of Michigan

Antenna Impedance in a Warm Anisotropic Plasma - H.C. Chen - University of Ohio

VLF Radiation Characteristics of Crossed Dipoles in a Magnetosphere - T.N.C. Wang - Stanford Research Institute

Electron Density Dependence of VLF Antenna Impedance - D.A. McPherson, W.B. Harbridge, and H.C. Koons - The Aerospace Corporation

Transmission Losses Associated with Plasma Perturbations - F.L. Scarf and R.W. Fredricks - TRW Systems Group

Efficiency Considerations for a Satellite Downlink at VLF - R.L. Smith, T.F. Bell, and T.N.C. Wang - Stanford University

ELF Propagation Effects in the Ionosphere - P. Rodriquez, D.A. Gurnett, and S.D. Shawhan - University of Iowa

Nonlinear Wave Interactions in the Ionosphere - F.W. Crawford - Stanford University

TUESDAY MORNING SESSION - 9:00 A.M. - 9 June 1970

Session Chairman: Dr. Wm. S. Ament, Consultant for Applications Research Division, NRL

Experimental Electric Antenna Characteristics in the Ionosphere at ELF/VLF - D.P. Cauffman, D.A. Gurnett, and S.D. Shawhan - University of Iowa

A Magnetoplasma Facility - S.Y.K. Tam - RCA Victor Research Laboratories

Sounding the Magnetosphere and Ionosphere at VLF - R.L. Smith, R.A. Helliwell, and B. Edgar - Stanford University

Nonlinear Sheath Conductance and Capacitance of a VLF Antenna at High Peak Voltage - I.P. Shkarofsky - RCA Victor Research Laboratories

TUESDAY AFTERNOON SESSION - 1:30 P.M. - 9 June 1970

Session Chairman: Mr. J. Plumer Leiphart, Head, Satellite Communication Branch, NRL

The Technique for Computation of Sheath Structure of a Long Antenna in the Ionosphere - L.W. Parker and E.C. Whipple, Jr. - Mt. Auburn Research Associates and ESSA Research Laboratories

Plasma Sheath Problems and Large Signal VLF Sources in the Ionosphere - T.W. Johnston - University of Houston

Proposed Satellite Observations of ELF Emissions - H. Killen and D.R. Criswell - Houston, Texas

Full Wave Method and Preliminary Results for Satellite Launching of ELF Waves in the Earth-Ionosphere Waveguide - F. Einaudi and J.R. Wait - University of Colorado

Full Wave Solution for the Transmission of ELF Waves through the Ionosphere - D.L. Shaeffer and Y. Inoue - University of Pittsburgh

Summary of NELC Full Wave Programs - R.A. Pappert - U.S. Naval Electronics Laboratory Center

Transmission of Electromagnetic Waves through Ambient and Disturbed Ionospheres - H.G. Booker, C.M. Crain, and E.C. Field, Jr. - The Rand Corporation

Excitation of the Terrestrial Waveguide by Sources in the Lower Ionosphere - J. Galejs - Sylvania Electronic Systems

WEDNESDAY WORKING GROUP SESSIONS - 10 June 1970

ANTENNAS

Antenna Impedance; Chairman: Mr. Dennis J. Baker
Antenna Radiation -- Linear Approaches; Chairman: Dr. Wm. E. Blair

TRANSIONOSPHERIC PROPAGATION

Ray Tracing; Chairman: Dr. Robert L. Smith
Full Wave Solution; Chairman: Dr. Janis Galejs

NONLINEAR PROBLEMS

Antenna Radiation and Propagation; Chairman: Dr. Tudor W. Johnston

OPEN DISCUSSION

Conference Chairman: Mr. Loren S. Bearce

SOME CONSIDERATIONS RELATED TO THE FEASIBILITY OF ELF/VLF DOWNLINK SATELLITE COMMUNICATIONS

Loren S. Bearce
Satellite Communication Branch
Communications Sciences Division
Naval Research Laboratory, Washington, D.C.

INTRODUCTION

This conference has been called to review recent results related to communicating from an Extremely Low Frequency (3 Hz to 3 kHz)/ Very Low Frequency (3 kHz to 30 kHz), ELF/VLF satellite source in the ionosphere. It is to serve as a forum for discussing action needed to evaluate the feasibility of such radio communications. An implicit premise is that no one has yet detected an ELF/VLF signal on the ground radiated from a spacecraft in the ionosphere. The purpose of this paper is to set the stage for conference discussion by first (a) outlining the historical background of the Navy's involvement in the field, (b) presenting a brief overview of key technical problem areas, and (c) outlining certain possible approaches under consideration for obtaining needed experimental and theoretical data. A reasonable perspective should emerge during the course of the conference as to the nature and scope of the major question areas which have been identified in the decade and more that NRL has been engaged in this fascinating, but very complicated, subject area.

HISTORICAL PERSPECTIVE

Serious NRL involvement commenced during the latter part of 1959 about the time Project Vanguard personnel were transferred to the newly created National Aeronautics and Space Administration (NASA). Navy officials had requested suggestions for appropriate research as they sought to chart the Navy's role in space; in response, a long list of radio propagation satellite experiments were compiled. The LOFTI satellite VLF receiving experiments developed from this effort [1].

Results of whistler studies were of considerable value in the design of LOFTI instrumentation. Two satellites in the LOFTI series were launched in February 1961 and June 1963; however, both barely achieved orbit with lifetimes of only about 30 days in each case due to launch vehicle failures. In the case of LOFTI-I the vehicle failure prevented payload separation, spin up, and electric dipole deployment. Otherwise, the payloads functioned essentially as planned. Narrowband receivers at 10.2 and 18 kHz in LOFTI-IIA, shown in Figure 1, measured signals from the Navy omega stations and the NBA and NPG VLF stations in Panama and Washington state, respectively.

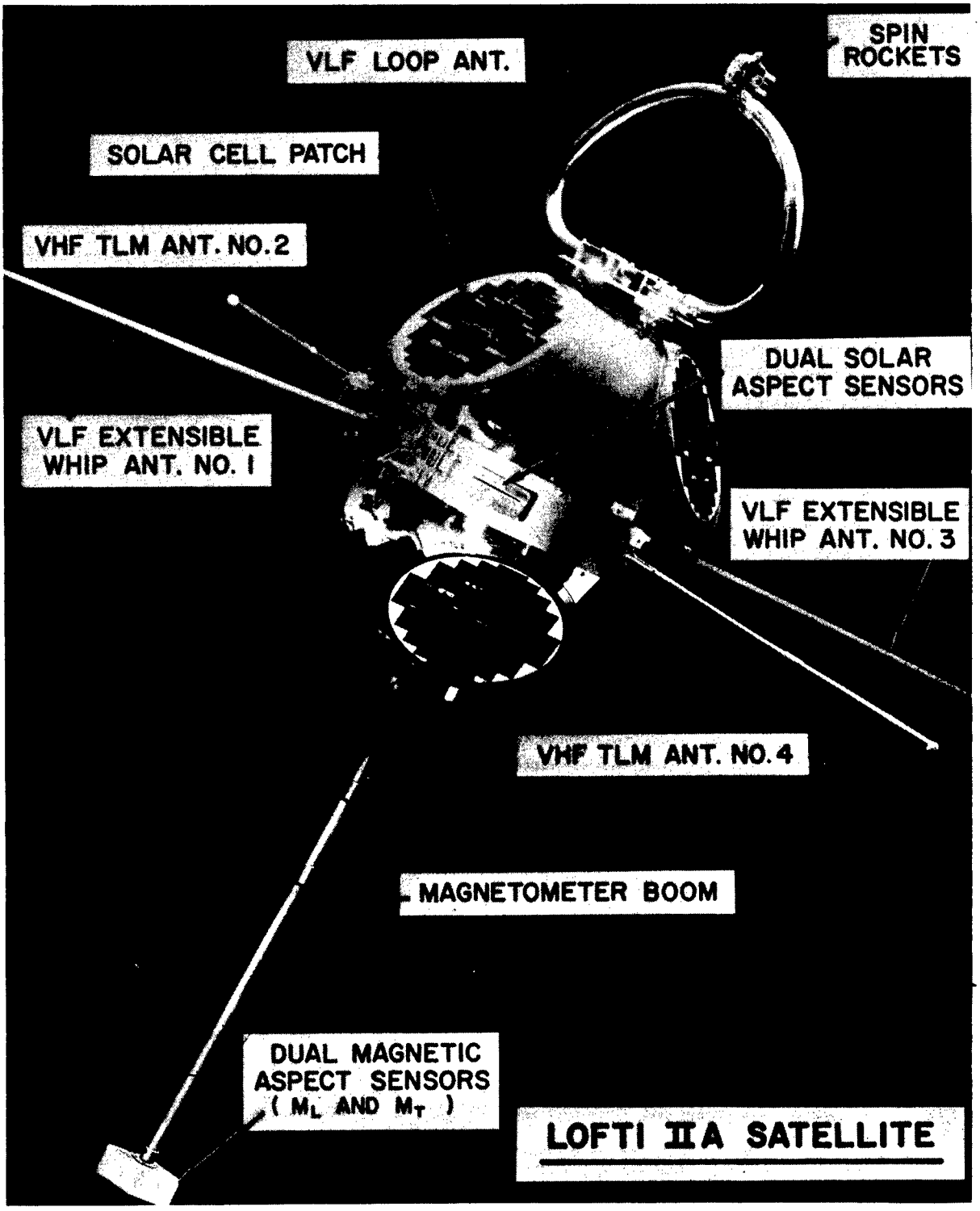

Fig. 1 The LOFTI-IIA VLF Receiving Satellite (Launched June 1963)

These early satellite experiments provided the first clear experimental evidence of what is now known as the non-ducted whistler mode of propagation -- coverage was unexpectedly extensive. Attenuation was shown to be predictable and especially low at night, most of it occurring in a thin shell in the D and E regions. The Gaussian distribution of received signal levels suggested that many uncorrelated propagation phenomena were involved along the path. Signals were at times received exclusively on the magnetic loop or the 20 foot electric dipole antennas. Whip antenna impedance was quite sensitive to orientation, plasma parameters, wake, and sheath effects; whereas, the loop antenna, as expected, was not.

Since that time some progress has been made; however, large gaps still exist in our knowledge as to how ELF/VLF signals might be used for downlink satellite communications. Significant insight was provided by several satellite series, including the INJUN, OGO, ARIEL, ALOUETTE, OV, PIONEER, FR-1, and ISIS programs.

PROBLEM AREAS

The first key problem area on the list in Figure 2 involves the selection of an appropriate type of source. An electric dipole antenna is attractive because it is much easier to deploy than a loop. The high refractive index of the medium at these frequencies suggests that a short antenna might be much more effective in the ionosphere than in free space. However, the electric dipole may generate sufficient electroacoustic energy as to make it undesirable for launching whistler mode waves. Further, it requires a dynamic tuner which responds quickly since the impedance is strongly influenced by changes in the plasma and orientation. But, how fast and over what range will the impedance change? Can a servo-controlled active tuner be expected to be effective? What should be a limit on the maximum drive? Should the elements be insulated, bare, or partially insulated? Will multipacting be a critical concern? How should a nonlinear reactive-like load which stores energy be most effectively driven? How long can an antenna be and yet be safely deployed? These are all satellite engineering questions which must be answered before proper spacecraft experiments can be designed to provide insight in another group of questions; will propagating modes be effectively excited; how serious are sheath effects; and is near-field nonlinear propagation an important consideration?

PROBLEM AREAS

- SATELLITE ENGINEERING
- DYNAMIC ANTENNA IMPEDANCE MATCHING
- ANTENNA RADIATION INTO ANISOTROPIC PLASMA
- WAVE PROPAGATION THROUGH AND OUT OF THE IONOSPHERE INTO THE EARTH-AIR-IONOSPHERE WAVEGUIDE

Fig. 2 Problem Areas

A loop antenna on the other hand would most likely maintain a rather stable known impedance and should be relatively independent of orientation and plasma parameters. Although notoriously poor radiators in free space, loops may prove reasonably effective in a magnetoplasma, if some of the theoretical predictions still under development are correct. However, the deployment of a large loop in orbit appears quite tricky, at best. If this problem could be solved, we would, of course, be much closer to an active test of radiation and downlink propagation.

It has been suggested that by properly phasing the drive to a crossed-dipole system, arranged either as a singly crossed dipole, or in a more extensive array, waves might well be launched which would match the structure of naturally propagating whistler-mode waves, as described by Storey [2]. However, we will not likely be able to confirm such concepts until we can explain and observe the behavior of a simple single dipole.

Triggered emissions may eventually prove to be a viable source for ELF/VLF energy. This concept has been suggested before by several workers in the field. Free charge or beam radiation has also been suggested, as well as the idea of radiating high power at HF (or some other frequency where we know effective radiation can be obtained) and using the nonlinear properties of the medium to generate a much lower frequency. However, interest to date has centered on first examining the characteristics of the simple electric dipole and loop for an appreciation of the basic radiation mechanisms involved with simple antenna sources.

An in-situ measurement of antenna impedance with high drive should be quite successful and should go a long way toward determining how to efficiently transfer energy into the antenna itself. However, the assessment of an antenna as a radiator is not as easy. Perhaps the major unknown in an ELF/VLF downlink system is the radiation characteristics of a high power antenna source in the ionospheric magnetoplasma. Wang and Bell [3] developed the radiation patterns shown in Figure 3 using a linear cold plasma model. It is evident that an experiment to verify such characteristics will be difficult to implement. Some experimental approaches are listed in Figure 4.

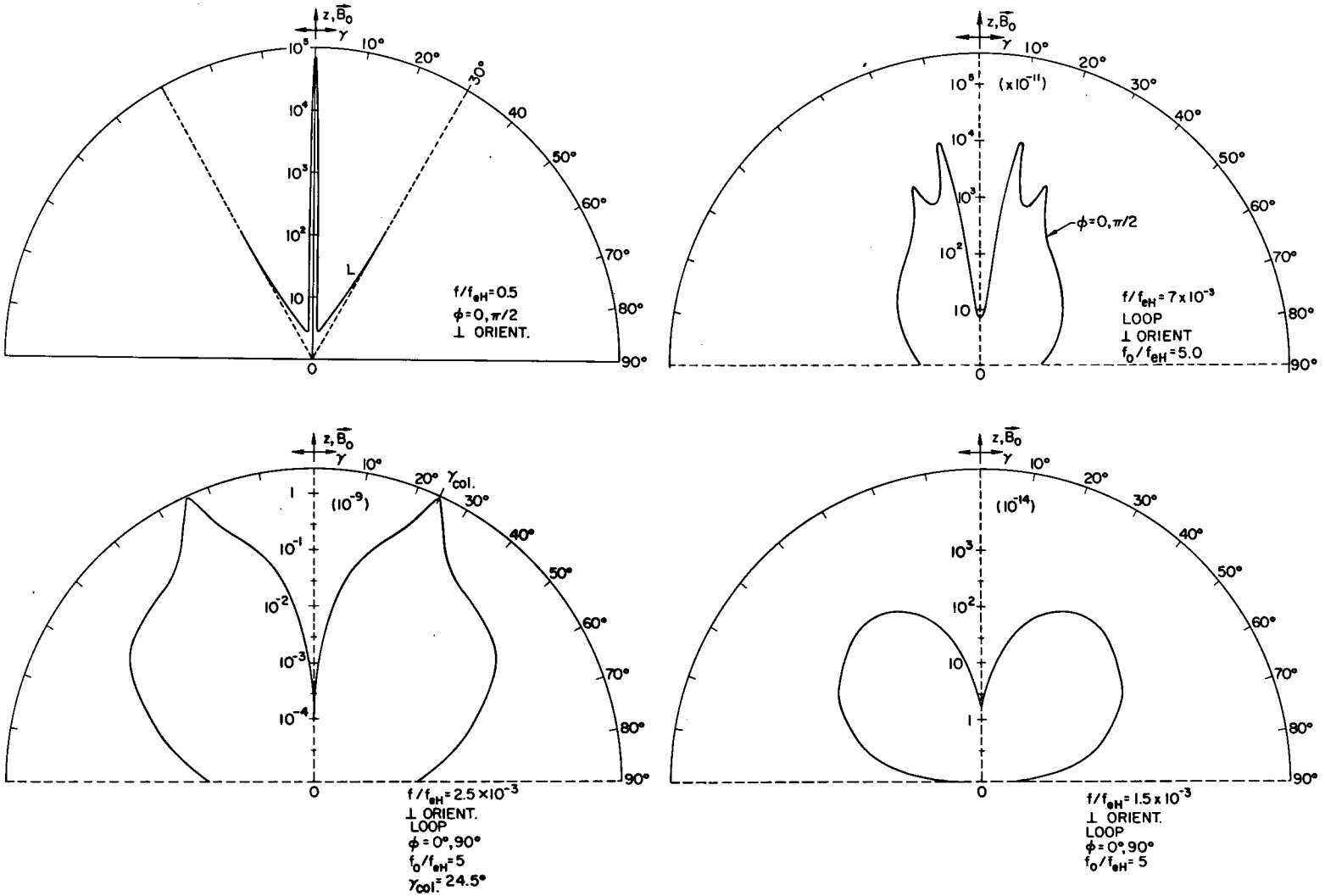

Fig. 3 Normalized Linear Cold Plasma Magnetic Dipole Radiation Patterns for Frequencies (a) above, (b) just below the Lower Hybrid Resonance, (c) at 4.6 f_{PH} , and (d) just above f_{PH}, the Proton Gyrofrequency (from Wang and Bell [3]).

POSSIBLE EXPERIMENTAL APPROACHES

ANTENNA IMPEDANCE:

IN SITU VS SCALED MODEL IN LABORATORY

SMALL LOW-COST SATELLITE VS ROCKET PROBE

ANTENNA RADIATION:

SOUNDING RECEIVER

COMPANION RECEIVING SATELLITE

GROUND-BASED RECEIVERS

RECEIVING SATELLITES OF OPPORTUNITY - OGO, ALOUETTE, ISIS

RECEIVING ROCKET PROBE - TIMED TO GET PROFILE

Fig. 4 Possible Experimental Approaches

The downlink transionospheric propagation problem is quite important too, but it is now considered to be relatively more predictable. Walter [4] has achieved some remarkable results with ray tracing which has explained some OGO-4 observations of ~100 Hz doppler-shifted nonducted 11.3 kHz signals from an Omega transmitter in the conjugate region (Aldra, Norway) to the satellite observation point. Figure 5 has been taken from his paper. The wave normals are nearly perpendicular to layered inhomogenities in the medium where the signal enters the ionosphere and although the medium changes significantly within the distance of a wavelength in that region, it can be expected that wave directions predicted by ray theory will be reasonably accurate. However, the intensity, of course, would be better determined by a full-wave treatment. This study is considered relevant to downlink propagation because of a reciprocity theorem developed by Pitteway and Jespersen [5] which indicates that had a wave been launched at the observation point but with an oppositely directed wave normal, it would have followed along the same path indicated in Figure 5 and emerged from the ionosphere with the same angle from the vertical as the corresponding reciprocal penetrating mode. Clearly, further full-wave analytical development in this area should prove productive toward predicting the penetration characteristics of downward propagation.

The detection problem is expected to be complicated due to the separate Doppler frequency shift which will be imparted to each wave leaving the antenna according to the dot-product of the refractive index along each wave normal and the satellite velocity. Hence, a given transmitter frequency can be expected to generate a bundle of frequencies at the point of transmission. Signal pulses are thus expected to be smeared out in both frequency and time -- as the different doppler shifted frequencies will each undergo a slightly different path delay in traveling from the source to an observer. The amount of doppler shift can be considerable because of the relatively large refractive indexes which exist at ELF/VLF frequencies in the ionosphere; the previous reference [4] reported direct observation of this phenomena. It does not appear very hopeful for satisfactory scaled experiments in a laboratory magnetoplasma because of the fixed masses of electrons and high collision rates.

Let's now examine the available theoretical models which represent our understanding of antenna sheath and impedance phenomena -- at least, when they are properly validated by experiments. Grard and Tunnely [6] were able to interpret FR-1 dipole impedance data in terms

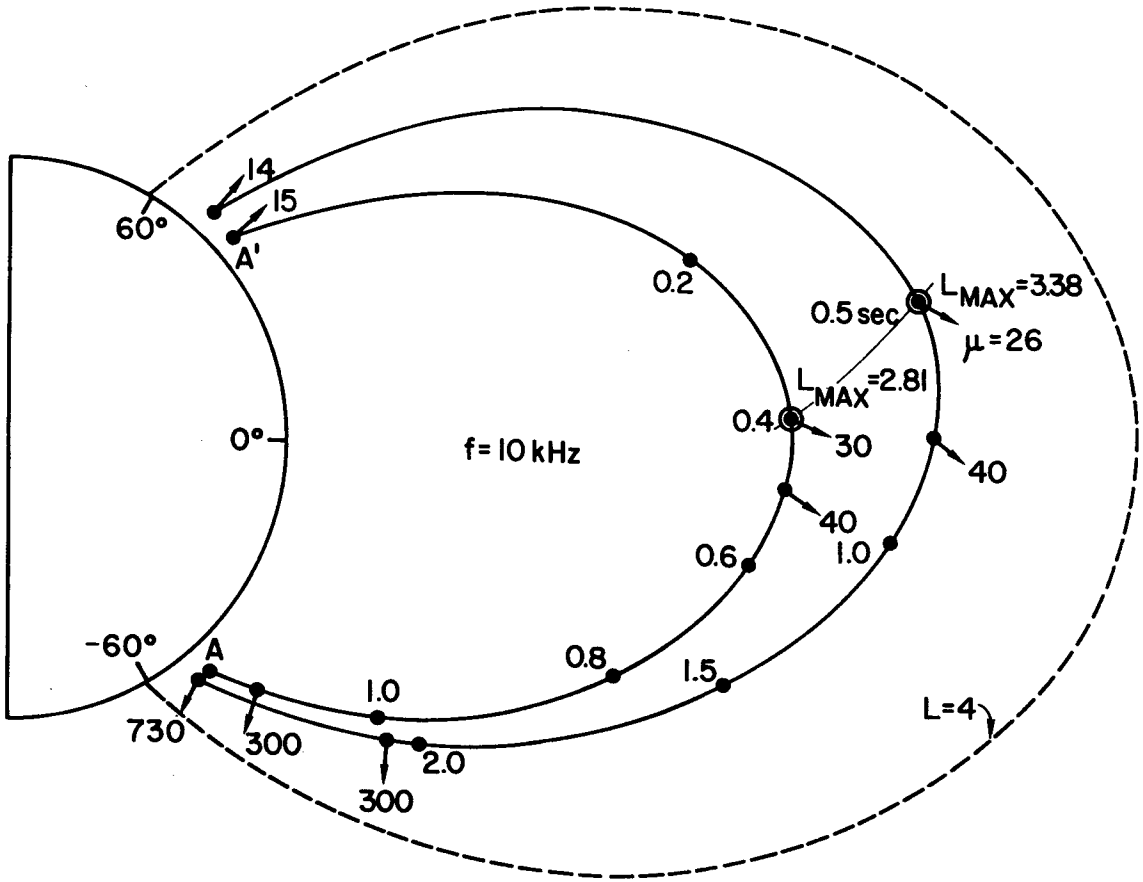

Fig. 5a — Ray paths calculated for wave packets at 10 kHz starting with vertical wave normals at 500 km and invariant latitudes of 44.3° (point A') and 49.9°. A dipole field line at $L = 4$ is shown for reference. Arrows indicate the wave normal directions, and the accompanying values of the phase refractive index μ are indicated. Travel times calculated from the starting points at 500 km are indicated at several points along the rays. The thin line shows the locus of the L_{max}.

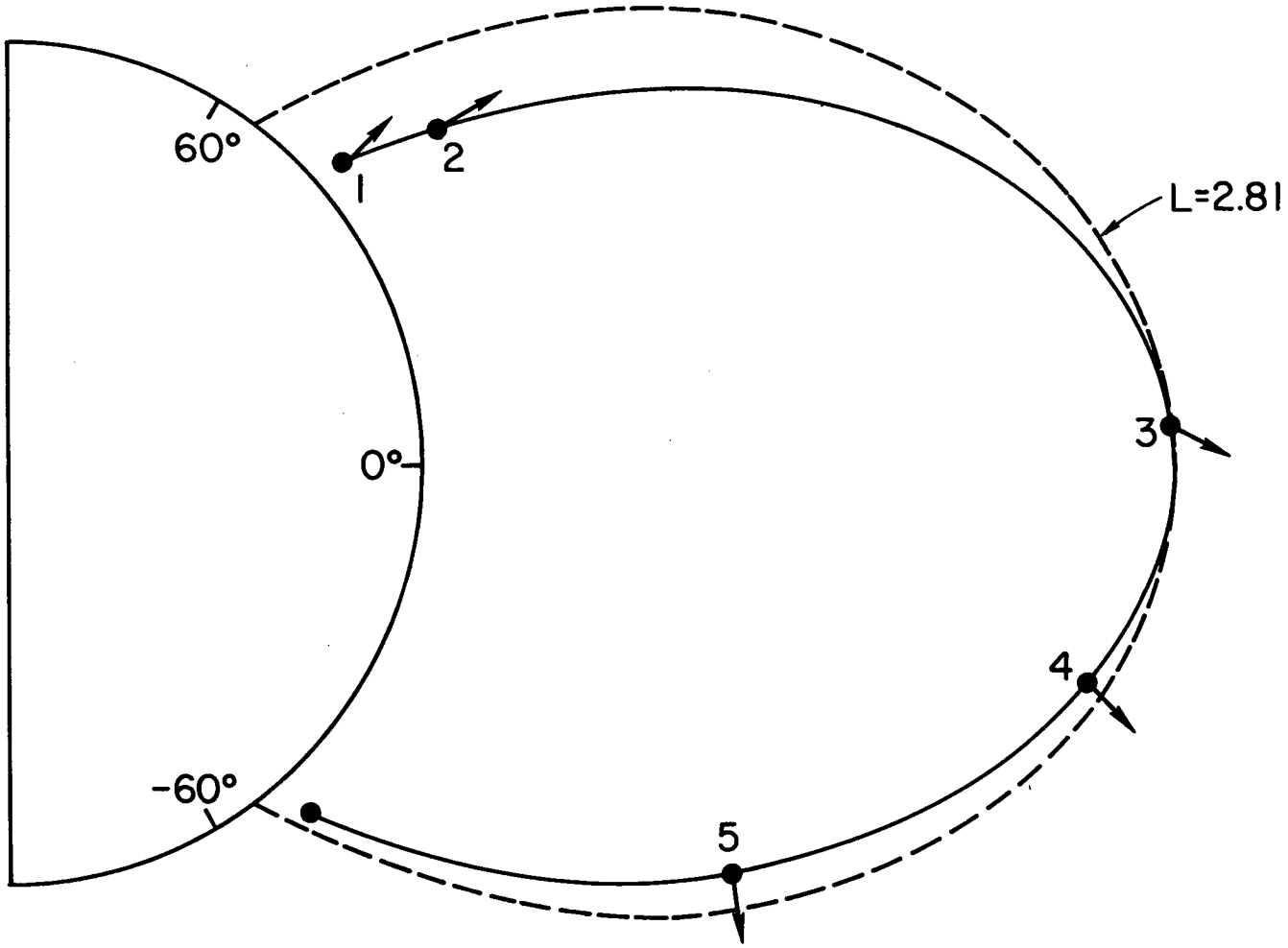

Fig. 5b — Sketch of the inner ray path from Figure 5a, showing the dipole field line through the maximum L along the path.

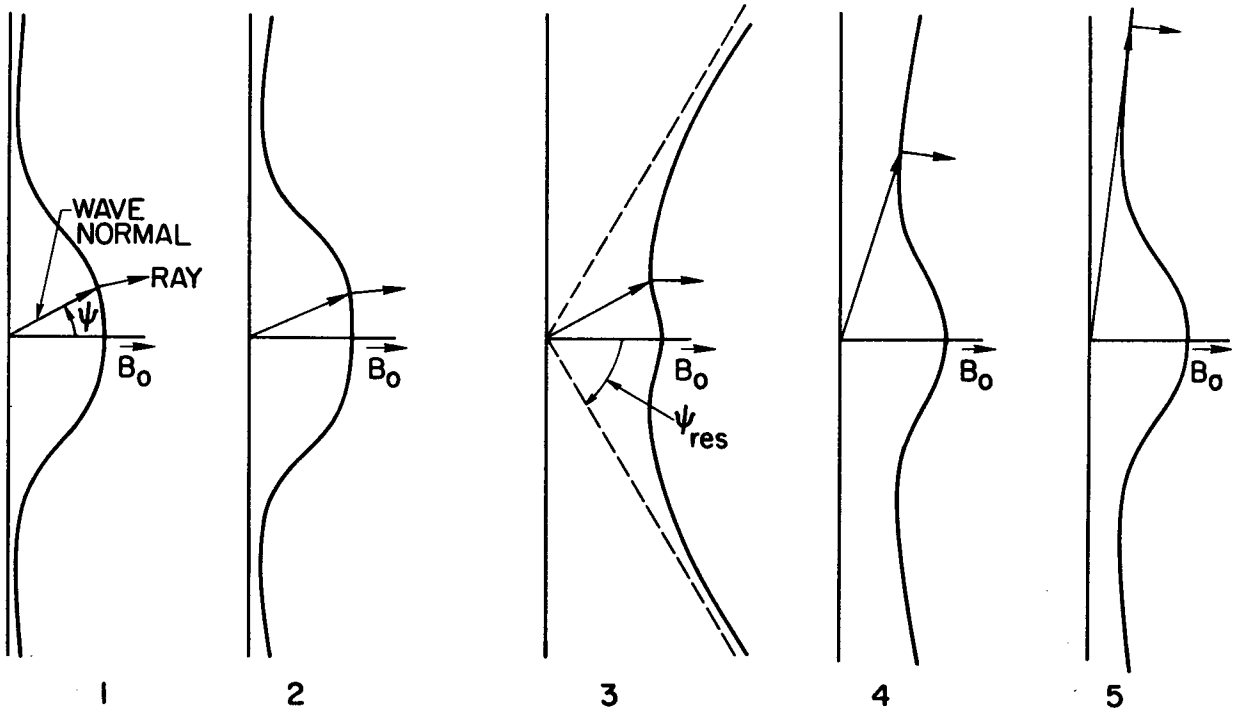

Fig. 5c — Five refractive index diagrams (not strictly to scale) indicating the wave normal and ray directions of four representative points along the ray path of Figure 5b.

of the impedance due to the medium using the quasi-static theories of Balmain [7] and/or Blair [8] in series with the impedance of the sheath as calculated using the small signal theory developed by Mlodnosky and Garriott [9]. This serves as evidence that the physical principle of charge equilibrium used in determining the sheath is essentially valid. Although their specific model probably will not be applicable to the strongly driven antenna case, the principle may be expected to still hold. Some workers [10 and 11] have extended the model to include the strongly driven electric dipole case using this principle. Other effects have also been included such as electron transmit time and $\underline{v} \times \underline{B}$ effects, photo-ionization, potential dependent ram currents, drive potentials, and satellite structures -- but generally wake effects, multipacting, effects of antenna insulation, changes to the local electron energy distribution, non-quasi-static medium impedance, and radiation have been neglected. The importance of considering antenna-particle interactions in determining antenna impedance has been clearly established; however, sheath dynamics are expected to have a major impact on both antenna impedance and radiation characteristics.

We need a satisfactory model to describe the nonlinear propagation phenomena which surely take place near such high energy sources. At this point it is anticipated that we will be forced to direct numerical solutions of nonlinearized equations. Perhaps this approach may suffice to predict fields at an imaginary surface enclosing the source, but at a distance sufficiently far from the source so that propagation beyond it is essentially linear -- that is, if someone can be found who can properly formulate the problem.

Presumably, full-wave techniques are well enough developed to project these fields to any point on the Earth's surface; although extensions may be necessary to allow for the effects of the moving source, electroacoustic modes, and horizontal inhomogenities in a curved-earth model.

EXPERIMENTAL APPROACHES

Before considering in-situ experiments, one examines what can be done without having to incur the major cost usually associated with satellite experiments. One of the important questions I'd like this

conference to consider is: "To what extent can useful experimentation be done within the laboratory?" It is quite clear that experimentation of several kinds is needed and could provide an important key to further progress. We have made real progress in theory although in many areas it too is still quite shy of what is required, but theoreticians also need the guidance of good experimentation.

The questions related to antenna impedance are the first questions to examine, for we must first know how to efficiently transfer energy into an antenna if it is to radiate. Does anyone have a suggestion as to how to even formulate this nonlinear drive problem? We do have reasonable confidence that in-situ experiments can successfully measure driving-point impedance and its variation under driven conditions. Also, we now have a reasonable basis for designing such an experiment and interpreting experimental data from it. Apparently, we are even beginning to have some fairly good theoretical models from which we can make reasonable predictions as to the nature of the driving-point impedance problem at low-drive levels. However, the situation with high drive in the presence of a magnetoplasma seems well beyond the scope of most theoretical treatments to date. Competent studies worthy of our trust eventually need carefully planned and pertinent experimentation for guidance and support.

I propose a set of three in-situ experiments to serve as strawmen for the purpose of stimulating discussion at this conference. The purpose of this series of three satellite experiments would be to explore the characteristics of high drive conditions at ELF/VLF in sufficient detail that the feasibility of ELF/VLF downlink communications could at least be predicted with reasonable confidence (as opposed to necessarily trying to demonstrate such a link). Such a continuing programmed series of experiments should allow us to efficiently learn as we progressively tackle the downlink system problems.

For cost effectiveness, the first launch would be a 300 lb. battery-powered piggy-back satellite instrumented primarily to investigate electric dipole impedance characteristics under typical strong drive conditions ($\sim$ 1 kw at 1 kHz -- perhaps up to 20 kv). Why a dipole? Because it's mechanically the easiest to deploy and the only large antenna type with which we've had any significant experience in space. Although the large loop impedance and drive problems are expected to be much simpler, the reliable deployment of a large loop is still considered to be a rather tough

engineering problem. Certainly, even if we could successfully deploy a large loop, we would want to also know what happens with a dipole in any case. Thus, an electric dipole seems most likely to be selected as the antenna for the first experiment even though it is believed to involve the most complicated physics. We simply must face and solve the secondary emission/multipacting problem if we are to use an electric dipole, since we are forced to impose quite high drive potentials on a reactive antenna in order to achieve sufficient emitted energy density for a communication link. A satellite is suggested instead of a rocket partly for greater coverage and partly in order to allow time to deploy a long antenna and to better explore the dependence on ionospheric plasma conditions. It should then be specially instrumented to measure both the instantaneous drive point current and voltage waveforms for a long ($\sim$100 meter elements) spin-stabilized electric-dipole antenna.

It is proposed that the next satellite launch should be a radiation experiment, again using a driven electric dipole but with the knowledge just gained on antenna impedance to assure that the antenna will load up properly -- an obvious and critical requirement for significant radiation. To obtain the needed data regarding radiation effectiveness, pattern, etc., the necessity of having a receiving antenna in the reasonably near vicinity is envisioned but not so near as to have its calibrations disturbed by the plasma excitation caused by the transmitting antenna. All satellite experiments should certainly carry sounding receivers and take advantage of existing "satellites of opportunity" which can receive signals as may be radiated; however, it cannot be expected that these will provide all of the detail information needed. It was to solve this problem that some years ago I conceived the idea of co-launching a receiving satellite with the transmitting satellite in such a manner that the receiving satellite would effectively "orbit" the other in synchronism with the orbit period around the earth [12]. If the receiving satellite were given a slightly different inclination and eccentricity, the relative motion of the receiving satellite with respect to the transmitting source could, with proper timing, be made to describe an elliptical path enclosing the source. Such orbits should be reasonably stable -- requiring at most only relatively minor orbit corrections, primarily to compensate for differential drag effects. Once established, no orbit corrections may even by necessary, particularly if the experiment period is short enough as, for example, with a battery-powered satellite. The cost is not quite as low as that of a rocket, yet the life can be some longer, and further, the dual-satellite approach appears to offer a reasonable way of obtaining otherwise near-unobtainable necessary data. It is hard to imagine how such data could be obtained via rockets or by any other means which would be less costly. The "super-orbiting" sister

satellite should be instrumented to measure the radiated fields, the characteristic ambient plasma parameters, the three components of the earth's magnetic field, and satellite attitude. If trusted instrumentation is available for measuring the disturbed plasma near the transmitter, then perhaps it should be included on the transmitting satellite as well.

The third satellite experiment is envisioned as a transmitter with a large loop, but otherwise like the second launch. Actually, it need not be last in the series, since it does not depend on preceding results, but merely requires sufficient time to work out the loop deployment problem. This brings up another question to be posed at this conference: "What are some large loop deployment techniques that are practical and not too risky?"

These experiments and associated studies are thus aimed at illuminating each of the critical areas involving the antenna as a source so as to provide enough insight that the feasibility of such a downlink can be predicted with some confidence. A thorough trans-ionospheric propagation survey is not considered to be warranted (or indeed hardly feasible) until more is definite as to how to radiate in such a medium at these frequencies. With several launches in the program, the opportunity should exist to recoup some of the losses should an earlier launch not be entirely successful and to take advantage of information gained from the earlier experiments to more effectively adapt instrumentation to later experiments.

Let's now examine the suggested orbit. Spinning satellites with near-polar inclination are of course desirable in order to scan the antenna orientation at all magnetic latitudes. Apogees as high as 2500 Km have been considered -- initially placed on the nighttime side of the earth toward the upper northern latitudes. Perigee would be between 300 and 400 Km; the lower, the better, so long as orbit life is sufficient and the differential drag problem does not become too troublesome. This arrangement should provide a maximum electron density at perigee near noon, local daytime, and a low value on the nighttime side at apogee. Another reason for placing the apogee in the North is that would permit command and data acquisition from the Alaska telemetry sites on every orbit, since it is assumed that there would likely be a need for real time interaction with the experiments during the week or so the batteries remain charged. With such an orbit, the line of apsides would rotate to where the apogee would be near the equatorial region within a week or so.

Approximate values suggested for other parameters are: spin rate - 0.2 to 1.0 RPM, weight - 300 lbs., antenna element lengths - 100 meters. RCA Astro-Electronics Division has made studies for NAVAIR on the dynamic stability of booms. They have shown that spin does greatly enhance the stability; however, there are lengths beyond which the problem is more serious, given a specific spin rate. We do not yet have much guidance from theory as to what lengths would be preferred. We would like at least 1 Kw of power transferred to the antenna. If the maximum power level which can be expected to be achievable from a spacecraft should be set at, say, 100 Kw, then a source radiating 1 Kw should surely be detected at least occasionally, on the ground, since at least a 20 dB variation in path loss seems reasonable -- that is, if it is ever going to be feasible to establish such a radio link. We must first, of course, determine how to radiate that 1 Kw. This we consider to be the toughest and most critical problem at hand, for it is clear that quite complicated nonlinear phenomena are involved.

Frequencies of interest range from below the proton gyro-frequency to a little above the lower hybrid resonance (LHR). In this range there are special considerations imposed by the tuner. If a variable high power tuner can be devised with sufficient range which is not too heavy and yet capable of following the fluctuations in antenna impedance, then a slowly "swept" (actually incrementally stepped) frequency drive would be preferred to the alternative--a tuner with several (5 to 10) fixed tuner reactors switched in turn and driven with a servo-controlled variable frequency to effect desired antenna loading. Perhaps a reasonable goal should be to deliver 1 to 2 Kw to the antenna at a frequency near 800 Hz.

Certain operating modes are clearly desirable. A low level drive below the electron thermal potential incrementally swept through the full frequency range would provide valuable data to check present theories that are based on linear approximations. A ramp function applied to the drive level while maintaining a fixed frequency would show where nonlinear level-dependent effects occur. A sequence consisting of a strong pulse preceded and succeeded by a pulse with reduced (about 10 dB) amplitude all at a given frequency would possibly provide some before and after indication of local ionospheric heating effects caused by the main pulse. Dr. R.A. Helliwell suggested this mode as linear operation should tend to result in the first and last pulses being received at the same level. Of course, there should also be a mode for simple "pulses" of various lengths, fixed frequencies, and drive levels.

A broadband sounding receiver should be on each transmitting satellite since such receivers would provide valuable information about reflected signals as well as an indication of radiation effects. The telemetry load presented by this data source presumably could be time shared with the direct measurements of antenna drive current and voltage for determining nonlinear waveform effects. The "sounding" receiver should also have narrowband (perhaps 10 Hz or less) capability to track several fixed frequencies in addition to the transmitted signal in order to enhance the likelihood of detecting "boomerang" signals as suggested by Dr. R.L. Smith. Supporting instrumentation would be a 3-axis magnetometer and aspect sensing system for determining unambiguous satellite attitude.

NRL and NAVAIR have recently been striving to find a way of achieving the objectives of the first experiment with little more cost to the program than that of a rocket experiment.

Compromises are generally necessary with satellite experimentation -- often because of cost -- hence, the set of experiments suggested here may never completely materialize. However, it is useful to discuss them to gain perspective as to the most meaningful approach to be taken, given existent constraints.

REFERENCES

1. Leiphart, J.P., R.W. Zeek, L.S. Bearce, and E. Toth (1962), "Penetration of the Ionosphere by Very-Low-Frequency Radio Signals -- Interim Results of the LOFTI I Experiment", Proc. IRE 50, No. 1, 6-17

2. Storey, L.R.O. (1959), "A Method for Measuring Local Electron Density from an Artificial Satellite", J. Res. of the NBS -- D. Radio Prop., 63D, No. 3, Nov-Dec 1959

3. Wang, T.N.C. and T.F. Bell (1969), "VLF Antenna Radiation Patterns in a Multi-Component Magnetoplasma", paper presented at 1969 Fall URSI Meeting, Austin, Texas, 8-10 Dec 1969

4. Walter, F. and J.J. Angerami (1969), "Non-Ducted Mode of VLF Propagation Between Conjugate Hemispheres; Observations on OGO's 2 and 4 of the 'Walking-Trace' Whistler and of Doppler Shifts in Fixed Frequeny Transmissions", J.G.R., Space Physics, 74, No. 26, p. 6352-6370, Dec. 1969

5. Pitteway, M.L.V. and J.L. Jespersen (1966), "A Numerical Study of the Excitation, Internal Reflection and Limiting Polarization of Whistler Waves in the Lower Ionosphere", J. Atmos. and Terr. Phys., 28, 17, 1966.

6. Grard, R.J.L. and J.K.E. Tunaley (1968), "The Impedance of the Electric Dipole Aerial on the FR-1 Satellite", Annales de Géophysique, 24, 1968, p. 49-61

7. Balmain, K.G. (1964), "The Impedance of a Short Dipole Antenna in a Magnetoplasma", IEEE Trans. Ant. Prop., AP-12, 605

8. Blair, W.E. (1964), "The Driving-Point Impedance of an Electrically Short Cylindrical Antenna in the Ionosphere", Tech. Report EE-109, EE Dept., Univ. of New Mexico, Albuquerque, N.M.

9. Mlodnosky, R.F. and O.K. Garriott (1963), "The VLF Admittance of a Dipole in the Lower Ionosphere", Proc. Int. Conf. on the Ionosphere, Inst. Phys. and Phys. Soc., London, p. 484

10. Baker, D.J. (1969), "Electric Dipole Impedance with Emphasis on $\underline{v} \times \underline{B}$ Effects", Appendix C, Report GDC PIN 69-082, Convair Div. of Gen. Dynamics, San Diego, Calif. of Feb 1969

11. Johnston, T.W. (1969), "The Low-Frequency Nonlinear Current Voltage Characteristics for Long Dipoles Mounted on Ionospheric Satellites", Section 6, Lab Report 7-801-80, RCA Research Labs, Montreal, Quebec, of Aug 1969

12. DeWitt, R.N. (1966), "Relative Motion of a Body About an Orbiting Satellite", J. of Spacecraft and Rockets, 3, No. 12, p. 1799, Dec 1966

THE COMPLEX REFRACTIVE INDEX FOR A TWO-COMPONENT WARM PLASMA

Dennis J. Baker
Physicist
Naval Research Laboratory
Washington, D.C.

INTRODUCTION

The concepts of the refractive index and the refractive index surface have proven to be valuable tools of the theoretician for understanding the phenomenon of radiation in plasmas. By far the greatest amount of work in this area has been devoted to the study of the real refractive indexes for plasmas in which collisions have been neglected. For lossy plasmas the refractive indexes have both real and imaginary parts. Our knowledge of the properties of these complex refractive indexes for plasmas containing both warm ions and warm electrons is rather incomplete. Hence this problem is presently being investigated at NRL and I am going to report some of the preliminary results of this study.

THEORY

The approach used here has been to regard the plasma as a homogeneous, infinite, multi-fluid continuum, consisting of electrons, various types of ions, and neutral molecules. The Maxwell curl equations and the relevant linearized hydrodynamic equations which form the basis for calculations are

$$\nabla \times \underline{E} = -\frac{\partial \underline{B}}{\partial t}$$

$$\nabla \times \underline{H} = K_o \frac{\partial \underline{E}}{\partial t} + \Sigma_s N_s^o q_s \underline{V}_s$$

$$-N_s^o m_s \frac{\partial \underline{V}_s}{\partial t} = -N_s^o q_s (\underline{E} + \underline{V}_s \times \underline{B}_o) + \delta_{e,i_1}^s \nabla P_s + N_s^o m_s \nu_s \underline{V}_s$$

$$N_s^o \nabla \cdot \underline{V}_s = -\frac{\partial N_s}{\partial t} \ .$$

In these equations $\underline{E}$ and $\underline{H}$ are the electric and magnetic fields, $\underline{B}$ is the magnetic induction, K_o represents the free space permittivity, and $\underline{B}_o$ the constant magnetic induction which we assume permeates

the plasma and is aligned along the z-axis of a cartesian coordinate system. The lower case s is an index which represents the various species of charged particles in the plasma. It may assume the values e, i_1, i_2, i_3, etc., where e stands for electrons and i_1, i_2, i_3 stand for ions of type 1, 2, 3, ... to as many ions as we wish to include. N_s, $\underline{V}_s$ and P_s are the average particle number density, velocity, and pressure, respectively, of the s type constituent fluid. The superscript (o) on the number density indicates the ambient unperturbed density. Finally, m_s and q_s are the mass and charge of the s type particle.

The present analysis allows for only one species of warm ions in addition to the warm electrons. This is indicated by the delta function appearing in the momentum conservation equation and defined as

$$\delta^s_{e,i_1} \equiv \begin{cases} 1, & s = e \text{ or } s = i_1 \\ 0, & \text{all other } s \end{cases} .$$

The term which contains ν_s, the effective collision frequency, is only an approximation, valid when the dominant losses are due to collisions between the s type particle and any other type particle having a much lower average velocity.

Applying a 4-D Fourier space-time transform and using an adiabatic equation of state relating P_s and N_s, we can obtain from this set the single equation for the electric field

$$\left[\delta_{\gamma\sigma} n^2 - n_\gamma n_{-\sigma} - \epsilon_{\gamma\sigma}\right] E_\sigma (\underline{k}, \omega) = 0 .$$

The indices γ and σ, when used as subscripts can assume either the values r, ℓ, and p or +1, -1, 0. However, when these indices are used other than as subscripts they can only take on the values +1, -1, and 0. This equation for $\underline{E}$ is written in terms of a space spanned by the unit vectors $\hat{r}$, $\hat{\ell}$, $\hat{p}$ which are related to the usual cartesian unit vectors $\hat{x}$, $\hat{y}$, $\hat{z}$ by the transformations

$$\hat{r} = (\hat{x} - i\hat{y})/\sqrt{2} \qquad \hat{\ell} = (\hat{x} + i\hat{y})/\sqrt{2} \qquad \hat{p} = \hat{z} .$$

In the equation for $\underline{E}$, $\delta_{\gamma\sigma}$ is the Kronecker delta, $\underline{k}$ is the wave propagation vector, and ω is the angular wave frequency.

The matrix $\epsilon_{\gamma\sigma}$ represents the relative dielectric tensor for our warm plasma and it depends on the refractive index $\underline{n}$. The dispersion relation is obtained by taking the determinant of the matrix multiplying $\underline{E}$ and setting it equal to zero. In this paper, c is the velocity of light

in a vacuum, and the sound speed, u_s, is taken as $u_s^2 = 3 k_b T_s/m_s$ where k_b is Boltzmann's constant and T_s is the temperature. Defining the quantities Γ_s, d_s, α_s^2 and β_s as

$$\Gamma_s \equiv 1 + i\nu_s/\omega \qquad d_s \equiv u_s^2/(c^2 \Gamma_s)$$

$$\alpha_s^2 \equiv N_s^o q_s^2/(K_o m_s \omega^2 \Gamma_s) \qquad \beta_s \equiv q_s B_o/(m_s \omega \Gamma_s)$$

the relative dielectric tensor can be written as

$$\epsilon_{\gamma\sigma} = \epsilon_\gamma \delta_{\gamma\sigma} - n_\gamma n_{-\sigma} \Sigma_s \delta^s_{e,i_1} d_s \alpha_s^2 \left[D_s (1 - \gamma\beta_s)(1 - \sigma\beta_s)\right]^{-1} .$$

Here

$$\epsilon_\gamma = 1 - \Sigma_s \alpha_s^2 (1 - \gamma\beta_s)^{-1}$$

which are recognized as the components of the cold plasma dielectric tensor. The quantity D_s

$$D_s = 1 - n^2 d_s \left[\sin^2\theta/(1 - \beta_s^2) + \cos^2\theta\right]$$

contains the magnitude of the refractive index and the angle θ between the external magnetic field and the wave propagation vector. In terms of these quantities the dispersion relation becomes a quartic in the square of the refractive index which we write

$$C_8 n^8 + C_6 n^6 + C_4 n^4 + C_2 n^2 + C_o = 0 .$$

The coefficient C_2, for example, may be written as

$$\begin{aligned} C_2 = &- \epsilon_r \epsilon_\ell \sin^2\theta - \epsilon_p \epsilon_\perp (1 + \cos^2\theta) \\ &- \Sigma_s \delta^s_{e,i_1} d_s \left\{\epsilon_r \epsilon_\ell \epsilon_p \left[\sin^2\theta/(1 - \beta_s^2) + \cos^2\theta\right]\right. \\ &+ \alpha_s^2 \left[\tfrac{1}{2} \epsilon_r \epsilon_p \sin^2\theta/(1 + \beta_s)^2 + \tfrac{1}{2} \epsilon_\ell \epsilon_p \sin^2\theta/(1 - \beta_s)^2\right. \\ &\left.\left. + \epsilon_r \epsilon_\ell \cos^2\theta\right]\right\} . \end{aligned}$$

In this expression for C_2, we use $\epsilon_\perp \equiv \frac{1}{2}(\epsilon_r + \epsilon_\ell)$.

The explicit form for some of the other coefficients are rather lengthy and will not be given here.

NUMERICAL RESULTS

Figures 1 through 7 show the refractive index curves which were obtained using the theory just outlined. For example, in Fig. 1 we have plotted the real part of the refractive index as a function of the ratio of the square of the electron plasma frequency to the wave frequency for propagation along the magnetic field. The present numerical results are for a plasma which contains only a single species of ions. Ionized hydrogen was the ion chosen. The temperatures and the ratio of electron gyro frequency to electron plasma frequency were chosen so as to facilitate the comparison of these preliminary calculations with those given elsewhere for a lossless plasma [1]. The agreement has been very good. For all the figures with the exception of Fig. 3, the collision frequencies have been rather arbitrarily set to 100 per second for electrons and 10 per second for ions.

When collisions are included, the refractive indexes have finite real parts for all frequencies. In Figs. 1-7 the complex refractive indexes are plotted only when the real part is larger than the imaginary part since the primary concern in this paper is to show how collisional absorption depends on the various plasma parameters. In those regions where the imaginary part is smaller than the real part, the wave has lost much of its evanescent character and the imaginary part is mainly due to absorption due to collisions.

The refractive index curves for propagation along the magnetic field, shown in Figs. 1-3, are labeled IP, EP, R, and L. IP and EP refer to ion-plasma waves and electron-plasma waves while L and R represent left circularly polarized electromagnetic waves and right circularly polarized electromagnetic waves, respectively.

In Fig. 2 is shown the imaginary part of the refractive indexes for propagation along the magnetic field. Note that for a given frequency the longitudinally polarized electron and ion plasma waves have much larger imaginary parts of n than the transverse electromagnetic waves R and L. Increasing the collision frequencies by an order of magnitude generally results in an increase in the imaginary part of n by an order of magnitude also as shown by Fig. 3. The curves for propagation across the magnetic field are given in Figs. 4 and 5. The various branches are labeled according to their behavior as $\omega \to \infty$. Thus, MIP, MEP, and MEM(X) refer to the modified ion-plasma, modified electron-plasma and modified extraordinary electromagnetic modes, respectively. The ordinary electromagnetic wave EM(0) is not modified by thermal effects for propagation across $\underline{B}_o$. Note that although from

cold plasma theory we expect an additional EM mode to occur on the low frequency side of both the upper and lower hybrid resonances (UHR and LHR), these resonances are somewhat masked for warm plasmas if one only looks at the real part of the refractive indexes. Actually, the UHR and LHR are approximately at the low part of the "knee" of the MEP and MIP modes. On the other hand, looking at the imaginary part of n it is easy to pick out the UHR and LHR. They occur near the sharp peaks in Fig. 5. On the high frequency side of these peaks which corresponds to completely longitudinal polarizations, the imaginary part of n is quite large and it drops considerably on crossing each hybrid resonance towards the lower frequencies where it has an appreciable transverse component. It seems very typical for the longitudinally polarized waves to have larger real and imaginary parts than the transverse polarized waves. Sudden changes in n often indicate that a wave is changing from a strictly longitudinal polarization to a more general polarization or vice versa. These transition points are much more evident on the graphs of the imaginary part of n than they are on the graphs of the real part.

For propagation at 45^{o} we have used the same labeling as for propagation across $\underline{B}_{o}$. The two branches which do not extend to $\omega = \infty$ appear to be continuations of the MEP and MEM(X) when n is plotted for all frequencies. The imaginary part of n shown in Fig. 7 exhibits three "hybrid resonances" which are somewhat masked in Fig. 6. Based on the previous examples it is to be expected that at these "resonances" the polarization switches from nearly purely longitudinal to a polarization which contains significant transverse components.

In conclusion it should be emphasized that although the curves presented here are for temperatures very much lower than those which normally occur in the ionosphere and only a single ion is included, the cases of higher temperatures and additional cold ions can also be handled by this analysis.

REFERENCE

1. Seshadri, S.R., "Wave Propagation in a Two-Component Warm Plasma", Radio Science J. Res., NBS/USNC-URSI 69D, No. 4, pp 579-597 (1965)

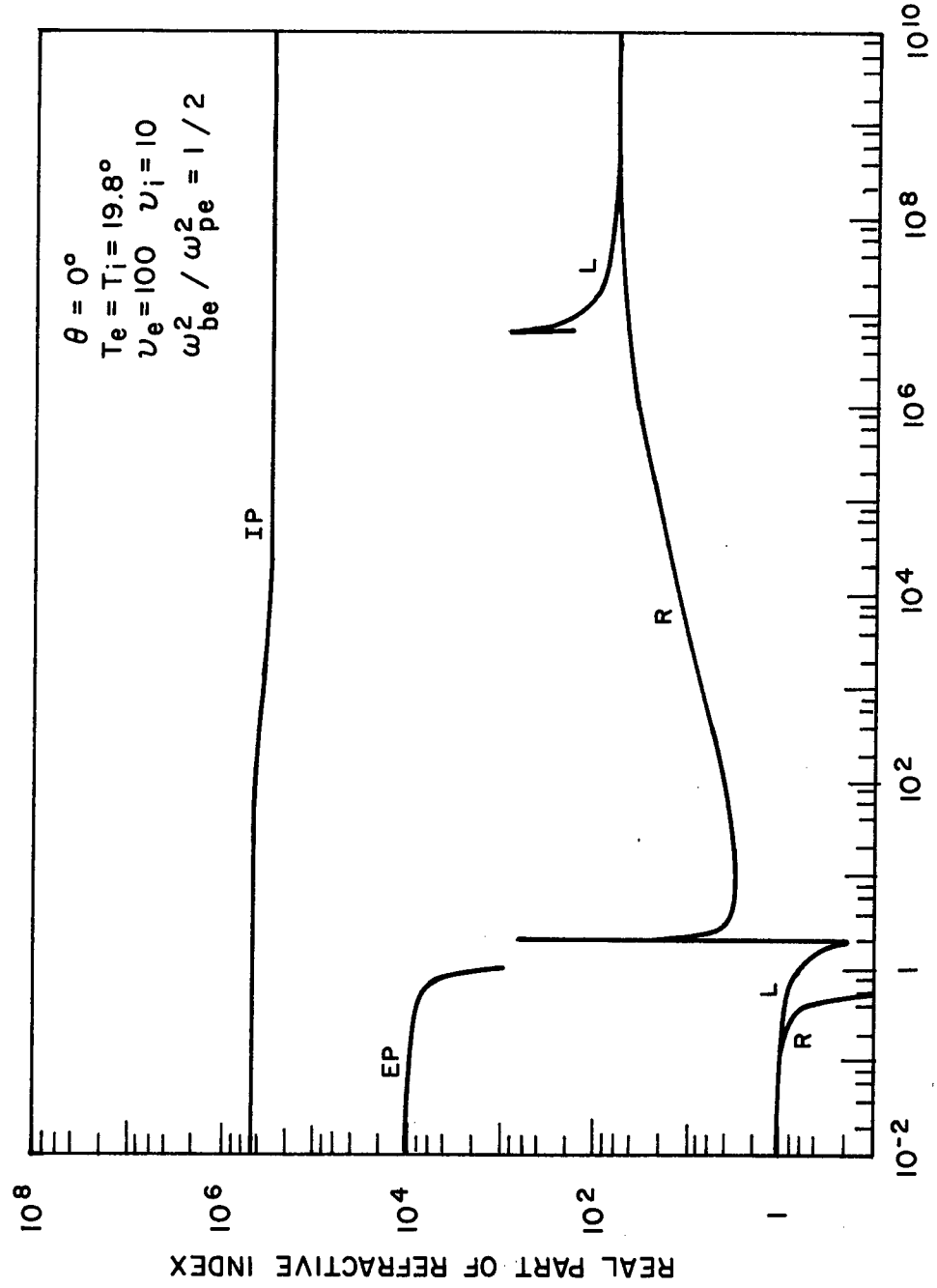
θ = 0°
Te = Ti = 19.8°
νe = 100 νi = 10
ω²be / ω²pe = 1 / 2
IP
EP
L
R
L
R
REAL PART OF REFRACTIVE INDEX
ω²Pe / ω²
10⁸
10⁶
10⁴
10²
1
10⁻²
1
10²
10⁴
10⁶
10⁸
10¹⁰

Figure 1

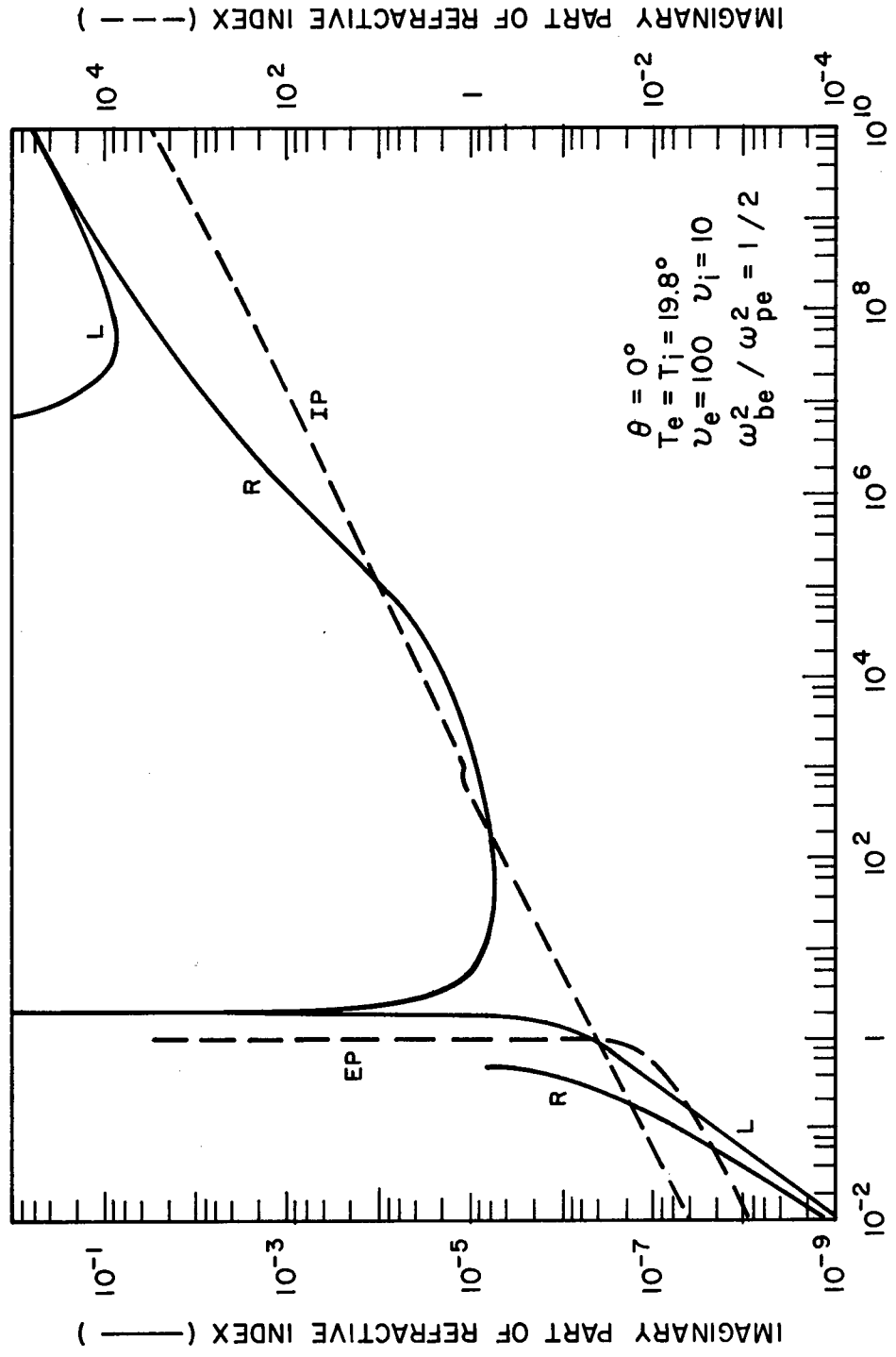
IMAGINARY PART OF REFRACTIVE INDEX (———)
IMAGINARY PART OF REFRACTIVE INDEX (– – –)
$\theta = 0°$
$T_e = T_i = 19.8°$
$\nu_e = 100$ $\nu_i = 10$
$\omega_{be}^2 / \omega_{pe}^2 = 1/2$
L
R
IP
EP
R
L
ω_{Pe}^2 / ω^2

Figure 2

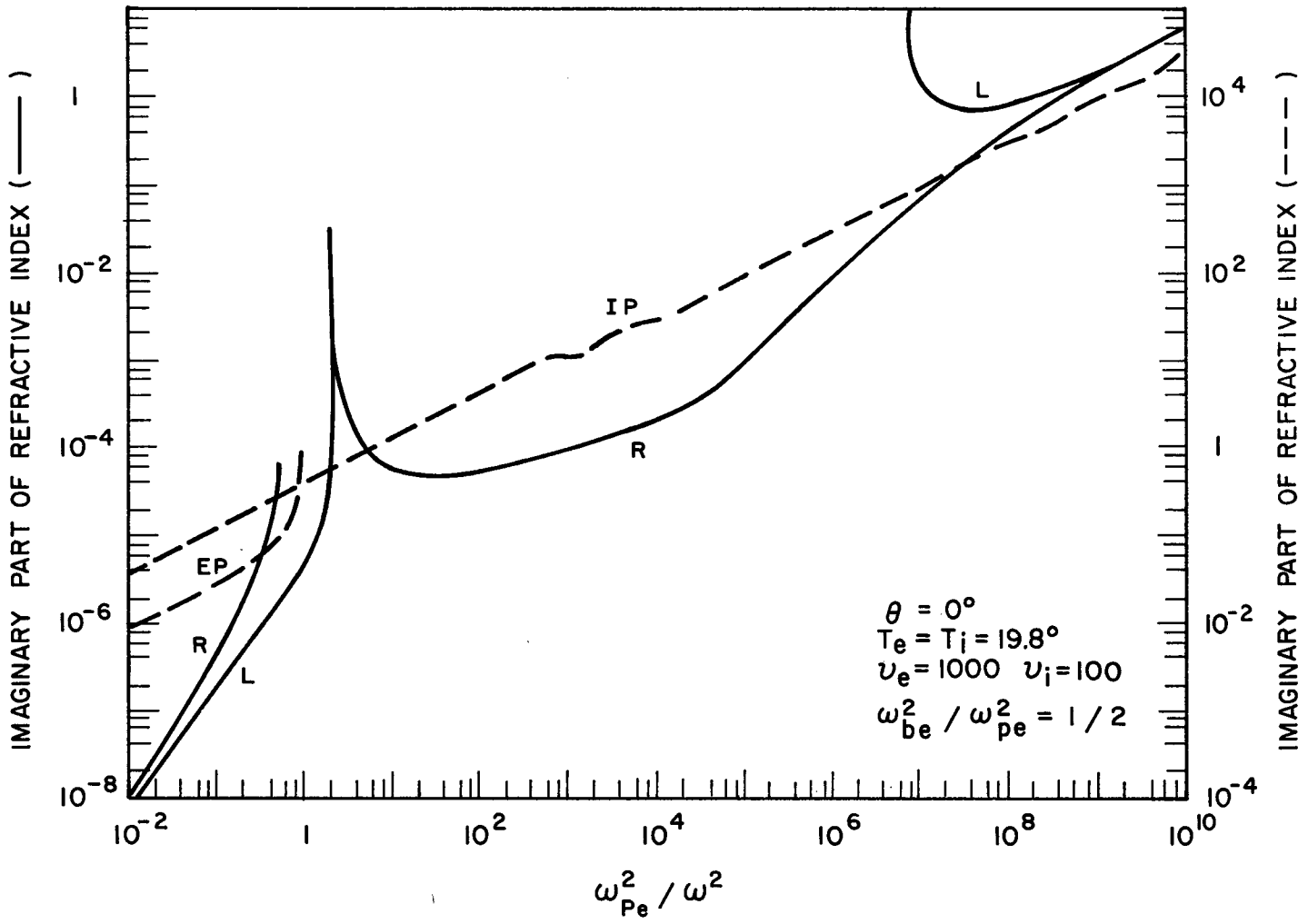

Figure 3

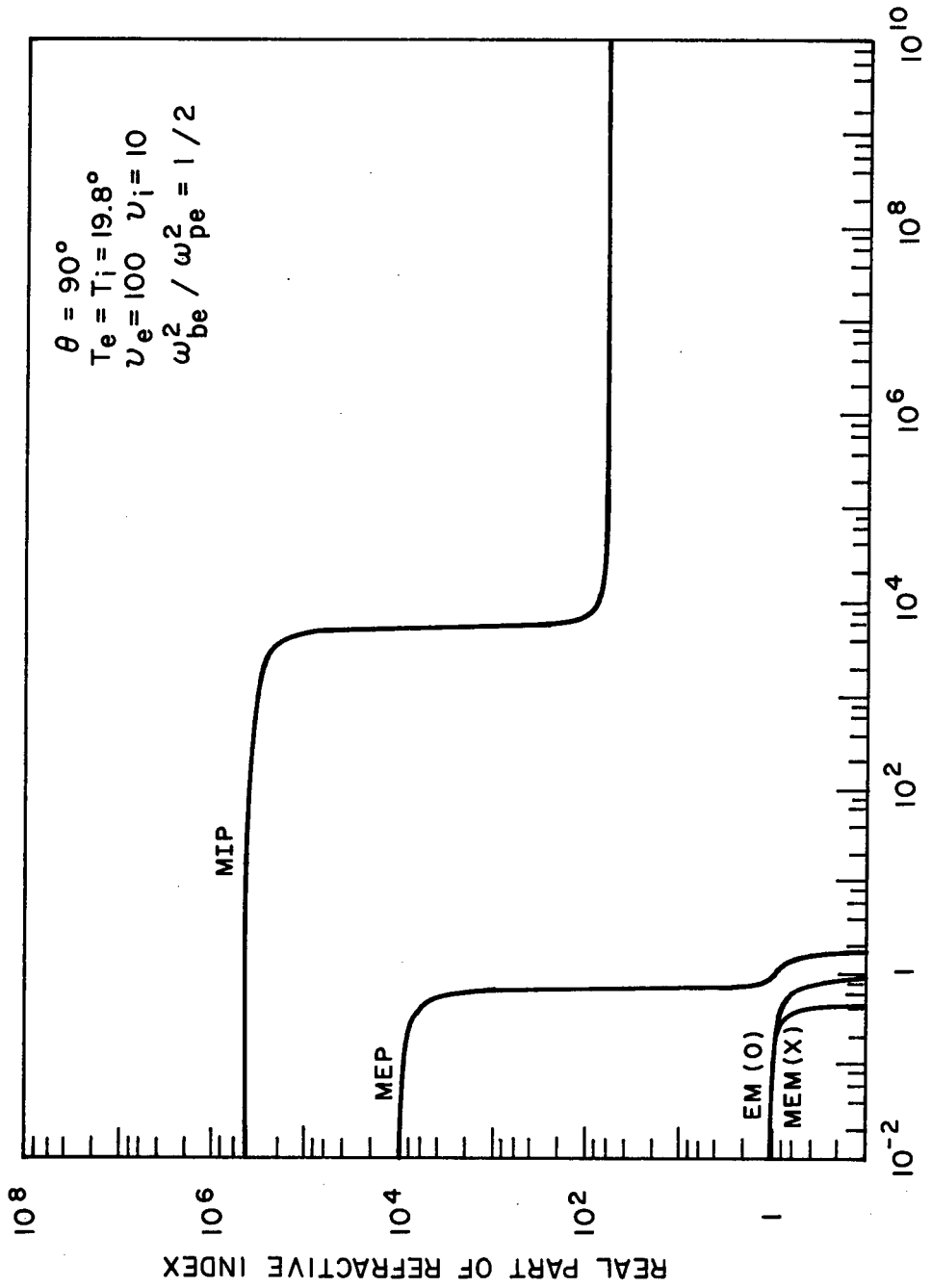
θ = 90°
Te = Ti = 19.8°
νe = 100 νi = 10
ω²be / ω²pe = 1 / 2
MIP
MEP
EM (O)
MEM (X)
REAL PART OF REFRACTIVE INDEX
10⁸
10⁶
10⁴
10²
1
10⁻²
10²
1
10⁴
10⁶
10⁸
10¹⁰
ω²Pe / ω²

Figure 4

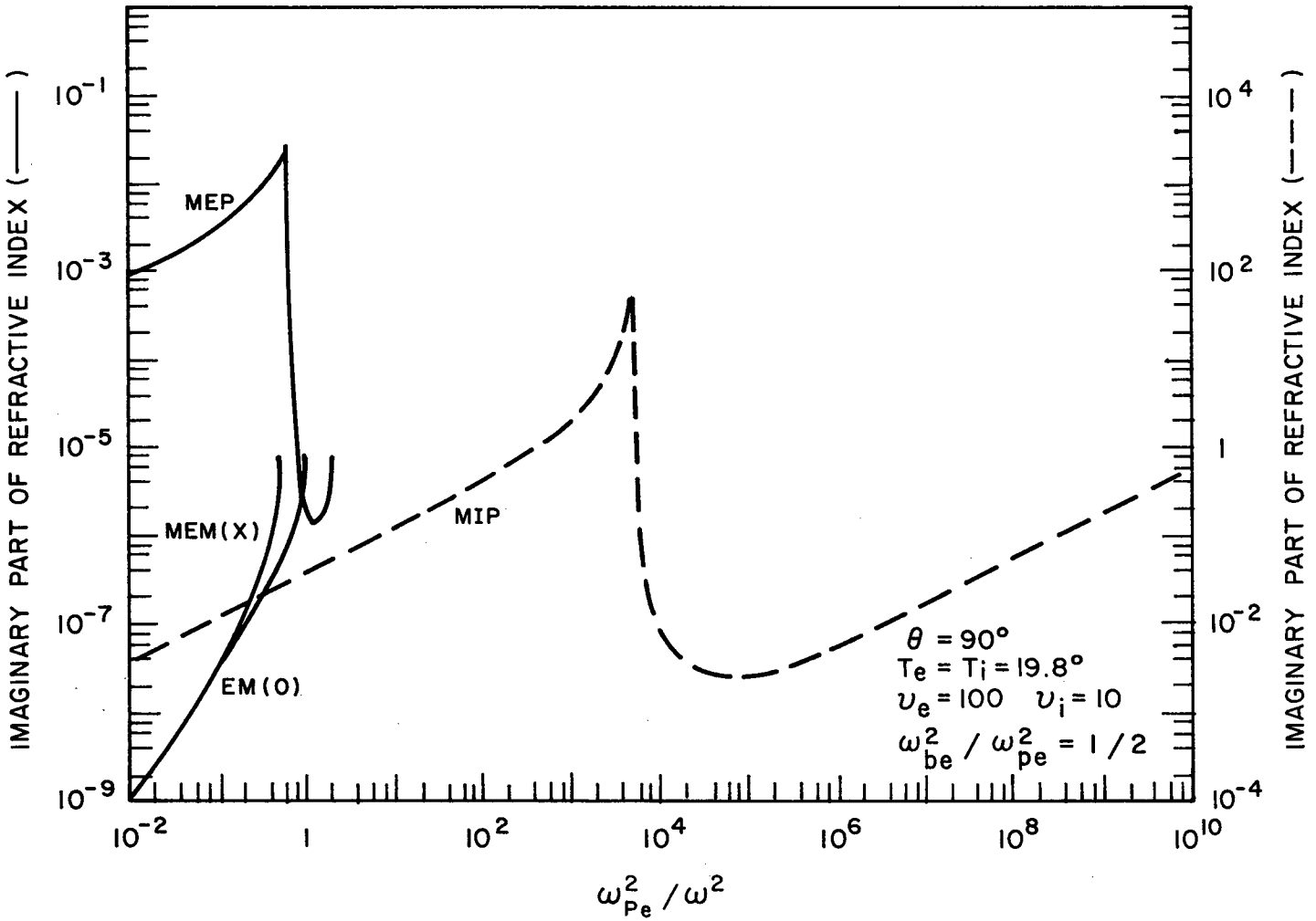

Figure 5

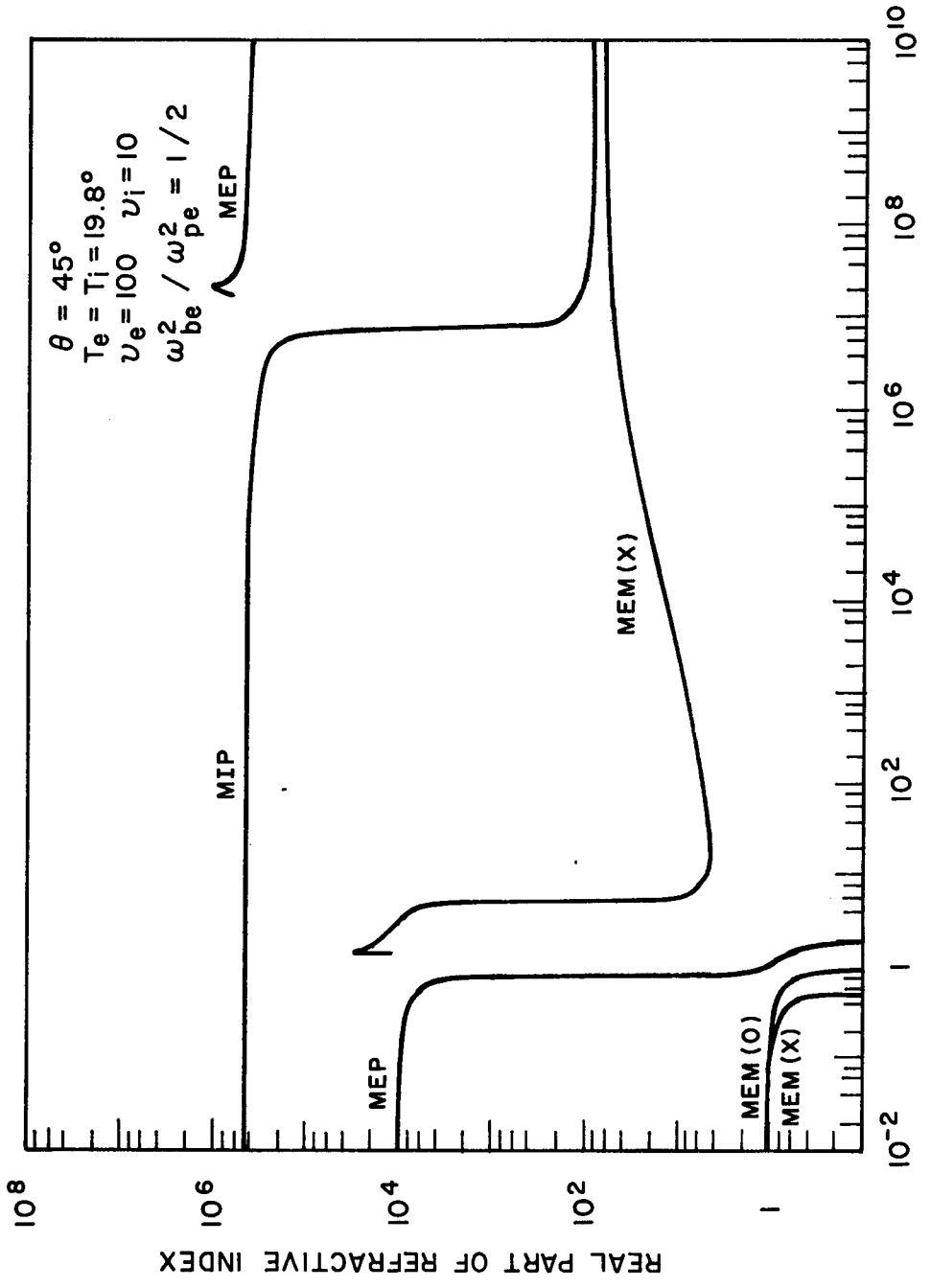
θ = 45°
Te = Ti = 19.8°
νe = 100 νi = 10
ω²be / ω²pe = 1/2
MEP
MIP
MEP
MEM(X)
MEM(O)
MEM(X)
REAL PART OF REFRACTIVE INDEX
10⁸
10⁶
10⁴
10²
1
10⁻²
10²
1
10⁴
10⁶
10⁸
10¹⁰
ω²Pe / ω²

Figure 6

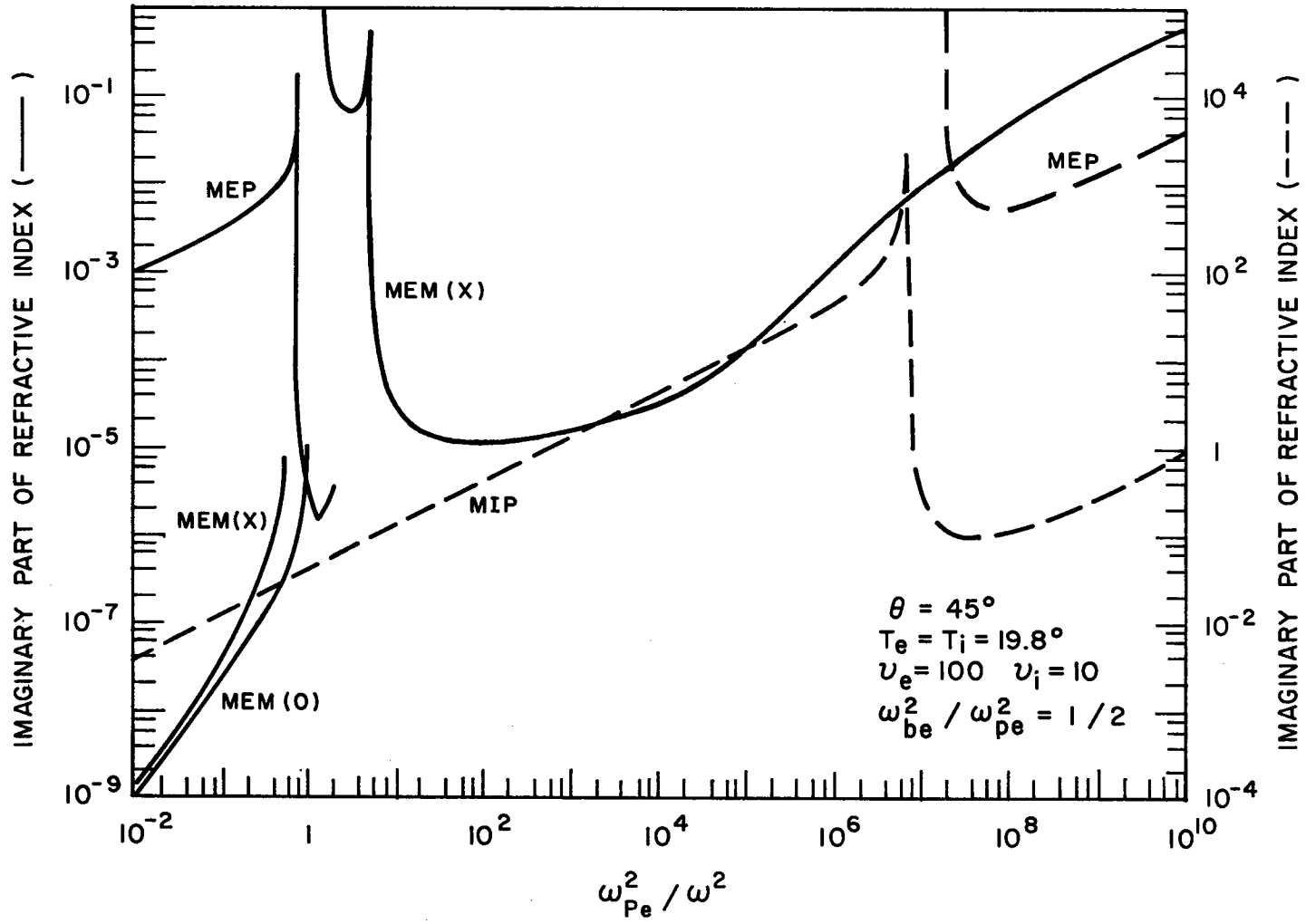

Figure 7

COLLISIONAL DAMPING OF ELECTROSTATIC WHISTLERS

I.P. Shkarofsky
Senior Member of Scientific Staff
RCA Limited, Research Laboratories
Montreal, Quebec, Canada

ABSTRACT

The procedure for properly calculating collisional damping of waves including warm plasma terms in a magnetoplasma is presented. Two cases are outlined, (1) any degree of ionization provided the total collision frequency is less than the angular wave frequency and (2) a slightly ionized gas for any ratio of collision to oscillation frequency. As an example, for the latter case we deduce the dispersion equation of electrostatic whistlers with collisions.

I. INTRODUCTION

The collisional damping of magnetoplasma waves is usually calculated by either using cold plasma theory or warm plasma theory based on an hydrodynamic approach with a pressure tensor. Neither of these two methods is reliable near resonant frequencies, where one should use warm plasma theory based on a kinetic approach. This is especially so if the collision frequency is velocity dependent as usually occurs in slightly ionized gases and always occurs in fully ionized gases. For a slightly ionized gas, most of the analysis has already been done by Johnston (1962). In fact, the sample result given here on the collisional damping of electrostatic whistlers is readily obtainable from his work. We closely follow his procedure for case 2. In case 1 where the collision frequency is less than the oscillation frequency, we follow the procedure of Shkarofsky (1968b), who has already accomplished this task for an isotropic plasma. Here we formally extend this procedure to an anisotropic plasma.

II. ANALYSIS

We apply the Cartesian tensor expansion of the electron velocity distribution function, namely $f(\underset{\sim}{v}) = f_0^0 + f_0(v) + \underset{\sim}{f}_1(v)\cdot\underset{\sim}{v}/v + \underset{\approx}{f}_2(v):\underset{\sim}{\underset{\sim}{vv}} + \ldots$, where f_0^0 is the zero-order isotropic part of the velocity distribution function and f_0 denotes its oscillatory part, $\underset{\sim}{f}_1$ is the directed part and $\underset{\approx}{f}_2$ is the second order tensor part. Johnston (1962, 1966), Shkarofsky (1963) and Shkarofsky et al (1966) derive from the Boltzmann and Fokker-Planck equation, sets of linked equations which for electron-electron collisions also involve integro-differential operators. Letting $\partial/\partial t = i\omega$ and omitting terms which will end up as quadratic in the electric field, the relations up to second order in the expansion are

$$i\omega f_0 = - v\underset{\sim}{\nabla}\cdot\underset{\sim}{f}_1/3 \tag{1}$$

$$i\omega\,\underset{\sim}{f}_1 + v\underset{\sim}{\nabla}\,f_0 + \underset{\sim}{\omega}_b \times \underset{\sim}{f}_1 + \frac{2}{5}\,v\underset{\sim}{\nabla}\cdot\,\underset{\approx}{f}_2 = \frac{e}{m}\,\underset{\sim}{E}\,\frac{\partial f_0^0}{\partial v} + C_1(\underset{\sim}{f}_1) \tag{2}$$

$$i\omega \underset{\approx}{f}_2 + \underset{\sim}{\omega}_b \times \underset{\approx}{f}_2 - \underset{\approx}{f}_2 \times \underset{\sim}{\omega}_b = -\frac{v}{2}\left(\underset{\sim}{\nabla} f_1 + (\underset{\sim}{\nabla} f_1)^T - \frac{2}{3}\underset{\sim}{\nabla}\cdot f_1 \underset{\approx}{I}\right) + C_2(\underset{\approx}{f}_2) \qquad (3)$$

where e, m, v, ω, and E have their usual significance, $\omega_b = eB/m$ is the electron cyclotron frequency, $\underset{\sim}{\nabla}$ is a space gradient, superscript T designates the transpose and $\underset{\approx}{I}$ is the unit tensor. Electron-electron collisional terms in f_0 do not contribute to the current (see Shkarofsky, 1968a) and electron-ion or neutral collisional terms for f_0 are negligible. Also

$$C_1(\underset{\sim}{f}_1) = -(\nu_1 + n_+ Y_{ei}/v^3)\underset{\sim}{f}_1 + C_{1ee}(\underset{\sim}{f}_1) \qquad (4)$$

$$C_2(\underset{\approx}{f}_2) = -(\nu_2 + 3n_+ Y_{ei}/v^3)\underset{\approx}{f}_2 + C_{2ee}(\underset{\approx}{f}_2) \qquad (5)$$

The electron-neutral velocity dependent collision frequencies (ν_1 and ν_2) are obtainable from the Boltzmann collision term [see Shkarofsky et al, 1966, Eq. (3-40a)]. That is

$$\nu_{1,2} = n_n v \int [1 - P_{1,2}(\cos\chi)] I(v,\chi) d^2\Omega$$

are solid angle averages of the electron-neutral differential scattering cross section I weighted by respective Legendre polynomials P_1 and P_2, and n_n is the neutral density. The electron-ion velocity-dependent collision frequencies for $\underset{\sim}{f}_1$ and $\underset{\approx}{f}_2$ are respectively $n_+ Y_{ei}/v^3$ and $3n_+ Y_{ei}/v^3$, derivable from the Fokker-Planck equation [see Shkarofsky et al, 1966, Eq. (7-80)]. Also

$$Y_{ei} = 4\pi(Ze^2/4\pi\varepsilon_0 m)^2 \ln\Lambda, \text{ and for } \omega_p > \omega,\ \Lambda = 3(4\pi\varepsilon_0 kT)^{3/2}/(2Ze^3(\pi n)^{\frac{1}{2}})$$

ω_p is the electron plasma frequency, T the temperature, n the density, and ε_0, κ have their usual meaning. Finally C_{1ee} and C_{2ee} are the Fokker-Planck collision terms required for electron-electron collisions. The reader is referred to either Shkarofsky et al (1966, Eqs. (7-75) and (7-77) or Shkarofsky (1968b) for their integro-differential forms.

III. THE SLIGHTLY IONIZED PLASMA

In this case, we assume $\nu_{ei} << \nu_{10}$, where ν_{ei} is an average electron-ion and ν_{10} an average electron-neutral collision frequency. Then we can neglect C_{1ee}, C_{2ee} and the Y_{ei} terms in Eqs. (4) and (5).

Let us define five vector operators, O_1 to O_5 where $\underset{\sim}{A}$ is a vector and $\underset{\approx}{B}$ is a tensor.

$$(O_1)^{-1}\underset{\sim}{A} \equiv i\omega_1 \underset{\sim}{A} + \underset{\sim}{\omega}_b \times \underset{\sim}{A} \quad \text{where } \omega_1 = \omega - i\nu_1 \qquad (6a)$$

$$(O_2)^{-1}\underset{\approx}{B} = i\omega_2 \underset{\approx}{B} + (\underset{\sim}{\omega}_b \underset{\sim}{x})\underset{\approx}{B} - \underset{\approx}{B}(\underset{\sim}{x}\underset{\sim}{\omega}_b) \quad \text{where } \omega_2 = \omega - i\nu_2 \qquad (6b)$$

$$O_3\underset{\sim}{\underset{\sim}{B}} = \underset{\sim}{\nabla}\cdot\underset{\sim}{\underset{\sim}{B}} \; ; \qquad O_4\underset{\sim}{\underset{\sim}{A}} = \underset{\sim}{\underset{\sim}{\nabla\nabla}}\cdot\underset{\sim}{\underset{\sim}{A}} \tag{6c,d}$$

and

$$O_5\underset{\sim}{A} = \underset{\sim}{\nabla}\,\underset{\sim}{A} + (\nabla\underset{\sim}{A})^T - \frac{2}{3}\,\underset{\sim}{\nabla}\cdot\underset{\sim}{A}\,\underset{\sim}{\underset{\sim}{I}} \tag{6e}$$

Explicit forms of O_1 and O_2 in vector notation are given in the Appendix. Then we can write Eq. (3) as $\underset{\sim}{f}_2 = (-1/2)O_2O_5v\underset{\sim}{f}_1$ and substituting this and Eq. (1) into (2) yields

$$\underset{\sim}{f}_1 = \frac{e}{m}\,O_1\underset{\sim}{E}\,\frac{\partial f_0^0}{\partial v} + \frac{1}{3i\omega}\,O_1O_4v^2\underset{\sim}{f}_1 + \frac{1}{5}\,O_1O_3O_2O_5\,v^2\underset{\sim}{f}_1 \tag{7}$$

The first term is the cold plasma result, the latter two are "warm" plasma terms, exemplified by the velocity squares within them. These thermal terms are small so to first order $\underset{\sim}{f}_1 = (e/m)O_1\underset{\sim}{E}\,\partial f_0^0/\partial v$. Substituting this into the right hand side of Eq. (6) gives the next order approximation, namely

$$\underset{\sim}{f}_1 = \frac{e}{m}\,O_1\underset{\sim}{E}\,\frac{\partial f_0^0}{\partial v} + \frac{e}{3i\omega m}\,O_1O_4O_1\underset{\sim}{E}\,v^2\,\frac{\partial f_0^0}{\partial v} + \frac{e}{5m}\,O_1O_3O_2O_5O_1\,\underset{\sim}{E}\,v^2\,\frac{\partial f_0^0}{\partial v} \tag{8}$$

The current and conductivity tensor are obtained by integration

$$\underset{\sim}{J} = -(4\pi en/3)\int\underset{\sim}{f}_1v^3dv \equiv \underset{\approx}{\sigma}\cdot\underset{\sim}{E} \tag{9}$$

We introduce the following notation for velocity averages over f_0^0, namely

$$\langle v^{-2}\partial A/\partial v\rangle = -\,4\pi\int A(\partial f_0^0/\partial v)dv \tag{10}$$

provided that the integrand Af_0^0 vanishes at both limits, 0 and ∞. Thus Eq. (7) yields for $\underset{\approx}{\sigma}$ with $\omega_p^2 \equiv ne^2/\varepsilon_0 m$:

$$\underset{\approx}{\sigma} = \omega_p^2\varepsilon_0\left[\left\langle\frac{1}{3v^2}\,\frac{\partial}{\partial v}\,(v^3O_1) + \frac{1}{9i\omega v^2}\,\frac{\partial}{\partial v}\,(v^5O_1O_4O_1) + \frac{1}{15v^2}\,\frac{\partial}{\partial v}\,(v^5O_1O_3O_2O_5O_1)\right\rangle\right]$$

$$\equiv \omega_p^2\varepsilon_0\left\langle\left\langle\frac{-j}{3v^2}\,\frac{\partial}{\partial v}\,(v^3\underset{\approx}{S})\right\rangle\right\rangle \tag{11}$$

The dielectric constant and dispersion equations then follow from

$$\underset{\approx}{\varepsilon} = \underset{\approx}{I} + \underset{\approx}{\sigma}/i\omega\varepsilon_0 \quad \text{and} \quad \left|\underset{\sim}{k}\underset{\sim}{k} - k^2\underset{\approx}{I} + \underset{\approx}{\varepsilon}\right| = 0 \tag{12a,b}$$

where we substitute $-i\underset{\sim}{k}$ for a space gradient $\underset{\sim}{\nabla}$. The explicit velocity dependent forms of the elements of $\underset{\approx}{\sigma}$ in terms of $\underset{\sim}{k}$ in Eq. (8) before velocity averaging are given by Johnston's (1962) $\underset{\approx}{S}$ matrix as defined above and need not be repeated here. Some mention will be made in Section V.

IV THE PARTIALLY IONIZED GAS WITH SOME COLLISIONS

In this section, all collisions are included subject to $C_{1,2} \ll \omega$. We redefine operators O_1 and O_2 (see Eqs. (6a,b)) to be

$$(O_1)^{-1}\underset{\sim}{A} \equiv i\omega\underset{\sim}{A} + \underset{\sim}{\omega}_b \times \underset{\sim}{A} \qquad (13a)$$

$$(O_2)^{-1}\underset{\approx}{B} = i\omega\underset{\approx}{B} + \underset{\sim}{\omega}_b \times \underset{\approx}{B} - \underset{\approx}{B} \times \underset{\sim}{\omega}_b \qquad (13b)$$

so that all operators O_1 to O_5 are now velocity independent. Eq. (3) now becomes after reiteration for small C_2

$$\underset{\sim}{f}_2 = -\tfrac{1}{2}O_2O_5v\underset{\sim}{f}_1 - \tfrac{1}{2}(O_2)^2O_5C_2(v\underset{\sim}{f}_1)$$

Substituting this and Eq.(1) into (2) results in

$$\underset{\sim}{f}_1 = \frac{e}{m}O_1\underset{\sim}{E}\frac{\partial f_0^0}{\partial v} + O_1C_1(\underset{\sim}{f}_1) + \frac{1}{3i\omega}O_1O_4v^2\underset{\sim}{f}_1 + \frac{1}{5}O_1O_3O_2O_5v^2\underset{\sim}{f}_1 + \frac{1}{5}O_1O_3(O_2)^2O_5vC_2(v\underset{\sim}{f}_1)$$

The dominant terms are the first two, namely

$$\underset{\sim}{f}_1 \approx (e/m)[O_1\underset{\sim}{E}\,\partial f_0^0/\partial v + (O_1)^2\underset{\sim}{E}\,C_1(\partial f_0^0/\partial v)]$$

We can substitute this approximation into all the other $\underset{\sim}{f}_1$ factors on the right-hand side, except for the second term with C_1 for which we have to reiterate twice. We find

$$\begin{aligned}\underset{\sim}{f}_1 = {} & \frac{e}{m}\left[O_1\underset{\sim}{E}\frac{\partial f_0^0}{\partial v} + (O_1)^2\underset{\sim}{E}C_1\left(\frac{\partial f_0^0}{\partial v}\right)\right] \\ & + \left[\frac{e}{3mi\omega}O_1O_4O_1\underset{\sim}{E} + \frac{e}{5m}O_1O_3O_2O_5O_1\underset{\sim}{E}\right]v^2\frac{\partial f_0^0}{\partial v} \\ & + \left[\frac{e}{3mi\omega}O_1O_4(O_1)^2\underset{\sim}{E} + \frac{e}{5m}O_1O_3O_2O_5(O_1)^2\underset{\sim}{E}\right]v^2C_1\left(\frac{\partial f_0^0}{\partial v}\right) \\ & + \frac{e}{5m}O_1O_3(O_2)^2O_5O_1\underset{\sim}{E}\,vC_2\left(v\frac{\partial f_0^0}{\partial v}\right) \\ & + \left[\frac{e}{3mi\omega}(O_1)^2O_4O_1\underset{\sim}{E} + \frac{e}{5m}(O_1)^2O_3O_2O_5O_1\underset{\sim}{E}\right]C_1\left(v^2\frac{\partial f_0^0}{\partial v}\right) \qquad (14)\end{aligned}$$

We now calculate the conductivity tensor using Eq. (9) and the following relations derived by Shkarofsky (1968b).

$$-\frac{4\pi}{3}\int dv\, v^3\frac{\partial f_0^0}{\partial v} \equiv 1; \qquad -\frac{4\pi}{3}\int dv\, v^5\frac{\partial f_0^0}{\partial v} \equiv 5\,v_t^2 \qquad (15a,b)$$

$$(4\pi/3)\int dv\, v^3C_1(\partial f_0^0/\partial v) = \nu_{1o} + \nu_{ei} \qquad (15c)$$

$$(4\pi/3)\int dv\, v^5C_1(\partial f_0^0/\partial v) = (4\pi/3)\int dv\, v^3C_1(v^2\partial f_0^0/\partial v) = v_t^2(5\nu_{1t} + 2\nu'_{ei}) \qquad (15d)$$

$$(4\pi/3)\int dv\ v^4 C_2(v\,\partial f_0^0/\partial v) = v_t^2(5\nu_{2t} + 6\nu'_{ei} + 3\sqrt{2}\,\nu'_{ee}) \qquad (15e)$$

where

$$v_t = (\kappa T/m)^{\frac{1}{2}} \equiv (4\pi/3)\int f_0^0\ v^4\ dv$$

$$\nu_{10} \equiv -(4\pi/3)\int v^3 \nu_1 (\partial f_0^0/\partial v)\ dv$$

$$\nu_{1t,2t} v_t^2 \equiv -(4\pi/15)\int v^5 \nu_{1,2} (\partial f_0^0/\partial v) dv$$

$$\nu_{ei} \equiv (4\pi/3) n_+ Y_{ei} f_0^0(v=0)$$

$$\nu'_{ei} v_t^2 \equiv (4\pi/3) n_+ Y_{ei} \int v\ f_0^0\ dv$$

$$\nu'_{ee} v_t^2 \equiv (8\pi\sqrt{2}/3) Y \int_0^\infty v\, f_0^0 dv \left(4\pi \int_0^v f_0^0 v^2\ dv\right)$$

$Y = Y_{ei}$ when $Z = 1$. For a Maxwellian distribution

$$\nu_{ei} = \nu'_{ei} = (4/3)(2\pi)^{\frac{1}{2}} n_+ (Ze^2/4\pi\varepsilon_0\kappa T)^2 (\kappa T/m)^{\frac{1}{2}} \ln \Lambda$$

The expression for the electron-electron collision frequency ν'_{ee} is as above for a Maxwellian with $n_+ = n_e$ and $Z = 1$. Its contribution appears only in C_2.

Thus we obtain

$$\begin{aligned} \underset{\approx}{g}\cdot\underset{\sim}{E} = \omega_p^2 \varepsilon_0 \Big\{ & 0_1 \underset{\sim}{E} - (\nu_{10} + \nu_{ei})(0_1)^2 \underset{\sim}{E} + (5v_t^2/3i\omega) 0_1 0_4 0_1 \underset{\sim}{E} \\ & + v_t^2 0_1 0_3 0_2 0_5 0_1 \underset{\sim}{E} - (v_t^2/5)(5\nu_{2t} + 6\nu'_{ei} + 3\sqrt{2}\,\nu'_{ee}) 0_1 0_3 (0_2)^2 0_5 0_1 \underset{\sim}{E} \\ & - (v_t^2/3i\omega)(5\nu_{1t} + 2\nu'_{ei}) [0_1 0_4 (0_1)^2 + (0_1)^2 0_4 0_1] \underset{\sim}{E} \\ & - (v_t^2/5)(5\nu_{1t} + 2\nu'_{ei}) [0_1 0_3 0_2 0_5 (0_1)^2 + (0_1)^2 0_3 0_2 0_5 0_1] \underset{\sim}{E} \end{aligned} \qquad (16)$$

It would be useful to complete the algebra of multiplying these 0 operators and present the final forms. Pytte (1969) has provided results based on a slightly different approach and a comparison should be made. This will however not be demonstrated here.

VI. APPLICATION TO ELECTROSTATIC WHISTLERS

Electrostatic whistlers satisfy the dispersion equation $\underset{\sim}{k}\cdot\underset{\approx}{\varepsilon}\cdot\underset{\sim}{k} = 0$, a simplification of (12b) valid for longitudinal waves. Furthermore since $\omega_p >> \omega_b, \omega, \nu$, the main contribution to $\underset{\approx}{\varepsilon}$ comes from $\underset{\approx}{\sigma}$ (see Eq. (12a)) so that a further simplification is

$$\underset{\sim}{k}\cdot\underset{\approx}{\sigma}\cdot\underset{\sim}{k} = 0 \tag{17}$$

In the ionosphere, conditions usually fall either into case 2 (Section III) or case 1 (Section IV). Section III is always applicable below 150 kms. Shkarofsky (1961) shows that if the electron temperature is three times the neutral or ion temperature above 150 km, the gas is only slightly ionized at least up to 250 km. A higher electron temperature is typical of daytime conditions. In this situation, Section III applies up to 250 km. Above 250 km, although one is dealing with a partially ionized gas, the total collision frequency is of the order of 1000 sec^{-1} or less, so that Section IV is applicable for frequencies $f > 10^3/2\pi$, say above 300 cycles/sec. During nighttime, when the electron and neutral temperatures are of the same order, our analysis is not applicable between 150 and 250 km unless the frequency is above 1000 cycles/sec in which case Section IV is again useful.

Consider the situations when Section III is applicable. The dispersion relation for electrostatic whistlers follows from Eq. (11) and Johnston's (1962, p. 1215) S matrix subject to $\omega_b > \omega_{1,2}$. We find with $\underset{\sim}{k}\cdot\underset{\sim}{B} \equiv kB\cos\theta$

$$\underset{\sim}{k}\cdot\underset{\approx}{S}\cdot\underset{\sim}{k} \approx -\frac{\omega_1 \sin^2\theta}{(\omega_b^2 - \omega_1^2)} + \frac{\cos^2\theta}{\omega_1} + \frac{k^2v^2}{3\omega_1}\cos^4\theta\left(\frac{1}{\omega} + \frac{4}{5\omega_2}\right)$$

$$+ \frac{k^2v^2\omega_1 \sin^4\theta}{3\omega_b^4}\left[\frac{\omega_1}{\omega} + \frac{\omega_1}{5\omega_2} - \frac{3\omega_2}{20\omega_1} - \frac{3}{5}\right] - \frac{k^2v^2\omega_2 \sin^2\theta\cos^2\theta}{5\omega_b^2\omega_1^2}$$

where we recall $\omega_{1,2} = \omega - i\nu_{1,2}$. The dispersion relation is thus

$$0 = \int\left[\frac{\omega_1 \sin^2\theta}{\omega_b^2 - \omega_1^2} - \frac{\cos^2\theta}{\omega_1}\right]\frac{\partial f_0^0}{\partial v} v^3\, dv$$

$$- k^2\int\left[\frac{\omega_1 \sin^4\theta}{3\omega_b^4}\left(\frac{\omega_1}{\omega} + \frac{\omega_1}{5\omega_2} - \frac{3\omega_2}{20\omega_1} - \frac{3}{5}\right)\right.$$

$$\left. + \frac{\cos^4\theta}{3\omega_1^2}\left(\frac{1}{\omega} + \frac{4}{5\omega_2}\right) - \frac{\omega_2 \sin^2\theta\cos^2\theta}{5\omega_1^2\omega_b^2}\right]\frac{\partial f_0^0}{\partial v} v^5\, dv \tag{18a}$$

which can also be represented in terms of averages as in Eqs. (10) and (11) thus

$$\left\langle \frac{\sin^2\theta}{3v^2}\frac{\partial}{\partial v}\left(\frac{v^3\omega_1}{\omega_b^2-\omega_1^2}\right) - \frac{\cos^2\theta}{3v^2}\frac{\partial}{\partial v}\left(\frac{v^3}{\omega_1}\right)\right\rangle$$

$$- k^2\left\langle\left\langle \frac{\sin^4\theta}{9v^2\omega_b^4}\frac{\partial}{\partial v}\left(\frac{v^5\omega_1^2}{\omega} + \frac{v^5\omega_1^2}{5\omega_2} - \frac{3v^5\omega_2}{20} - \frac{3v^5\omega_1}{5}\right)\right\rangle\right\rangle$$

$$- k^2\left\langle \frac{\cos^4\theta}{9v^2}\frac{\partial}{\partial v}\left(\frac{v^5}{\omega_1^2\omega} + \frac{4v^5}{5\omega_2\omega_1^2}\right)\right\rangle + \frac{k^2\sin^2\theta\cos^2\theta}{5\omega_b^2}\left\langle\frac{1}{3v^2}\frac{\partial}{\partial v}\left(\frac{v^5\omega_2}{\omega_1^2}\right)\right\rangle = 0 \qquad (18b)$$

For example if ν_1 and ν_2 are independent of velocity, then we obtain to first order, omitting $\langle v^2\rangle = 3v_t^2$ terms:

$$\omega_1 = \omega_b\cos\theta \quad \text{or} \quad \omega = \omega_b\cos\theta + i\nu_1 \quad \text{and} \quad \omega_2 = \omega_b\cos\theta + i(\nu_1 - \nu_2)$$

namely the electrostatic whistler resonance. If $\omega << \omega_b$, then θ is near 90^o so that $\sin\theta \approx 1$. We can substitute these approximations into the right hand thermal terms to yield

$$\omega \approx \omega_b\cos\theta + i\nu_1 + \frac{k^2v_t^2\cos\theta}{2\omega_b}\left(\frac{10}{3}\frac{\omega_1}{\omega} + \frac{5}{3}\frac{\omega_1}{\omega_2} - \frac{5}{4}\frac{\omega_2}{\omega_1} - 1\right) \qquad (19)$$

If ν_1 is velocity dependent and $\sin\theta \approx 1$, we obtain to first order a frequency shift

$$\omega \approx [\omega_b^2\cos^2\theta/h_o - \nu_{1o}^2(1 - g_o/h_o)^2/4]^{\frac{1}{2}} + i\nu_{1o}(1 + g_o/h_o)/2 \qquad (20)$$

where g_o and h_o are correction factors given by Shkarofsky et al (1966, p. 316).

Equations (18a,b) and (19) contain collisional terms both in the cold and warm parts of the dispersion relation. We see that the wave is severely damped if $\nu_1 \gtrsim \omega$. This is to be expected for electrostatic whistlers. This conclusion is in contrast to the damping of circular wave (em) whistlers which are only damped if $\nu_1 \gtrsim \omega_b$.

VII. CONCLUSION

We provided the warm magnetoplasma dielectric constant including collisional damping (in the cold and warm terms) for two cases. The dispersion relation was then illustrated for electrostatic whistlers in a slightly ionized plasma.

APPENDIX

To proceed with the operations we need the forms of O_1 and O_2. Ogasawara (1969) has deduced the vector form of O_2 and also gives O_1.

$$O_1\underset{\sim}{A} = [i\omega(\omega_b^2 - \omega_1^2)]^{-1}\ [-\omega^2\underset{\sim}{A} + \underset{\sim}{\omega_b}\underset{\sim}{\omega_b}\cdot\underset{\sim}{A} - i\omega_1\ \underset{\sim}{\omega_b} \times \underset{\sim}{A}]$$

$$O_2\underset{\approx}{B} = [i\omega(\omega_b^2 - \omega_2^2)(4\omega_b^2 - \omega_2^2)]^{-1}\Big\{(\omega_b^2 - \omega_2^2)(2\omega_b^2 - \omega_2^2)\ \underset{\approx}{B}$$

$$-(\omega_2^2 + 2\omega_b^2)(\underset{\sim}{\omega}_b\ \underset{\sim}{\omega}_b \cdot \underset{\approx}{B} + \underset{\approx}{B} \cdot \underset{\sim}{\omega}_b \underset{\sim}{\omega}_b) - 2(\omega_b^2 - \omega_2^2)\ \underset{\sim}{\omega}_b \times \underset{\approx}{B} \times \underset{\sim}{\omega}_b$$

$$- i\omega_2(\omega_b^2 - \omega_2^2)(\underset{\sim}{\omega}_b \times \underset{\approx}{B} - \underset{\approx}{B} \times \underset{\sim}{\omega}_b) + 6\ \underset{\sim}{\omega}_b(\underset{\sim}{\omega}_b \cdot \underset{\approx}{B} \cdot \underset{\sim}{\omega}_b)\ \underset{\sim}{\omega}_b$$

$$+ 3i\omega_2(\underset{\sim}{\omega}_b \underset{\sim}{\omega}_b \cdot \underset{\approx}{B} \times \underset{\sim}{\omega}_b - \underset{\sim}{\omega}_b \times \underset{\approx}{B} \cdot \underset{\sim}{\omega}_b\ \underset{\sim}{\omega}_b\Big\}$$

Matrix forms can also be written for O_1 to O_5 in Cartesian coordinates as illustrated by Johnston (1962).

REFERENCES

Johnston, T.W. (1962), Can. J. Phys. 40, 1208.

Johnston, T.W. (1966), J. Math. Phys. 7, 1453.

Ogasawara, M. (1969), J. Phys. Soc. Japan 27, 271. See also 28, 748 (1970).

Pytte, A. (1969), Phys. Rev. 179, 138. See also Phys. Fluids 13, 767 (1970).

Shkarofsky, I.P. (1961), Proc. IRE, 49, 1857.

Shkarofsky, I.P. (1963), Can. J. Phys. 41, 1753, 1776, 1787.

Shkarofsky, I.P., T.W. Johnston and M.P. Bachynski (1966), The Particle Kinetics of Plasmas, Addison-Wesley Publishing Company, Inc. Reading, Massachusetts.

Shkarofsky, I.P. (1968a), Plasma Physics 10, 169.

Shkarofsky, I.P. (1968b), Phys. Fluids 11, 2454, Appendix.

PROCEDURES FOR ESTIMATING IMPEDANCE AND RADIATION PROPERTIES OF ELF/VLF ANTENNAS IN THE IONOSPHERE

W. S. AMENT
Physicist (Consultant)
Applications Research Division
Naval Research Laboratory

A useful theory of satellite antennas in warm magnetoplasmas should give:

- The impedance Z seen from the antenna feed line

- The far-field radiation resistance R, a term of Z corresponding to power delivered to usefully propagating waves

- Perhaps some indication of the angular pattern of the propagating EM power or of power in other useful modes

For thin dipoles of half-length L, radius a, and thin looped-strip antennas of small width 2a, loop radius L, procedures have been developed giving roughly 99% of the "reactive" part of the impedance Z in closed form and giving the radiation resistance R as a machine-programmed numerical integral. These procedures are effective for a cold magnetoplasma, one described by an anisotropic dielectric tensor, and for finite, though not too large, antenna scales L.

We sketch these procedures and discuss their adaptation to the ELF/VLF satellite antenna problem, which should include the following:

- Some allowance for ohmic losses in the antenna metal, particularly for loops

- Effect of satellite motion as Lorentz-transforming the medium seen by the antenna into a triaxial medium

- Effect of a finite plasma temperature

- Effect of ion sheath, including V×B or other bias

- Effect of satellite wake and nonideal geometry

- All combinations of the above together with effects of nonlinearities due to the high RF power levels in radiating antennas

Naturally, the methods proposed here are adaptations of the cold-plasma methods and do not pretend to cope with all the problems, as will be seen.

The simplest formal procedures for computing Z and R are the complex-power method and the emf variational method. We find no textbook giving a clear account of the interpretations of the Z and R even for the free-space case. Therefore, we deal at some length with interpretations. All discussion is qualitative.

As a general antenna, we have a closed, perfectly conducting, smooth metal surface necked down to a small radius at a feed point; the feed is at a gap or "slice generator" cut through the neck. A uniform driving surface current totaling I_g flows across the gap from and to the metal surface against a uniform gap-voltage $V_g = ZI_g$, where Z is the impedance to be determined. The current I_g distributes itself continuously over the metal according to some surface current density $\mathbf{j}(\sigma)$, which also represents current *density* across the gap. The electric field $\mathbf{E}(\mathbf{p})$ radiated to a general point $\mathbf{p}$ by all currents is given by

$$\mathbf{E}(\mathbf{p}) = \iint_{\text{ant + gap}} \mathbf{G}(\mathbf{p} - \sigma) \cdot \mathbf{j}(\sigma)\, d\sigma\,, \tag{1}$$

where $\mathbf{G}$ is the dyadic Green's function for the ambient medium, assumed homogeneous here. Let σ' be a second point on the metal; $\mathbf{j}^*(\sigma')$ is the (complex conjugate) surface current density, a vector tangential to the metal. The integral

$$\mathbf{j}^*(\sigma') \cdot \mathbf{E}(\sigma') = \iint_{\text{ant + gap}} \mathbf{j}^*(\sigma') \cdot \mathbf{G}(\sigma' - \sigma) \cdot \mathbf{j}(\sigma) \cdot d\sigma \tag{2}$$

vanishes (because the tangential $\mathbf{E}$ vanishes on the perfectly conducting metal) *except* when σ' is in the gap. Then

$$I_g^* V_g = ZI_g^* I_g = \iint_{\text{ant + gap}} d\sigma \iint_{\text{ant + gap}} d\sigma'\, \mathbf{j}^*(\sigma') \cdot \mathbf{G}(\sigma' - \sigma) \cdot \mathbf{j}(\sigma) \tag{3}$$

gives the "complex power" introduced in driving the gap current across the gap against the total radiated $\mathbf{E}$ field, evaluated in the gap. That is, V_g is taken as (gap width) $\times$ (component of $\mathbf{E}$ transverse to the gap), the latter being taken as uniform over the (small) gap circumference. Finally, the relation between surface current $\mathbf{j}$ and rf magnetic field $\mathbf{H}$ permits the integral over the antenna to be construed as

$$Z|I_g^2| = (\pm) \iint_{\text{ant + gap}} \mathbf{H}^* \times \mathbf{E} \cdot \hat{\mathbf{n}}\, d\sigma\,, \tag{4}$$

where $\hat{\mathbf{n}}$ is the unit vector normal to the antenna; this integral gives the "complex power" as the integral of the complex Poynting vector over the antenna. By Poynting's theorem, with a *lossless* medium, the integral in Eq. (4) is equivalent to the integral of $\mathbf{E} \times \mathbf{H}^* \cdot \hat{\mathbf{n}}$ over a large sphere centered on the antenna, i.e., of the "complex power" radiated; the real part of the integral is the electromagnetic radiated power, and so the real part of Z in Eq. (3) corresponds to power radiated to great distances—for a lossless medium and a

perfectly conducting antenna. For a slightly lossy medium, the integrals of Eqs. (3) and (4) remain expressions of power introduced into a radiated field, except that these powers are attenuated on their way to the surface of the distant sphere; correspondingly, when the full Poynting theorem is applied, there are volume integrals representing losses in the medium. The practical point is that the real part of Eq. (3), or of Eq. (4), remains the radiation resistance R ($\equiv R_{cp}$), but we must take account of losses in the medium in calculating the magnitude and the angular distribution of the power actually reaching distant points.

But we must use the correct antenna current $\mathbf{j}(\sigma)$, and the complex-power method gives no clue to this. The emf variational method does, as follows:

The current density $\mathbf{j}(\sigma)$ is a correct antenna current distribution when the tangential component of the radiated **E** field

$$\mathbf{E}(\sigma') = \iint_{\text{metal + gap}} \mathbf{G}(\sigma' - \sigma) \cdot \mathbf{j}(\sigma)\, d\sigma$$

vanishes everywhere on the metal. If we consider the expression

$$\iint_{\text{ant + gap}} \mathbf{j}_t(\sigma') \cdot \mathbf{G}(\sigma' - \mathbf{p})\, d\sigma' ,$$

we find it to be the electric field $\mathbf{E}_t(\mathbf{p})$ radiated by the current distribution $\mathbf{j}_t$ in the so-called *transposed* medium, the medium obtained by replacing the dielectric tensor by its transpose. (This, for the magnetoionic medium, is the result of reversing the sign of the geomagnetic field.) So if I_t is related to $\mathbf{j}_t$ as I is to **j**, the expression

$$Z_{emf}\, I_t I = \iint_{\text{ant + gap}} d\sigma \iint_{\text{ant + gap}} d\sigma'\, \mathbf{j}_t(\sigma') \cdot \mathbf{G}(\sigma' - \sigma) \cdot \mathbf{j}(\sigma) \qquad (5)$$

gives the same gap impedance Z for both the medium and its transpose. (Theorem: antenna impedance is independent of the sign of the geomagnetic field; this is presumably true for moving antennas but becomes increasingly dubious as sheaths, V×B, etc., are encountered in nonsymmetric, lossy antenna structures.) The expression Z_{emf} is variational in the sense that if we add an error term **Dj** to **j** in the neighborhood of some point σ on the metal, **j** and $\mathbf{j}_t$ being assumed correct, then no error is thereby made in the computed Z_{emf}; this error would be

$$\int_{\text{ant}} \mathbf{E}_t(\sigma) \cdot \mathbf{Dj}(\sigma)\, d\sigma .$$

This error vanishes, because $\mathbf{E}_t$ vanishes for the correct $\mathbf{j}_t$ everywhere on the metal.

The conclusion is that Z_{emf} represents a better calculation of the reactive impedance as seen from the antenna feed line, given the plausibility of the slice-generator picture of the antenna in the first place. On the other hand, Z_{cp} has a real part directly interpretable, for a lossless medium, as far-field radiation resistance $R_{cp} = R$. Therefore, it seems best to use Z_{emf} for antenna tuning and to take advantage of its variational properties for determining antenna current $\mathbf{j}(\sigma)$, but to use the computed $\mathbf{j}$ in Z_{cp} for calculating R and, in some direct far-field power calculation, for finding radiation patterns. As to the validity of the slice-generator assumptions, they work well enough in free-space calculations and experiments for the thin antennas likely to be used in VLF satellites, so that errors here seem ignorable compared with the approximations we are forced to make concerning the physics of the ambient magnetoplasmas.

We now turn to calculational details that need to be understood for cold magnetoplasmas before calculations can be extended to more difficult cases. There is no closed-form Green's function for the medium with dielectric tensor

$$\epsilon = \epsilon_0 \begin{pmatrix} \alpha & i\beta & 0 \\ -i\beta & \alpha & 0 \\ 0 & 0 & \gamma \end{pmatrix}, \quad \mu = \mu_0 , \quad k_0 = \omega\sqrt{\mu_0\epsilon_0} , \tag{6}$$

and the usual Fourier representation is used:

$$\mathbf{G}(\mathbf{x}) = \iiint \frac{\mathbf{N}(\mathbf{k})}{D(\mathbf{k})}\, e^{i\mathbf{k}\cdot\mathbf{x}}\, d^3k , \tag{7}$$

where $\mathbf{N}$ is a matrix of second degree in k^2 and D is a polynomial of second degree in k^2. For a given direction $\hat{\mathbf{k}}$, the two pairs of roots of $D(k\hat{\mathbf{k}}) = 0$ correspond to (differently polarized) plane waves traveling in the $\hat{\mathbf{k}}$ direction according to $\exp(ik\hat{\mathbf{k}}\cdot\mathbf{x})\exp(-i\omega t)$. So the term of Z expressing power propagated to a far field must be explicit in the roots of $D(\mathbf{k})$.

The calculation begins by doing the integrals over the antenna first, leaving the k-space integrals for last. To get underway, we need a convenient antenna geometry and parametrized form of the current distribution. For a thin dipole antenna of half-length L oriented in some $\mathbf{z}'$ direction at angle θ with respect to the geomagnetic field (which points in the $\mathbf{z}$ direction of an x,y,z rectangular coordinate system) we take $\mathbf{j}$ as $\mathbf{z}'$ sin $[K(L - |z'|)]$, and j_t as the same sinusoidal form with K_t replacing K. The "propagation constants" K and K_t are to be determined variationally by the equations $\partial Z/\partial K = 0$ and $\partial Z/\partial K_t = 0$. (To follow the calculation in I, let the symbol K^* be K_t rather than the complex conjugate of K.) The remaining k-space integrals are done by converting to spherical coordinates in k space and doing the radial integration there by residues; the integrals over the antenna gave added "weight" in k in the denominator to make the residue calculation proper. For the final integral over the unit sphere in k space, we are forced to make some approximation, conveniently a power-series expansion in (k_0a) plus log (L/a) times a second such expansion. From the leading term Z_0 of the latter expansion, we calculate $\partial Z_0/\partial K_t = 0$ or $\partial Z_0/\partial K = 0$ or both and get

$$K = K_t = k_0[\alpha(\alpha \cos^2\theta + \gamma \sin^2\theta)]^{1/4} . \tag{8}$$

This result (a) is independent of L, (b) is in agreement with values for special θ's calculated by others, (c) reduces to the free-space k_0 when $\alpha \to 1$, $\gamma \to 1$, (d) is the only K allowing good comparison of the resulting Z with the quasistatically calculated radiationless short-dipole impedance calculated by Blair and Balman, (e) is required for physical interpretations of the resulting Z, and (f) is independently derivable by computing the decay of a wave standing on an infinite continuous straight wire, inverting the resulting $\omega(K)$ for real K and continuing the result analytically to find $K = K(\omega)$ for real ω.

With the above K, the dominant term Z_0 takes the form

$$Z_0 = \pm i\, 120\, k_0\, \frac{\cot (KL)}{K} \left\{ \log\left(\frac{L}{a}\right) + C \right\} . \tag{9}$$

For small L, cot (KL) $\approx$ 1/KL, and the result is identical with that of Balmain up to differences in the constant C in { }, (C << log (L/a) for "thin" dipoles), differences presumably arising from Balmain's triangular current in contrast to our sinusoidal current.

For appropriate frequencies, collisionless cold magnetospheric parameters, and dipole orientational angles θ, the factor

$$(\alpha \cos^2 \theta + \gamma \sin^2 \theta)$$

becomes zero at some $\theta = \theta_0$ and changes sign there as a function of θ. When the factor is negative, K = (real const) $\cdot$ (1 + i), resembling the K of a skin-depth wave in a finitely conducting metal. The corresponding reactance Z_0 becomes resistive. In examining the significance of these behaviors, we find that in the secular polynomial $D(\mathbf{k})$, of the form $A(\theta)|k^4| + B(\theta)|k|^2 + C(\theta)$ in $|k|, \theta, \phi$ coordinates in k space, the coefficient $A(\theta)$ vanishes for

$$(\alpha \sin^2 \theta_c + \gamma \cos^2 \theta_c) = 0 ,$$

so there is a "resonance cone" of plane-wave propagation directions, making an angle θ_c with the geomagnetic field, for which the plane-wave propagation constants are infinitely large. The plane normal to the dipole is tangential to this cone when the dipole has orientation $\theta = \theta_0$, and $K \approx (1 + i)$ and Z_0 is resistive (is real) when the normal plane, pivoting about the tip of the resonance cone, intersects the cone along two of its generators. In such orientations the thin dipole is aligned so as to deliver power to the short-wavelength plane waves propagating in directions determined by the cone's generators.

Putting in a finite collision frequency z (as is often necessary to see where roots lie with respect to the real k axis, etc.) and reverting to the cold-plasma physics, we find that the electrons, for plane waves along the resonant directions, have large-radius orbits traversed at large speeds at the period set by the rf; reducing z merely enlarges the radii and increases the speeds, so that the heat loss per electron remains finite as $z \to 0$. Thus the medium remains lossy through a resonance, although $z \to 0$ would appear superficially to remove any loss mechanism. So the resistive Z_0 corresponds to power going into orbiting local electrons, *not* to power delivered to distant points.

An elementary example of the kind of resonance at hand is found in the case of the right- (or perhaps, left-) handed circularly polarized wave traveling in the $\theta = 0$ direction of the magnetic field. The wave is strictly transverse, so plasma frequencies do not enter.

Ignoring ions, the electrons have speeds v (in circular orbits) related to the amplitude E of the circularly polarized electric field through

$$v = \frac{eE/m}{[\nu + i(\omega - \omega_g)]},$$

where ω is the rf, ω_g is gyrofrequency, and ν is the collision frequency, entering as a phenomenological damping factor behaving like a viscous-drag coefficient. The power loss per unit volume of medium is

$$\frac{\nu v^2}{2} = \frac{\nu}{2} \frac{|Ee/m|^2}{\nu^2 + (\omega - \omega_g)^2} .$$

In a band of width $|\omega - \omega_g| \leq \nu$, we have a power loss proportional to $1/\nu$, so that when $\nu \to 0$ and the medium is ostensibly lossless, one gets no attenuation except at $\omega \approx \omega_g$, a resonance condition.

For $\omega < \omega_g$, such resonance occurs for plane waves propagating at angles $\theta = \theta_c$, and analogously, attenuations $\approx 1/\nu$ occur for plane-wave propagation directions θ in a band of width $d\theta \propto \nu$ about the resonance cone angle $\theta = \theta_c$.

The term resonance is well justified, since the medium, for small ν, behaves like a high-Q resonant cavity, the collision frequency ν being analogous to the resistivity of the cavity walls.

The resistive Z is confirmed by rocket probe measurements by NASA, and the close coupling with local electrons is confirmed by sharp rises of noise levels seen on reception, as parameters move into resistive—Z_0 combinations (NASA and U. of Michigan measurements at 1 to 10 MHz).

It is suggested that the sharply defined noise bands seen in passive swept-frequency experiments at VLF/ELF may well have the same origin, i.e., may represent parameter regions of good coupling of the antenna with resonance cones of the local medium. Any structure of the noise seen there may represent burbling in the satellites' wake as well as large-scale modulations arising from a distant disturbance.

When such resonant cones exist, there is always some arc of the loop antenna oriented so as to excite waves in the resonance cone. The corresponding term in the loop's "resistive reactance" represents power delivered to churning up the medium locally, not power delivered to any far field.

For the dipole, there are further closed-form terms of the impedance $Z = Z_{emf}$ available in closed form; these are found in Eqs. (86) and (99) of Ref. 1 in which we replace Λ and Λ^* with KL where the present Eq. (8) gives K. This substitution simplifies the evaluations. The result accounts for about 99% of the impedance in all cases computed, so that excessively tedious numerical integral terms contribute insignificantly and can evidently be discarded.

For the far-field radiation resistance R, however, we must perform numerical integrations. The formal integral here is Eq. (70) of Ref. 1, again with Λ, $\Lambda^* \to KL$ for R_{emf}, or (believed preferable), $\Lambda \to KL$, $\Lambda^* \to K^*L$ for R_{cp}. In either case, the results are

identical for a collisionless cold plasma in which all waves propagate (for $Z = 0$, $X < 1$, $Y < 1$, K real). Identification of the numerical integral with far-field radiation resistance is based on the fact that (1) it is the *only real* term in Z of magnitude $O(\log a)$ or $O(a^0)$ in the above $X < 1$, $Y < 1$, $Z = 0$ case, where the only possible sink of delivered power is into far-field radiation, (2) it is the term of the integral for Z depending explicitly on the roots of $D(k)$, i.e., on the plane-wave propagation constants for the medium, (3) in the small-L limit the R integral agrees formally with the short-dipole radiation-resistance integral of Weil and Walsh (similar agreement is found for small loops), and (4) it reduces to the free-space R for that limiting case.

So the radiation resistance is computed as a numerical integral, essentially as a power series in L with recursively evaluated coefficients, according to I. The integral, somewhat entangled with others of a similar nature for $O(a^0)$ terms of the reactance, failed to converge for dipoles as short as $L = 30$ for 18-kHz magnetospheric parameters, suggesting that the dipole was already too long here. This suggests that for R we might well take $L = \infty$ with small error; curves of R vs L for free-space dipoles already suggest this since beyond $k_0 L \approx 1/2$ the curve shows weak oscillations subsiding about an $L = \infty$ value. The numerical integral for $R(L = \infty)$ has not been programmed, but since no recursions are needed, the integral ought to converge well in a relatively rapid machine calculation. But one needs the finite-L calculations to check the L-infinite ones on occasion.

Joyce McLaughlin has generated an impressive asymptotic expansion of the large-L R's for certain high-frequency parameter regions. These results, in manuscript, need studying for their apparent relevance to the far-field patterns and for extension to VLF/ELF. The development here begins with the formally complete integrals over appropriate analytically defined zones on the unit sphere in k space, after the radial k-space integration is done by residues. The Kline-Kay asymptotic procedure, for real exponents with large parameters in two-dimensional integrals, has evidently not been extended to the complex exponents encountered in the VLF asymptotics.

In all of the preceding, the "axial-concentration" assumption was made: one of the current distributions **j** in the integrands **j.G.j** was construed as concentrated on the axis of the dipole, thus eliminating one integral over the circumference of the dipole. If the result is represented as $Z'(a)$, then any error made by the axial concentration assumption is eliminated by finding

$$Z(a) = \frac{1}{\pi} \int_0^{\pi} Z'(2a \sin\phi)\, d\phi \,. \tag{10}$$

(This correction doctrine is readily discovered in the explicit form of the integrals, Eq. (5), when we use the Fourier-represented Green's function, Eq. (7).) With this, the $O(\log a)$ and $O(a^0)$ terms retained in the present formulation are correct as they stand.

As the interpretation would have to be confirmed by direct calculation anyhow, it seems preferable to obtain far-field patterns by direct calculation, from the known antenna current **j**, of the far-field Poynting vector. For a lossy medium, further study of the meaning of "radiation pattern" and its analytic manifestation seems advisable.

We discuss means of extending the calculation of Z and R for lossy dipole antennas in more realistic media. The first consideration is to find the appropriate propagation constant K for waves guided on the thin dipole; this is basic to determining the antenna

current **j**. For the lossy infinite dipole (or straight wire), we first suggest assuming **j** of the form $[\exp(iKz')\exp(-r/a)]/r$. Here r measures radial distance from the axis of the dipole and a is a thinness parameter rather than the radius of a hard metal dipole. Such a smeared-out current distribution was proposed first by Staras, for analytic convenience, and the choice here of $[\exp(-r/a)]/r$ is most convenient since the $rdrd\phi$ parts of the double integrals over the dipole now combine to give a simple pole in k^2 in the remaining k-space integrations, rather than confusing the issue with Bessel functions. Further, for the cold plasma, the resulting changes in Z and R were found insignificant.

To represent ohmic losses, we begin again, replacing the original $\mathbf{j}_t \cdot \mathbf{G} \cdot \mathbf{j}$ with

$$\mathbf{j}_t(\sigma) \cdot \left\{\mathbf{G}(\sigma - \sigma') + C(r)\delta(\sigma - \sigma')\right\} \cdot \mathbf{j}(\sigma') , \tag{11}$$

where $C(r)$ is perhaps best taken as $c_0 r$ so that the integral converges. Constant c_0 is then to be adjusted so that the I^2R' loss at rf, for current on the dipole having rf resistance R' per unit length, matches the loss

$$\int_0^{2\pi} d\phi \int_0^{\infty} j^2(r)\, C(r)\, rdr ,$$

the gap current being

$$I = \int_0^{2\pi} d\phi \int_0^{\infty} j(r)\, rdr .$$

Easy calculation gives $c_0 = 8\pi aR'$. The basic physical notion is that the "power density" $\mathbf{j}_t(\sigma) \cdot \mathbf{G}(\sigma - \sigma') \cdot \mathbf{j}(\sigma')\, d\sigma$ on the antenna "metal" now balances the power $j^2C(r)$ lost because of the antenna's local resistance, rather than vanishing as on the surface of a perfect conductor. Anyhow, we must consider distributed current because of skin depth in a real metal antenna, and the problem is to make the calculation as easy as possible without violating the essential physics.

Computation of the propagation constant K and of Z and R can be done by methods identical with those used for the former case $c_0 = 0$. This has not been done, but we try to anticipate the results: For the free-space medium, the K should reduce to that of waves guided along a resistive wire (as found, e.g., in Stratton) having the same I^2R' per unit length. The "reactance" Z_0 will now be found to have a resistive term for free space, a term representing power delivered to heating the antenna metal. For the free space or birefringent lossless medium, R_{cp} will now differ from R_{emf} because of the imaginary, attenuating part of the wire's propagation constant K; R_{cp} is to be preferred; the added delta-function term of Eq. (11) enters neither calculation since R is computed from poles in the secular polynomial $D(k)$ only.

The same augmentation of **G** by a "lossy delta function" is particularly important in loop calculations because of the high currents required for radiating power. The loop geometry, chosen so that the integrals over the antenna could be done first, was that of a metal strip of width 2a, length $2\pi L$, bent into a circle of radius L. For the perfectly conducting strip, the current depended on transverse distance x from the center of the strip according to $(a^2 - x^2)^{1/2}$ to conform with the DC current distribution; clearly we must multiply a delta-function augmentation by some $C(x)$, vanishing at $x = \pm a$, to have a

finite resistive loss. Of course one could find the exact transverse distribution of rf current flowing on a resistive strip, but the smallness of the width parameter *a* rules out significant corrections to the antenna's Z or R in any result. That is, Z and R are not importantly dependent on the choice of transverse distribution of current, so long as the antenna is thin and I^2R' is modeled correctly.

The satellite's speed in orbit is comparable to wave speeds in certain conditions, and means of estimating the resulting effects should be studied. As seen by the moving satellite, the cold medium is Lorentz-transformed into one having presumably triaxial dielectric and permeability tensors. The variational calculation of K and Z, based on the transposed-medium concept, is valid here, and the foreseen difficulties are (a) excessive algebra and (b) a likelihood that the secular polynomial D(k) is no longer a biquadratic in k, so that we would have to find some alternative to a residue calculation for the radial integration in k space or reargue its justification.

For the warm magnetoplasma, there are electroacoustic waves, and D(k) is of sixth degree in k (or higher) rather than of fourth degree. The "EM" waves of interest arise from two roots of D, and the other roots, corresponding to uselessly propagating electroacoustic waves generated by the antenna, have no place in a calculation of R, although they directly affect K and Z.

We advocate calculating the propagation constant K, for a wave guided by a generally oriented infinite wire, as the first problem in a warm-plasma extension. The wire is actually to be a current distributed radially according to say [exp (−r/a)]/r, rather than being a hard metal cylinder about which a sheath would normally form. This problem is the simplest of the warm-plasma type and is chosen on the grounds that if it cannot be handled satisfactorily, there is no hope for the more difficult Z and R calculations, which anyway require having found K. A preliminary inspection of the mathematics of this problem shows that the K for a "slightly" warm plasma can be obtained as a perturbed version of the cold-plasma K, but whether a mere perturbation is adequate for the magnetosphere at VLF is not known. We suppress speculations about the sheath, wake, and nonlinearity problems as probably requiring drastic revision of the present methods, and if not, logically following the working-out of the problems qualitatively discussed above.

REFERENCES:

1. Ament, Katzin, Katzin, and Koo, "Impedance of a Cylindrical Dipole having a Sinusoidal Current Distribution in a Homogeneous Anisotropic Ionosphere," Radio Science 68D, 379 (1964).
2. "Theoretical Investigations Related to Ionospheric Probing," Electromagnetic Research Corp. Report No. 1 on Contract NASw-835, 1964.
3. "Satellite Antenna Radiation Properties at VLF in the Ionosphere," Electromagnetic Research Corp. final report on Contract Nonr-4250(00)(X), 1965; available as AD 654,737.

Reference 1 gives the computational route for getting R and Z as closed-form terms plus programmed numerical integrations. The reports give the variational version, including the propagation constant K, and give parallel results for loop antennas, physical interpretations, and peripherally related matters. Reference to Blair's and Balmain's report is given in the above NASA-contract report.

The best single discussion of reciprocity and variational methods using the transposed-medium concept seems to be that of Cairo and Kahan in Cahiers de Physique, No. 170 18, 405 (1964).

ON THE VLF/LF DRIVING-POINT IMPEDANCE OF A FINITE ELECTRIC ANTENNA IN A UNIFORM, WARM IONOSPHERE

T. N. C. Wang and W. E. Blair

Stanford Research Institute
Menlo Park, California 94025

ABSTRACT

This paper considers the driving-point impedance at VLF/LF of a finite cylindrical dipole embedded in a warm ionosphere. A uniform magnetoplasma containing a warm electron species and cold ions is used for the model of the ionosphere. The finite temperature of the electrons is taken into account through the use of a scalar pressure in the dynamical equation. Input reactance and radiation resistance (due to the radiation of both the whistler and the electron-thermal modes) are calculated for typical ionospheric parameters. It is found that dipole whistler-mode efficiency increases in each of three situations: (1) decrease in plasma density, (2) increase in "dipole length," and (3) increase in dipole orientation angle with respect to the earth's magnetic field. The first-order input-reactance term due to the thermal effect is found to be small compared to the cold plasma result for the dipole of parallel orientation, and in the same order of magnitude for the dipole of perpendicular orientation.

I INTRODUCTION

Wang and Bell have considered the problem of the VLF/LF radiation characteristics of a finite electric dipole embedded in a uniform warm magnetoplasma.[1*] Specifically, they have derived a general full-wave

*References are listed at the end of each paper.

formal expression for the driving-point impedance of an electric antenna oriented either parallel or perpendicular ($Z_{\parallel,\perp}$) to the static magnetic field ($\vec{B}_o$). From the formal solutions of $Z_{\parallel,\perp}$, the radiation resistances $R_{\parallel,\perp}$ (= $\Re e Z_{\parallel,\perp}$) have been calculated in Ref. 1 for the VLF/LF range and for plasma parameters suitable for magnetospheric whistlers.

It is the purpose of this work to extend the results in Ref. 1 by calculating the first-order correction for the VLF/LF dipole input reactance caused by the thermal electron effects.

II INPUT REACTANCE

Assuming a skin-triangular current distribution for a finite cylindrical antenna (total length, 2h, and radius, r_o), and using a warm magnetoplasma model that includes only the finite temperature for the electrons (from a scalar pressure), the formal solution for the driving-point impedance is:[1]

$$Z_{\parallel} = \frac{jZ_o(h\beta)^2}{8\pi^3}\int_{-\infty}^{\infty} dn \int_0^{2\pi} d\psi \int_0^{\pi/2} d\theta\, G_{\parallel}(n,\theta)\left[\frac{\sin \lambda n_z}{\lambda n_z}\right]^4 J_o^2(\beta r_o n_{\perp})\, n^2 \sin\theta \qquad (1)$$

$$Z_{\perp} = \frac{jZ_o(h\beta)^2}{16\pi^3}\int_{-\infty}^{\infty} dn \int_0^{2\pi} d\psi \int_0^{\pi/2} d\theta\, G_{\perp}(n,\theta)\left[\frac{\sin \lambda n_x}{\lambda n_x}\right]^4 J_o^2(\beta r_o n'_{\perp})\, n^2 \sin\theta \qquad (2)$$

where all the notations are the same as those given in Ref. 1 and are summarized in the Appendix of this paper.

In view of the VLF/LF propagation properties of the characteristic roots of the dispersion equation discussed in Section IV of Ref. 1, it is convenient to split the θ integration interval of Eqs. (1) and (2)

into $\int_o^{\pi/2} = \int_o^{\theta_2} + \int_{\theta_2}^{\theta_1} + \int_{\theta_1}^{\pi/2}$ for the frequency range $f_{He} > f > f_q$,

and into $\int_o^{\pi/2} = \int_o^{\theta_1} + \int_{\theta_1}^{\theta_2} + \int_{\theta_2}^{\pi/2}$ for the frequency range $f_q > f > f_{LHR}$,

where f_{He} and f_{LHR} are electron gyrofrequency and lower-hybrid-resonance frequency, respectively, and where the definitions of θ_1 , θ_2 , and f_q , as well as their significance, are as given in Ref. 1.

It has been shown that in the intervals of $0 < \theta < \theta_2$ and $\theta_1 < \theta < \pi/2$ for the frequency range $f_{He} > f > f_q$ or $0 < \theta < \theta_1$, and $\theta_2 < \theta < \pi/2$ for the frequency range $f_q \geq f > f_{LHR}$, the finite electron temperature ($T \lesssim 10^5$ °K) does not drastically affect the propagation structure of electromagnetic waves.[1] Therefore, in those intervals, we can expand $G_{\parallel,\perp}(n,\theta)$ by using the fact that $\tilde{u}^2 \ll 1$ ($\tilde{u}^2$ from Ref. 1 is the square of the electron thermal velocity normalized to the velocity of light in free space). The leading terms, $G^{\infty}_{\parallel,\perp}(n,\theta)$, for the two cases, are

$$G^{\infty}_{\parallel}(n,\theta) = F_{\parallel}(n,\theta) = \frac{1}{n^2 - \varepsilon_o} - \frac{n_z^2(n^2 - \varepsilon_{+1})(n^2 - \varepsilon_{-1})}{\alpha(\theta)(n^2 - n_+^2)(n^2 - n_-^2)(n^2 - \varepsilon_o)} \tag{3a}$$

$$G^{\infty}_{\perp}(n,\theta) = F_{\perp}(n,\theta) = \frac{1}{n^2 - \varepsilon_{+1}} + \frac{1}{n^2 - \varepsilon_{-1}} - \frac{2n^2 \sin^2\theta (n^2 - \varepsilon_o)}{\alpha(\theta)(n^2 - n_+^2)(n^2 - n_-^2)}$$

$$\times \left[\cos^2\psi + \frac{\varepsilon_d^2}{(n^2 - \varepsilon_{+1})(n^2 - \varepsilon_{-1})}\right] . \tag{3b}$$

The $F_{\parallel,\perp}(n,\theta)$ given in Eq. (3) are those for the case of a cold magnetoplasma,[2,3] and the notations, such as $n_{\pm}^2$, $\alpha(\theta)$, can be found in Refs. 2 and 3.

From the above discussion, it follows that Eqs. (1) and (2) can be approximated in the following form:

$$Z_{\parallel,\perp} \simeq \frac{jZ_o(h\beta)^2}{8\pi^3} \int_{-\infty}^{\infty} dn \int_o^{2\pi} d\psi \left[\int_o^{\pi/2} F_{\parallel,\perp}(n,\theta)\, S_{\parallel,\perp}\, d\theta \pm \int_{\theta_2}^{\theta_1} [G_{\parallel,\perp}(n,\theta) - F_{\parallel,\perp},\theta)]\, S_{\parallel,\perp}\, d\theta \right] \tag{4}$$

where

$$S_{\parallel} = \left[\frac{\sin \lambda n_z}{\lambda n_z}\right]^4 J_o^2(\beta r_o n_{\perp}) n^2 \sin\theta$$

$$S_{\perp} = \frac{1}{2}\left[\frac{\sin \lambda n_x}{\lambda n_x}\right]^4 J_o^2(\beta r_o n'_{\perp}) n^2 \sin\theta$$

and where the ± sign on the right-hand side is for the frequency ranges $f_{He} > f > f_q$ and $f_q > f \geq f_{LHR}$, respectively. The first term on the right is the formal solution of the input impedance for the antenna in a cold magnetoplasma. This integral has been evaluated previously.[4-6] The quasi-static input reactance calculated from this integral agrees with previous results at VLF/LF range ($f_{He} > f > f_{LHR}$) by:[4,5]

$$X_{\parallel}^{Q} = \frac{Z_o}{j\, h\beta\, \epsilon_s \pi}\left[\log\left(\frac{h}{r_o \sigma}\right) - 1\right], \quad \sigma = |\epsilon_o/\epsilon_s|^{\frac{1}{2}} \tag{5a}$$

$$X_{\perp}^{Q} = \frac{Z_o}{j\, h\beta\, |\epsilon_o \epsilon_s|^{\frac{1}{2}}} \tan^{-1} \left|\frac{\epsilon_s}{\epsilon_o}\right|^{\frac{1}{2}} \tag{5b}$$

where the superscript Q indicates a zero temperature result (for cold magnetoplasma), based on a quasi-static calculation [i.e., only the leading term of $F_{\parallel,\perp}(n,\theta)$, as $n^2 \to \infty$, is kept in the integration]. This approximation is valid for calculating the input reactance for short antennas.[4] The second term in Eq. (4) can be considered a correction term $Z^t_{\parallel,\perp}$ to the dipole input impedance $Z^Q_{\parallel,\perp}$ in a cold magnetoplasma, owing to the finite temperature of the electrons. Since any pole contributions from $G_{\parallel,\perp}(n,\theta)$ and $F_{\parallel,\perp}(n,\theta)$ to the integral contribute to the $\Re e Z^t_{\parallel,\perp}$ (resistance), it is sufficient to use a quasi-static limit to estimate a leading term for the input reactance $X^t_{\parallel,\perp}(X^t_{\parallel,\perp} \equiv \Im m\, Z^t_{\parallel,\perp})$. The quasi-static term of $X^t_{\parallel,\perp}$ can be obtained from Eq. (4) by taking the leading terms in $G_{\parallel,\perp}(n,\theta)$ as $(n^2\tilde{u}) \to \infty$ and those in $F_{\parallel,\perp}(n,\theta)$ as $n^2 \to \infty$. This approximation leads to

$$X^t_{\parallel} \simeq \pm \frac{2j\, Z_o}{\pi^2} \int_o^\infty dn \left[\int_{\theta_2}^{\theta_1} \frac{\sin^4(\lambda n_z)}{(\lambda n_z)^2} J_o^2(\beta r_o n \sin\theta) \sin\theta d\theta \right.$$

$$\left. - \int_{\theta_2}^{\theta_1} \frac{\sin\theta}{\alpha(\theta)} \frac{\sin^4(\lambda n_z)}{(\lambda n_z)^2} J_o^2(\beta r_o n \sin\theta) d\theta \right] \tag{6a}$$

$$X^t_{\perp} \simeq \pm \frac{Z_o \lambda^2}{j\pi^3} \int_o^\infty dn \int_o^\pi d\psi \left[\int_{\theta_2}^{\theta_1} n^2 \sin^3\theta \cos\psi \left[\frac{\sin(\lambda n_x)}{\lambda n_x}\right]^4 J_o^2(\beta r_o n'_\perp) d\theta \right.$$

$$\left. - 2 \int_{\theta_2}^{\theta_1} \frac{n^2 \sin^3\theta \cos^2\psi}{\alpha(\theta)} \left[\frac{\sin \lambda n_x}{\lambda n_x}\right]^4 J_o^2(\beta r_o n'_\perp) d\theta \right] \tag{6b}$$

where the $\pm$ sign corresponds to the frequency ranges $f_{He} > f > f_q$ and $f_q > f > f_{LHR}$, respectively, and where the $\int$ indicates that the principal value of the integral should be taken.

To evaluate Eq. (6), we make an approximation by letting $J_o^2(\beta r_o x) = 1$ ($x = n \sin\theta, n_\perp'$) if $\lambda n_z \geq \beta r_o n \sin\theta$ or $\lambda n_x \geq \beta r_o n_\perp'$, and zero otherwise. In this case, the integration with respect to n can easily be performed, and the remaining integrations with respect to θ and ψ can be performed straightforwardly to yield

$$X_{\parallel}^{t} \simeq \pm \frac{Z_o}{j\pi h \beta \epsilon_s} \left[\log A_1 - \frac{1}{2\sqrt{\epsilon_s/(\epsilon_s - \epsilon_o)}} \log \left(\frac{1 + \sqrt{\epsilon_s/(\epsilon_s - \epsilon_o)}}{1 - \sqrt{\epsilon_s/(\epsilon_s - \epsilon_o)}} \right) \right.$$

$$\left. + \epsilon_s \log Y \left(\sqrt{\epsilon_s/(\epsilon_s - \epsilon_o)} - \tilde{u}^2 \delta/2 \right) \right] \tag{7a}$$

$$X_{\perp}^{t} \simeq \pm \frac{2Z_o}{j\pi^2 h \beta} \left[\left| \frac{\epsilon_s}{\epsilon_o} \right|^{\frac{1}{2}} - \frac{1}{\sqrt{Y^2 - 1}} + \frac{\tilde{u}^2(\epsilon_o + \epsilon_s - Y\epsilon_d)}{2\epsilon_s(1 - Y^2)} + \log A_2 \right] \log \left(\frac{h}{r_o} \right) \tag{7b}$$

where

$$A_1 = \frac{2\sqrt{\epsilon_s/(\epsilon_s - \epsilon_o)} + (\tilde{u}^2/2)\delta}{Y[\sqrt{\epsilon_s/(\epsilon_s - \epsilon_o)} + (\tilde{u}^2/2)\delta](\sqrt{\epsilon_s/(\epsilon_s - \epsilon_o)} + 1/Y)}$$

$$\delta = \frac{2\epsilon_s}{\epsilon_s - \epsilon_o} - \frac{\epsilon_o(\epsilon_o - \epsilon_d Y + \epsilon_s)}{(Y^2 - 1)\epsilon_s(\epsilon_s - \epsilon_o)}$$

$$A_2 = \frac{(\sqrt{\epsilon_s}\tan\theta_1 + |\epsilon_o|^{\frac{1}{2}})(\sqrt{\epsilon_s}\tan\theta_2 - |\epsilon_o|^{\frac{1}{2}})}{(\sqrt{\epsilon_s}\tan\theta_1 - |\epsilon_o|^{\frac{1}{2}})(\sqrt{\epsilon_s}\tan\theta_2 + |\epsilon_o|^{\frac{1}{2}})}$$

, and where $\pm$ sign in Eq. (7) corresponds to the frequencies $f_{He} > f > f_q$ and $f_q > f > f_{LHR}$, respectively.

In the limit of zero electron temperature, $\tilde{u} \to 0$, we note that $\sqrt{(\epsilon_s - \epsilon_o)/\epsilon_s} \to Y$ for the high-density plasma $X \gg Y^2$, hence it can be shown that $X_{\parallel,\perp}^{t} \to 0$. Comparisons of $X_{\parallel,\perp}^{t}$ with $X_{\parallel,\perp}^{Q}$ are given in Section IV.

III RADIATION RESISTANCE

To evaluate the numerical values for the dipole radiation resistance for both the whistler mode $R^{w}_{\parallel,\perp}$ and the thermally modified whistler mode (the TMW mode as defined in Ref. 1) $R^{t}_{\parallel,\perp}$, we have used the integrals developed in Section V of Ref. 1 and have integrated numerically for typical VLF/LF plasma parameters in the ionosphere.

By using Eqs. (16) through (19) of Ref. 1, $R^{w}_{\parallel,\perp}$ is plotted in Figure 1 and $R^{t}_{\parallel,\perp}$ is plotted in Figure 2 for normalized VLF/LF frequencies in the range $0.1 \lesssim f/f_{He} \lesssim 0.975$. The curves in Figures 1 and 2 are parametric in normalized antenna length h_o ($h_o \equiv 2\pi f_{He} h/c$) and normalized plasma frequency f_o/f_{He}, and for a fixed ratio $h/r_o = 10^3$. Two values of f_o/f_{He} are used [$f_o/f_{He} = 2, 5$], which represent the range of typical electron density and earth magnetic-field strength in the ionosphere. The electron temperature in the plots has been chosen to be $T \simeq 10^4\ ^{o}K$.

As shown in Ref. 1, the antenna radiation power associated with $R^{t}_{\parallel,\perp}$ may be considered as a loss. We may then define the relation $\eta^{w} = R^{w}/(R^{w} + R^{t})$ to estimate the dipole radiation efficiency for the whistler mode. Using the definition of η^{w} together with the results of Figures 1 and 2 we have calculated η^{w} for representative parameters of the ionosphere and magnetosphere; the results are given in Table 1.

In the frequency range $f_{LHR} > f \gg f_{Hp}$, we note that the electron thermal mode does not propagate[9]. Following the discussions presented in Refs. 1 [illegible], we use Eqs. (1) and (10) of Ref. 3 to compute $R^{w}_{\parallel,\perp}$. The numerical results for $R^{w}_{\parallel,\perp}$ are presented in Figure 3.

Table 1

WHISTLER-MODE EFFICIENCY FOR REPRESENTATIVE IONOSPHERIC PARAMETERS

f (kHz)	f/f_{He}	f_o/f_{He}	h (m)	h_o	$\eta^{w}_{\perp}$ (%)	$\eta^{w}_{\parallel}$ (%)
100	0.1	5	25.0	0.5	97	88
100	0.1	2	25.0	0.5	99	97
100	0.1	5	2.5	0.05	85	60
500	0.5	5	25.0	0.5	96	83
30	0.3	5	25.0	0.05	83	42

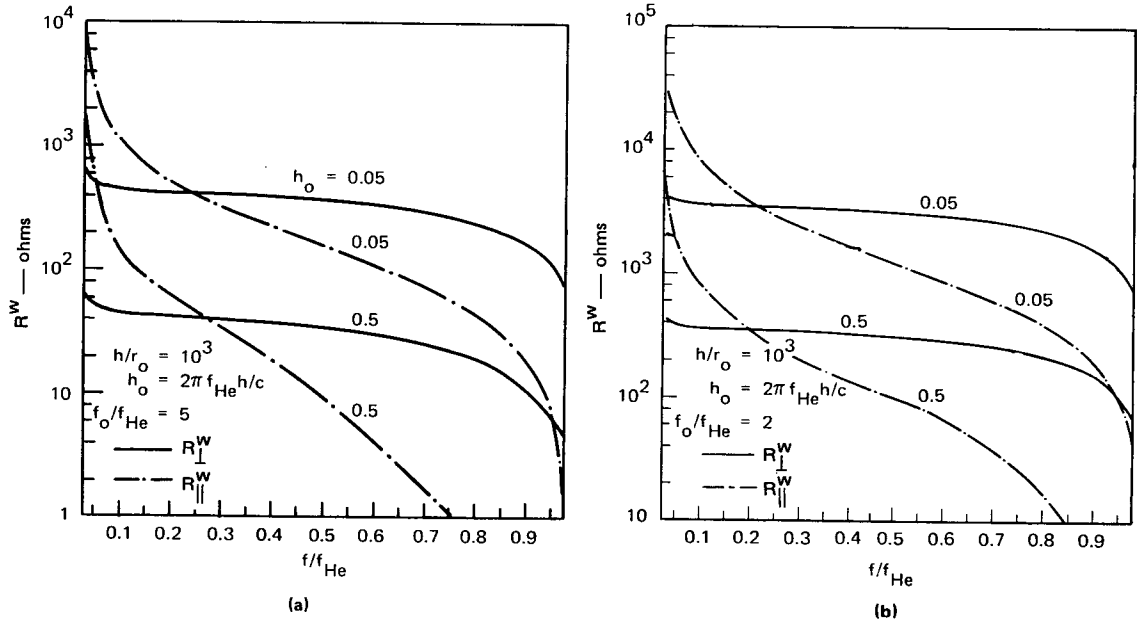

FIGURE 1 VLF-DIPOLE RADIATION RESISTANCE OF THE WHISTLER MODE AS A FUNCTION OF NORMALIZED ANTENNA LENGTH, ANTENNA ORIENTATION, AND DRIVING FREQUENCY FOR $f_{LHR} \ll f < f_{He}$. Two normalized densities are considered: (a) $f_o/f_{He} = 5$, and (b) $f_o/f_{He} = 2$.

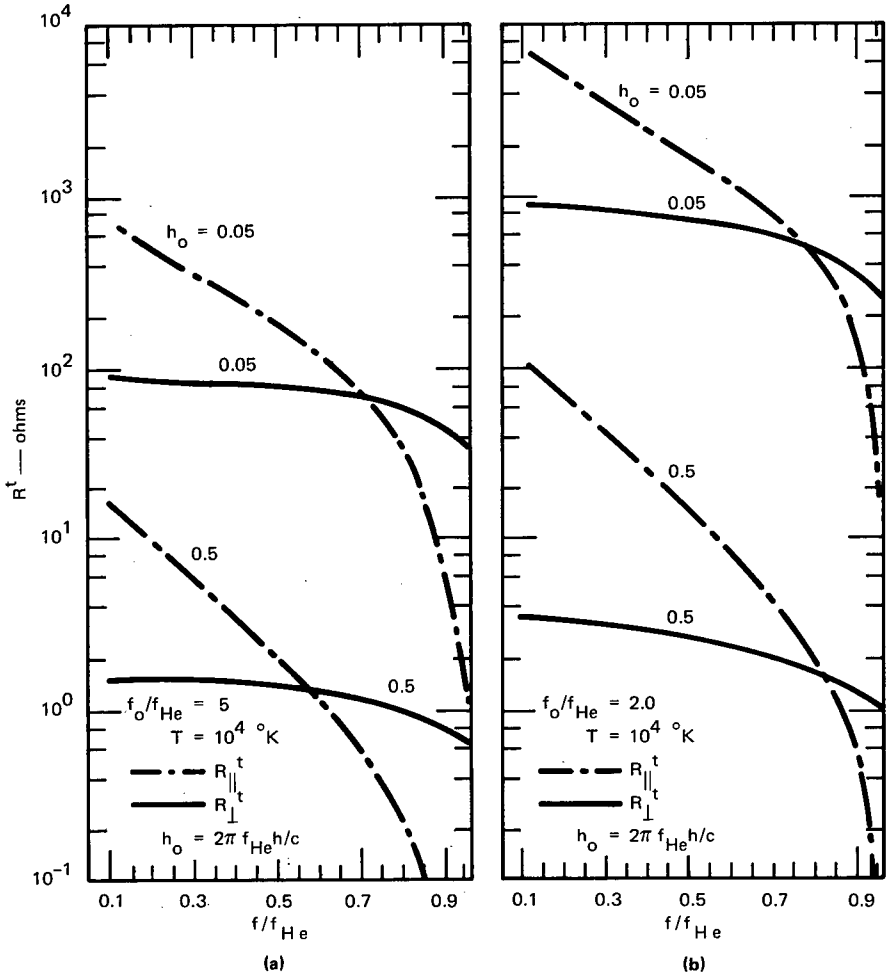

FIGURE 2 VLF-DIPOLE RADIATION RESISTANCE OF THE ELECTRON THERMAL MODE AS A FUNCTION OF NORMALIZED ANTENNA LENGTH, ANTENNA ORIENTATION, AND DRIVING FREQUENCY FOR $f_q < f < f_{He}$. Two normalized densities are considered: (a) $f_o/f_{He} = 5$, and (b) $f_o/f_{He} = 2$.

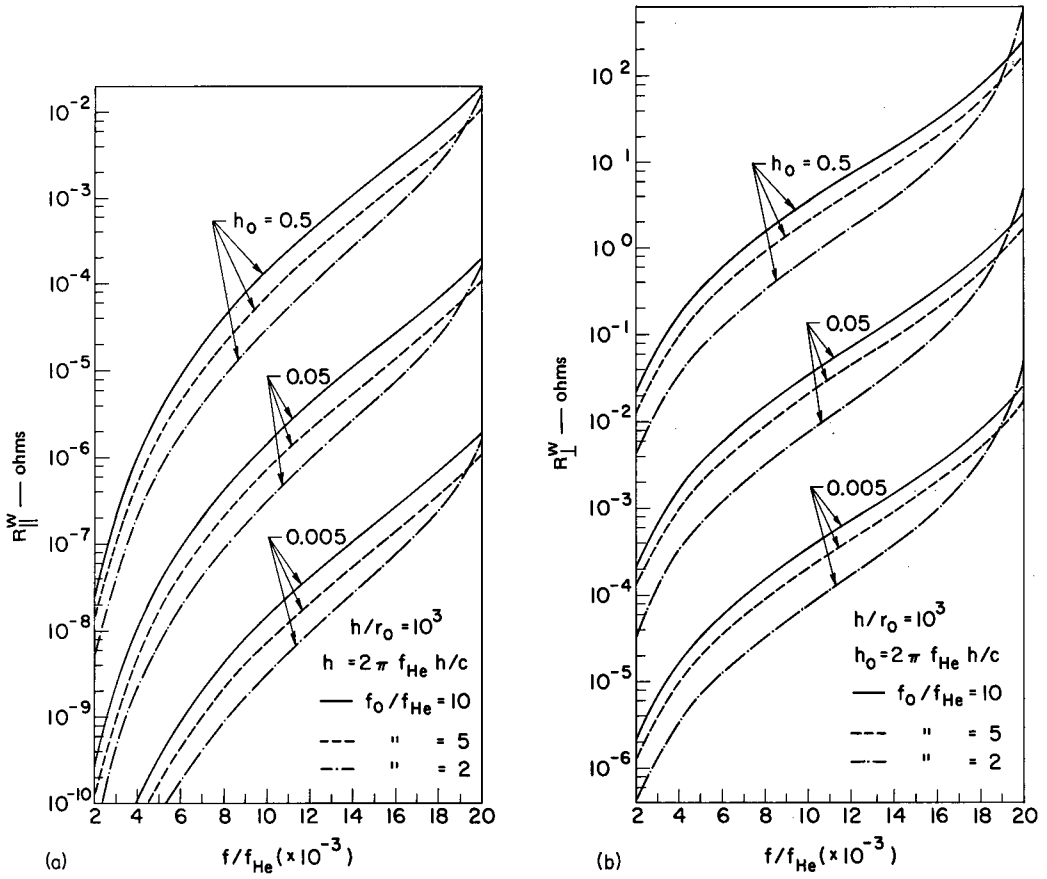

FIGURE 3 VLF-DIPOLE RADIATION RESISTANCE OF THE WHISTLER MODE AS A FUNCTION OF NORMALIZED ANTENNA LENGTH, ANTENNA ORIENTATION, AND DRIVING FREQUENCY FOR $f_{LHR} > f > f_{Hp}$. Three normalized densities are considered: f_0/f_{He} = 2, 5, and 10.

IV DISCUSSION

The efficiencies for the cases in Table 1 are used to emphasize several points pertinent to VLF/LF propagation in the ionosphere and magnetosphere. In general, whistler-mode coupling and efficiency are shown to increase in three situations: (1) perpendicular orientation as opposed to parallel orientation, (2) increase in antenna length (h_o), and (3) minimum electron density (nighttime, sunspot minimum) at any given altitude. For example, to demonstrate the maximum effect, the whistler-mode efficiency for a 25-m antenna, at 100 kHz, in perpendicular orientation, in 300-km orbit, and at local midnight, is 99 percent, whereas the efficiency of a 2.5-m antenna in parallel orientation at local noon (the other parameters being the same) is 60 percent. These three situations conducive to whistler-mode increase can be explained physically. The perpendicular orientation of the dipole is more efficient for propagation parallel to the field line.[8] The antenna is considered to be long compared to the thermal wavelength and short compared to the whistler wavelength; hence, increasing the length increases the whistler-mode efficiency relative to the thermal-mode efficiency. Finally, increasing the local thermal electron density (all other parameters being constant) can increase the coupling of the energy to the thermal mode and hence decrease the whistler-mode efficiency.

It is useful to compare the thermal-reactance component to the quasi-static reactance for the VLF/LF range. Using the conventional approximations $X_e \gg Y_e^2 \gg 1$ for $f_q < f < f_{He}$, the quasi-static reactances in Eq. (5) are capacitive, and are approximately

$$X_{\parallel}^{Q} \simeq \frac{Z_o Y^2}{\pi h \beta X} \left[\log\left(\frac{h}{r_o Y}\right) - 1 \right] \tag{8a}$$

$$X_{\perp}^{Q} \simeq \frac{Z_o}{\pi h \beta X} \quad . \tag{8b}$$

The thermal-reactance terms are inductive and are approximately

$$X_{\parallel}^{t} \simeq \frac{Z_o \tilde{u}^2}{\pi h \beta} \frac{Y^3}{X} \tag{9a}$$

$$X_{\perp}^{t} \simeq \frac{2Z_o \tilde{u}^2}{\pi^2 h \beta} \frac{X}{Y^2} \log\left(\frac{h}{r_o}\right) . \tag{9b}$$

Using Eqs. (8) and (9), the ratios of the thermal reactance to the quasi-static reactance are

$$r_{\parallel} = \left|\frac{X_{\parallel}^{t}}{X_{\parallel}^{Q}}\right| \simeq \frac{\tilde{u}^2 Y}{\log(h/r_o Y)} \tag{10a}$$

and

$$r_{\perp} = \left|\frac{X_{\perp}^{t}}{X_{\perp}^{Q}}\right| \simeq \frac{2\tilde{u}^2 X^2}{\pi Y^2} \log\left(\frac{h}{r_o}\right) . \tag{10b}$$

The $r_{\parallel}$ and $r_{\perp}$ vary with frequency as f^{-1}, and f^{-2}, respectively. Assuming f = 50 kHz and typical ionospheric conditions, for an altitude of 300 km: $r_{\parallel} \sim 0(10^{-4})$ and $r_{\perp} \sim 0(1)$; and for an altitude of $1R_E$: $r_{\parallel} \sim 0(10^{-5})$ and $r_{\perp} \sim 0(10^{-2})$. These results indicate that the inductive thermal reactance is a negligible correction term for parallel orientation (for which case, $X_{\parallel}^{Q} \gg R_{\parallel}^{Q}$), but that it is an important, possibly dominant, term for perpendicular orientation (for which case, $X_{\perp}^{Q} \ll R_{\perp}^{Q}$). Since $X_{\parallel}^{Q}$ and $R_{\perp}^{Q}$ are the dominant terms in the quasi-static impedance, the impedance magnitude is negligibly affected by the thermal reactance terms.

Appendix

DEFINITIONS OF NOTATIONS USED IN EQS. (1) AND (2)

β = Wave number in free space

(n,θ,ψ) = Spherical polar coordinates in wave-normal $\vec{n}$ space

$\lambda = h\beta/2$, $Z_0 = 120\pi$ ohms , $j = \sqrt{-1}$

$n_\perp^2 = n_x^2 + n_y^2$ and $(n'_\perp)^2 = n_y^2 + n_z^2$

$J_o(x)$ = Bessel function of the first kind and zero order

and

$$G_{\parallel}(n,\theta) = \frac{1+(\alpha_o-1)n_z^2}{(n^2-\epsilon_o)}\left[1 + \frac{\alpha_o n_z^2 (n^2-\epsilon_{+1})(n^2-\epsilon_{-1})}{N(n)}\right]$$

$$+ \frac{\alpha_o n_z^2 n_\perp^2}{N(n)}\left[(\alpha_s - 1)n^2 - \frac{1}{2}(\alpha_{+1}\epsilon_{-1} + \alpha_{-1}\epsilon_{+1}) + \epsilon_s\right]$$

$$G_\perp(n,\theta) = A_{+1} + A_{-1} + \frac{\Pi(n)}{N(n)}\left[\frac{\alpha_{+1} n_{+1}}{n^2-\epsilon_{+1}} + \frac{\alpha_{-1} n_{-1}}{n^2-\epsilon_{-1}}\right]$$

$$\times \left[n_{-1}A_{+1} + n_{+1}A_{-1} + \sqrt{2}\, n_x n_z^2 \frac{\alpha_o - 1}{n^2-\epsilon_o}\right]$$

where

$$A_{\pm 1} = \frac{1 + \sqrt{2}\,(\alpha_{\pm 1} - 1)\, n_x n_{\pm 1}}{n^2 - \epsilon_{\pm 1}}$$

$$\epsilon_\nu = 1 - \sum_r \frac{X_r}{1 - \nu Y_r} \qquad \text{(sum over r-species)}, \qquad (\nu = +, -, 0)$$

$X_r = f_{pr}^2 / f^2$ and $Y_r = f_{Hr} / f$ and f_{pr}, f_{Hr} = plasma frequency and gyrofrequency, respectively, for r^{th} species

$\vec{n} = \vec{k}/\beta \qquad n_{\pm 1} = (n_x \pm j n_y)/\sqrt{2} \qquad n_o = n_z \qquad n^2 = n_x^2 + n_y^2 + n_z^2$

$$\Pi(n) = (n^2 - \epsilon_{+1})(n^2 - \epsilon_{-1})(n^2 - \epsilon_o)$$

$$N(n) = C_1 n^6 + C_2 n^4 + C_3 n^2 + C_4$$

$$C_1 = \tilde{u}^2 \left(\frac{\sin^2 \theta}{1 - Y^2} + \cos^2 \theta \right)$$

θ = wave-normal angle between $\vec{n}$ and $\vec{B}_o$

$$C_2 = -\tilde{u}^2 \left[\frac{(\epsilon_o + \epsilon_s - \epsilon_d Y)}{1 - Y^2} \sin^2 \theta + 2\epsilon_s \cos^2 \theta \right] - \alpha(\theta)$$

$$\epsilon_s = (\epsilon_{+1} + \epsilon_{-1})/2 \qquad \epsilon_d = (\epsilon_{+1} - \epsilon_{-1})/2$$

$$\alpha(\theta) = \epsilon_o \cos^2 \theta + \epsilon_s \sin^2 \theta$$

$$C_3 = \tilde{u}^2 \left[\frac{\epsilon_o (\epsilon_s - \epsilon_d Y)}{1 - Y^2} \sin^2 \theta + \epsilon_{+1}\epsilon_{-1} \cos^2 \theta \right] + \epsilon_s [2\epsilon_o + (a - \epsilon_o) \sin^2 \theta]$$

$$a = \epsilon_{+1}\epsilon_{-1} / \epsilon_s$$

$$C_4 = -\epsilon_o \epsilon_{+1} \epsilon_{-1}$$

$\tilde{u}^2 = u_e^2 / C^2$, u_e = electron thermal speed, and C = speed of light in vacuum

$$\alpha_\nu = 1 - \frac{\tilde{u}^2}{1 - \nu Y} \qquad \nu = +1, -1, 0 \qquad Y = f_{He}/f$$

$$\alpha_s = (\alpha_{+1} + \alpha_{-1}) / 2$$

ACKNOWLEDGMENTS

The authors are grateful to Mr. L. S. Bearce for helpful discussions. This work was sponsored by U.S. Navy Contract No. N00014-70-C-0088.

REFERENCES

1. T. N. C. Wang and T. F. Bell, "Electric Dipole Radiation at VLF in a Uniform Warm Magnetoplasma," Revue de Physique Appliquée (to be published, March 1972).

2. T. N. C. Wang and T. F. Bell, "Radiation Resistance of a Short Dipole Immersed in a Cold Magnetoionic Medium," Radio Sci., Vol. 4, No. 2, pp. 167-177 (1969).

3. T. N. C. Wang and T. F. Bell, "On VLF Radiation Resistance of an Electric Dipole in a Cold Magnetoplasma," Radio Sci., Vol. 5, pp. 605-610 (1970).

4. K. G. Balmain, "The Impedance of a Short Dipole Antenna in a Magnetoplasma," IEEE Trans., Ant. and Prop., AP-12, pp. 605-617 (1964).

5. W. E. Blair, "The Driving-Point Impedance of an Electrically Short Cylindrical Antenna in the Ionosphere," D.Sc. Thesis, University of New Mexico, Albuquerque, New Mexico (June, 1964).

6. W. E. Blair, "Ionospheric Diagnostics Using Resonances of an Electric Dipole Impedance," Radio Sci., Vol. 3, pp. 155-161 (1968).

7. T. N. C. Wang, "VLF Input Impedance Characteristics of Electric Dipole on a Magnetoplasma," Ph.D. Thesis, Stanford University, Stanford, California (May 1970).

8. T. N. C. Wang and T. F. Bell, "On VLF Radiation Fields Along the Static Magnetic Field from Sources Immersed in a Magnetoplasma," IEEE Trans., Ant. Prop., Vol. AP-17, No. 6, pp. 824-827 (November 1969).

9. W. P. Allis, S. J. Buchsbaum, and A. Bers, Waves in Anisotropic Plasmas (M.I.T. Press, Cambridge, Mass., 1963).

ANTENNA IMPEDANCE IN THE IONOSPHERE

Herschel Weil
Professor of Electrical Engineering
University of Michigan
Ann Arbor, Michigan U.S.A.

This paper deals with the work at the University of Michigan Radio Astronomy Observatory concerning the effects of the ambient ionospheric magnetoplasma on spacecraft antennas which are electrically short in free space. Specifically, we consider the effects on the impedance, Z, defined in terms of the antenna current density, $\bar{J}$, the electrical field $\bar{E}$ which this current generates and the input current, I_o as

$$Z = -I_o^{-2} \int \bar{E} \cdot \bar{J}^* dv.$$

The solution of the problem is dependent on a determination of $\bar{J}$. At frequencies for which the anisotropy of the ambient ionosphere has a predominant influence on the fields and currents $\bar{J}$ has not been determined analytically, even neglecting the inevitable non-uniformity of the medium due to the sheath and vehicle wake. In general $\bar{J}$ has been assumed, then $\bar{E}$ and Z computed, either for a uniform medium or for a simple model of a sheath. Even this is difficult and often further assumptions are made such as quasi-static fields or zero thickness wire antennas. The former approximation loses the radiation resistance contribution to the impedance, the latter loses the reactive part. These two simplifications were avoided by Lafon and Weil in Ref. (1) and by Weil in Ref. (2) so that both real and imaginary parts of Z could be computed simultaneously. These papers treat cylindrical tubular or helical antennas by reducing the three dimensional integral for Z to one dimensional integrals more suitable for numerical evaluation, and "sorting out" the effects of the longitudinal and circumferential components of the current and their interactions. No simple analytic solution results for $\mathrm{Im}Z$ as is the case for the quasi-static reactance of a cylindrical tube antenna.

Ref. (1) which deals with the case where the antenna axis is aligned with the earth's magnetic field includes numerical results, but they are not applicable to VLF. Results based on the final integral given in Ref. (1) and indicative of impedances for a short cylindrical antenna radiating VLF frequencies in the ionosphere are presented here in the Figure. The parameters were chosen to enable direct comparison with numerical results published by Seshadri (Ref. 3) for the radiation resistance of a short infinitely thin wire, and for the same reason were computed neglecting the ion contributions to the permittivity matrix, thus ignoring ion resonance effects. $\mathrm{Im}Z$ is also compared with the results of

Balmain's quasi-static formula (Ref. 4).

All non-uniformity of the ambient plasma has been neglected in the above analyses. One source of non-uniformity is the perturbation of the ionosphere by the spacecraft. Primarily this takes the form of a non-neutral wake region of highly non-uniform electron and ion distributions. Yorks and Weil in Ref. 5 describe experimentally observed effects of the wake on measured antenna impedance of an 18 meter cylindrical monopole antenna aboard the OGO-II satellite. The data were obtained as part of a University of Michigan Radio Astronomy experiment with a continuously operating 2.5 MHz impedance bridge and made use of the fact that the spacecraft rotation moved the antenna cyclically through the wake. The data described in Ref. 5 plus additional data from this experiment show that theories of the types described above can, at best, only partially account for the observed impedance variations. Some of the characteristic impedance features predicted by the theory discussed above, such as reactance sign changes which occur in passing from one region of the ionosphere to another with differing propagation characteristics, are indeed observed, but other similar features cannot be correlated with the theory in a consistent manner. This is true even under conditions when the antenna was roughly at right angles to the flight direction and well out of the wake. Although the above data was obtained with a frequency everywhere greater than the local gyro frequency in contrast to VLF which is well below the gyro frequency, one nevertheless suspects that similar difficulties in correlating the existing theory to experiment are to be found at VLF. The physical base in the theoretical work is oversimplified. Both additional theory based on more realistic physical pictures and more experimental data are needed. As one example of a lack in the theory we point out that there does not appear to be any analysis of the cylindrical antenna taking into account a longitudinal variation in the electron density along the antenna; yet this is the case for an antenna extending behind the vehicle into the wake.

REFERENCES

1. J.P. Lafon, H. Weil, "Impedance of cylindrical and helical antennas in lossy magnetoplasma including conditions of refractive index resonance," Radio Science, 5, 1970 (to appear).

2. H. Weil, "Impedance of arbitrarily oriented cylindrical and helical antennas in magnetoplasma," Radio Science, 5, April, 1970 (to appear).

3. S.R. Seshadri, "Radiation resistance of elementary electric-current sources in a magnetoionic medium," Proc. IEE, 112, No. 10, 1856-1869, 1965.

4. K.G. Balmain, "The impedance of a short dipole antenna in magnetoplasma," IEEE, Ant. Prop., AP-12, No. 5, 605-617, 1964.

5. H. Weil and R.G. Yorks, "OGO satellite wake structure deduced from antenna impedance measurements," Planetary and Space Science, (to appear).

This work was supported by NASA Grant NGL-23-005-017.

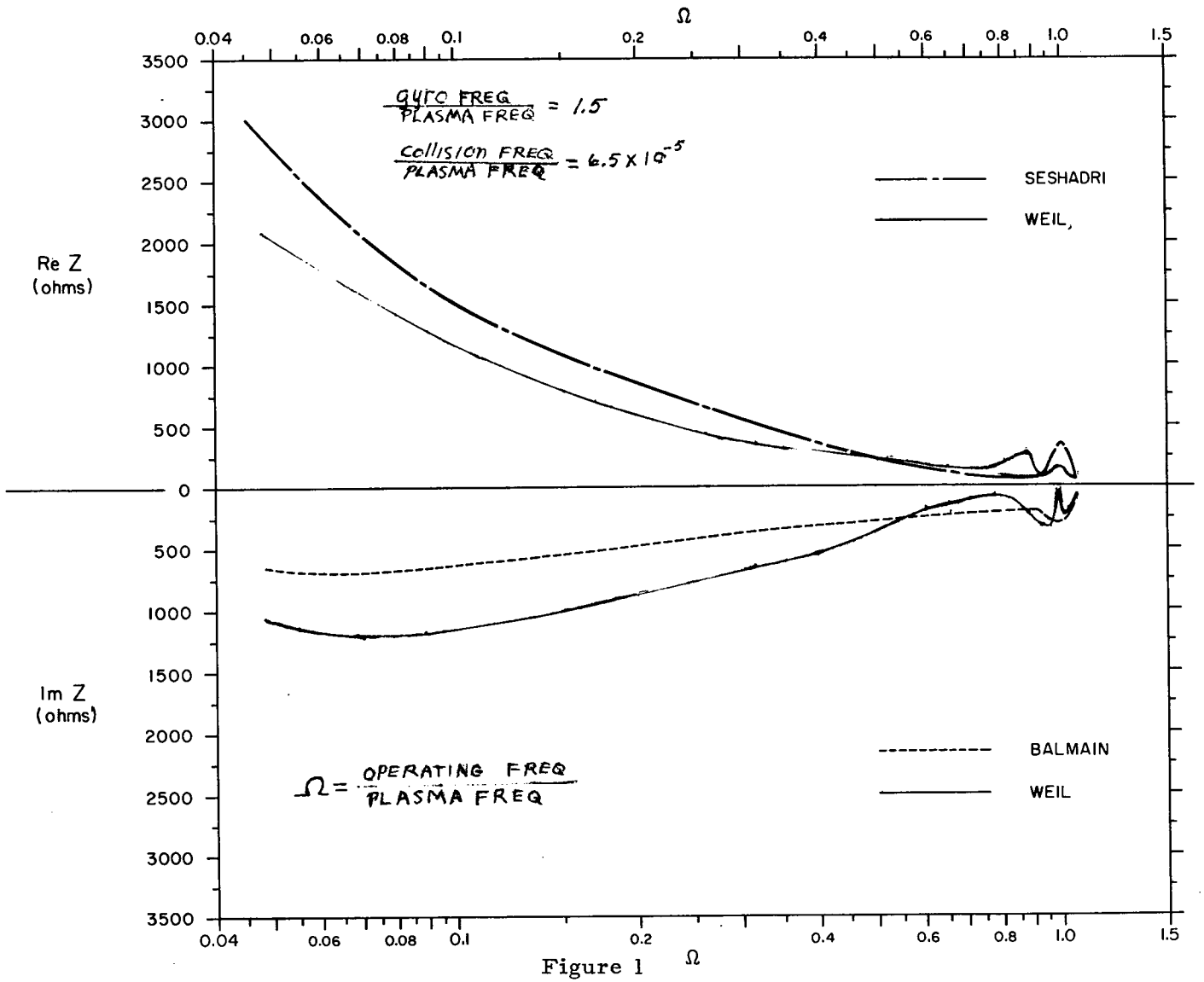

Figure 1

IMPEDANCE vs. IONOSPHERIC PARAMETER Ω

ANTENNA IMPEDANCE IN A WARM ANISOTROPIC PLASMA

by

Hollis C. Chen
Electrical Engineering Department
Ohio University
Athens, Ohio 45701

ABSTRACT

In this paper, we first reformulate the governing equations for a lossy, compressible and anisotropic electron plasma by introducing the compressivity and the permittivity tensors. The compressivity tensor takes into account the thermal motions of the electrons, while the permittivity tensor characterizes the anisotropy of the medium due to an external static magnetic field. With the dyadic Green's function method, we then obtain a formula for the impedance matrix of an electric current source immersed in such a medium. The results are expressed in terms of the components of the compressivity and the permittivity tensors. It is shown that the power radiated by an electric dipole in such a medium can be written as a Hermitian form associated with the impedance matrix. Some results have been reported in the reference, further numerical computations are in process.

Reference:

Chen, H.C., "Radiation characteristics of an electric dipole in a warm, anisotropic plasma," Journal of Applied Physics, Vol. 40, No. 10, p. 4068-4073. September, 1969.

RADIATION CHARACTERISTICS OF A CIRCULARLY PHASED DIPOLE ARRAY AT VLF IN A MULTICOMPONENT MAGNETOPLASMA

T. N. C. Wang
Radio Physics Laboratory
Stanford Research Institute
Menlo Park, California 94025

ABSTRACT

Using a linear full-electromagnetic-wave theory, a study is made to investigate radiation characteristics at VLF for a circularly phased dipole array in a multi-component magnetoplasma. Formal solutions for the total radiated complex power are derived. From these solutions, approximate closed-form expressions have been obtained for the increment on the input impedance, ΔZ, of either dipole of the array valid for the VLF range. Approximate closed-form expressions for the VLF power flux flowing parallel and perpendicular to the static magnetic field line are also derived.

It is found that in the VLF range a right-circularly phased dipole array can be used as a radiating source to increase total radiated power and to enhance the power density along the field line by a factor of four compared to that from a single dipole. The corrections for the input reactance $\Delta X(\equiv \jmath m\ \Delta Z)$ due to the effects of circularly-phasing are found to be negligible.

It is also found that the power flux along the field line from a right-hand circularly phased dipole array peaks by at least one order of magnitude at a frequency approximately half the electron gyrofrequency.

I INTRODUCTION

At present there is a strong interest in the study of VLF antenna radiation characteristics in a magnetoplasma because of the applications of this study to satellite-based wave-particle-interaction experiments and to diagnostic probes in the magnetosphere. The problem of antenna radiation at VLF in a magnetoplasma must be solved for the application of these antennas to VLF satellite communication systems. In all these applications, the knowledge of antenna radiation characteristics, such as the input impedance and the radiation pattern, is of primary concern. In the past, a considerable amount of work has been accomplished in the study of radiation properties from a single-element antenna (e.g., an isolated electric dipole or magnetic loop) embedded in a magnetoplasma. The bulk of knowledge in these subjects has been reviewed in recent reports[1,2] and research papers.[3-9]

It is known that the electromagnetic radiation and propagation in a cold multicomponent magnetoplasma can be generally characterized by the two basic modes known as the ordinary and extraordinary mode (see, e.g., Ratcliffe).[10] These two modes are in general either right-hand elliptically polarized or left-hand elliptically polarized. The details on the cutoff, the resonance, the propagation range, and the polarization for these two modes depend on the frequency range, the plasma composition, the relative densities, the strength of the static magnetic field ($\vec{B}_o$), and the direction of propagation with respect to $\vec{B}_o$. These propagation characteristics have been studied by a number of workers.[10-13]

In view of the polarization properties of the two modes we may anticipate that a properly phased antenna array (properly phased in the sense that it produces a resultant antenna current with its polarization matching that of the modes) in a magnetoplasma can increase

the total radiation power and enhance the radiation flux in some directions.[9] To the author's knowledge, little work has been accomplished for the problem of radiating arrays in a magnetoplasma. It is the purpose of this paper to investigate the VLF radiation characteristics for a pair of circularly phased dipole arrays in a multicomponent magnetoplasma.

The plan of our paper is as follows: In Section II, we shall present a basic formulation of the problem. The formal solution of Δp (increment of mean complex power due to the effect of circularly phasing) is derived. The increment of the formal expression of antenna input impedance ΔZ is then given by the relation, $\Delta Z = 2\Delta p/I_o^2$. In Section III, the increment of the radiation resistance $\Delta R = \Re e \Delta Z$ (for the lossless case) is studied for the VLF range. In Section IV, an approximate closed-form expression for ΔZ is derived by using a quasi-static calculation. The useful ratio, $\Delta Z/2Z_\perp$ ($Z_\perp$ is the impedance for a single isolated dipole), is estimated. In Section V some considerations on the effects of power flux due to the effects of circular phasing are examined. Finally, in Section VI several numerical plots for $\Delta R/2R_\perp$ and power flux are presented and discussed. From the results of our study it is found that a right-circularly phased dipole array should be used to increase total radiation resistance for the VLF range. The increment of radiation resistance possesses maxima at the frequencies close to the electron-gyrofrequency (f_{He}) and the proton gyrofrequency (f_{Hp}), and becomes a minimum at the lower-hybrid-resonance frequency (f_{LHR}). The increment in input reactance (and thus, the reactive power) due to the effects of circular phasing is bounded by 10 percent for the VLF range. For the frequencies $f_{LHR} < f < f_{He}$, the power flux along the magnetic field line from a right-circularly phased array is found to enhance by a factor of four compared with that from an isolated dipole; furthermore, this power flux peaks by

at least one order of magnitude at $f \simeq 0.5\ f_{He}$. On the other hand, the power flux along the magnetic field line from a left-circularly phased array approaches zero. The foregoing results suggest that for propagation of VLF waves or whistlers along the earth's magnetic field line, a right-circularly phased dipole array as a radiating source be used and, further, that the operating frequency should be close to half of the electron gyrofrequency.

II FORMULATION

Consider a pair of dipoles oriented in spatial quadrature on the x-y plane. The uniform static magnetic field $\vec{B}_o$ is oriented along the positive z-axis. The geometry of the problem is indicated in Figure 1.

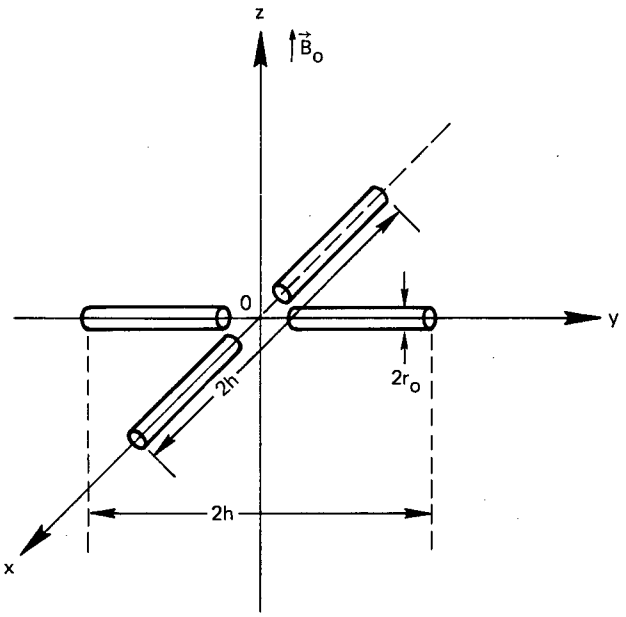

FIGURE 1 THE COORDINATE SYSTEM — GEOMETRICAL ORIENTATION OF THE CROSSED-DIPOLE ARRAY

Assuming a skin-triangular distribution for the dipole currents, and that the current for the dipole along the y-axis is in phase quadrature, either leading or lagging with respect to the phase of the dipole along the x-axis, we can write the total current density in the form:

$$\vec{J}_{\pm}(\vec{x}) = I_o\left[(1 - \frac{|x|}{h})\frac{\delta(\rho - r_o)}{2\pi\rho}\hat{x} \pm j(1 - \frac{|y|}{h})\frac{\delta(\rho' - r_o)}{2\pi\rho'}\hat{y}\right], \quad |x|,|y| \le h$$

$$= 0, \quad |x|,|y| \ge h \qquad (1)$$

where $\rho = \sqrt{y^2 + z^2}$, $\rho' = \sqrt{x^2 + z^2}$, $\hat{x}$, $\hat{y}$ and $\hat{z}$ are unit vectors, h represents the half length of the dipole, r_o is the dipole radius, and I_o is the effective current at the dipole driving terminals. In Eq. (1) the time factor $e^{j\omega t}$ is omitted.

It can be shown that the current vector $\vec{J}_+(\vec{x})$ rotates in a counter-clockwise direction about the positive z-axis, whereas $\vec{J}_-(\vec{x})$ rotates in a clockwise direction (see, e.g., Plonsey and Collin).[14] We shall therefore refer to the cross-dipole arrays with current $\vec{J}_{\pm}(\vec{x})$ defined in Eq. (1), as the left ($\vec{J}_+$) and the right ($\vec{J}_-$) circularly polarized dipole arrays, respectively.

Applying a three-dimensional Fourier transform to Eq. (1) yields

$$\vec{\mathcal{J}}_{\pm}(\vec{k}) = \frac{4I_o}{h}\left[\hat{x}\frac{\sin^2(hk_x/2)}{k_x^2}J_o(r_o k_\perp) \pm j\,\hat{y}\frac{\sin^2(hk_y/2)}{k_y^2}J_o(r_o k_\perp')\right] \qquad (2)$$

where $k_\perp = \sqrt{k^2 - k_x^2}$, $k_\perp' = \sqrt{k^2 - k_y^2}$ and $k^2 = k_x^2 + k_y^2 + k_z^2$, and where $J_o(x)$ is the zero-order Bessel function of the first kind.

Using Eqs. (2) and (6) of Ref. 3, the principal polarized components of Fourier-transformed current are given by

$$\mathcal{J}_{+1}(\vec{k}) = \frac{4I_o}{\sqrt{2}\,h}\left[\frac{\sin^2(hk_x/2)}{k_x^2} J_o(r_o k_\perp) \mp \frac{\sin^2(hk_y/2)}{k_y^2} J_o(r_o k_\perp)\right]$$

$$\mathcal{J}_{-1}(\vec{k}) = \frac{4I_o}{\sqrt{2}\,h}\left[\frac{\sin^2(hk_x/2)}{k_x^2} J_o(r_o k_\perp) \pm \frac{\sin^2(hk_y/2)}{k_y^2} J_o(r_o k_\perp)\right]$$

$$\mathcal{J}_o(\vec{k}) = 0 \quad . \tag{3}$$

By the use of Eqs. (3), (12), and (15) of Ref. 3 and after some manipulation, it can be shown that the mean complex power radiated from the dipole array is formally given by

$$P_{R,L} = P_x + P_y \pm \Delta P(\text{"+" sign for } P_R \text{ and "-" sign for } P_L) \tag{4}$$

where

$$P_x = \frac{C_o}{2}\int\left\{\frac{1}{n^2 - \epsilon_{+1}} + \frac{1}{n^2 - \epsilon_{-1}} - \frac{2n^2(n^2 - \epsilon_o)\sin^2\theta}{\alpha(\theta)(n^2 - n_+^2)(n^2 - n_-^2)} M(n,\psi)\right\} S_x(\vec{n})\,d\vec{n}$$

$$P_y = \frac{C_o}{2}\int\left\{\frac{1}{n^2 - \epsilon_{+1}} + \frac{1}{n^2 - \epsilon_{-1}} - \frac{2n^2(n^2 - \epsilon_o)\sin^2\theta}{\alpha(\theta)(n^2 - n_+^2)(n^2 - n_-^2)} [M(n,\psi) - \cos 2\psi]\right\} S_y(\vec{n})\,d\vec{n}$$

$$\Delta P = C_o\int\left\{\frac{1}{n^2 - \epsilon_{+1}} - \frac{1}{n^2 - \epsilon_{-1}} - \frac{2\epsilon_d n^2 \sin^2\theta(n^2 - \epsilon_o)(n^2 - \epsilon_s)}{\alpha(\theta)(n^2 - n_+^2)(n^2 - n_-^2)(n^2 - \epsilon_{+1})(n^2 - \epsilon_{-1})}\right\}$$

$$\times \sqrt{S_x(\vec{n})S_y(\vec{n})}\;d\vec{n} \tag{5}$$

and where

$$M(n,\psi) = \cos^2\psi + \frac{\epsilon_d^2}{(n^2 - \epsilon_{+1})(n^2 - \epsilon_{-1})}$$

$$S_x(\vec{n}) = \left(\frac{\sin \lambda n_x}{n_x}\right)^4 J_o^2(\beta r_o \sqrt{n^2 - n_x^2}) \ , \ S_y(\vec{n}) = \left(\frac{\sin \lambda n_y}{n_y}\right)^4 J_o^2(\beta r_o \sqrt{n^2 - n_y^2})$$

$$n_{\pm}^2 = \frac{(\epsilon_{+1}\epsilon_{-1} - \epsilon_o\epsilon_s)\sin^2\theta + 2\epsilon_o\epsilon_s \pm \sqrt{(\epsilon_o\epsilon_s - \epsilon_{+1}\epsilon_{-1})^2 \sin^4\theta + 4\epsilon_o^2\epsilon_d^2\cos^2\theta}}{2\alpha(\theta)}$$

$$\alpha(\theta) = \epsilon_o\cos^2\theta + \epsilon_s\sin^2\theta \ , \ \epsilon_s = (\epsilon_{+1} + \epsilon_{-1})/2 \ , \ \epsilon_d = (\epsilon_{+1} - \epsilon_{-1})/2$$

$\epsilon_\nu = 1 - \sum_r \frac{X_r}{1 + \nu Y_r}$ (sum over species), ν = +1, -1, 0, and X_r and Y_r (carrying charge sign) are standard notations for the normalized frequencies for r^{th} species (see, e.g., Ratcliffe[10])

$C_o = \frac{jI_o^2 Z_o}{\pi^3 (h\beta)^2}$, $Z_o \cong 120\pi$ ohms, $\lambda = h\beta/2$, $\beta = \omega/c$, free-space wave number

$\vec{n} = \vec{k}/\beta$, θ and ψ are the polar angle and azimuthal angle in spherical $\vec{n}$-space .

The derivation of Eq. (4) together with Eq. (5) is facilitated by noting the fact that the factors $n_x n_y$, $n_x^2 + n_y^2$, n^2 are in symmetry and that $n_x^2 - n_y^2$ is in antisymmetry with respect to interchange of n_x and n_y in the original integral after a direct substitution of Eq. (3) into Eqs.(12) and (15) of Ref. 3.

In Eq. (4), P_R is the total complex radiated power for the right-circularly polarized dipole array, whereas P_L is for the left-circularly polarized dipole array. P_x and P_y in Eq. (4) can be identified with the mean complex power radiated from an isolated dipole oriented at x-axis and y-axis, respectively.[3] The increment of complex power Δp is introduced due to relative phase quadrature (time and spatial) between the two dipole antennas.

Two interesting properties are directly noticeable from Eq. (4), which can serve to check for the correctness of Eq. (4):

(1) Suppose we superpose a right-circularly polarized dipole array upon a left-circularly polarized array, so that the antenna current for this combined array $J_c(\vec{x})$ is given by $J_c(\vec{x}) = 2I_o(1 - |x|/h)\delta(\rho - r_o)/2\pi\rho$, $|x| \leq h$ and zero otherwise. From Eq. (4), it is clear that $P_c = P_R + P_L = 4P_x$: Using Eq. (5), together with the symmetries contained in the integral, it is easy to show $P_x \equiv P_y$, which is the correct power radiated from an isolated antenna with current density $J_c = 2J_x$, while J_x yields a total power P_x.

(2) Whenever $\epsilon_{+1} = \epsilon_{-1}$, $\epsilon_d = 0$, it is clear from Eq. (5) that $\Delta P \equiv 0$, which indicates that at $\epsilon_{+1} = \epsilon_{-1}$, there is no increment in radiated power due to the effect of circularly phasing between the two dipoles. In a multicomponent magnetoplasma the condition $\epsilon_d = 0$ occurs at the so-called "crossover" frequencies, f_{co}.[13] At $f = f_{co}$, the polarization on the x-y plane of the two characteristic waves in the medium are identical, and further, this wave polarization becomes linear.[13] In the z-direction the medium becomes an isotropic one, and thus the circularly phasing dipole array considered should not radiate any power increment at f_{co}.

Using Eq. (4) together with the relation $Z_{R,L} = 2P_{R,L}/I_o^2$, the total input impedance (self plus mutual impedances) referring to driving terminals of either antenna takes the form: $Z_{R,L} = 2Z_\perp \pm \Delta Z$, where $Z_\perp$ represents the input impedance for an isolated antenna oriented perpendicular to $\vec{B}_o$. The calculation for $Z_\perp$ has been completed elsewhere.[2-4] In the remainder of this paper, we shall devote our efforts to the evaluation of the increment ΔZ.

III RADIATION RESISTANCE ΔR

Using the definitions of $n_\pm^2(\theta)$ and ΔP given in Eq. (5) and omitting a straightforward algebra we can cast ΔZ ($\Delta Z = 2\Delta P/I_o^2$) into the form

$$\Delta Z = j\tilde{C} \int_o^\infty dn \int_o^\pi d\theta \int_o^{2\pi} d\psi \frac{(\varepsilon_o - n^2\sin^2\theta)n^2\sin\theta}{\alpha(\theta)(n^2 - n_+^2)(n^2 - n_-^2)} \sqrt{S_x(\vec{n})S_y(\vec{n})} \qquad (6)$$

where $\tilde{C} = 4Z_o\varepsilon_d/\pi^3(h\beta)^2$.

For a lossless case (zero collision and perfectly conducting antenna), the real part of Eq. (6), ΔR ($\equiv \Re e\, \Delta Z$), can be considered as the increment of the radiation resistance caused by circular phasing. To calculate the real part of Eq. (6) we introduce small finite losses into the medium so that the pole-singularities [$n^2 = n_\pm^2$, $\alpha(\theta) = 0$] are removed from the real line. A contour integration can then be employed to obtain the proper pole contributions corresponding to the outgoing waves. After a contour integration, the losses are then allowed to vanish and the results are valid for the original lossless system. For convenience of performing a contour integration, we make use of the symmetries of the integrand and change the integration limits of Eq. (6) to the form: $\int_{-\infty}^{\infty} dn \int_o^{\pi/2} d\theta \int_o^{\pi/2} d\psi$. It is clear that this change of limit is suitable

to make a contour integration with respect to the variable n. Following a procedure similar to that discussed in earlier papers,[3-6] the contour integration with respect to n yields the following expression for ΔR:

$$\Delta R = \frac{16Z_o}{(\pi h\beta)^2}\,\epsilon_d \int_o^{\pi/2} d\psi \int_\theta d\theta \sum_\pm \frac{(n_\pm^2 \sin^2\theta - \epsilon_o)}{G(\theta)}\, S_\pm(\theta,\psi) n_\pm \sin\theta \qquad (7)$$

where $G_\pm(\theta) = +\sqrt{(\epsilon_o\epsilon_s - \epsilon_{+1}\epsilon_{-1})^2 \sin^4\theta + 4\epsilon_o^2\epsilon_d^2\cos^2\theta}$, $S_\pm(\theta,\psi) = \sqrt{S_x^\pm S_y^\pm}$,

and where $S_x^\pm$, $S_y^\pm$ are given by the substitution of $n_x = n_\pm \sin\theta\cos\psi$ and $n_y = n_\pm \sin\theta \sin\psi$ into the definitions of $S_x(\vec{n})$ and $S_y(\vec{n})$, respectively.

The domain for θ-integration covers the whole range of θ for which $n_\pm^2(\theta)$ is positive (the region of propagation for each mode in the wave normal space).

A. Two Important Features of ΔR

Before we proceed with any further evaluation of Eq. (7), there are two important features of ΔR, which are of interest to discuss. The first is to show the validity of the inequality $\Delta R < 2R_\perp$, where $R_\perp$ is the radiation resistance for a single dipole oriented perpendicular to $\vec{B}_o$. To show the validity of this inequality, we need a convenient form of $R_\perp$. Using P_x, P_y, and $n_\pm^2(\theta)$ of Eq. (5) and omitting some algebra, it can be shown that

$$R_x = \frac{8Z_o}{(\pi h\beta)^2} \int_o^{\pi/2} d\psi \int_\theta \sum_\pm \frac{[n_\pm^2(n_\pm^2 - \epsilon_o)\sin^2\theta\cos^2\psi - \alpha(\theta)n_\pm^2 + \epsilon_o\epsilon_s]}{G(\theta)}\, n_\pm \sin\theta\, S_x(\vec{n}_\pm) d\theta \qquad (8a)$$

$$R_y = \frac{8Z_o}{(\pi h\beta)^2} \int_o^{\pi/2} d\psi \int_\theta \sum_\pm \frac{[n_\pm^2(n_\pm^2 - \epsilon_o)\sin^2\theta \sin^2\psi - \alpha(\theta)n_\pm^2 + \epsilon_o\epsilon_s]}{G(\theta)} n_\pm \sin\theta\, S_y(\vec{n}_\pm) d\theta \ . \tag{8b}$$

From Eqs. (7) and (8), the difference $\delta \equiv 2R_\perp - \Delta R$ is given by

$$\delta = \frac{8Z_o}{(\pi h\beta)^2} \int_o^{\pi/2} d\psi \int_\theta \sum_\pm \frac{(n_\pm^2 \sin^2\theta - \epsilon_o)[(n_\pm^2 - 2\epsilon_s)S_x - 2\epsilon_d\sqrt{S_x S_y}]}{G(\theta)} n_\pm \sin\theta\, d\theta \ . \tag{9}$$

Using the limiting values of $n_\pm(\theta)$ derivable from Eq. (5), together with definitions of ϵ_o, ϵ_s, and ϵ_d, it is not difficult to show that the condition $\delta > 0$ holds for all frequencies.

The second important feature of ΔR to be discussed is related to the sign of ΔR. Using the definitions $n_\pm^2(\theta)$ it can be shown that, for the entire domain of θ-integration, $n_\pm^2 \sin^2\theta > 1$, $\epsilon_o < 1$ for $f > f_o$, and that $n_\pm^2 \sin^2\theta > 0$, $\epsilon_o < 0$ for $f < f_o$, where f_o is the plasma frequency. The integral itself in Eq. (7) is therefore always positive so that the sign of ΔR is determined by the sign of ϵ_d. The sign of ϵ_d can be easily determined from its definition. In the VLF range ($f_{He} > f > f_{Hp}$, $f_o > f_{He}$, where f_{He} and f_{Hp} are the electron gyrofrequency and proton gyrofrequency, respectively), $\epsilon_d > 0$, whereas in the ELF range ($f_{Hp} > f \geq 0$), $\epsilon_d < 0$ for the frequencies $f_{HI_i} > f > f_{coi}$, and $\epsilon_d > 0$ for $f_{coi} > f > f_{HI_{i+1}}$ (f_{HI_i} and $f_{HI_{i+1}}$ stand for the gyrofrequencies for the i^{th} and $i+1^{th}$ adjacent ion species and f_{coi} is the unique cross-over frequency between them).[13] These sign changes of ϵ_d for the ELF range hold for the frequencies between every pair of adjacent ion gyrofrequencies for the ELF range.

In view of Eq. (4), together with the above discussions, it is clear that in order to maximize the total radiated power we should use a right-circularly phased antenna array for the frequencies in the VLF range and $f_{coi} > f > f_{HI_{i+1}}$ in the ELF range, while a left-circularly phased antenna array should be used for the frequencies $f_{HI_i} > f > f_{coi}$ in the ELF range.

B. ΔR in the VLF Range

In the VLF range ($f_{He} > f > f_{HP}$, $f_o > f_{He}$), it can be shown from Eq. (5) that n_+ mode is not propagating ($n_+^2 < 0$). The term with subscript "+" in Eq. (7) is not present and the contribution of ΔR comes entirely from the n_- mode, known as the whistler mode. Since the refractive index surface of the n_- mode changes drastically from the frequencies above f_{LHR} (f_{LHR} denotes the lower-hybrid-resonance frequency) to the frequencies below f_{LHR}, it is convenient to make the separate analysis for ΔR in the frequency ranges $f \gtrless f_{LHR}$.

1. $f_{LHR} > f > f_{Hp}$

In this frequency range, $n_-(\theta)$ surface* is closed [$n_-(\theta)$ is bounded for all θ] and the maximum value of $n_-(\theta) \sin\theta$ is given by $a^{1/2}$ ($a = \varepsilon_{+1}\,\varepsilon_{-1}/\varepsilon_s$). For the case of antenna length subject to the constraint $h\beta\sqrt{a} \ll 1$ and $h \gg r_o$, we can use the small argument expansion of the sine and Bessel functions. This approximation leads to the following term:

$$\Delta R \simeq \frac{Z_o (h\beta)^2 \varepsilon_d}{2\pi} \int_o^{\pi/2} d\theta \, \frac{(n^2 \sin^2\theta - \varepsilon_o)}{G(\theta)} \, n \sin\theta \qquad (10)$$

where the subscript "-" is omitted.

---

* A refractive index surface for n_- mode obtained by plotting $n_-(\theta)$ as a function of θ in the wave normal space.

Using Eqs. (4) and (5) of an earlier paper[4] we can transform Eq. (10) into a new variable $y = n^2$ and recast Eq. (10) into the form:

$$\Delta R = \frac{Z_o (h\beta)^2 \epsilon_d}{4\pi} \frac{\epsilon_o}{(\epsilon_o - \epsilon_s)\sqrt{\epsilon_s(\epsilon_s - \epsilon_o)}} \int_{\epsilon_{+1}}^{a} \frac{y - \epsilon_s}{y - b}\sqrt{\frac{y - \epsilon_o}{(y - b)(y - a)}}\, dy \tag{11}$$

where $b = (\epsilon_{+1}\epsilon_{-1} - \epsilon_o\epsilon_s)/(\epsilon_s - \epsilon_o)$. The integral of Eq. (11) can be integrated exactly in terms of elliptical functions. For the frequency range considered, the ordering of the plasma parameter is such that $a > \epsilon_{+1} > 0 > b \geq \epsilon_o$, and by using tabulated integrals in Gradshteyn and Ryzhik,[15] Eq. (11) is integrated in the following closed form:

$$\Delta R = \frac{3R_o \epsilon_d |b|^{\frac{1}{2}}}{(\epsilon_s - \epsilon_o)} \left[F(p,q) - (1 + \frac{\epsilon_o}{\epsilon_s})E(p,q) + \sqrt{\left|\frac{\epsilon_{+1}}{b}\right|}\right] \tag{12}$$

where $R_o = (h\beta)^2 Z_o/6\pi$, the radiation resistance for a short dipole ($h\beta \ll 1$) in free space, and where $F(p,q)$ and $E(p,q)$ are the general elliptic integrals of the first and the second kind, respectively, with the arguments given by $p = \arcsin\sqrt{(a - \epsilon_{+1})/(a - b)}$ and $q = \sqrt{(a - b)/(a - \epsilon_o)}$.

The solution given in Eq. (12) is appropriate so long as $b \geq \epsilon_o$, and this condition is met for frequencies $f_{LHR} > f \geq f_{Hp}(1 + \Delta)$, in which $\Delta \sim 0(10^{-3})$. For the special cases of the three frequency ranges $f \rightarrow f_{LHR}$, $1/2\, f_{LHR} > f > 5f_{Hp}$, and $f \cong f_{Hp}$, we use the approximations discussed in Ref. 4, and the leading terms of Eq. (12) or Eq. (11) are given by

$$\Delta R \simeq \frac{3}{2} R_o \frac{\epsilon_{+1}\epsilon_d}{|\epsilon_o|^{\frac{1}{2}}|\epsilon_s|} \quad , \quad \tfrac{1}{2} f_{LHR} < f \lesssim f_{LHR} \qquad (13a)$$

$$\Delta R \simeq \frac{3\pi}{8} R_o \frac{\epsilon_d}{|\epsilon_s|^{\frac{1}{2}}} \quad , \quad 5 f_{Hp} < f < \tfrac{1}{2} f_{LHR} \qquad (13b)$$

$$\Delta R \simeq \frac{3}{\sqrt{2}} R_o \epsilon_{+1}^{\frac{1}{2}} \quad , \quad f_{Hp} \leq f \lesssim f_{Hp}(1 + \Delta) \quad . \qquad (13c)$$

2. $f_{LHR} < f < f_{He}$

In this frequency range, the refractive-index surface is not closed, and $n_-^2(\theta)$ varies from ϵ_{+1} to ∞ as θ increases from 0 to θ_r ($\theta_r = \arctan\sqrt{-\epsilon_o/\epsilon_s}$, known as the whistler mode resonance cone angle--see, e.g., Refs. 3 or 4). For the angular range $\theta > \theta_r$, $n_-^2(\theta) < \theta$ so the $n_-(\theta)$ mode is cutoff within the resonance cone, and the interval for θ-integration in Eq. (7) for this case is $0 \leq \theta \leq \theta_r$. Since the argument of the sine function as well as that of the Bessel function can be both large and small in the entire range of θ-integrations, it is difficult to integrate analytically. For this case, Eq. (7), with subscript "-", is conveniently integrated numerically and the results will be given in Section VI.

IV QUASI-STATIC CALCULATION

The quasi-static approximation ΔZ^Q can be obtained from Eq. (6) by taking the leading term as $n^2 \to \infty$:

$$\Delta Z^Q = -\frac{j8 Z_o \epsilon_d}{\pi^3 (h\beta)^2} \int_0^\infty d\alpha \int_0^\pi d\theta \int_0^\pi d\psi \frac{\sin^3\theta}{\alpha(\theta)} \sqrt{S_x(\vec{n}) S_y(\vec{n})} \quad . \qquad (14)$$

In the limit of $\beta r_o \to 0$, the integrations with respect to n and ψ can be performed straightforwardly to yield:

$$\Delta Z^Q = - \frac{j3\, Z_o \epsilon_d (h\beta)}{2\pi^2} \int_o^\pi d\theta \; \frac{\sin^2\theta}{\alpha(\theta)} \tag{15}$$

For the plasma parameters such that $\epsilon_o/\epsilon_s > 0$ (this condition is met for the frequencies $f_{LHR} > f > f_{Hp}$ in the VLF range considered), $\alpha(\theta)$ has no zero. Equation (15) is then purely reactive. A straightforward integration yields

$$\Delta X^Q = \frac{3Z_o h\beta\epsilon_d |\epsilon_s|^{\frac{1}{2}}}{j2\pi\epsilon_s (|\epsilon_s|^{\frac{1}{2}} + |\epsilon_o|^{\frac{1}{2}})} \quad , \quad \epsilon_s/\epsilon_o > 0 \tag{16}$$

On the other hand, when $\epsilon_o/\epsilon_s < 0$ (this condition is met for the frequencies $f_{He} > f > f_{LHR}$ in the VLF range), $\alpha(\theta)$ has a unique zero at $\theta = \theta_r$. Following a procedure discussed by Snyder and Weitzer,[16] Eq. (15) can be recast into the form

$$\Delta Z^Q = \frac{3Z_o \epsilon_d h\beta}{j\pi^2} \left\{ \frac{j\pi}{2} \frac{\sin\theta_r}{(\epsilon_s - \epsilon_o)\cos\theta_r} + \frac{\tan\theta_r}{2(\epsilon_s - \epsilon_o)} \log \frac{1 + \cos\theta_r}{1 - \cos\theta_r} + \frac{1}{2} \int_o^\pi \frac{\sin\theta(\sin\theta - \sin\theta_r)}{\alpha(\theta)} d\theta \right\} \tag{17}$$

The integral in Eq. (17) is now defined in the ordinary sense. From Eq. (17) we obtain

$$\Delta R^{Q} = \frac{3Z_o \epsilon_d h\beta}{2\pi(\epsilon_s - \epsilon_o)} \sqrt{-\frac{\epsilon_o}{\epsilon_s}} \quad , \quad \epsilon_o/\epsilon_s < o \tag{18a}$$

$$\Delta X^{Q} = \frac{3Z_o \epsilon_d (h\beta)}{j2\pi(\epsilon_s - \epsilon_o)} \quad , \quad \epsilon_o/\epsilon_s < o \quad . \tag{18b}$$

By comparison with the numerical results of Eqs. (18a) and (7), it is shown (in Section VI) that the approximate formula Eq. (18a) is in agreement to within 8 percent with Eq. (7). It is of interest to derive the ratio $\Delta Z/2Z_\perp$, where $Z_\perp$ presents the driving-point impedance for an isolated antenna oriented perpendicular to $\vec{B}_o$. To a good approximation, the leading terms of $Z_\perp$ are given by[2,17]

$$Z_\perp \simeq \frac{Z_o}{h\beta\pi\sqrt{-\epsilon_o\epsilon_s}} \left\{ \left(\log \frac{2h\alpha}{r_o} - 1 \right) - j \tan^{-1} \left| \frac{\epsilon_s}{\epsilon_o} \right|^{\frac{1}{2}} \right\} \quad , \quad \epsilon_o/\epsilon_s < 0 \tag{19a}$$

where $\alpha = \sqrt{\dfrac{\epsilon_o}{\epsilon_o - \epsilon_s}}$

$$Z_\perp \simeq \frac{Z_o}{h\beta\pi\sqrt{\epsilon_o\epsilon_s}} \left(\frac{\pi(h\beta)^3 \sqrt{\epsilon_o\epsilon_s\epsilon_{+1}}}{16} \tilde{R} - j \left\{ \log \left[\frac{2h}{(r_o + r_o\sqrt{\epsilon_s/\epsilon_o})} \right] - 1 \right\} \right) \tag{19b}$$

where $\tilde{R} = 8\epsilon_s^{-2}\epsilon_{+1}^{5/2} \Big/ 3\pi|\epsilon_o|^{\frac{1}{2}}$, $(\epsilon_{+1}/|\epsilon_s|)^{3/2}$, $\frac{8}{\pi}$ for the frequencies $\frac{1}{2}f_{LHR} < f \lesssim f_{LHR}$; $f_{LHR}/2 > f \geq 5f_{Hp}$ and $5f_{Hp} > f \gtrsim f_{Hp}$, respectively (see Ref. 5). Using Eq. (19) together with the approximate formulas, Eqs. (13), (16), and (18), we obtain the following ratios for $\Delta Z/2Z_\perp$:

$$\frac{\Delta R}{2R_{\perp}} \simeq \frac{3}{4} \frac{\epsilon_d \alpha^2 (h\beta)^2}{\log\left(\frac{2h\alpha}{r_o}\right)} \qquad , \ \epsilon_o/\epsilon_s < 0 \tag{20a}$$

$$\frac{\Delta X}{2X_{\perp}} \simeq \frac{3}{2} \frac{\sqrt{-\epsilon_o \epsilon_s}\,\epsilon_d (h\beta)^2}{(\epsilon_s - \epsilon_o) \tan^{-1}\left|\frac{\epsilon_s}{\epsilon_o}\right|^{\frac{1}{2}}} \tag{20b}$$

where

$$\frac{\Delta R}{2R_{\perp}} \simeq \frac{3}{4} \left|\frac{\epsilon_s}{\epsilon_{+1}}\right| \quad , \quad f_{LHR} \gtrsim f > f_{Hp}(1 + 10^{-3})$$

$$\simeq 2^{-3/2} \quad , \quad f \simeq f_{Hp} \tag{21a}$$

$$\frac{\Delta X}{2X_{\perp}} \simeq \frac{3}{2} \frac{\epsilon_d (h\beta)^2}{\log \frac{2h}{r_o(1 + \sqrt{\epsilon_s/\epsilon_o})}} \frac{|\epsilon_o|^{\frac{1}{2}}}{\left(|\epsilon_s|^{\frac{1}{2}} + |\epsilon_o|^{\frac{1}{2}}\right)} , \quad \epsilon_o/\epsilon_s > 0 . \tag{21b}$$

V EFFECTS ON POWER FLOW

In this section we shall examine some effects of circularly phasing between the two dipole elements on the power flux. Consideration is made only for the power flux in two directions: parallel and perpendicular to the magnetic field $\vec{B}_o$. For the lossless system considered, the power flux in configuration space $\vec{r}$ (e.g., in terms of spherical coordinates r, γ, φ) can be conveniently obtained by taking the power-

spectrum density in wave-normal space [i.e., the integrand of the real radiated power integral given by multiplying $I_o^2/2$ by Eq. (7) or Eq. (8)] and multiplying it by a proper Jacobian.[9,18] The details of this method in calculating the radiation pattern are described in Ref. 9. Using Eqs. (5), (10), (13), and (15) of Ref. 9, it is not difficult to show that for the cases of the waves from the saddle points $\theta = 0$, $\pi/2$, and π, the Jacobians are given by

$$\left.\frac{\partial(\theta,\psi)}{\partial(\gamma,\varphi)}\right|_{\theta = 0,\pi} = \left|\frac{2\epsilon_o}{\epsilon_o + \epsilon_{\pm 1}}\right| \quad ; \quad \left(\epsilon_{\pm 1} \text{ for } n^2(\theta = o) = \epsilon_{\pm 1}\right) \tag{22a}$$

$$\left.\frac{\partial(\theta,\psi)}{\partial(\gamma,\varphi)}\right|_{\theta = \pi/2} = \left|\frac{2\epsilon_s}{\epsilon_s + \epsilon_{\mp 1}}\right| \tag{22b}$$

[$\epsilon_{\mp 1}$ in Eq. (22b) corresponds to the two cases, $\epsilon_d > 0$ and $\epsilon_d < 0$, respectively.] The power flux in either direction parallel to $\vec{B}_o$ (from the rays in the wave normal angles $\theta = 0,\pi$) and in the directions perpendicular to $\vec{B}_o$ (rays at $\theta = \pi/2$) can be obtained by evaluating the power-spectrum density (in wave normal space) at $\theta = 0$, π, and $\pi/2$, and multiplying it by Eq. (22).

Using Eqs. (4), (7), (8), and (22a), and omitting a straightforward algebra, it can be shown that VLF power flux in either side along the static magnetic field ($\gamma = 0,\pi$) is given by

$$P_{\parallel}^{R} = \frac{2C'|\epsilon_o|\epsilon_d\epsilon_{+1}^{\frac{1}{2}}}{|\epsilon_o\epsilon_s - \epsilon_{+1}\epsilon_{-1}|}\left|\frac{2\epsilon_o}{\epsilon_o + \epsilon_{\pm 1}}\right| J_o^2(\beta r_o\sqrt{\epsilon_{+1}}) \quad , \quad f_{He} > f > f_{Hp} \tag{23a}$$

$$P_{\parallel}^{L} = 0 \tag{23b}$$

where $C' = Z_o (h\beta I_o)^2/32$, and where the superscripts R and L denote again, respectively, the right- and left-circularly phased dipole arrays.

Similarly, the VLF power flux flowing perpendicular to the static magnetic field is given by

$$P_{\perp}^{R,L} = 0 \quad , \quad f_{He} > f > f_{LHR} \tag{24a}$$

$$P_{\perp}^{R,L} = \frac{C'(a - \epsilon_o)a^{3/2}}{2|\epsilon_o \epsilon_d|} \left| \frac{2\epsilon_s}{\epsilon_s + \epsilon_{-1}} \right| \left| \frac{\epsilon_{\mp 1}}{\epsilon_{\pm 1}} \right| \quad , \quad f_{LHR} > f > f_{Hp} \tag{24b}$$

(the upper sign in $|\epsilon_{\mp 1}/\epsilon_{\pm 1}|$ is used for $P_{\perp}^{R}$, whereas the lower sign is used for $P_{\perp}^{L}$).

In Eq. (24b), it is assumed that the dipole is thin and short, and that the condition $(h\beta)^2 a \ll 1$, $h \gg r_o$ is satisfied.

Let $P_{\parallel}^{s}$ be the VLF power flux along $\vec{B}_o$ for an isolated dipole oriented perpendicular to $\vec{B}_o$. We can use either Eq. (8a) or Eq. (8b) to calculate $P_{\parallel}^{s}$, and it can be shown that $P_{\parallel}^{R} = 4P_{\parallel}^{s}$, which indicates a strong enhancement of VLF power flux along the magnetic-field line when employing a right-circularly phased dipole array.

It should be noted that for the frequency range $1/2\ f_{He} > f > f_{LHR}$, Eq. (23a) does not represent the total power flux flowing along the magnetic field. In this portion of the VLF range, in addition to $\theta = 0, \pi$, there are four more saddle points (two on each quadrature) on the whistler-mode refractive-index surface, which are given by $\theta = \theta_m$, $\pi - \theta_m$, $\pi + \theta_m$, and $2\pi - \theta_m$, where $\theta_m = \arccos (2\epsilon_s/\epsilon_d)$ [9]. The far fields from these saddle points are focused along field lines, with the enhancement of the ray proportional to the first power of the distance.[9,19] We shall not consider these focused rays along the field line for the present paper. Other than the case discussed above,

Eqs. (23) and (24) present the total power flux flowing parallel and perpendicular to $\vec{B}_o$, respectively, for the VLF range considered.

VI NUMERICAL RESULTS AND DISCUSSIONS

Our numerical data for the ratio $\Delta R/2R_\perp$ have been obtained by evaluating Eqs. (7) and (8) through the use of computer integration techniques. In Figure 2 we plot the ratio of the radiation resistance $r = \Delta R/2R_\perp$ as a function of normalized frequencies for various values of plasma density, plasma composition, static-magnetic-field strength, and dipole length. The curves are parametric in the variables h_o ($= 2\pi f_{He} h/c$, in which c is the velocity of light in free space), and f_o/f_{He} (f_o is the plasma frequency). The three values of f_o/f_{He} that are used ($f_o/f_{He} = 2, 5, 10$) were chosen as being representative of the range of values that can be encountered in the topside ionosphere and in the inner magnetosphere.

Figure 2(a) is a plot of r versus normalized frequency f/f_{He} in the range $0.05 < f/f_{He} < 0.975$. The lowest frequency plotted is sufficiently above the lower-hybrid-resonance frequency f_{LHR} ($f_{LHR}/f_{He} = 0.0232, 0.0228, 0.0207$ for $f_o/f_{He} = 10, 5, 2$, respectively). The plasma is assumed to consist of electrons and protons. The highest value of $h_o f_o/f_{He}$ for the curves plotted in Figure 2(a) is 2.5. For $h_o f_o/f_{He} \leq 2.5$, the r-curves are approximately proportional to f/f_{He} and to $(h_o f_o/f_{He})^2$. These curves agree with the approximate formulas of Eq. (20a) to within a few percent. Figure 2(b) is a plot similar to that of Figure 2(a) for the frequencies in the range $f_{Hp} \leq f < f_{LHR}$. The curves in this figure are plotted subject to the antenna-length constraint $h\beta\sqrt{a} \ll 1$, so that they are not parametric in h_o. The curves agree with the approximate formulas of Eq. (21a) to within a few percent. From these curves it is concluded that the increment in total radiation

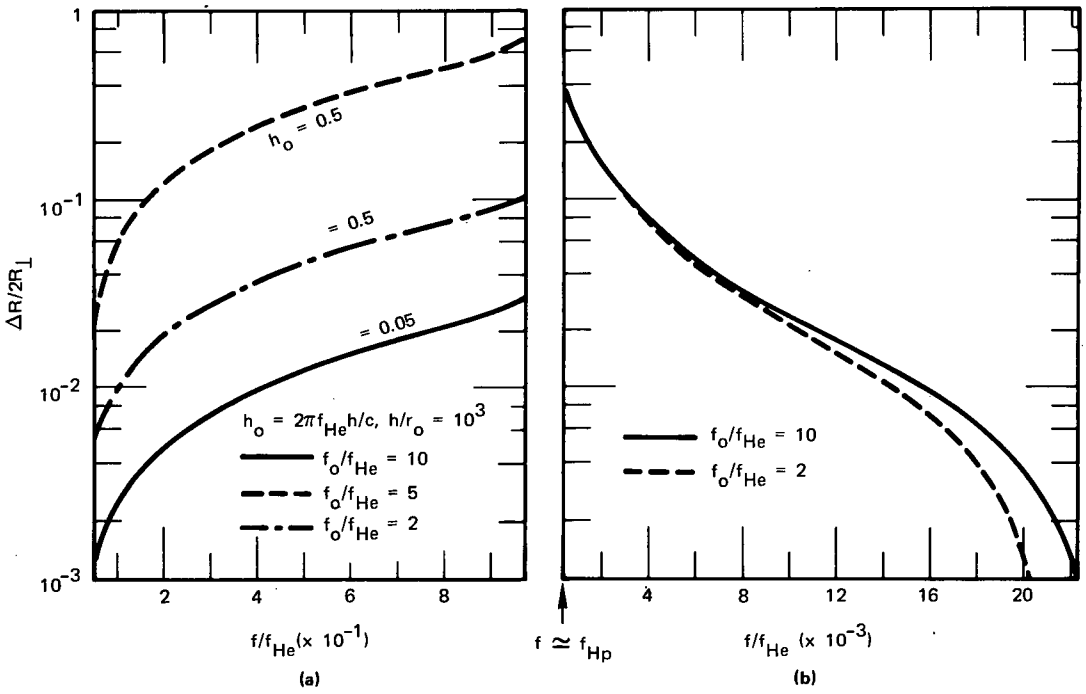

FIGURE 2 NORMALIZED RADIATION RESISTANCE $\Delta R/2R_\perp$ AS A FUNCTION OF NORMALIZED FREQUENCY IN THE VLF RANGE FOR THREE VALUES OF NORMALIZED PLASMA FREQUENCY, f_o/f_{He} = 10, 5, 2

power due to the effects of circularly phasing is significant ($r \gtrsim 0.1$) for the two cases: (a) $f_{He} \gtrsim f \gtrsim 0.2\ f_{He}$ and $(h_o f_o/f_{He}) \gtrsim 2.5$, and (b) $f_{Hp} \gtrsim f \gtrsim 8 f_{Hp}$. The ratio $r = \Delta R/2R_\perp$ reaches relative maximums at $f \simeq f_{He}$, f_{Hp}, and reaches minimum at $f \simeq f_{LHR}$.

Using Eqs. (20b) and (21b), we have also calculated the numerical data for the ratio $\Delta X/2X_\perp$ for the frequencies $f_{Hp} < f < f_{He}$. It is found that this ratio is bounded by 0.1, and much less than 0.1 for most cases. The input reactance correction due to circular phasing between the two dipoles is therefore not important. The numerical curves for $\Delta X/2X_\perp$ are thus omitted.

Figure 3 is a plot for the power flux $P_{\parallel,\perp}^{R,L}$ for the VLF frequency range. These curves are normalized with respect to the Factor $C = Z_o (h_o I_o)^2/32$. The curves in Figure 3(a) are plotted for the frequencies $1.5 \times 10^{-3}\ f_{He} < f < 2 \times 10^{-2}\ f_{He}$, which includes frequencies $f_{Hp} < f < f_{LHR}$. It is seen that $P_{\parallel}^{R} > P_{\perp}^{R,L}$ [note that $P_{\parallel}^{L} \equiv 0$--see (23b)] and $P_{\perp}^{R} \gtrsim P_{\perp}^{L}$ for most frequencies in the range. The $P_{\parallel}^{R}$ curves in Figure 3(b) are plotted for the frequencies $f_{LHR} < 0.05\ f_{He} < f < 0.95\ f_{He}$. [In this frequency range, $P_{\parallel}^{L} \equiv P_{\perp}^{L,R} \equiv 0$--see Eqs. (23b) and (24a).] The relative peak at $f \simeq 0.5$ is due to the focusing of the far-wave fields from the merging of the three saddle points $\theta = 0,\ \theta_m,\ 2\pi - \theta_m$.[9]

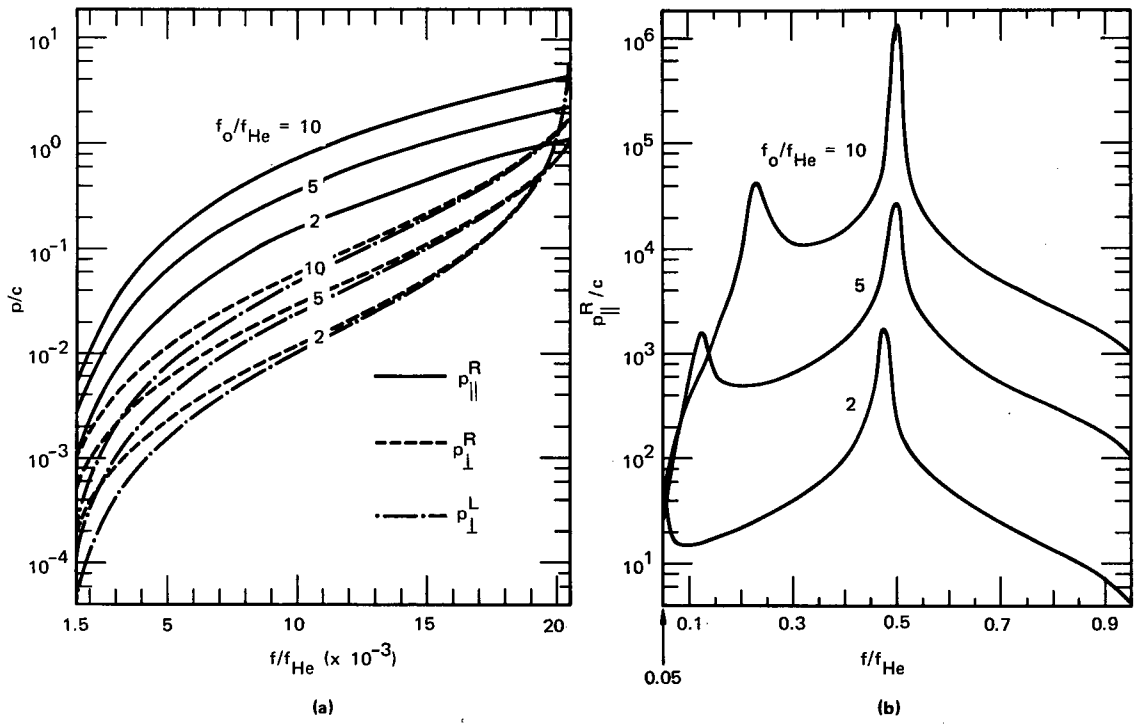

FIGURE 3 NORMALIZED POWER FLUX $P_{\parallel,\perp}/C$ ($C = Z_o h_o^2 I_o^2/32$) AS A FUNCTION OF NORMALIZED FREQUENCY IN THE VLF RANGE FOR THREE VALUES OF NORMALIZED PLASMA FREQUENCY, f_o/f_{He} = 10, 5, 2

The portions of the curves for the frequencies $1/2\ f_{He} \lesssim f \lesssim f_{He}$ represent the total power flux along the field line, whereas for the range $0.05\ f_{He} \lesssim f \lesssim 1/2\ f_{He}$, they represent only the power flux from the wave related to the saddle points, $\theta = 0, \pi$.

ACKNOWLEDGMENTS

The author is grateful to Drs. T. F. Bell and W. E. Blair for reading of the manuscript and for helpful discussions. This work was sponsored by U.S. Navy Contract No. N00014-70-C-0088.

REFERENCES

1. S. W. Lee and M. J. Al-Hakkak, "Impedance of Cylindrical Antennas in Plasma--A Review," Report No. 70-3, Antenna Lab., University of Illinois, Urbana, Ill. (January 1970).

2. T.N.C. Wang, "VLF Input Impedance Characteristics of Electric Dipole in a Magnetoplasma," Ph.D. thesis, TR No. 3414-1, Stanford University, Radio Science Laboratory, Stanford, California (May 1970).

3. T.N.C. Wang and T. F. Bell, "Radiation Resistance of a Short Dipole Immersed in a Cold Magnetoionic Medium," Radio Sci., Vol. 4, No. 2, pp. 167-177 (1969).

4. T.N.C. Wang and T. F. Bell, "On VLF Radiation Resistance of an Electric Dipole in a Cold Magnetoplasma," Radio Sci., Vol. 5, No. 3, pp. 605-610 (1970).

5. T.N.C. Wang and T. F. Bell, "On VLF Radiation Fields Along the Static Magnetic Field from Sources Immersed in a Magnetoplasma," IEEE Trans., Ant. Prop., Vol. AP-17, No. 6, pp. 824-827 (November 1969).

6. T. F. Bell and T.N.C. Wang, "Radiation Resistance of a Small Filamentary Loop Antenna in a Cold, Multicomponent Magnetoplasma," IEEE Trans., Ant. Prop., Vol AP-19, No. 4, pp. 517-522 (1971).

REFERENCES (Continued)

7. T.N.C. Wang, "ELF/VLF Radiation Resistance of an Arbitrary Oriented Finite Dipole in a Cold, Uniform Multicomponent Magnetoplasma," Journal de Physique, 32, pp. 877-885 (Nov.-Dec. 1971).

8. T.N.C. Wang and R. F. Bell, "Electric Dipole Radiation at VLF in a Uniform Warm Magnetoplasma," Revue de Physique Appliquée (to be published, March 1972).

9. T.N.C. Wang and T. F. Bell, "VLF Radiation Focusing and Patterns of Electric and Magnetic Dipoles in a Cold Magnetoplasma," J. Geophys. Res. (in press).

10. J. A. Ratcliffe, The Magnetoionic Theory and Its Application to the Ionosphere (Cambridge University Press, London, England, 1959).

11. W. P. Allis, S. J. Buchsbaum, and A. Bers, Waves in Anisotropic Plasmas, (M.I.T. Press, Cambridge, Mass., 1963).

12. T. H. Stix, The Theory of Plasma Waves (McGraw-Hill Book Co., Inc., New York, N.Y., 1962).

13. R. L. Smith and N. Brice, "Propagation in Multicomponent Plasmas," J. Geophys. Res., Vol. 69, No. 23, pp. 5029-5040 (1964).

14. R. Plonsey and R. E. Collin, Principles and Applications of Electromagnetic Fields, p. 474 (McGraw-Hill Book Co., Inc., New York, N.Y., 1961).

15. I. S. Gradshteyn and I. M. Ryzhik, Table of Integrals, Series, and Products, 4th ed. (Academic Press, New York, N.Y., 1965).

16. M. A. Snyder and H. Weitzner, "VLF Electromagnetic Radiation in a Magnetoionic Medium," Radio Sci., Vol. 3, No. 9, pp. 943-954 (1968).

17. K. G. Balmain, "The Impedance of a Short Dipole Antenna in a Magnetoplasma," IEEE Trans., Ant. Prop., Vol. 12, No. 5, pp. 605-617 (1964).

18. H. Staras "The Impedance of an Electric Dipole in a Magneto-ionic Medium," IEEE Trans., Ant. Prop., Vol. 12, No. 6, pp. 695-702 (1964).

19. E. Arbel and L. B. Felsen, "Theory of Radiation from Sources in an Anisotropic Media, Part II," in Symp. on Electromagnetic Theory and Antennas, Part I, pp. 421-459, E. C. Jordan, Ed. (Pergamon Press, New York, N.Y., 1963).

ELECTRON DENSITY DEPENDENCE OF VLF ANTENNA IMPEDANCE

D. A. McPherson, W. B. Harbridge, and H. C. Koons
The Aerospace Corporation
Los Angeles, California 90045

INTRODUCTION

Most satellite measurements of very low frequency (VLF) waves in the magnetosphere have been made with a loop antenna as the sensor. As a result, most of the data pertaining to VLF emissions are magnetic field measurements of waves propagating primarily in the whistler mode. In addition to detecting chorus, hiss, and whistlers, satellite-borne receivers have also observed phenomena that have not been detected on the ground because of the propagation characteristics of the wave modes involved. These include lower hybrid resonance emissions [Brice and Smith, 1965] and ion cyclotron waves [Shawhan, 1966].

VLF receivers have also been used with electric dipole antennas as the sensor [Barrington and Belrose, 1963; Scarf, 1968a; Shawhan and Gurnett, 1968]. Unlike the loop antenna, which has a relatively low impedance and is unaffected by the plasma environment, the electric dipole antenna may have a high free-space impedance that can be substantially altered by the electrical properties of the magnetospheric plasma [Storey, 1963]. This leads to an uncertainty in the ambient electric field intensity obtained from the potential measured across the antenna.

This problem may be circumvented by making the receiver input impedance high enough to be unaffected by antenna impedance changes [Scarf, 1968a], by measuring the antenna impedance in flight [Gurnett, et al., 1969], or by making the dipole long enough to make its free-space impedance small compared to the receiver input impedance. The latter was the case for the 45-meter dipole on Alouette [Barrington and Belrose, 1963].

A theoretical analysis of the impedance of an electric dipole antenna in a cold plasma has been performed by Balmain [1964]. This theory has been extended to include ion effects by Miller and Schulte [1968]. The effects of the plasma sheath on the impedance of an antenna in a warm, nonmagnetized, collisionless plasma have been investigated by Mlodnosky and Garriott [1963] and Fahleson [1967]. Aggson and Kapetanakos [1966] have calculated the impedance of a short cylindrical antenna aboard a satellite. They conclude that the resistive component dominates the capacitive component along magnetospheric orbits and that the output signal is proportional to the product of the ambient signal level and the plasma density.

This paper presents data from an electric field VLF experiment on board the USAF-OAR spacecraft OV3-3 (1966-70A). Most of the signal observed on the electric field antenna was caused by onboard sources of electrical interference. It was observed that the response of the instrument to this interference varied with altitude, magnetic latitude, and local time in a reproducible manner from orbit to orbit. This variation is attributed to antenna impedance changes caused by variations in the ambient plasma electron density. To support this conclusion, the predicted theoretical potential across the input to the preamplifier for an antenna potential induced by a constant near-field source is compared to the experimental data. The calculated potentials are obtained with both the cold, magnetized and the warm, nonmagnetized plasma antenna impedance theories. A magnetospheric ion plasma density based on OGO-2 data is used as an input for these calculations. The agreement of the experimental data with the theories is discussed. Detailed comparison of data and theory demonstrates that the warm plasma model of Mlodnosky and Garriott is more applicable to this experiment. It is also shown that the electron density may be obtained from a measurement of the antenna impedance at VLF frequencies.

DESCRIPTION OF EXPERIMENT

The OV3-3 spacecraft was launched from the Western Test Range at 10 h 45 m UT, on August 4, 1966, into a polar orbit with a 137-minute period, an 81.6° inclination, a 4488-km apogee, and a 362-km perigee. The orbit was initially in the 4 o'clock meridian with perigee on the morning side. The spacecraft was spin stabilized with an initial spin rate of 8.8 rpm.

Figure 1 shows a block diagram of the Aerospace VLF experiment. The magnetic antenna is a ferrite-core coil 35.6 cm long and 3.5 cm in diameter, with an effective area of 100 m^2. The electric field antenna consists of an aluminum vapor coating on the fiberglass housing of the magnetic antenna. The antenna was deployed in the equatorial plane of the satellite, with the axis of the ferrite core oriented perpendicular to the spin axis of the spacecraft. Thus the antennas respond to the components of the electric and magnetic field fluctuations that are perpendicular to the spacecraft spin axis.

After preamplification, the antenna signals are alternately switched for processing. The selected signal is further amplified and fed to an array of ten bandpass filters (15% bandwidth) at 400 Hz, 730 Hz, 1.3 kHz, 2.3 kHz, 3.9 kHz, 5.4 kHz, 7.35 kHz, 10.5 kHz, and 14.5 kHz. The bandpass filters are connected to automatic gain control amplifiers that compress the dynamic range from 60 dB to 30 dB. After rectification, the filtered, compressed signals are telemetered directly to the ground station or stored on an onboard

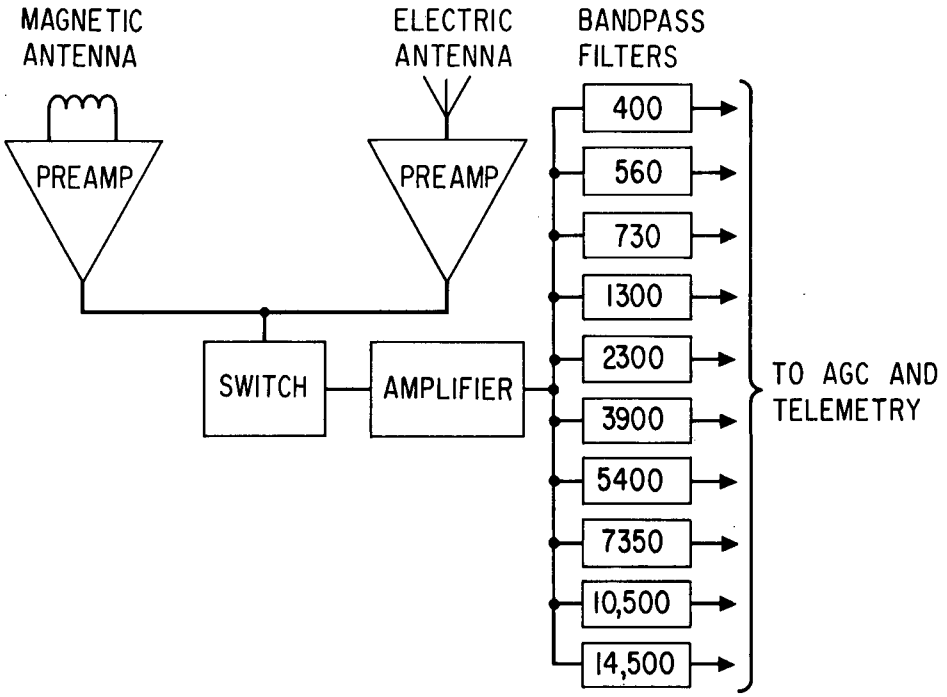

Block diagram of the Aerospace VLF experiment.

Figure 1

tape recorder for later transmission. The data then consist of 20 voltages that represent the electric and magnetic field intensities at ten frequencies between 400 Hz and 14.5 kHz. Each voltage is sampled once every four seconds and represents the average signal intensity over the preceding 30 msec. The sensitivity of the instrument is 1 μV for electric potentials and 1 mγ for magnetic fields. The dynamic range is 60 dB.

In this paper, we present some of the experimental data obtained from the Aerospace electric field antenna on OV3-3 and discuss antenna impedance variations that are manifested in the data and that can be used to determine properties of the thermal plasma in the magnetosphere.

COMPARISON OF OBSERVED ELECTRIC POTENTIALS WITH MAGNETOSPHERIC ION DENSITIES

Data obtained from the electric field antenna during orbit 706 are shown in Figure 2. The data have been averaged over 1-minute intervals. The variations observed in the data do not necessarily represent variations in the electric field intensities in the magnetosphere, but rather they are proportional to the variations in the input voltage Φ_{in} across the preamplifier of the electric field antenna. The two are not directly related unless the impedance of the antenna is constant.

This orbit is approximately in the dawn-dusk meridian, and the potential variations observed in all of the channels show rough symmetry about the magnetic pole. The over-all structure, particularly at higher altitudes south of the magnetic equator, is similar to the hydrogen ion densities measured by the RF ion mass spectrometer aboard spacecraft OGO-2 during an orbit in the dawn-dusk meridian plane [Taylor et al., 1968]. Figure 3 shows the composition of the dominant species, H^+ and O^+, on the dawn-dusk meridian at 1000 km, as obtained from the OGO-2 data. A more direct comparison can be made by scaling the densities of the OGO-2 orbit to the OV3-3 orbit. The ion composition at a magnetic latitude ϕ_m and altitude h may be obtained from these data if the species are assumed to be in diffusive or chemical equilibrium along a field line [Taylor et al., 1968]. The altitude dependence of the density of the ith ion species is assumed to be given by

$$N_i(h) = N_i(h_0, \phi_0) \exp(-h/H_i) \qquad (1)$$

where $N_i(h_0,\phi_0)$ is the density of the ith ion species at h_0 = 1000 km at the magnetic latitude ϕ_0 of the field line passing through the spacecraft. For a dipole magnetic field, ϕ_0 is related to ϕ_m and h by

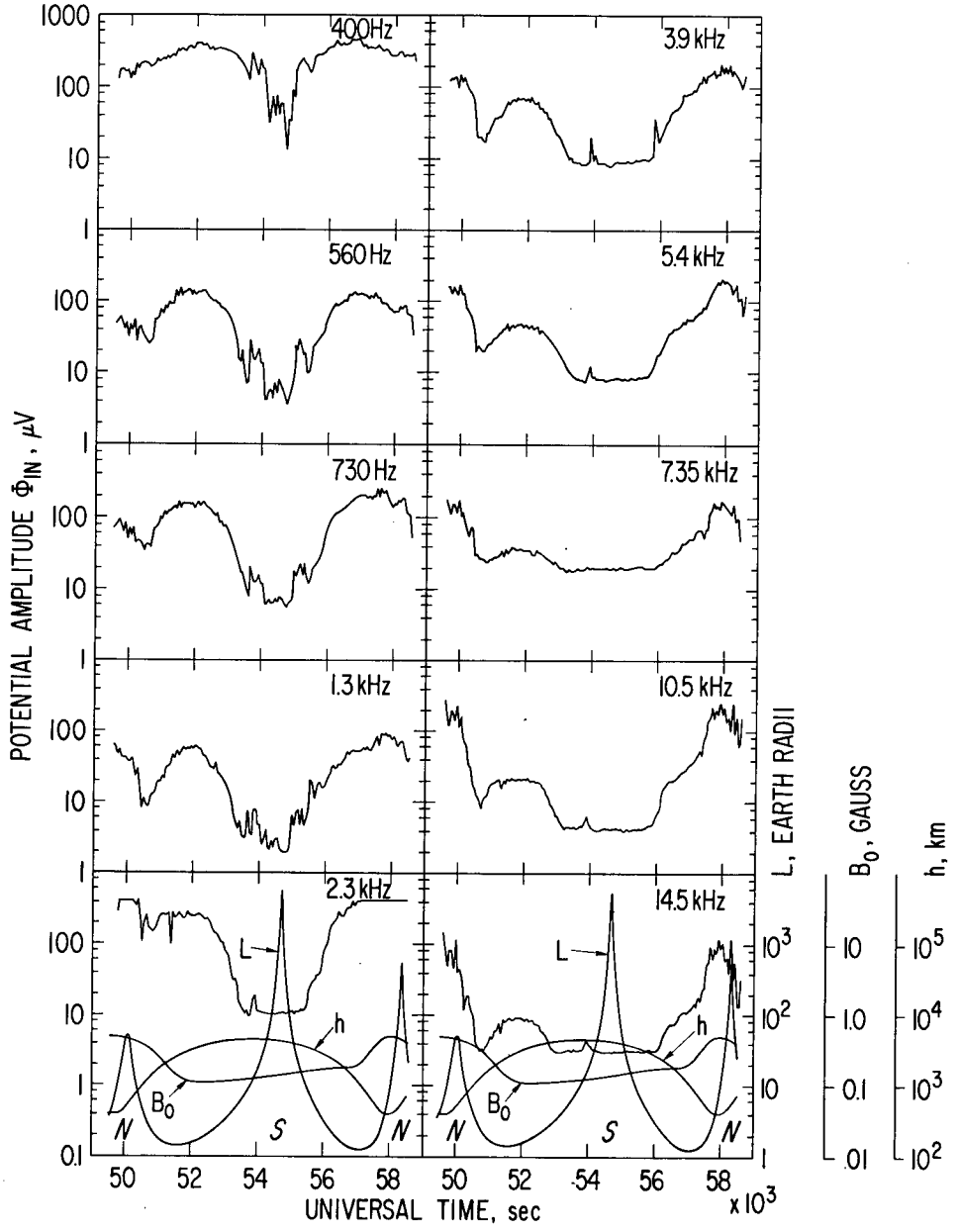

Data from the electric field antenna obtained during orbit 706.

Figure 2

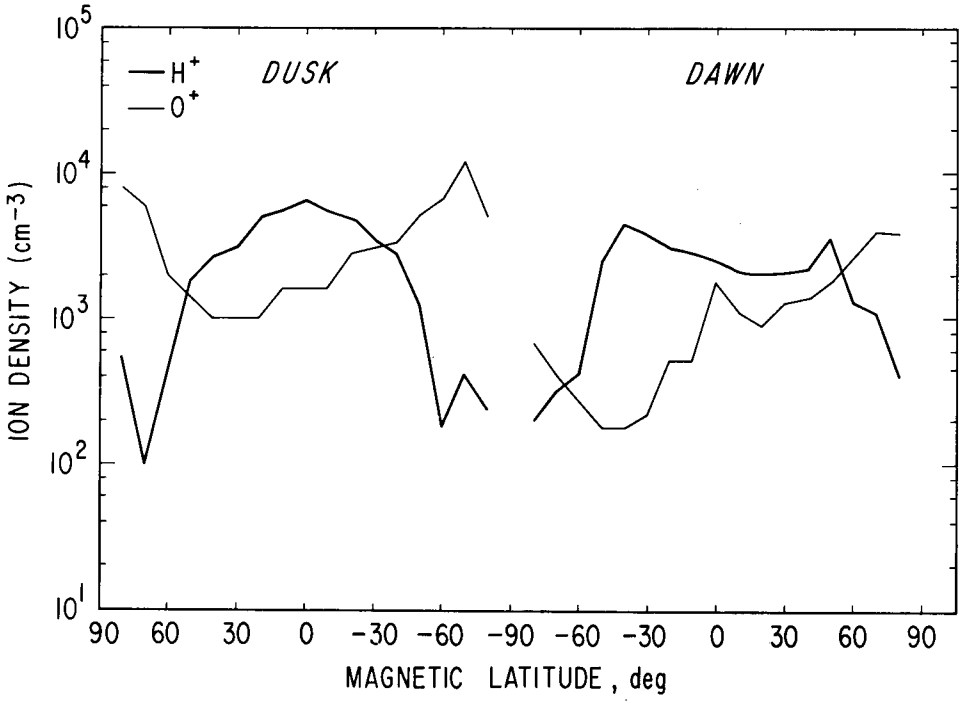

Densities of H^+ and O^+ at 1000 km obtained by the RF ion spectrometer aboard OGO-2 in the dawn-dusk meridian [Taylor et al., 1968].

$$\phi_0 = \cos^{-1}\left[\left(\frac{R_0 + h_0}{R_0 + h}\right)^{1/2} \cos \phi_m\right] \tag{2}$$

where $R_0 = 6370$ km is the radius of the earth. In equation 1, the scale height H_i may be written as

$$H_j = RT/M_i g \tag{3}$$

where $R = 8.3 \times 10^7$ erg deg^{-1} is the gas constant and g is the gravitational acceleration at an altitude h,

$$g = g_0 \left(\frac{R_0}{R_0 + h}\right)^2 \tag{4}$$

where $g_0 = 980$ cm sec^{-2}; T is the plasma temperature, which is assumed to be constant over the dusk or dawn portion of the orbit; and M_i is the effective mass of the ith species. The value of M_i depends on the ion species and on the type of equilibrium assumed. Following the analysis of Taylor et al., O^+ is assumed to be in diffusive equilibrium over the entire orbit with $M_i = 8$, and H^+ is assumed to be in diffusive equilibrium above 600 km with $M_i = 1/2$ and in chemical equilibrium below 600 km with $M_i = 7$.

The densities of H^+ and O^+ along the dusk portion of orbit 706 were calculated using equations 1 through 4 with the value of N_i (h_0, ϕ_0) obtained from the OGO-2 data. For this two-ion model the total ion density is equal to the sum of the hydrogen and oxygen densities. This is also taken to be the electron density. The resulting total density is plotted in Figure 4 together with the signal from the 730-Hz electric field channel for the dusk portion of orbit 706. The general agreement between the shape of the observed signal and that of the total density suggests that the response of the electric field antenna depends upon the local plasma density.

The relationship between local plasma density and signal level can be caused either by an increase in the ambient electric field or a decrease in the antenna impedance with ion density. A qualitative description of antenna signal potential will demonstrate that most of the signal is caused by currents between the antenna and the solar cell array. It will be shown that the variation of signal level shown in Figure 2 is mainly caused by changes in the antenna impedance as a function of ion density.

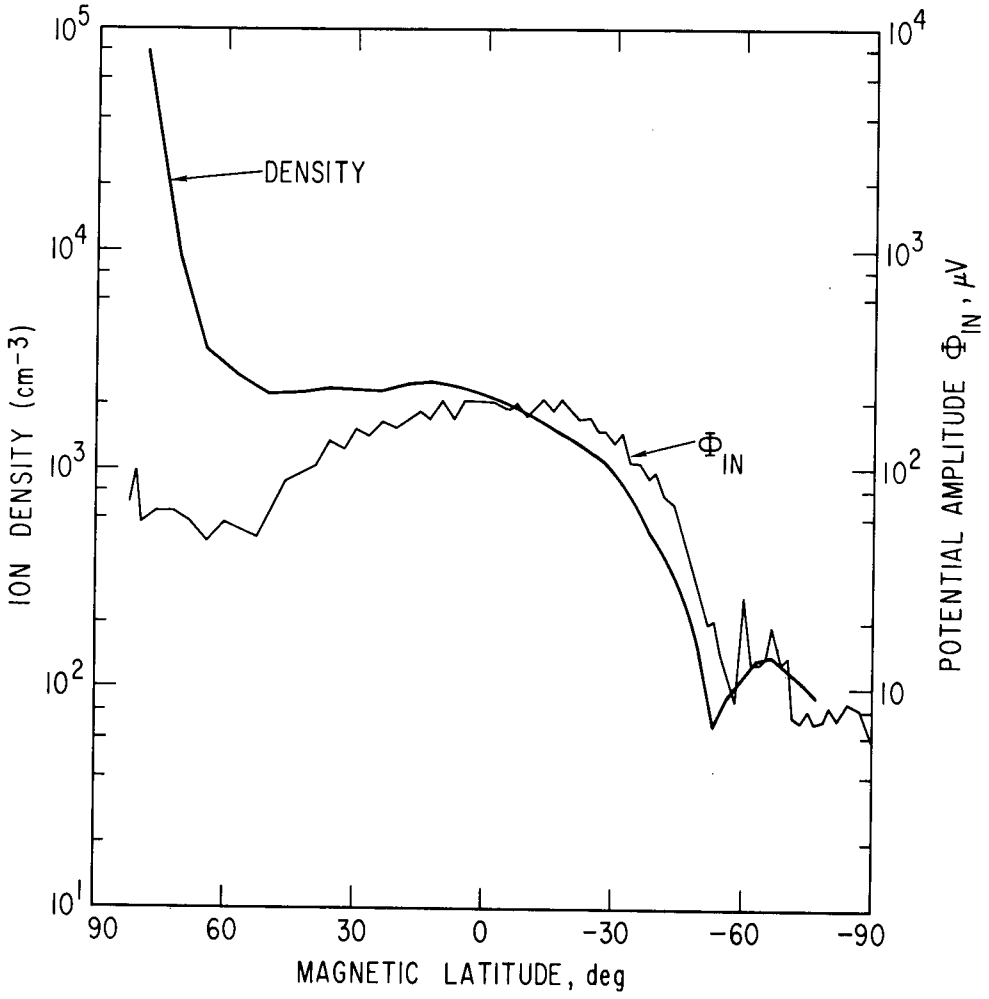

Total ion density along the dusk portion of OV3-3 orbit 706 computed by scaling the H^+ and O^+ densities shown in Figure 3 from 1000 km to the altitude of OV3-3. The 730-Hz data from the electric field antenna from orbit 706 are shown for comparison.

Figure 4

SIGNAL SOURCE

Figure 5 shows data obtained from the electric field antenna during orbit 523. The spacecraft was in shadow from 16060 to 18029 UT. Except at 2.3 kHz, all data show a sharp decrease as the spacecraft entered the shadow and a sharp increase as it emerged. A detailed examination of the data shows that the abrupt changes correspond precisely with changes in the solar cell current level. The signal on the 2.3-kHz channel is caused by a 2-kHz modulation of the Faraday cup instrument. The signal level of this channel is unaffected by transition from sun to shadow, showing that the antenna impedance is likewise unaffected by this change. During orbits in which the Faraday cup was off, the data on the 2.3-kHz channel behaved the same way as the other frequency channels did to sun or shadow conditions.

Shot noise from photoelectric currents produced on the antenna has been calculated and found to be small compared to the signal levels observed. In addition, photoelectric currents should produce a smooth spectrum of noise rather than the irregular dependence on frequency actually observed. The frequency spectrum of the electric field antenna data is similar to the noise induced on the magnetic antenna by spacecraft systems such as the tape recorder.

It is concluded that most of the signal observed on the electric field antenna is caused by currents between the solar cell array and the antenna. The potential of the solar array is modulated by several dc-dc converter oscillators on the spacecraft. Real currents can flow from the array into the ambient plasma through the many solder points connecting the individual cells. Because the impedance of the power system is low and the area encompassed by the near-field is large, it is assumed that the solar array constitutes a potential source that is independent of ambient plasma conditions. On the basis of this assumption, the antenna impedance is calculated as a function of ion density at the position of the spacecraft, using both a sheathless cold plasma formulation and a sheath-dominated warm plasma formulation.

ANTENNA IMPEDANCE IN A COLD PLASMA

Balmain [1964] has derived an expression for the impedance of a short cylindrical dipole antenna in a cold electron plasma in the absence of a sheath for an arbitrary angle between the antenna axis and a dc magnetic field. At VLF frequencies, the conductivity of the ions cannot be neglected with respect to the conductivity of the electrons. Miller and Schulte [1968b] have formulated the problem at VLF frequencies by including ion terms in the expression for the impedance derived by Balmain. This formulation has given quite good agreement for the frequency response of the impedance of an electric field antenna aboard an ionospheric rocket probe at frequencies above the electron cyclotron frequency [Miller and Schulte, 1968a]. It has also given good agreement for the angular dependence

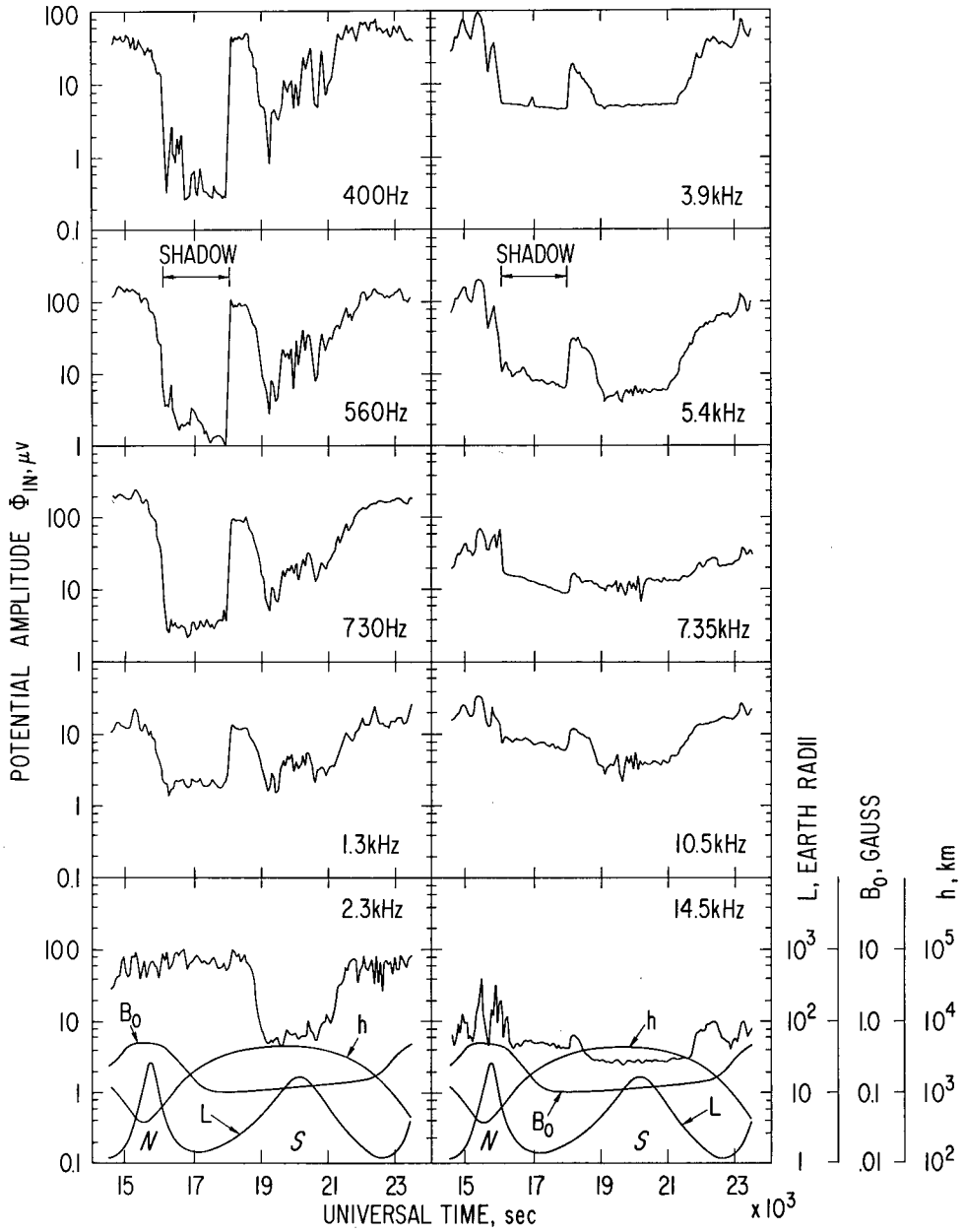

Data from the electric field antenna obtained during orbit 523. The decrease in signal from 16060 to 18029 UT occurs while the spacecraft is in shadow. Note that the 2.3-kHz data do not show a decrease in the shadow.

Figure 5

of the modified plasma resonance, which occurs between the electron plasma frequency and the upper hybrid resonant frequency. This resonance has been described by Oya [1968] and measured in the ionosphere by a rocket-borne "gyroplasma probe" by Ejiri, Oya, and Obavashi [1968].

The validity of the cold, magnetized plasma theory as applied to the OV3-3 VLF antenna is determined quantitatively by calculating the antenna impedance and comparing the prediction to the experimental results. The input circuit to the electric field antenna preamplifier on OV3-3 is shown in Figure 6a. As discussed, the source potential Φ_s is assumed constant and its impedance Z_s small. C_A is the capacitance between the aluminum vapor coating and the ground plane, which are separated by the fiberglass cover of the magnetic antenna. The resistor R and capacitor C_{in} form an RC network to provide rolloff with increasing frequency.

In the absence of a plasma, $Z = Z_0 = 1/j\omega C_0$ is the capacitance between the antenna and the solar cell array. The value of C_0 obtained from preflight calibrations at 1000 Hz is 13.3 pF. This value gives a good agreement between the frequency response of the circuit at constant Φ_s and the measured preflight frequency response.

According to the formulation of Miller and Schulte, the complex impedance of the antenna in the magnetoplasma is

$$Z = \frac{a}{2\pi j\omega\epsilon_0 L\kappa_\perp F^{1/2}} \left\{ \ln \left[\frac{L}{r} \frac{2F}{(a + F^{1/2})} \right] - 1 \right\} \qquad (5)$$

where

- L = half-length of dipole antenna
- r = antenna radius
- $\kappa_\parallel$ = diagonal element of dielectric tensor parallel to magnetic field
- $\kappa_\perp$ = diagonal element of dielectric tensor perpendicular to magnetic field
- a^2 = $\kappa_\perp/\kappa_\parallel$
- F = $\sin^2\theta + a^2 \cos^2\theta$
- θ = angle between antenna axis and magnetic field
- ϵ_0 = permittivity of free space
- ω = angular frequency of the signal

The elements of dielectric tensor $\kappa_\perp$ and $\kappa_\parallel$ depend upon magnetic-field and charged-particle densities and collision frequencies [Allis et al., 1963].

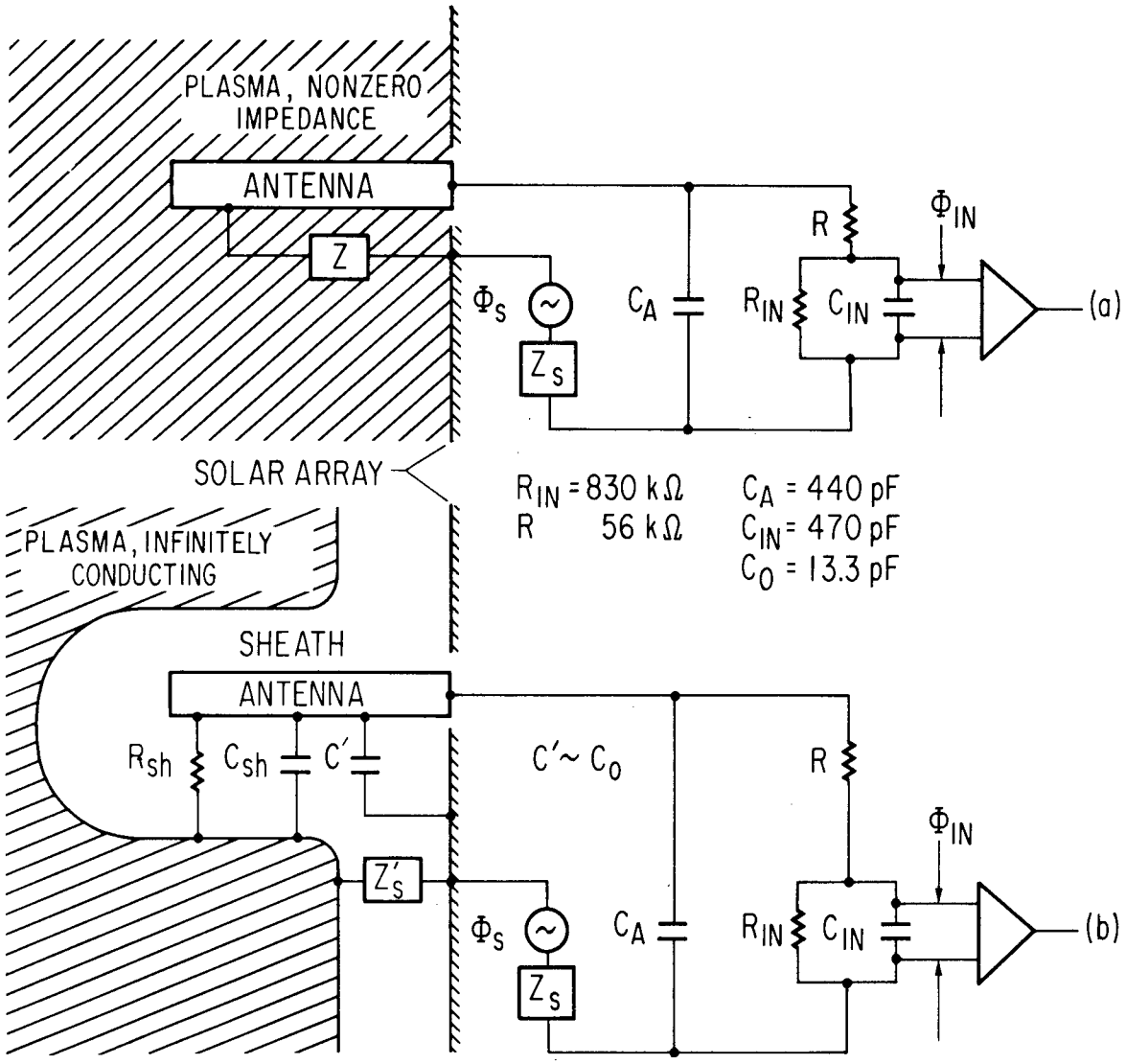

(a) Input circuit for the electric field antenna for the case of a cold, sheathless plasma.
(b) Input circuit for the case of a sheath-dominated, warm plasma. The source impedance Z_S is assumed to be much smaller than the antenna and input impedance.

Figure 6

Equation 5 was used to calculate the impedance of the OV3-3 electric field antenna for the ion density model, derived from the OGO-2 data. The geomagnetic field intensity was calculated from the Jensen and Cain 99-term multipole expansion, and the plasma was assumed collisionless. Using the computed impedance Z, values of the ratio Φ_{in}/Φ_s were obtained. The computed value of this ratio is plotted in Figure 7 for the frequencies corresponding to the ten bandpass filters. For this computation the angle between the antenna and the earth's magnetic field was zero. The agreement between the theoretical calculations based on the OGO-2 ion density distributions and the signal variations measured by the VLF antenna is reasonably good for several of the frequencies.

Several serious discrepancies do, however, appear between the predictions of the cold plasma theory and the observations. First, the sharp minima that are noted in the computed curves in Figure 7 at frequencies between 2.3 kHz and 7.4 kHz are not observed experimentally. These minima occur when the antenna impedance becomes large at the ion-electron hybrid resonant frequency. This lower hybrid resonance is associated with ion motion in the geomagnetic field. Because the ion gyro radii are generally larger than the dimensions of the antenna system, it is reasonable that the antenna impedance is independent of ion gyromagnetic motion. Second, the shape of the calculated curves at low altitude appears to depart significantly from the predicted shape. This will be considered in more detail in relation to the second model discussed below. The third and most serious discrepancy is the angular dependence predicted for the impedance in equation 5. At $\theta = 0$, $F = \kappa_\perp/\kappa_{||}$, which is of the order of 10^{-4} for most of the orbit. However, for moderate angles between the antenna and the magnetic field, F is essentially independent of $\kappa_\perp$ and $\kappa_{||}$. The ratio Φ_{in}/Φ_s for a frequency of 730 Hz is plotted in Figure 8 for $\theta = 10^\circ$. This calculation bears no resemblance to the experimental observations. Φ_{in}/Φ_s is approximately 1 at nonzero angles because the extremely large value of the conductivity along the magnetic field, which appears in the denominator of equation 5 at nonzero angles, greatly reduces the antenna impedance.

These discrepancies indicate that the sheathless cold plasma theory is not valid when applied to the calculation of the impedance of a short dipole antenna at VLF frequencies.

SHEATH-DOMINATED ANTENNA IMPEDANCE

In a warm plasma the antenna is coupled to the plasma by the sheath that surrounds the antenna and spacecraft. Mlodnosky and Garriott [1963] have shown that the impedance of a dipole in the lower ionosphere is determined by the impedance of the ion sheath that forms around the antenna. Their calculations of the complex admittance of a dipole for an assumed electron density profile agree well with the experimental measurements obtained from a dipole flown by Lomax, [1961] on a Nike-Cajun rocket.

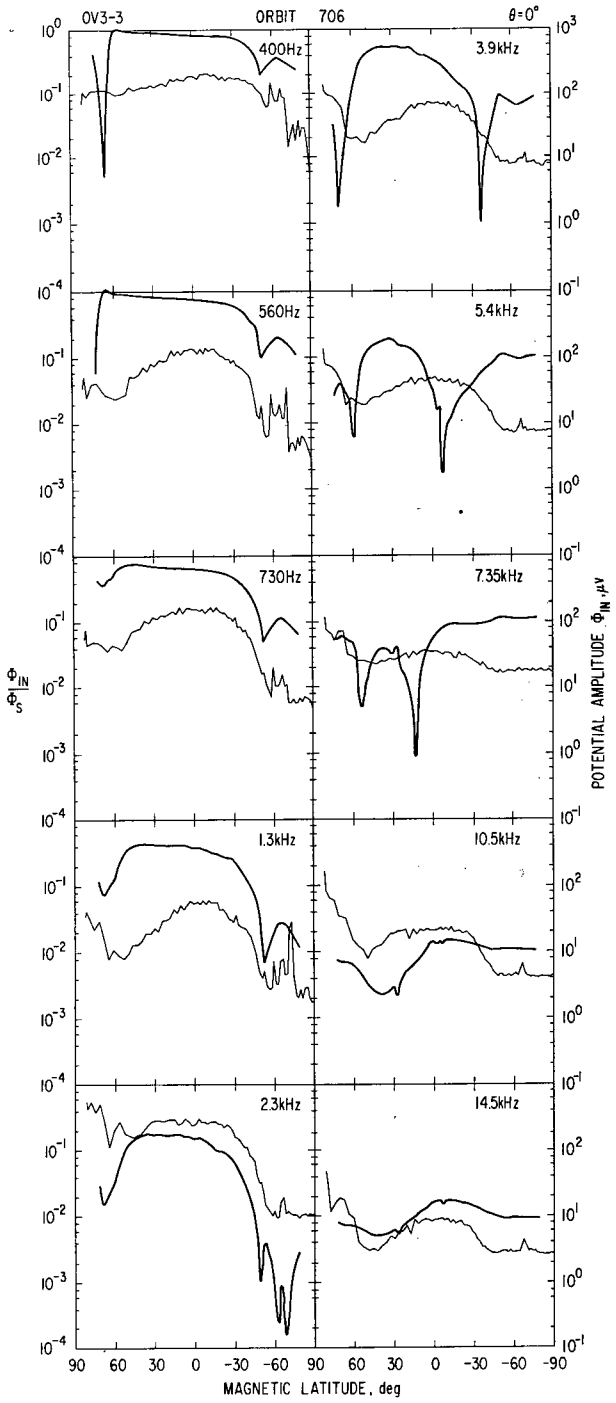

Φ_{in}/Φ_s computed from the cold plasma, sheathless antenna model for the dusk portion of orbit 706. The angle between the antenna axis and the geomagnetic field is 0^o. The experimental data (drawn in with a lighter line) are shown for comparison.

Figure 7

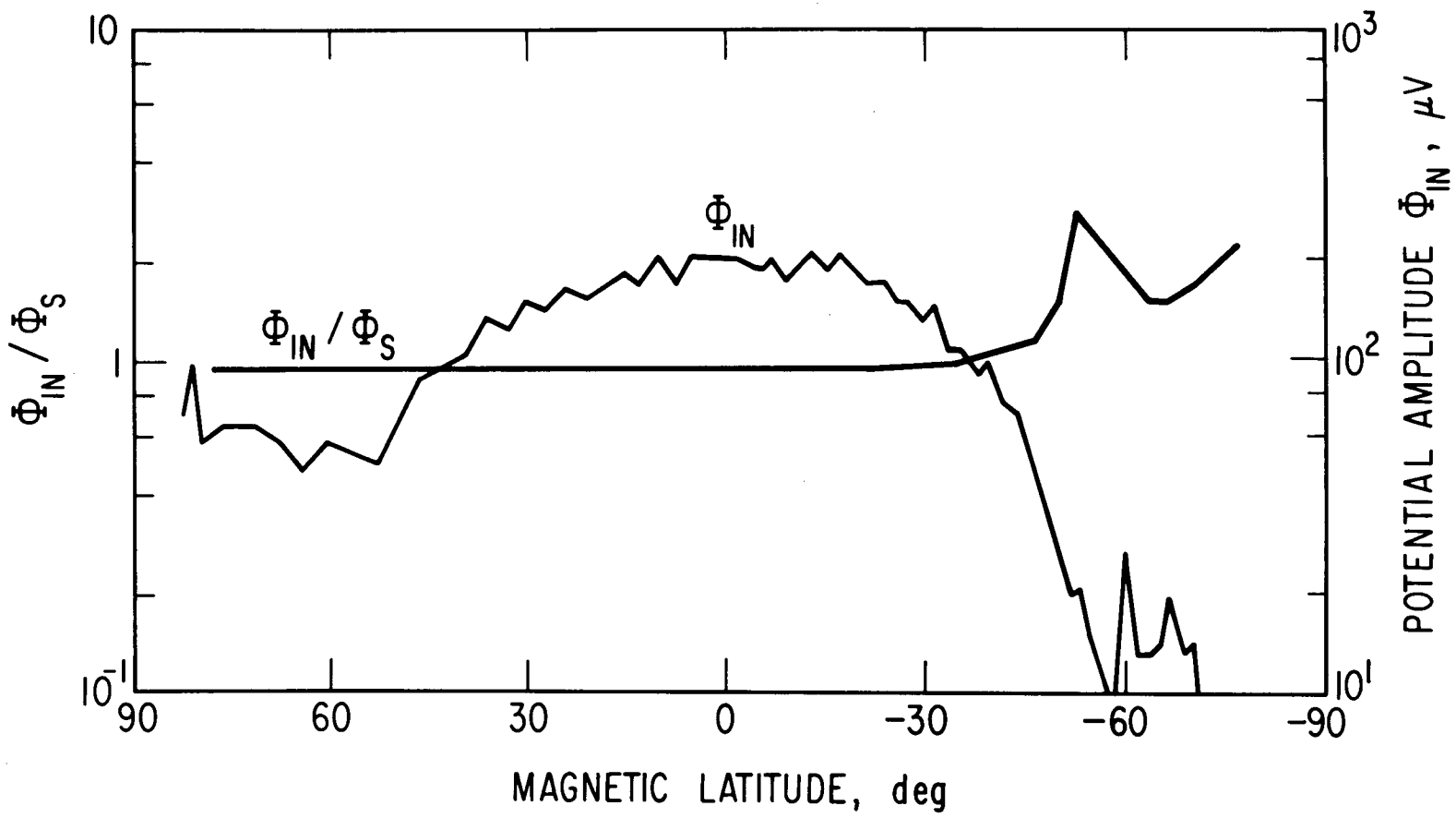

Φ_{in}/Φ_s computed at 730 Hz from the cold plasma sheathless antenna model for the dusk portion of orbit 706. The angle between the antenna axis and the geomagnetic field is 10^{o}. The experimental data, Φ_{in}, at 730 Hz is shown for comparison.

Figure 8

The terminal admittance of the antenna is represented as a sheath resistance and sheath capacitance in parallel with a capacitance C' which represents the current path through the common sheath near the antenna base. The input circuit for this model is shown in Figure 6b. In the analysis, C' is approximated by C_0 which is valid in the limit of zero plasma densities. For large plasma density the sheath admittance dominates, and the inclusion of C_0 is unimportant. The largest error occurs for small plasma density where the sheath admittance is of the magnitude, $1/\omega C_0$. The sheath resistance obtained by Mlodnosky and Garriott is

$$R_{sh} = \frac{kT_-}{Ne^2 A_+ (v_s^2 + 8kT_+/\pi m_+)^{1/2}} \qquad (6)$$

Assuming $T_+ = T_- = 1200^\circ K$, $8kT_+/\pi m_+ = 0.25 \times 10^8 \text{ m}^2 \text{ sec}^{-2}$. Hence, the square of the spacecraft velocity, $v_s^2 \simeq 10^8 \text{ m}^2 \text{ sec}^{-2}$, is the larger term in the parenthesis. At low altitudes where O^+ is the dominant ion, the spacecraft velocity dominates the ion thermal velocity.

There is some discrepancy in the literature concerning the correct expression to be used for the effective velocity in the denominator in equation 6. Mlodnosky and Garriott [1963] use $v_s + (2kT_+/\pi m_+)^{1/2}$, while Fahleson [1967] used $(v_s^2 + 8kT_+/\pi m_+)^{1/2}$. Tests of electrostatic probes in a magnetic shock tube support the latter formulation, which is used in equation 6 [Scharfman, 1964]. Since v_s is significantly larger than the ion thermal velocities, the term involving velocities is approximately v_s in any case. Also, since A_+ undoubtedly depends upon the characteristics of the sheath as well as on the orientation of the antenna with respect to the spacecraft velocity, uncertainties in A_+ would be expected to be larger than uncertainties in the effective velocity.

As the potential applied to the antenna varies, the sheath dimensions change, and hence, the number of ions within the sheath also changes. This change is neutralized by an equal change in the electron charge on the antenna. Mlodnosky and Garriott show that this contributes a reactive term to the admittance. For the OV3-3 electric field antenna the reactive term is represented by an effective sheath capacitance that is given by

$$C_{sh} = \frac{2\pi\epsilon_0 L}{\ln(r_{sh}/r)} \qquad (7)$$

where r_{sh} is the sheath radius and r is the radius of the antenna. The numerical calculations of Self [1963] show that $r_{sh} \simeq 2\pi\lambda_D$ where λ_D is the Debye length.

The impedance of the antenna-sheath combination is

$$Z = \frac{R_{sh}}{1 + j\omega R_{sh}(C_{sh} + C_0)} \tag{8}$$

At low frequencies and high densities, $\omega R_{sh}(C_{sh} + C_0) \ll 1$ and $Z \simeq R_{sh}$; at high frequencies and low densities, $\omega R_{sh}(C_{sh} + C_0) \gg 1$ and $Z \simeq 1/j\omega(C_{sh} + C_0)$. Both of these conditions are encountered by OV3-3 and are evident in the experimental data.

R_{sh} and C_{sh} have been evaluated for orbit 706 using equations 6 and 7, assuming $A_+ = 2\pi rL$ and $T_- = T_+ = 1200^{\circ}K$ for the OGO-2 ion density model. The ratio Φ_{in}/Φ_s was then computed using the value for Z obtained from equation 8. The results are plotted for each bandpass frequency in Figure 9 for the dusk portion and in Figure 10 for the dawn portion of the orbit. Considering that the OGO-2 data were obtained a year before OV3-3 orbit 706 and, in addition, were scaled in altitude by as much as a factor of 5, the agreement between the shape of the computed curves and the shape of the experimental data is very good. The main discrepancies between the shape predicted by the sheathless cold plasma model and the experimental data are eliminated by the sheath-dominated model. The ion-electron hybrid resonances do not appear, and the impedance is independent of the angle between the antenna and the earth's magnetic field.

The dependence of Φ_{in}/Φ_s on the electron density is plotted for all of the bandpass frequencies in Figure 11. For the OV3-3 instrument, Φ_{in}/Φ_s is a monotonically increasing function of density at all frequencies. The frequency dependence of the structure of the experimental data shown in Figure 2 or in Figures 9 and 10 can be understood from the curves in Figure 11. They predict that a nearly constant value of Φ_{in}/Φ_s will be reached at both very high and very low densities and that the lower bound will occur at higher densities as the frequency is increased. This is evident in Figure 2 for times centered about 54,500 sec when the spacecraft was at apogee over the south pole. Starting with the lowest frequency of 400 Hz, the minimum signal level occurs from 54,500 to 55,000 sec. For successively higher frequencies, the minimum occurs for a longer duration until it extends from 53,000 to 56,000 sec at 14.5 kHz.

The observed ratio of the peak signal to the minimum signal generally decreases as the frequency increases. This behavior agrees with that predicted by the sheath-dominated antenna impedance model.

The discrepancy between the measured and predicted values of Φ_{in}/Φ_s at the lower frequencies for magnetic latitudes greater than $+30^{\circ}$ in Figures 9 and 10 is probably caused by saturation of the main amplifier by the large 2-kHz signal due to the Faraday cup.

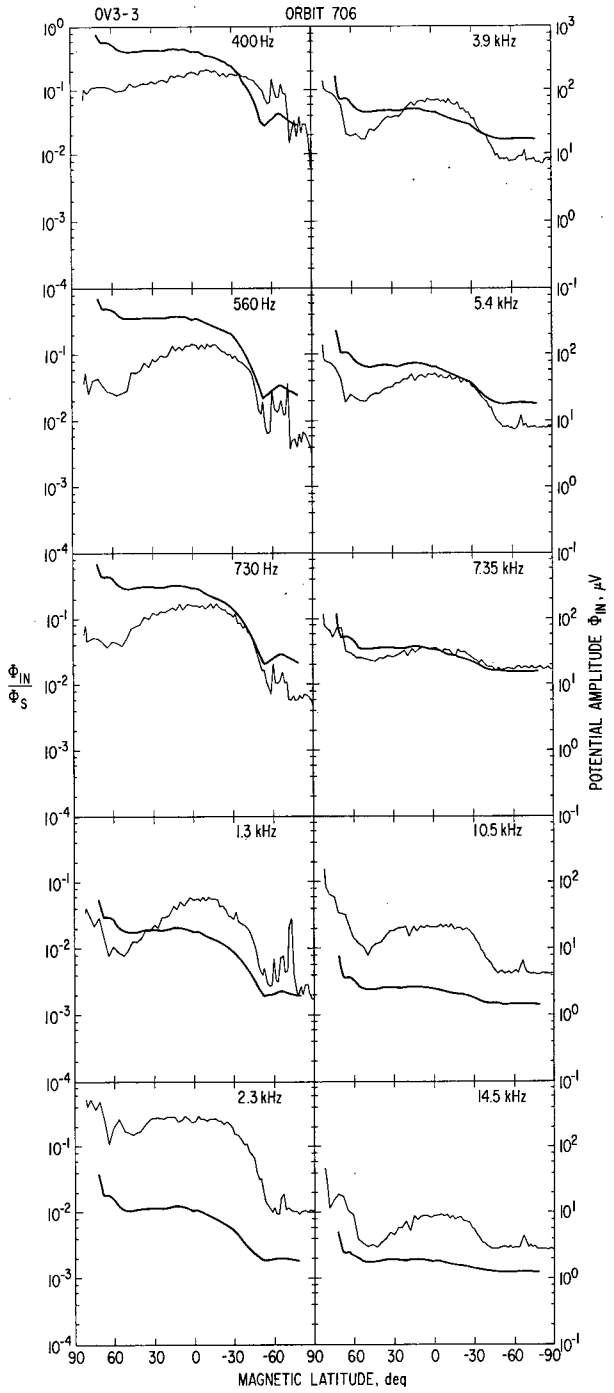

Φ_{in}/Φ_s computed from the warm plasma, sheath-dominated antenna model for the dusk portion of orbit 706. The experimental data (drawn in with a lighter line) are shown for comparison.

Figure 9

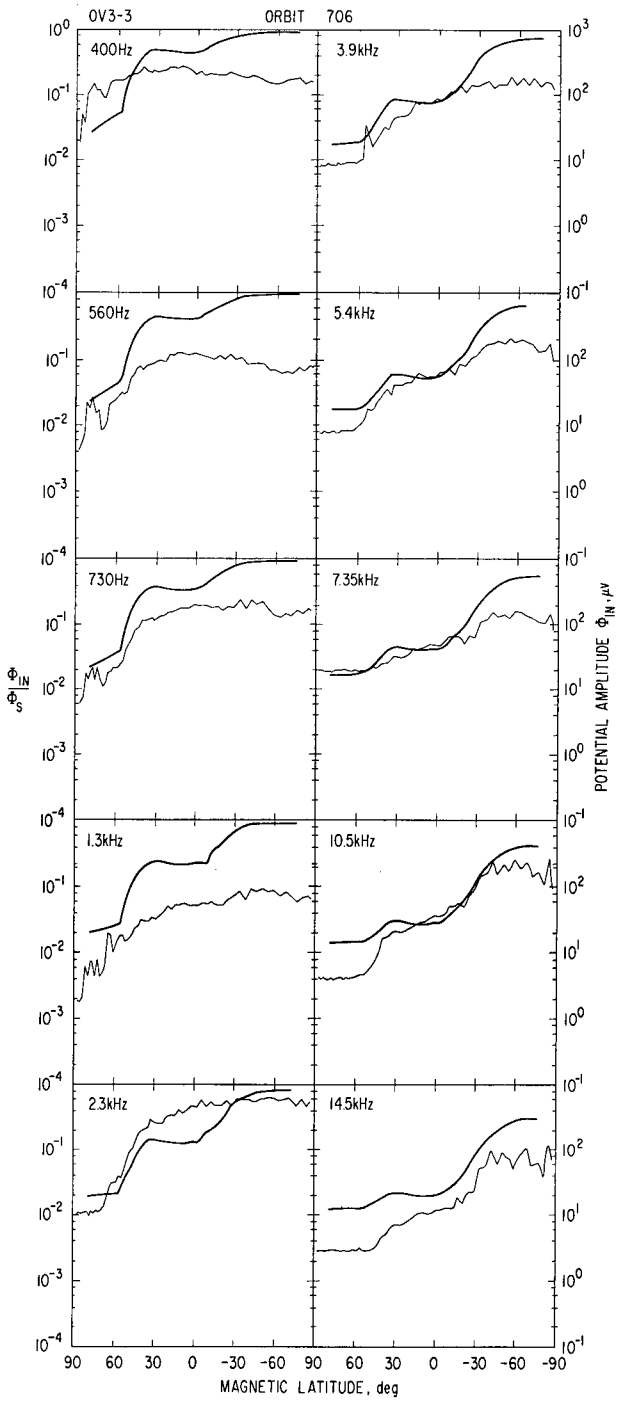

Φ_{in}/Φ_s computed from the warm plasma, sheath-dominated antenna model for the dawn portion of orbit 706. The experimental data (drawn in with a lighter line) are shown for comparison.

Figure 10

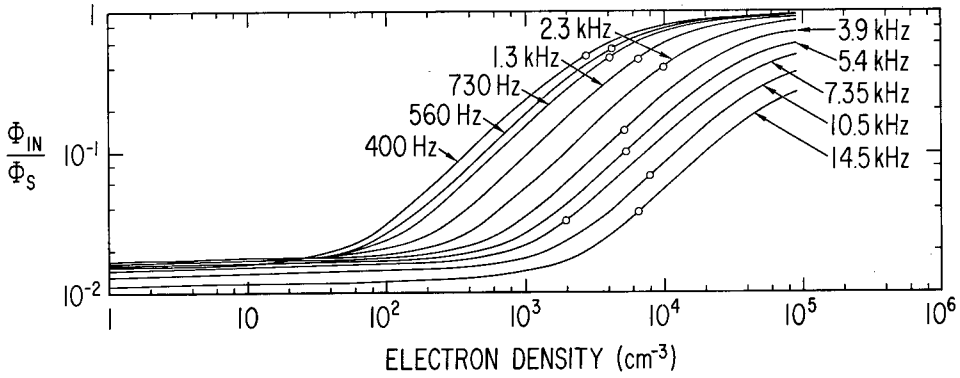

Dependence of Φ_{in}/Φ_s on the electron density computed from the warm plasma, sheath-dominated antenna model at the ten frequencies used in the OV3-3 instrument.

Figure 11

If the source potential Φ_s at a given frequency were known, the plasma density could be calculated from the observed values of Φ_{in}. Although the potentials Φ_s are not known, the data can be used to determine the local plasma density in the following manner. For high altitudes over the pole, it is assumed that the plasma density is small and that for each frequency the ratio Φ_{in}/Φ_s is the lower bound shown for that frequency in Figure 11. From the observed minimum values of Φ_{in}, values of Φ_s are calculated for each frequency. It is assumed that Φ_s does not change over the orbit and can be used to calculate the ratios Φ_{in}/Φ_s at any other point in the orbit.

As an example, values of Φ_{in}/Φ_s were calculated from the data of orbit 706 for a point near the magnetic equator and are plotted on the curves of Φ_{in}/Φ_s versus density in Figure 11. Ideally, all of the points for the ten frequencies should occur at the same density. The actual variation in density is probably a result of Φ_s varying over the orbit rather than being constant as assumed. The density may be obtained by averaging the individual values obtained from each frequency. Using this technique, the resulting density is shown as a function of magnetic latitude in Figure 12. The standard deviation of the individual values, calculated at several magnetic latitudes, was approximately 100% of the average. This systematic error is primarily due to the 2.3 kHz data, which are consistently high, and the 7.35 kHz data, which are consistently low. The general shape of the density profile is not, however, affected by this systematic error.

Since the signals reach a well defined minimum value at high altitudes over the pole, the density over the pole must be less than 10^2 cm^{-3}. The sharp decrease in density above 40° magnetic latitude represents a crossing of the plasmapause. This decrease was first observed in the analysis of multipath whistler data [Carpenter, 1966; Angerami and Carpenter, 1966]. It was also observed by OGO-2 measurements of the densities of the lighter ions, H^+ and He^+, at altitudes up to 1500 km and by OGO-3 at corresponding L values at the equator.

DETECTION OF THE PLASMAPAUSE WITH ANTENNA IMPEDANCE

As noted in Figure 12, significant features such as the plasmapause are readily apparent in the antenna impedance data. Passage of the spacecraft through the plasmapause is observed only at high altitudes where H^+ is the dominant ion. At low altitudes where O^+ is dominant, the plasmapause is not as evident. This is consistent with the OGO-2 data which indicates that the plasmapause is a light ion phenomenon.

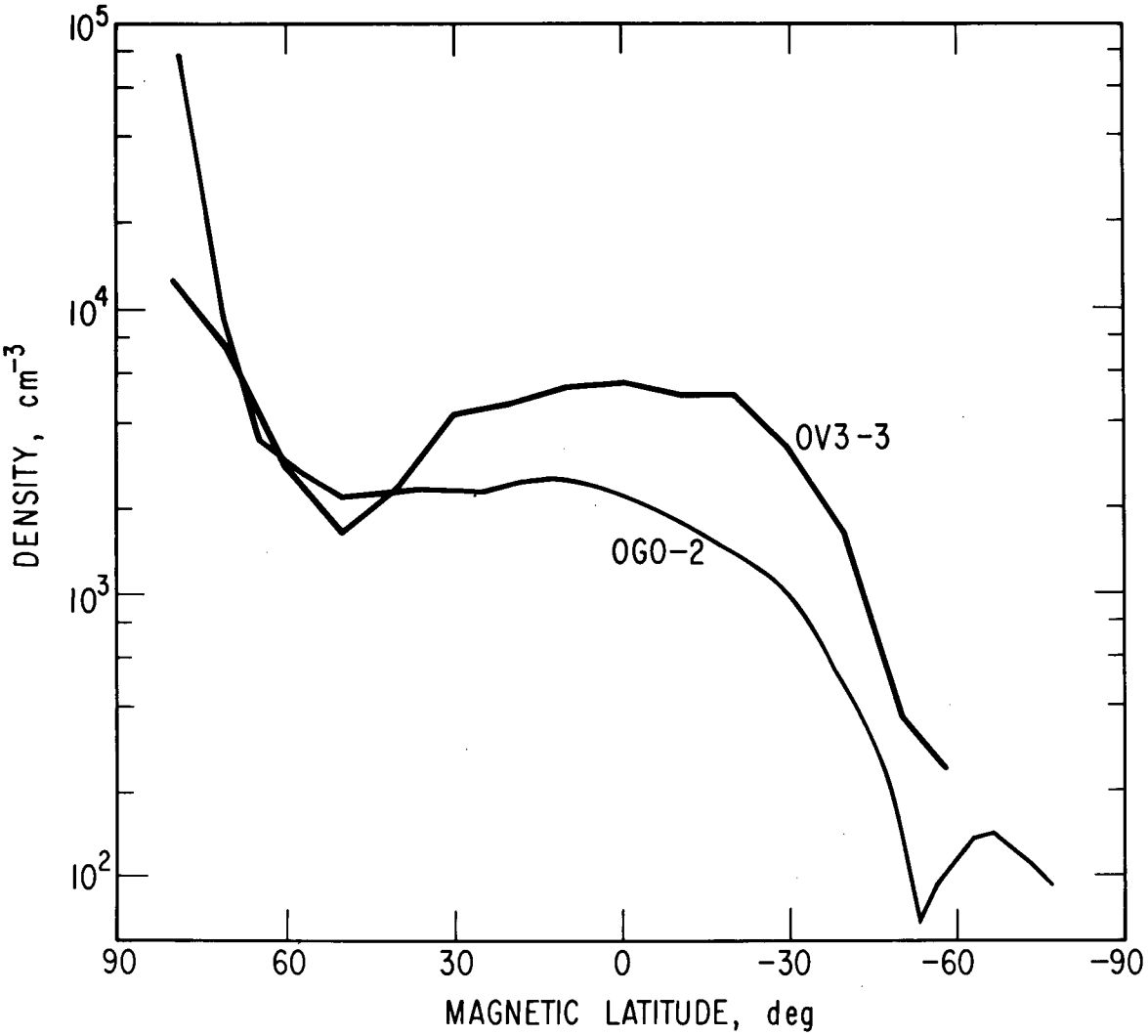

Electron density along the dusk portion of orbit 706 calculated from the electric field antenna data under the assumptions that the signal source is constant and that the observed variations are due to changes in the sheath impedance. Scaled ion density from OGO-2 is included for comparison.

Figure 12

Criteria for determining the plasmapause location is somewhat controversial. For this study, the plasmapause location is taken to be the L value where the antenna impedance at 3.9 kHz begins to be affected by the increasing electron density. This definition is completely arbitrary but it is easily identified in the antenna impedance data. It corresponds to the point at which the electron density reaches a value of approximately 200 cm^{-3} at the OV3-3 altitude.

A comparison of the plasmapause location determined from the OV3-3 antenna impedance data with the recent data of [Chappell, 1970] shows fair agreement. In Figure 13, the L-shell position of the plasmapause versus maximum K_p in the preceding 24 hours, has been reproduced from Figure 3 of Chappell. The OGO-5 data are for 1000 ± 0200 hours local time. The solid circles are the OV3-3 data for 1100 ± 0200 hours local time and for the current three hour average of K_p. It is seen that the plasmapause position versus K_p determined from the OV3-3 data agrees both in magnitude and slope with that of Chappell, even though the data were taken at considerably different altitudes.

A straight line fit to the OV3-3 plasmapause location data of Figure 7 is given by

$$L = (4.81 \pm 0.39) - (0.17 \pm 0.13)K_p \qquad (9)$$

As noted by Chappell et al., Equation (9) shows that on the average the plasmapause moves to lower L values with increasing geomagnetic field activity. The scatter in the data shows that there is considerable variability in the plasmapause position for all levels of geomagnetic field activity.

EXAMPLES OF NATURALLY OCCURRING EMISSIONS

Irregular signal variations are superimposed on the systematic change in signal levels associated with the varying plasma density. These signals are either caused by local fluctuations in plasma density or are true ambient electric fields. A knowledge of the antenna impedance and its characteristic variations with frequency make it possible to determine which signal variations are real and which are caused by impedance changes.

Examples of real signals are shown in Figure 14. Data are also shown from the VLF receiver supplied by TRW Systems [Scarf, et al., 1968b]. The most intense fields detected by the electric antennas are the sharp peaks at 64,000 and 66,000 UT. These signals were detected during each orbit as the satellite passed over a pole at high altitude. For the Aerospace antenna the signals correspond to fields of ~50 mV/m at 400 Hz decreasing to ~1 mV/m at 15 kHz. The waves have been shown to be electrostatic

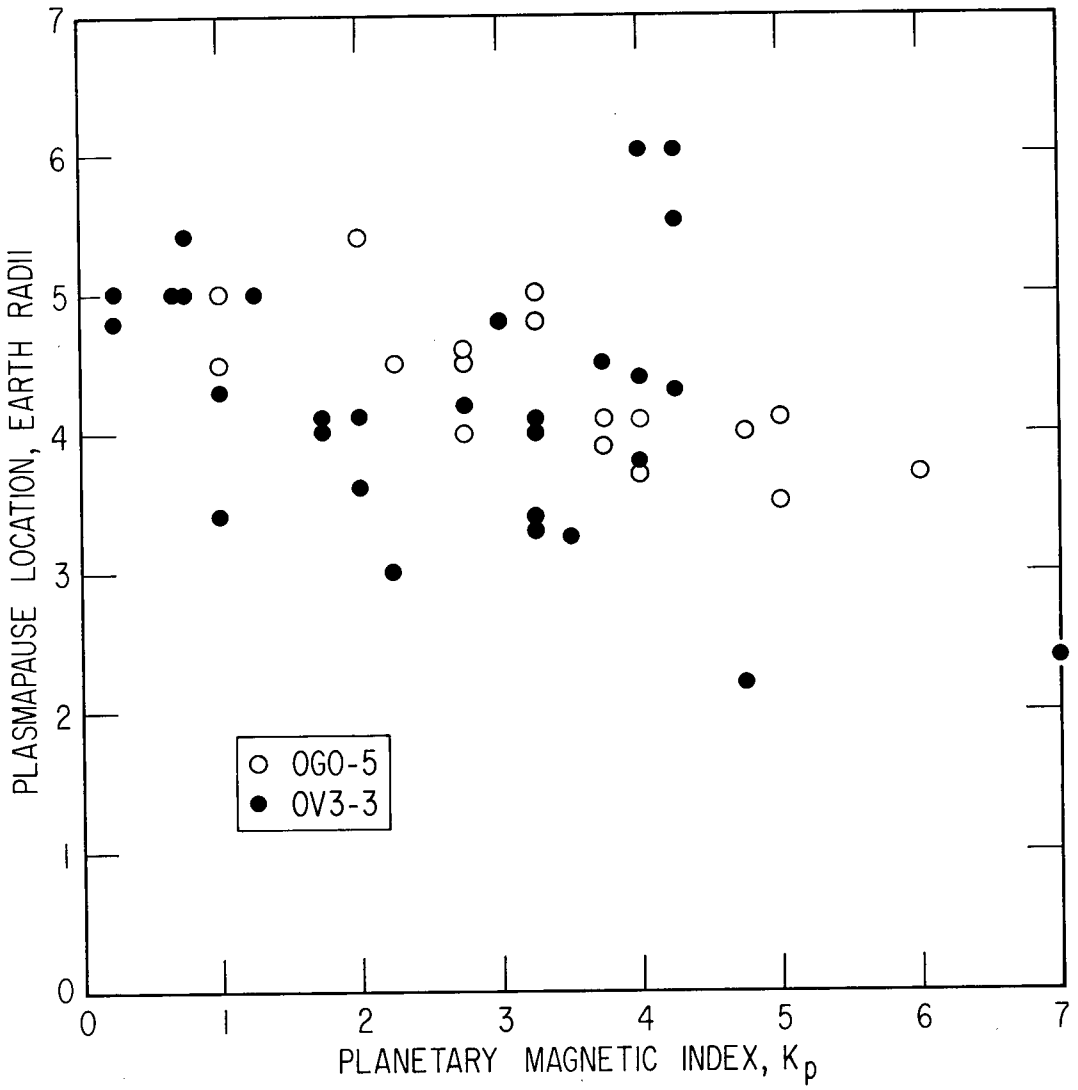

Plasmapause L-shell position versus K_p from OGO-5 and OV3-3 data. OGO-5 K_p values were maximum in preceding 24 hours whereas OV3-3 K_p values were current three hour average.

Figure 13

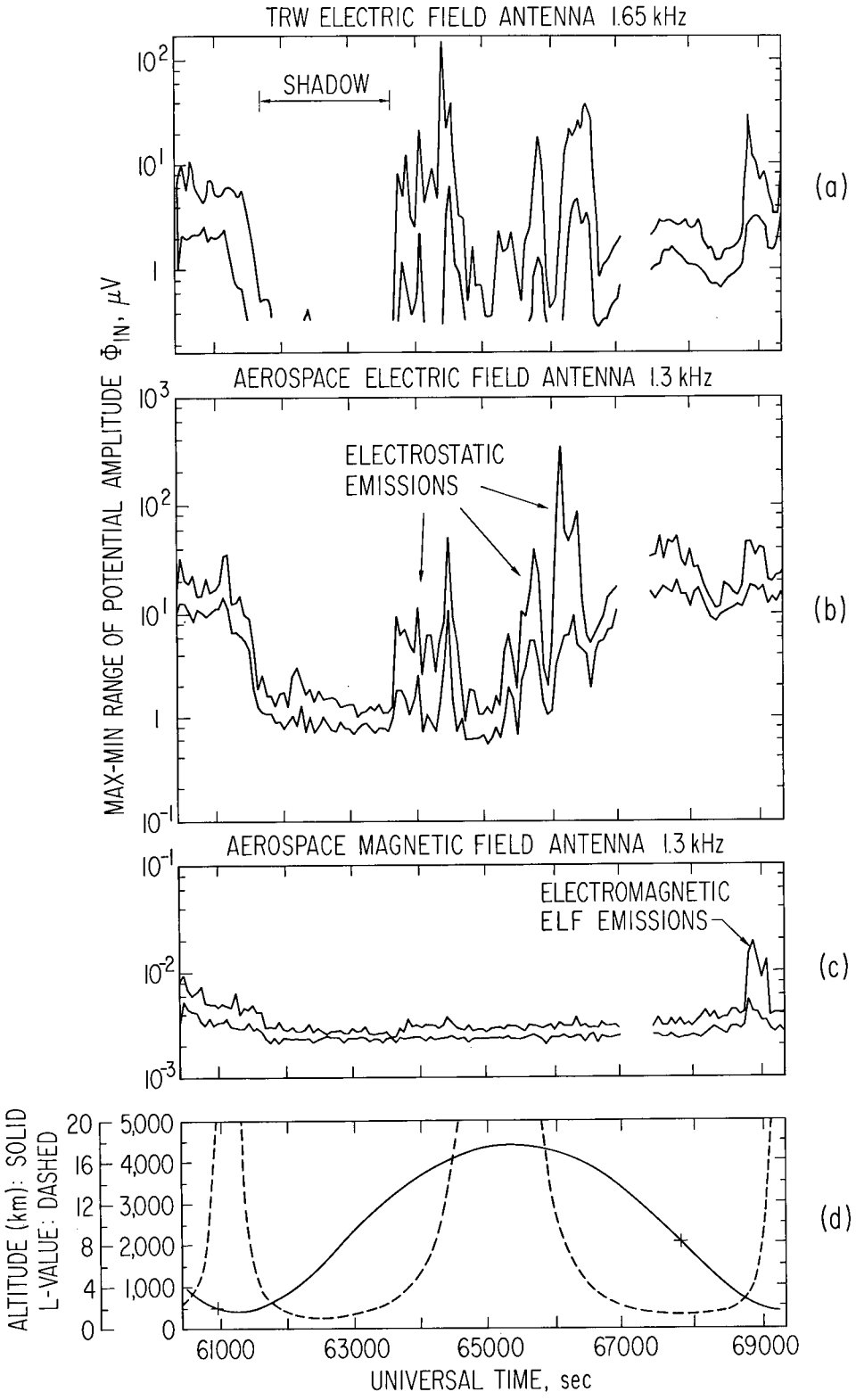

(a) Maximum and minimum potential amplitudes at 1.65 kHz versus time as measured by the TRW electric field antenna during orbit 497.
(b) Similar data obtained at 1.3 kHz with the Aerospace electric field antenna.
(c) Maximum and minimum magnetic field strengths at 1.3 kHz from the Aerospace magnetic field antenna.
(d) Satellite altitude and L-shell location.

Figure 14

oscillations [Koons, et al., 1970] generated by an instability resulting from the flow of H^+ through O^+ in the polar wind [Banks, 1969].

Another emission evident in the data is the peak at 69,000 UT. This has been shown to be an electromagnetic wave traveling in the whistler mode [McPherson, 1970]. Note that there is a magnetic field signal in Figure 14c. Even though the potential induced on the antenna for this emission is comparable to that for the polar wind electrostatic waves, the electric field is smaller (~ 30 μV/m) than that of electrostatic wave because of the decrease in antenna impedance.

SUMMARY

The principal results of the electric field antenna impedance analysis for the OV3-3 spacecraft are:

1. The antenna impedance is dominated by the characteristics of the warm, collisionless plasma sheath.

2. The magnetospheric plasma density can be determined from a measurement of electric field antenna impedance at several frequencies.

3. The source of most of the signal observed on the OV3-3 electric field antenna was caused by electromagnetic interference potentials on the solar array.

4. The over-all structure of the electric field antenna signal, which repeated from orbit to orbit, was caused by the variation of the antenna impedance as a function of the magnetospheric plasma density.

5. A knowledge of the antenna impedance and its characteristic variations with frequency make it possible to determine which signal variations are real and which are caused by impedance changes.

REFERENCES

Aggson, T.L., and C.A. Kapetanakos, On the impedance of a satellite borne VLF electric field antenna, NASA-Goddard Space Flight Center, Report X-612-66-380, August, 1966.

Allis, W.P., S.J. Buchsbaum, and A. Bers, Waves in Anisotropic Plasmas, MIT Press, Cambridge, Mass., 1963.

Angerami, J.J., and D.L. Carpenter, Whistler studies of the plasmapause in the magnetosphere, 2, electron density and total tube electron content near the knee in magnetsopheric ionization, J. Geophs. Res., 71, 770-726, 1966.

Balmain, K.G., The impedance of a short dipole antenna in a magnetoplasma, IEEE Trans. Antennas Propagation, AP-12, 605-617, 1964.

Banks, P.M., and T.E. Holzer, High-Latitude plasma transport: thepolar wind, J. Geophys. Res., 74, 6317, 1969.

Barrington, R.E., and J.S. Belrose, Preliminary results from the very-low frequency receiver aboard Canada's Alouette satellite, Nature, 198, 651-656, 1963.

Brice, N.M., and R.L. Smith, Lower hybrid resonance emissions, J. Geophys. Res., 70, 71-80, 1965.

Carpenter, D.L., Whistler studies of the plasmapause in the magnetospere, 1, temporal variations in the position of the knee and some evidence of plasma motions near the knee, J. Geophys. Res., 71, 693-710, 1966.

Chappell, C.R., K.K. Harris, and G.W. Sharp, A study of the influence of magnetic field activity on the location of the plasmapause as measured by OGO 5, J. Geophys. Res., 75, 50, 1970.

Ejiri, M., H. Oya, and T. Obayashi, A modified plasma resonance observed by a rocket-borne gyro-plasma probe, Rpt. Ionosphere Space Res. Japan, 22, 201, 1968.

Fahleson, U., Theory of electric field measurements conducted in the magnetosphere with electric probes, Space Sci. Rev., 7, 238, 1967.

Gurnett, D.A., G.W. Pfeiffer, R.A. Anderson, S.R. Mosier, and D.P. Cauffman, Initial observations of VLF electric and magnetic fields with the Injun 5 satellite, J. Geophys. Res., 74, 4631, 1969.

Koons, H.C., and D.A. McPherson, Electrostatic VLF waves observed above the auroral and polar ionosphere, Trans. Am. Geophys. Union, 51, 386, 1970.

Lomax, J.B., Final Rept. Contract NOw 60-0405 (FBM), Stanford Research Institute, June, 1961.

McPherson, D.A., and H.C. Koons, Dependence of the occurrence of chorus upon the location of the plasmapause, Aerospace Corp., TR-0066(9220-02)-3, January, 1970.

Miller, E.K., and H.F. Schulte, Jr., Antenna admittance in an ionospheric-type plasma, Tech. Rept. 05627-18-S, Michigan University, April, 1968a.

Miller, E.K., and H.F. Schulte, Jr., Ionospheric composition measurements with an R.F. impedance probe, Tech. Rept. 05627-20-T, Michigan University, May, 1968b.

Mlodnosky, R.F., and O.K. Garriott, The V.L.F. admittance of a dipole in the lower ionosphere, Proc. Intern. Conf. Ionosphere, pp. 484-491, Institute of Physics and Physical Society, London, 1963.

Oya, H., Theoretical prediction of discrimination of modified and hybrid plasma resonances, Rept. Ionosphere Space Res. Japan, 22, 119, 1968.

Scarf, F.L., R.W. Fredericks, and G.M. Crook, Detection of electromagnetic and electrostatic waves on OV3-3, J. Geophys. Res., 73, 1723-1744, 1968a.

Scarf, F.L., G.M. Crook, R.W. Fredericks, I.M. Green, and C.F. Kennel, Observations of plasma waves in space, in Plasma Waves in Space and in the Laboratory, edited by J. Thomas, University of Edinburgh Press, 1968b.

Scharfman, W.E., The use of the Langmuir probe to determine electron densities surrounding re-entry vehicles, SRI Project No. 4556 Final Report, Stanford Research Institute, January, 1964.

Self, S.A., Exact solution of the collisionless plasma sheath equation, Phys. Fluids, 6, 1762, 1963.

Shawhan, D., Experimental observations of proton whistlers from Injun 3 VLF data, J. Geophys. Res., 71, 29-45, 1966.

Shawhan, S.D., and D.A. Gurnett, VLF electric and magnetic fields observed with the Javelin 8.45 sounding rocket, J. Geophys. Res., 73, 5649, 1968.

Storey, L. R. O., The design of an electric dipole antenna for VLF reception within the ionosphere, Tech. Rept. 308TC, Centre National D'Etudes des Telecommunications, Department Telecommande, July, 1963.

Taylor, H.A., Jr., H.C. Brinton, M.W. Pharo, III, and N.K. Rahman, Thermal ions in the exosphere; evidence for solar and geomagnetic control, J. Geophys. Res., 73, 5521-5533, 1968.

TRANSMISSION LOSSES ASSOCIATED WITH PLASMA PERTURBATIONS

by

F. L. Scarf and R. W. Fredricks

Space Sciences Laboratory
TRW Systems Group
Redondo Beach, California 90278
U.S.A.

INTRODUCTION

Problems associated with downlink VLF transmission through the ionosphere are generally treated using a zero temperature formalism, and this may seem especially appropriate when the proposed transmitter platform is a low altitude spacecraft. At low altitudes (say $h \lesssim 1000$ km) right-hand polarized whistler mode waves ($f \lesssim 20$ kHz, for instance) have oscillation frequencies well below local gyrofrequencies: thus local cyclotron damping phenomena (Scarf, 1962) are completely unimportant. Moreover, since the plasma β-value ($\beta = 4\pi N\kappa T/B^2$) is also very small, thermal corrections to the expressions for the phase and group speeds are also negligible. Finally, the thermal energy density in the low altitude plasma is very low compared to values that might be associated with a powerful transmitter perturbation, and it is therefore customary to neglect finite (κT) effects.

However, this last assumption is generally very misleading when the plasma is collisionless on time scales of physical interest. A steady electric field impressed on the plasma for a sufficiently long time interval can produce very significant perturbations that ultimately lead to irreversible energy dissipation phenomena. In this report, we describe two processes that can provide dissipation at low altitudes, and we speculate on a program to study such energy losses.

Section 2 contains a description of runaway phenomena induced by large amplitude electric field fluctuations having wave frequencies less than the local ion plasma frequencies. In Section 3 we discuss the diffuse resonances or emissions at $f = (n + 1/2)f_{ce}$. These modes were recently studied using ac electric field experiments on Alouette II and OGO 5. A possible explanation for the observations is presented, and it is conjectured that E-field configurations produced by strong radiation fields may momentarily perturb the plasma so that some energy goes into this mode. Section 4 contains additional discussion and conclusions.

RUNAWAY AND TURBULENT PLASMA CONDUCTIVITY

When a quasi-stationary electric field is impressed on a collisional plasma, the electrons and positive ions are initially accelerated in opposite directions and the current begins to grow with time. However, for $\nu t >> 1$ the many binary collisions produce enough scattering to limit the current. Ohm's law then applies and the electrical conductivity is roughly given by the coulomb value, $\sigma = Ne^2/m\nu$, where ν is the coulomb collision frequency.

The question of interest here concerns the relevance of this conventional collisional formalism when a low frequency, large amplitude perturbing field (i.e., the near field or the radiation field from a downlink VLF transmitting antenna) is applied to the moderately cool and dilute plasma that exists above the ionosphere. For simplicity, let us first consider characteristics of the medium at an altitude of 1000 km; the problems to be discussed are more severe for $h \simeq 1000$ km than for $h \simeq 300$ km, but it is easier to illustrate the concepts for a low density hydrogen plasma.

Table 1 contains a description of possible physical conditions to be encountered at $h \simeq 1000$ km. The top four entries describe the nominal density, temperature, Debye length, and index of refraction for a 2 kHz whistler mode wave, assuming $B \simeq 0.2$ gauss. The Debye length is always extremely small compared to $\lambda(2\ \text{kHz}) = c/n$, and all gyroradii are also small compared to the wavelength. Thus, to a first approximation, one may use the collisionless magneto-ionic theory to describe small amplitude wave characteristics.

Some first-order finite temperature effects are described in the central panels. For a hydrogen plasma the electron-on-proton collision frequency is (Delcroix, 1960)

$$\nu_c = 2.6\ NT^{-3/2}\ \ell n\ \Lambda\ (\text{Hz}) \qquad (1)$$

where $\Lambda = [3\ (\kappa^3 T^3/\pi N)^{1/2}/2e^3]$ and the associated electrical conductivity along the magnetic field lines is (Delcroix, 1960)

$$\sigma \simeq 1.5 \times 10^{-2} T^{3/2}/\ell n\ \Lambda\ (\text{ohm-meter})^{-1} \qquad (2)$$

For $h \simeq 1000$ km, $\ell og\ \Lambda \simeq 16$, and it can be seen that the collision frequency is quite low, while the resultant conductivity is high. Using magneto-ionic theory, the appropriate corrections associated with these effects are again small.

However, these concepts do <u>not</u> apply when a long duration pulse of sufficiently large amplitude is impressed on the plasma. The critical field is the so-called "runaway field", E_R. As discussed by Spitzer and Harm (1953), Delcroix (1960), and many others, the effect of collisions

Table 1

Quantity	Mid-Latitude	Auroral	Polar
Density (cm^{-3})	$2x10^4$	10^3	10^2
Temperature (°K)	10^3	$2x10^3$	$2x10^3$
Debye Length (cm)	1.5	9.6	31
Index of Refraction ($n^2=R$, f=2 kHz, B=0.2 g)	38	8.5	2.8
Coulomb Collision Frequency (Hertz)	26	0.5	0.05
Coulomb Conductivity $(ohm\ meter)^{-1}$	31	90	90
Ion Plasma Frequency (Hertz)	26,000	6,300	2,100
Runaway Electric Field (volts/meter)	$3x10^{-4}$	$8x10^{-6}$	$8x10^{-7}$
Sagdeev Conductivity $(ohm\ meter)^{-1}$	$7x10^{-2}$	$1.6x10^{-2}$	$5x10^{-3}$

decreases as the electrons become accelerated. If E exceeds E_R, with E_R given by

$$E_R \simeq \frac{Ne^3}{\kappa T_e} \ell n \Lambda, \tag{3}$$

then no steady state develops and the current tends to increase indefinitely. For h ≃ 1000 km, this runaway electric field is exceedingly small. As shown in Table 1, the critical values range from 0.3 millivolts/meter at midlatitudes to less than one microvolt/meter in the low density polar region.

When the plasma temperature is finite, Cerenkov radiation effects actually limit this acceleration and wave-particle scattering provides a finite and low plasma conductivity. As the electron-proton drift speed rises to match the phase speeds for various wave modes, the waves are radiated by two-stream instabilities and the resultant plasma turbulence scatters the particles, further reducing the currents. Figure 1 shows results of a calculation carried out by Fried and Field (1964). A steady

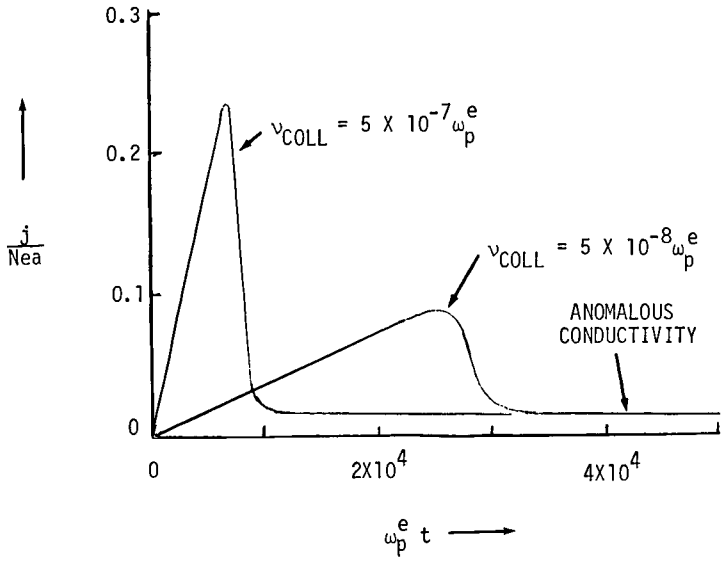

CURRENT DEVELOPMENT IN A NEARLY COLLISIONLESS PLASMA WHEN A DC ELECTRIC FIELD IS ENCOUNTERED (FIELD AND FRIED, 1964)

Figure 1

electric field larger than the runaway field has been impressed on a plasma (here an unmagnetized system), and the actual current parallel to E is plotted as a function of time. For $\nu_c = 5 \times 10^{-7}$ $\omega_{pe} = 4.5 \times 10^{-3}$ $N^{1/2}$ (a value appropriate for the h = 1000 km, polar region parameters of Table 1), the current begins to limit at $\omega_p t \sim 10^4$; for N = 100 cm^{-3} (polar region), this severe limiting appears at t ≃ 20 milliseconds after the pulse is initiated. In other words, for h = 1000 km, N = 10^2, any electric field with E > 1 microvolt/meter (E_R) impressed on the plasma for more than 20 milliseconds ($t = 10^4/\omega_{pe}$) will produce anomalous conductivity. Two-stream instabilities provide growing plasma oscillations (ion sound waves) that lead to severe dissipation.

This calculation actually describes one of the worst possible cases. At lower altitudes and mid-latitudes N increases and the runaway field is bigger. Moreover, the index of refraction increases so that the E-field impressed on the plasma is reduced. Nevertheless, runaway remains a serious problem for a high powered transmitter above the ionosphere. The peak free space electric field at a large distance from a dipole antenna is (Stratton, 1941)

$$E_{wave} = \frac{9.5 \sin \theta \, (W)^{1/2}}{R} \text{ volts/meter} \qquad (4)$$

where W is the radiated power in watts and R is the distance in meters. If we consider 100 watts of radiated power, then even at 10 km from the transmitter the equivalent free space wave has E(peak) ≃ 10^{-2} volts/meter. Thus the wave field strength at 10 km distance is four orders of magnitude larger than E_R at h = 1000 km, N = 10^2, and it is also much larger than all other E_R-values shown in Table 1.

The 1964 Field and Fried calculation was carried out for $T_e/T_i \gg 1$, but T_e/T_i is usually less than two in the ionosphere. Fried and Gould (1961) discussed the stability of a current-carrying plasma as a function of T_e/T_i and they found that for $T_e \simeq (1\text{-}2)T_i$ the plasma stability is greatly enhanced, so that relative drift speeds near $(\kappa T_e/m_e)^{1/2}$ are needed to generate plasma oscillations. If this result described all physical cases, we might discontinue the investigation. However, it has always been known from laboratory experiments that physical plasmas are much more easily destabilized than indicated by the 1961 Fried and Gould curves (Stix, 1962). Recently, some explanations for these discrepancies have been proposed. Kan (1970) showed that in the presence of a dc magnetic field, electrostatic waves propagating at large angles (50-70°) to the $\vec{B}$-field have instability thresholds for $T_e \simeq 2T_i$ comparable to the Fried and Gould values for $T_e \gg T_i$. In another physical context, Forslund (1970) showed how heat conduction effects can lower the two-stream instability threshold. Moreover, in the sunlit ionosphere the presence of superthermal photoelectrons can enhance the wave levels (Yngvesson and Perkins, 1968).

Whenever strong plasma turbulence develops, the effective scattering collision frequency may be on the order of 10 percent of the maximum angular wave frequency (Coroniti, 1969). For ion acoustic waves we then have $\sigma = Ne^2/m\nu(\text{eff})$ and $\nu(\text{eff}) \simeq 0.1\ \omega_{p+}$. Many laboratory and space measurements now appear to confirm that this estimate of the Sagdeev or turbulent conductivity has rough validity, and in the last line of Table 1 we show the appropriate estimates. Clearly, if σ is reduced to these values by current driven instabilities associated with intense transmitter fields, then very severe dissipation will occur.

The runaway phenomena described in Figure 1 will occur if $E > E_R$ for a sufficiently long time. For $N \simeq 10^2 cm^{-3}$ we have shown that the perturbing pulse must persist for about 20 milliseconds, so that wave frequencies from zero to about 50 Hz might stimulate these processes. If the wave frequency exceeds the critical value the wave perturbation becomes less effective. However, it would seem that these effects can be induced by a sufficiently strong transmitter field for all f capable of stimulating wave growth. Thus, irreversible dissipation might be operative for perturbing frequencies as high as $f_{p+} = 210\ N^{1/2}$. As shown in Table 1, this means all $f \lesssim 2$ kHz for $h \lesssim 1000$ km.

TRANSIENT PRODUCTION OF UNSTABLE PLASMA DISTRIBUTIONS

Aside from the generation of two-stream instabilities via runaway discussed in Section 2, large amplitude perturbations can, under some circumstances, reorder the local plasma particles and produce transient unstable distributions. In this event one or more local wave emissions can be generated and some waves will then be damped or will propagate away from the spacecraft. In either case, energy from the transmitter system is lost without producing radiation.

It is well known that the Alouette sounder antennas produce zero-range echoes at the RF Bernstein modes [nf_{ce}, f(UHR)] and at f_{pe}. The customary interpretation of these observations is that local resonances are stimulated. For true resonance generation, little energy is lost from the system, and these returns present no serious problem. However, Alouette-type sounder antennas can also stimulate propagating modes that provide energy convection and a net dissipation.

Little experimental information is available on the local energy balance in the VLF range, but some recent measurements of additional RF signal returns are suggestive. Oya (1969) described so-called "diffuse resonances" found at $f \simeq (n + 1/2)f_{ce}$. He showed that an $f \simeq 3\ f_{ce}/2$ wave appears when $2.2 < f_{pe}/f_{ce} < 3.6$, and that $n > 1$ modes are found when the local $(f_p/f_c)_e$ ratio is increased. Oya noted that these observations cannot be interpreted in terms of pure Bernstein modes, and one must consider the possibility that the waves convect energy away from the sounder. These waves disappear (2-20) msec after the sounder pulse (Oya, private communication) and it is conceivable that the large RF voltages on the sounder antennas (reported to be several hundred volts by D. Muldrew, private communication) has momentarily distorted the plasma distribution so that the waves are spontaneously emitted from the disturbed region.

Our interest in this problem has been stimulated by the detection of natural $(n + 1/2)f_{ce}$ emissions on OGO 5. Figure 2 shows one example, taken from a forthcoming paper by Kennel et al. (1970). In Figure 2 the frequency-time diagram has a 2.46 kHz OGO interference line, narrow rubidium magnetometer signals at 5 f_c(local)/4 and 7 f_c(local)/4, and a relatively diffuse 3 f_c(local)/2 emission. The B-field had small amplitude $\tau \sim 3$ sec oscillations at this time, and Figure 2 shows that the electric field amplitude was modulated with the same period.

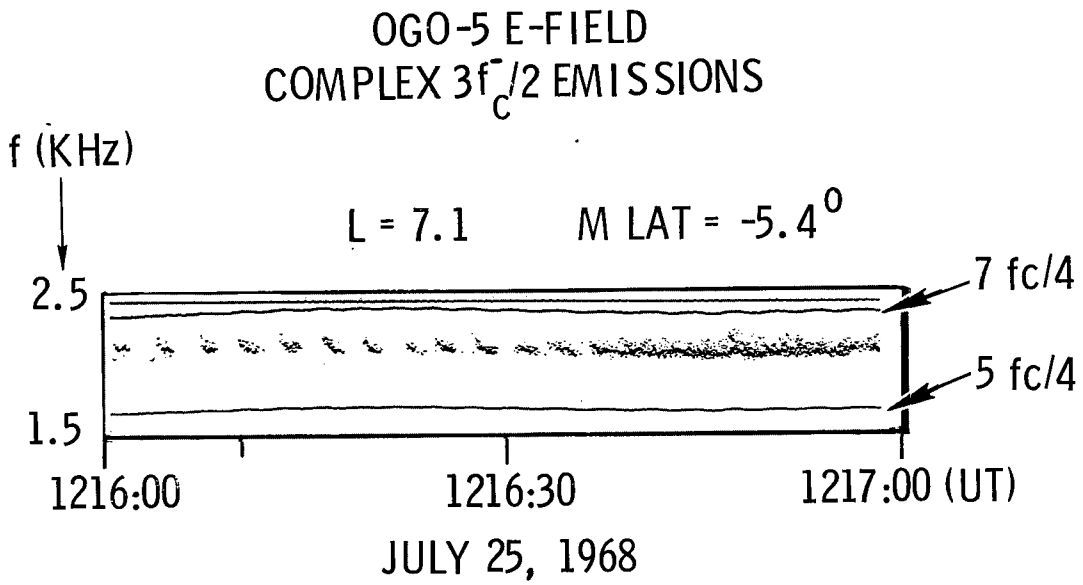

Figure 2

On OGO 5 these emissions are found to be well localized ($L \simeq 4$-10, magnetic latitude $\lesssim 10°$). Here the (f_{pe}/f_{ce}) ratios are similar to those found by Oya in the ionosphere. The OGO-5 observations appear to be correlated with substorms, and we interpret these as natural emissions, rather than locally stimulated waves. Our basis for this interpretation

is: 1) the wave frequencies vary with $|\underset{\sim}{B}|$, and the intensity variation does not correlate with f(wave) being equal to any on-board interference tone; 2) the waves are seen when the rubidium magnetometer telemetry output is off. Moreover, the waves are seen on our digital channels, and therefore they do not arise from the (internal) rubidium signals; 3) the appearance of large amplitude waves has been correlated with simultaneous, but distant precipitation events on nearly the same L-shells; 4) the waves persist for many minutes (or even hours) in contrast to the 2-20 msec duration of the Alouette events.

Despite these source differences, it is tempting to speculate that the OGO 5 and Alouette 2 observations both arise from the same wave-particle interactions or plasma instabilities. In the OGO 5 case, natural geophysical processes presumably generate unstable plasma distributions. In the Alouette case, we speculate that the sounder itself produces a transient distorted distribution leading to emission of the wave. In this case, if the instability is convective, we have an additional energy loss mechanism.

Detailed studies of relevant wave generation mechanisms have been carried out, and the theory will be described in a forthcoming report (Fredricks et al., 1970). Here we present a brief summary of these findings.

The so-called "diffuse resonances" occur at, near or above $(2n+1)f_c/2$. Such waves can be produced by a (non-resonant) plasma instability driven by a distortion of the perpendicular velocity distribution $g_0(v_\perp)$. The required distortion is a strong peak in $g_0(v_\perp)$ away from $v_\perp = 0$, and a width of such a peak that is sufficiently small. We outline the general features of this warm plasma instability here.

Fredricks et al. (1970) have investigated the small-signal stability of electrostatic wave modes in a warm, magnetized plasma. The dispersion relation for such waves, in a form due to Harris (1961) can be written

$$D(\omega,\underset{\sim}{k}) = 1 + \sum_j D_j(\omega,\underset{\sim}{k}) = 0 \tag{5}$$

where the index j runs over all charged species present, and

$$D_j(\omega,\underset{\sim}{k}) = 2\pi \frac{\omega_{pj}^2}{k^2} \int_{-\infty}^{\infty} dv_{\parallel} \int_0^{\infty} dv_\perp v_\perp \sum_{n=-\infty}^{\infty} \left\{ \frac{n\Omega_j}{v_\perp} \frac{\partial f_0}{\partial v_\perp} + k_{\parallel} \frac{\partial f_0}{\partial v_{\parallel}} \right\} \frac{J_n^2(k_\perp v_\perp/\Omega_j)}{\omega - k_{\parallel} v_{\parallel} - n\Omega_j} \tag{6}$$

Here $\omega_{pj} = (4\pi n_j e^2/m_j)^{1/2}$ defines the plasma frequency of the j-th species, $\Omega_j = e|\underset{\sim}{B}_o|/m_j c$ is the gyrofrequency of that species; $\underset{\sim}{v}(v_{||}, v_\perp)$ is the particle velocity in cylindrical coordinates whose axis is along $\underset{\sim}{B}_o$; $\underset{\sim}{k}(k_\perp, k_{||})$ is the similarly defined plasma wave number vector; ω is the plasma wave frequency; $f_o(\underset{\sim}{v})$ is the zero-order particle velocity distribution function, and it contains free energy.

Consider a plasma containing a cold ion component

$$f_{o+}(\underset{\sim}{v}) = (2\pi v_\perp)^{-1} \delta(v_\perp)\delta(v_{||})$$

of density n_+, and a cold electron component

$$f_{o-}(\underset{\sim}{v}) = (2\pi v_\perp)^{-1} \delta(v_\perp)\delta(v_{||}) \qquad (7)$$

of density n_c, plus an electron beam of density n_b described by the ring-like distribution

$$f_{ob}(\underset{\sim}{v}) \simeq (2\pi bc)^{-1} \delta(v_{||}) \exp\left[-(v_\perp - b)^2/c^2\right] \qquad (8)$$

where the normalization factor is approximately valid for the ordered speed $b \gtrsim 2c$, where $c = \langle v_\perp^2 \rangle^{1/2}$.

An extreme example of a distorted distribution is the case $n_c = 0$, $n_b = n_+$. The dispersion relation (5) for such an electron distribution has been studied using the following set of plasma parameters:

$$\omega_{p-}/\Omega_- = 3.0,\ b/c = 4.6,\ 89° \leq \theta \leq 76°$$

where $\theta = \arctan(k_\perp/k_{||})$. The instability occurs in a wavenumber band defined by the values $4.3 \leq \rho_o \leq 4.7$ where $\rho_o = k_\perp b/\Omega_-$, and the real part of the frequency $\omega \gtrsim 1.5\ \Omega_-$, while the growth rates (imaginary part of the frequency) can be as large as $\gamma \lesssim 0.28\ \Omega_-$.

The real part ω/Ω_- is shown in Figure 3a vs propagation angle θ, while the normalized growth rates γ/Ω_- are plotted in Figure 3b, for the values $\rho_o = 4.4$, 4.5, and 4.6 (Note: $\Omega_- = \omega_{ce}$). These unstable modes have phase speeds across and along $\underset{\sim}{B}_o$

$$V_{ph\perp} = \omega/k_\perp \sim 0.3\ b$$
$$V_{ph||} = \omega/k_{||} \sim 0.3\ b \tan\theta \qquad (9)$$

while their group speeds are found to be very strong functions of propagation angle θ, such that for angles $\theta \to 90°$, the instability is essentially absolute, while for $\theta \to 78°$, the instability tends to become convective. For example

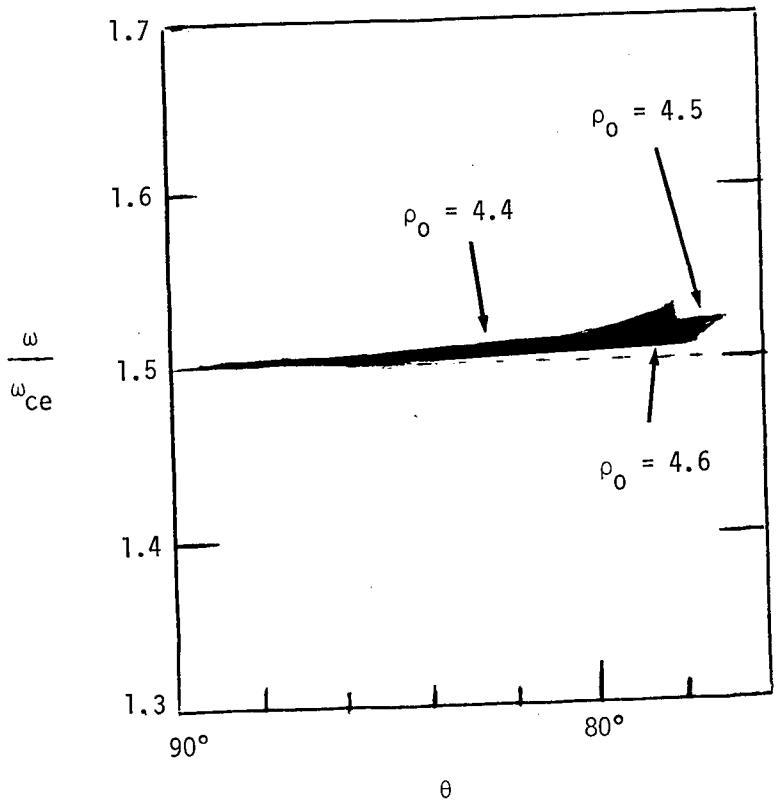

$\omega' = \omega + i\gamma$

$\rho_o = k_\perp b/\omega_{ce}$

WHERE b IS THE PERPENDICULAR "RING" SPEED

Figure 3a

$$V_{g\perp}(\theta = 89°,\ \rho_o \sim 4.6) \simeq (3 \times 10^{-4})b$$

$$V_{g\parallel}(\theta = 89°,\ \rho_o \sim 4.6) \simeq (1.9 \times 10^{-2})b$$

while

$$V_{g\perp}(\theta = 78°,\ \rho_o \sim 4.6) \simeq (8 \times 10^{-2})b$$

$$V_{g\parallel}(\theta = 78°,\ \rho_o \sim 4.6) \simeq (0.39)b$$

Since $V_{g\parallel} \sim 50$ to 60 times $V_{g\perp}$, the energy in these unstable modes tends to be guided along $\underset{\sim}{B}_o$ even though $k_\perp >> k_\parallel$. This result is extremely important with respect to the Alouette observations. If the waves are locally stimulated [in the sense that the sounder wave fields perturb $f_-(\underset{\sim}{v})$ to a form such as given in Equations (7), (8)], then the transmitter has generated a convective instability. In this case, energy flows away, and this mechanism does indeed provide an additional dissipation process.

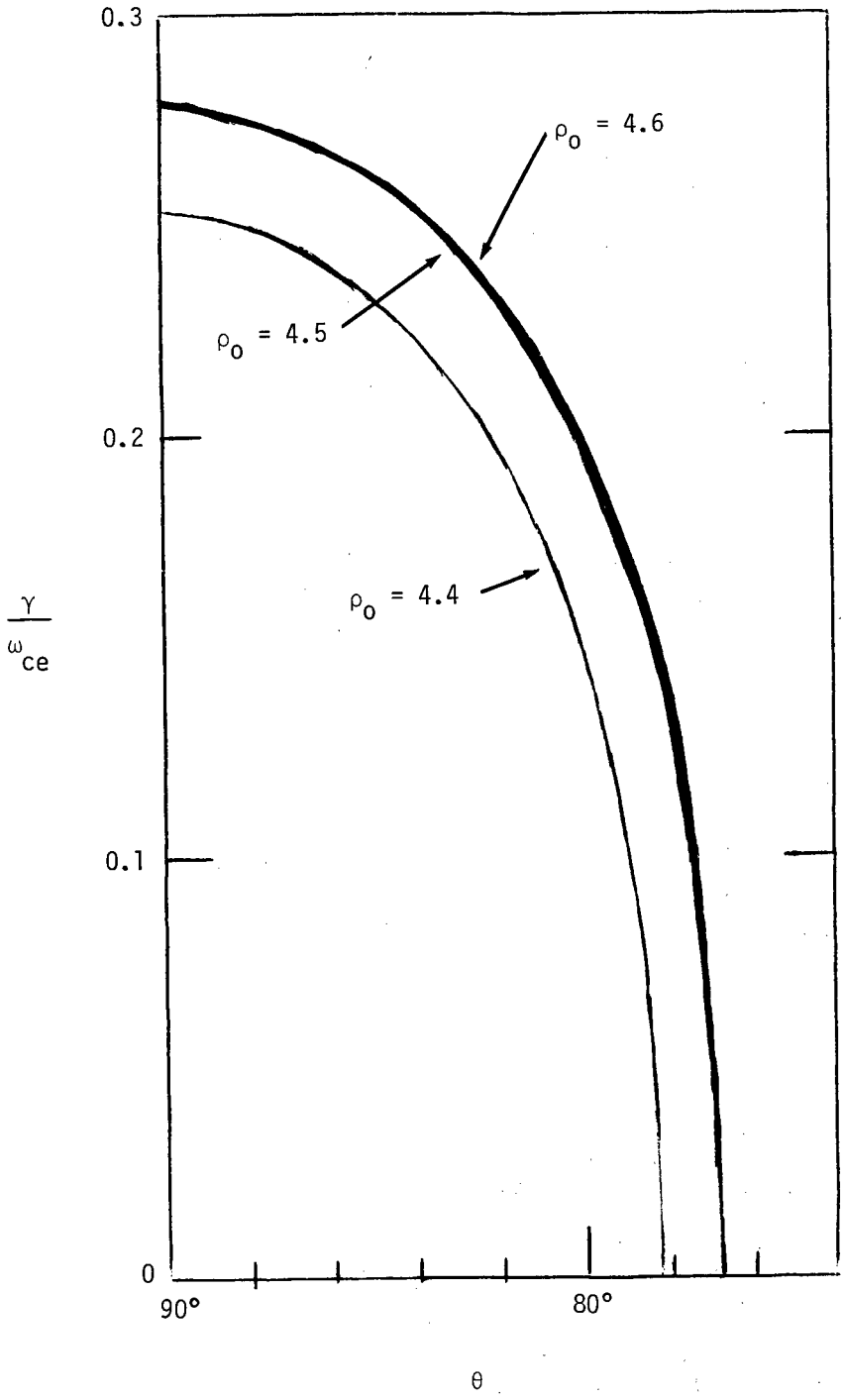

Figure 3b

DISCUSSION

A plasma behaves as a simple medium for wave propagation if the wave field is sufficiently small and the wave frequency sufficiently high. However, when a powerful transmitter operating from within the plasma generates perturbations of sufficiently low frequency, it is sometimes more useful to approach the problem from a dc-field point of view. In this case, theory and recent laboratory experiments both indicate that irreversible non-linear phenomena can readily be stimulated in a dilute and nearly collisionless plasma. For instance, Lonngren et al (1967) have shown experimentally that voltage pulses with $e\phi >> \kappa T_e$ and time duration τ of $1/\omega_{pe} < \tau < 1/\omega_{p+}$ cause the sheath region to expand in an "explosive" manner; Joyce and Montgomery (1967) provided a theoretical analysis of these effects.

Clearly, similar theoretical and experimental studies of intense perturbations should be carried out for the region above the ionosphere. Some direct understanding of the achievable energy balance and its distribution into true radiation and local perturbation effects must be acquired before any detailed system designs are formulated. Alternate approaches for transionospheric VLF transmission should also be examined. For instance, if the transmitter is to operate at a given wave frequency, f_0, then it may be advisable to place the transmitter at a sufficiently high altitude so that f_0 exceeds f_{p+}; in this case the potential runaway problem might be alleviated.

We now know that one very high altitude region, the equatorial "emission sheet" (Helliwell, 1969), is a natural source for many VLF waves (e.g., chorus and other discrete emissions) that are detectable below the ionosphere. Another approach to the transionospheric transmission problem might involve utilization of this natural VLF transmitter on the geomagnetic equator. If we could learn to modulate the natural plasma instability, it might then be possible to transmit signals with oscillators of modest power.

REFERENCES

Coroniti, F. V., Planetary Electrodynamics, Vol. 2 (ed. by S. C. Coroniti and J. Hughes), Gordon and Breach Science Publisher, New York, 309, 1969.
Delcroix, J. L., Introduction to the Theory of Ionized Gases, Interscience Publishers, New York, 1960.
Field, E. C., and Fried, B. D., Phys. Fluids, 7, 1937, 1964.
Forslund, D. W., J. Geophys. Res., 75, 17, 1970.
Fredricks, R. W., et al., to be published, 1970.
Fried, B. D., and R. W. Gould, Phys. Fluids, 4, 139, 1961.
Harris, E. G., J. Nucl. Energy, Part C, 2, 138, 1961.
Helliwell, R. A., Rev's. of Geophys., 7, 281, 1969.
Joyce, G., and D. Montgomery, University of Iowa Report 67-4, 1967.
Kan, J. R., Phys. Rev. Letters, 25, 348, 1970.

Kennel, C. F., F. L. Scarf, R. W. Fredricks, J. H. McGehee, Jr., and F. V. Coroniti, J. Geophys. Res., 31, 6136, 1970.
Lonngren, K., D. Montgomery, I. Alexoff, and W. D. Jones, Bull. Ninth Annual Meeting, APS Div. of Plasma Phys., 102, 1967.
Oya, H., J. Geophys. Res., Space Physics, 75, 4279, 1970.
Scarf, F. L., Phys. Fluids, 5, 6, 1962.
Spitzer, L., Jr., and R. Harm, Phys. Rev., 89, 977, 1953.
Stix, T. H., The Theory of Plasma Waves, McGraw Hill Book Company, New York, 1962.
Stratton, J. A., Electromagnetic Theory, McGraw-Hill Book Company, New York, 1941.
Yngvesson, K. O., and F. W. Perkins, J. Geophys. Res., 73, 97, 1968.

EFFICIENCY CONSIDERATIONS FOR A SATELLITE DOWNLINK AT VLF

R.L. Smith, T.F. Bell & T.N.C. Wang
Radioscience Laboratory
Stanford University Stanford, California

USEFUL RADIATED POWER

Let us examine some very simple but important considerations for the overall efficiency of a communication system involving a satellite transmitter at VLF and a receiver near the ground. An important consideration results from a simple application of Snell's Law. Only a small fraction of waves generated in a medium of high refractive index (the ionosphere at VLF) can penetrate to the region of low refractive index (the free space below the ionosphere). Waves having a wave normal direction outside of a small cone around the vertical are completely internally reflected. A typical example of this can be seen by looking upward while submerged in a pool of water. The energy that is internally reflected cannot be used in transmission of signals to the ground except for a negligible contribution from evanescent waves.

A useful formulation of Snell's Law states that the component of the propagation vector $\overline{k}$ (or the component of refractive index vector) along the boundary is conserved on both sides of the boundary. Since the maximum size of a real $\overline{k}$ on the "free space" side of the ionosphere to atmosphere boundary is restricted to k_0, corresponding to speed-of-light propagation, this limits the useful transverse components of k in the ionosphere to k_0, or a refractive index of unity. (This conclusion will be modified at frequencies below about 500 Hz since the height of the ionosphere will then be comparable to the decay distance for evanescent waves.)

In most cases of interest at VLF, the refractive index and the corresponding power per unit solid angle in $\overline{k}$ space varies considerably with the direction of $\overline{k}$. To simplify calculations, let us, however, assume that the medium is isotropic (using the value for propagation normal to the boundary) and that

power is radiated uniformly with respect to wave normal directions. This is an optimistic assumption. In most cases, the actual ratio of power is less than that derived in the isotropic assumptions.

The actual refractive index is a function of frequency, wave normal direction and position in space. Let us consider two different altitudes: One near the peak of the F-layer, and the second in the 1000-2000 km height range. In the first case, the refractive index is typically 100 for longitudinal propagation and frequencies in the 3-10 kHz range. At the altitude of 1000-2000 km, the longitudinal refractive index is of the order of 10. For a high refractive index, transmission angle is roughly 1/n where n is the refractive index. The corresponding solid angle is π/n^2 steradians. The total solid angle is 4π steradians. Thus, if the radiator is isotropic, the maximum fraction of the radiated power which may radiate across the ionospheric boundary is $1/(4n^2)$. For n = 100, the maximum useful power relative to an isotropic radiator is 2.5×10^{-5}. For n = 10, the value is 2.5×10^{-3}. This factor is obviously of first order importance.

LOWER HYBRID RESONANCE EFFECTS

The discussion in the previous section suggests that a very important part of the results of antenna radiation theory must include the power radiated per unit solid angle (in wave normal or $\overline{k}$ space) compared to the total radiated power. For frequencies above the lower hybrid resonance, theories indicate that a large fraction of the power is radiated in directions related to the resonance cone where the cold plasma refractive index becomes infinite. In almost all cases of a relatively low altitude satellite, this part of the energy is not available for transmission to the ground, so that the net efficiency is even lower than that computed on the basis of the preceding section. One possibility of relieving this difficulty is to operate at a frequency well below the Lower Hybrid Resonance (LHR). In this case, the refractive index approaches the isotropic case, and the resonance cone effects are eliminated.

ELF PROPAGATION EFFECTS IN THE IONOSPHERE

Paul Rodriguez, Donald A. Gurnett, and
Stanley D. Shawhan

Department of Physics and Astronomy
University of Iowa
Iowa City, Iowa 52240

I. INTRODUCTION

The propagation of electromagnetic waves in the ionosphere at frequencies of the order of the ion gyrofrequencies is well known from the study of ion cyclotron whistlers (1). A low-frequency cutoff associated with the two-ion cutoff frequency has been explained as a reflection of downgoing ELF waves (2). The effects of mode coupling on the propagation of ion cyclotron whistlers are important at mid-latitudes (3).

II. THE LOW-FREQUENCY CUTOFF

Figure 1 shows the observed low-frequency cutoff variation with altitude and latitude. Typically, there is a steady decrease in the cutoff frequency F_c with increasing altitude at any given latitude. Figure 2 shows the relationship between F_c and the proton gyrofrequency Ω_p. Generally, F_c is found to be in the range of $0.8\Omega_p$ - $1.0\Omega_p$. Direct evidence that a reflection mechanism is responsible for the low-frequency cutoff is shown in Figure 3 where a measurement of the direction of propagation of a whistler is made by determining the sign of the average Poynting flux (4).

Figure 4 shows a plot of various critical frequencies versus altitude for a model of the mid-latitude ionosphere. These frequencies are the proton gyrofrequency Ω_p, the cross-over frequency (D=0) at which polarization reversal occurs, and the two-ion cutoff frequency (L=0) at which the extraordinary mode is reflected. Not shown on the figure is the ion hybrid resonance (S=0) which occurs at a frequency between the L=0 cutoff frequency and the helium gyrofrequency at any given altitude.

The role that these critical frequencies play for ELF waves propagating downward from a source at high altitudes

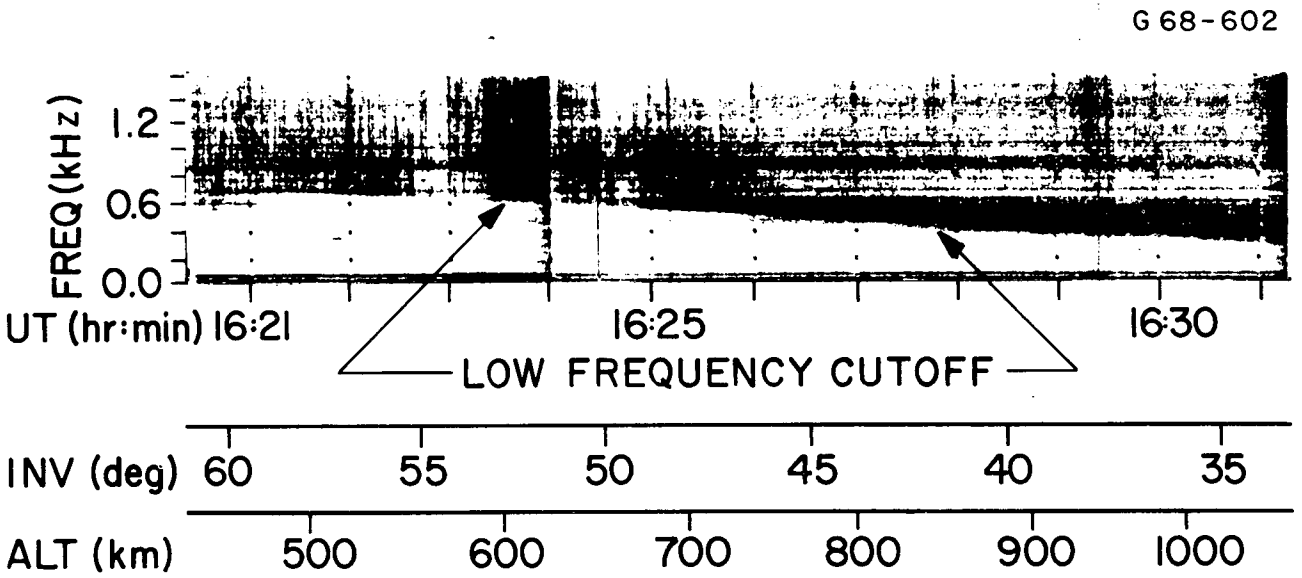
G 68-602
FREQ(kHz)
1.2
0.6
0.0
UT (hr:min) 16:21
16:25
16:30
LOW FREQUENCY CUTOFF
INV (deg) 60 55 50 45 40 35
ALT (km) 500 600 700 800 900 1000

Figure 1

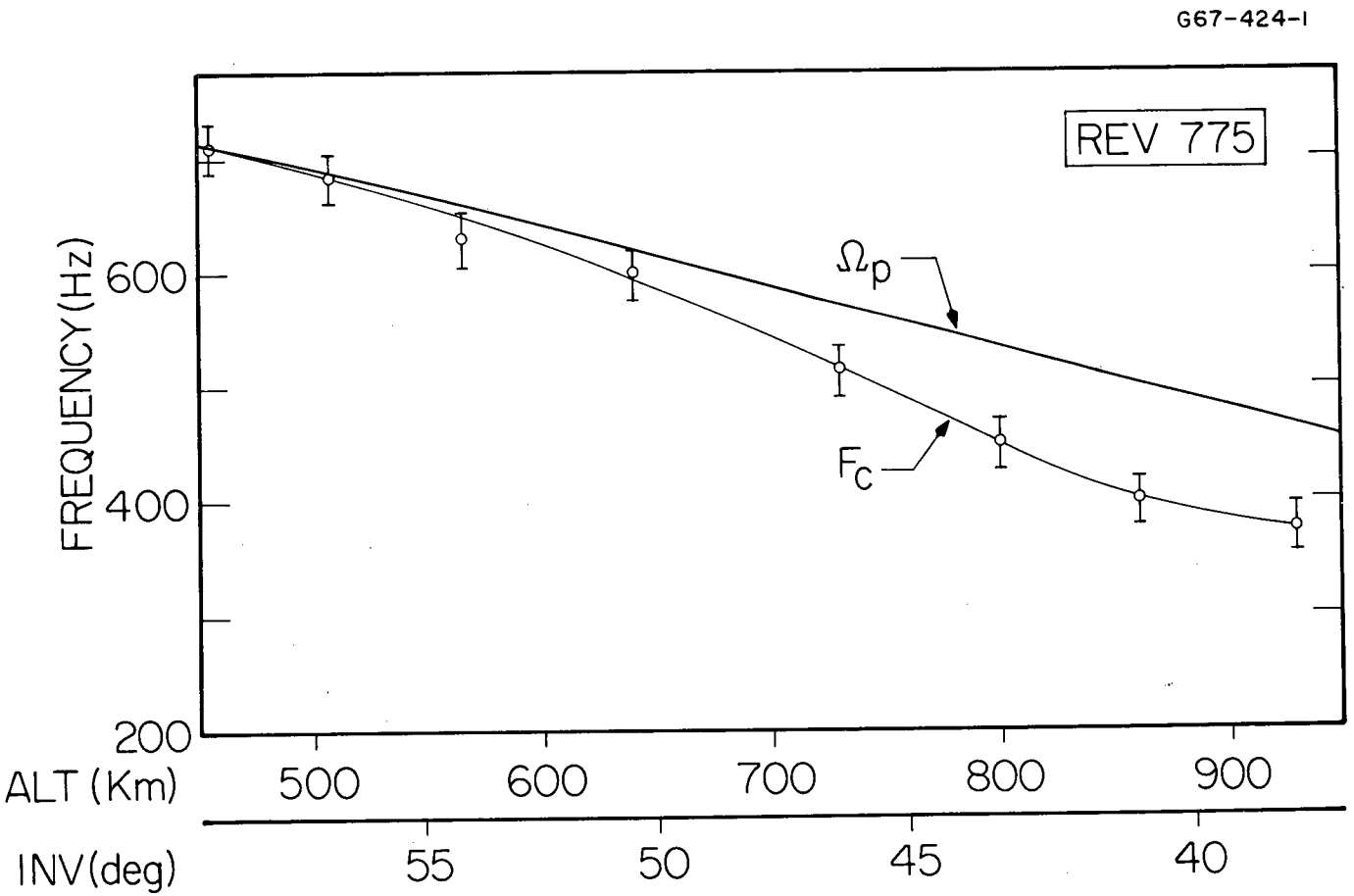

Figure 2

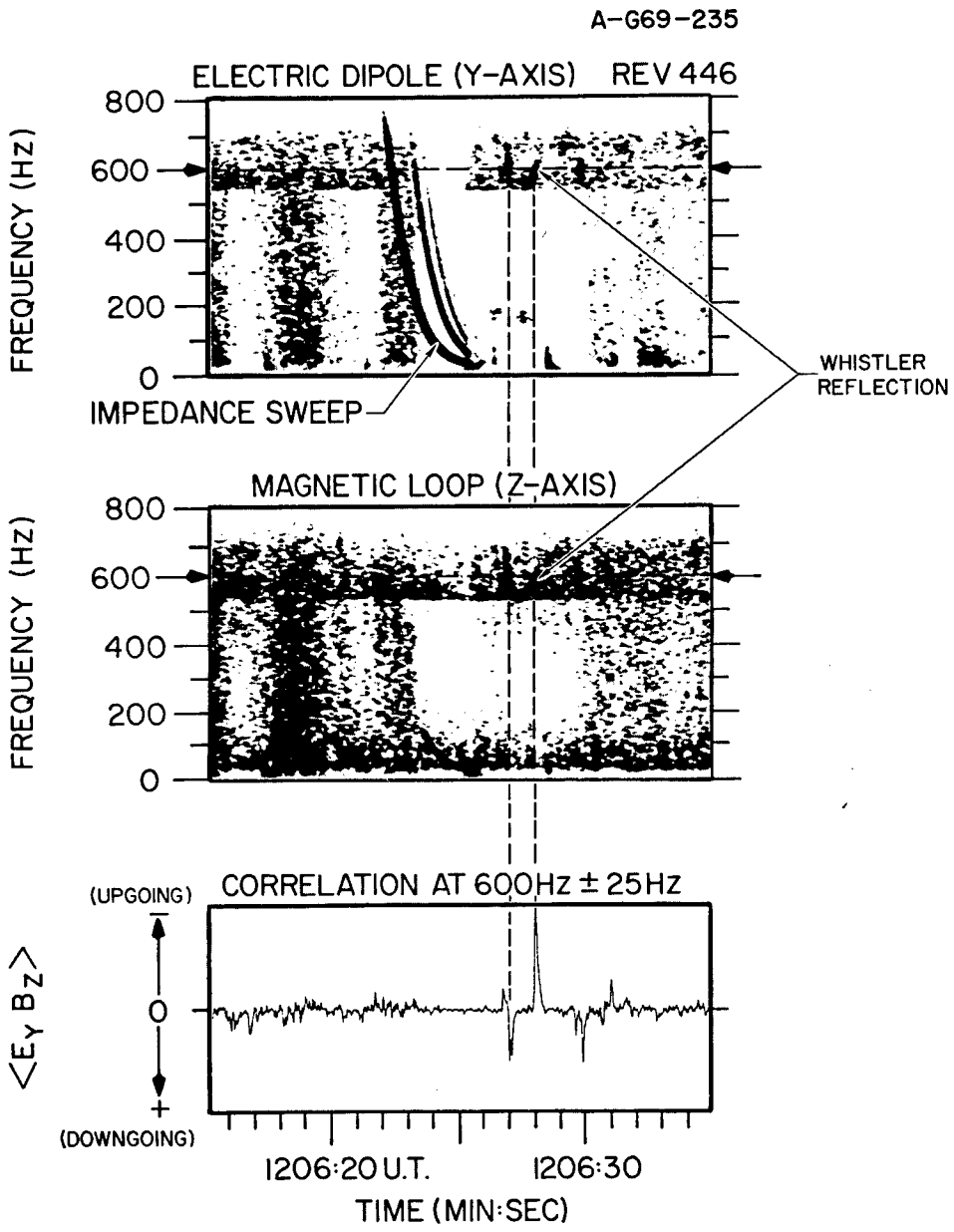
A-G69-235
ELECTRIC DIPOLE (Y-AXIS) REV 446
FREQUENCY (HZ)
800
600
400
200
0
IMPEDANCE SWEEP
WHISTLER REFLECTION
MAGNETIC LOOP (Z-AXIS)
FREQUENCY (HZ)
800
600
400
200
0
CORRELATION AT 600Hz ± 25Hz
(UPGOING)
<EY BZ>
0
+
(DOWNGOING)
1206:20 U.T.
1206:30
TIME (MIN:SEC)

Figure 3

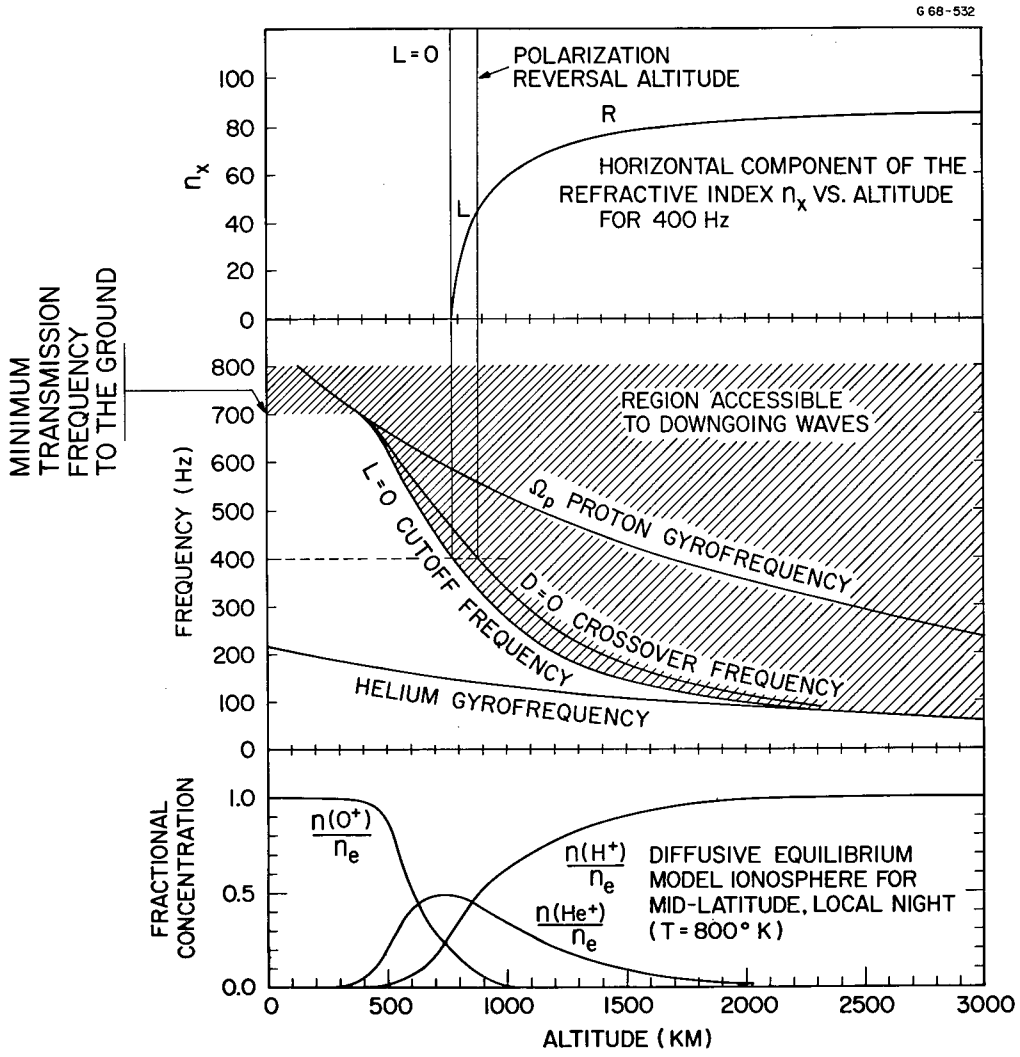
G 68-532
L=0
POLARIZATION REVERSAL ALTITUDE
R
L
HORIZONTAL COMPONENT OF THE REFRACTIVE INDEX n_x VS. ALTITUDE FOR 400 Hz
n_x
MINIMUM TRANSMISSION FREQUENCY TO THE GROUND
REGION ACCESSIBLE TO DOWNGOING WAVES
Ω_p PROTON GYROFREQUENCY
L=0 CUTOFF FREQUENCY
D=0 CROSSOVER FREQUENCY
HELIUM GYROFREQUENCY
FREQUENCY (Hz)
FRACTIONAL CONCENTRATION
$\frac{n(O^+)}{n_e}$
$\frac{n(H^+)}{n_e}$
$\frac{n(He^+)}{n_e}$
DIFFUSIVE EQUILIBRIUM MODEL IONOSPHERE FOR MID-LATITUDE, LOCAL NIGHT (T = 800° K)
ALTITUDE (KM)

Figure 4

can be illustrated by following a wave of frequency 400 Hz starting at an altitude of 3000 km. The wave must be in the extraordinary mode since above the proton gyrofrequency the ordinary mode is evanescent up to frequencies of the order of the electron gyrofrequency. The extraordinary mode is right-hand polarized at this altitude and as it propagates downward, no major effect occurs until the wave reaches the crossover altitude (D=0). As the wave crosses D=0, the polarization is changed to left-hand. The wave continues to propagate until the altitude is reached at which the wave frequency is equal to the L=0 cutoff frequency. At this altitude the index of refraction for the extraordinary mode goes to zero for all angles of propagation and reflection occurs. For a horizontally stratified ionosphere, a downward propagating wave will in general be reflected before reaching L=0 since all that is required is that the horizontal index of refraction n_x become equal to the horizontal component of the initial refractive index vector ($n_x = n \sin \theta$) where θ is the initial wave normal angle.

III. MODE COUPLING AT THE CROSSOVER ALTITUDE

Transmission past the L=0 cutoff is possible if mode coupling occurs at D=0. Over a latitude range of about 35°-55° magnetic latitude mode coupling can be an important effect due to the large vertical gradient in polarization near D=0. A downgoing wave passing the crossover altitude would therefore produce both right and left-hand polarized waves below D=0. Since the L=0 cutoff reflects only the left-hand polarized wave, the right-hand component can be transmitted past L=0. When consideration is given to collisions, mode coupling also occurs for waves propagating near a critical coupling angle θ_c which is of the order of 10°. This condition is more likely to occur at high latitudes where downgoing waves would have small wave normal angles.

Assuming that a downgoing wave has been transmitted past the L=0 cutoff, a reflection may occur at the ion hybrid resonance indicated by S=0. This mechanism has been used to explain the cutoff observed at the lower hybrid resonance ($\sim$5 kHz) and there is some evidence for its occurrence below the proton gyrofrequency.

IV. ELF WAVE TRAPPING

For some ranges of initial wave normal angles and altitudes it is possible to trap ELF waves near the L=0 cutoff frequency. The trapping mechanism involves the L=0 cutoff reflection and the decreasing refractive index above D=0 (due to the decreasing electron density). Assuming horizontal stratification, conservation of the horizontal component of the refractive index vector (Snell's law) leads to reflection both near L=0 and above D=0 resulting in trapping of a wave as in a waveguide.

REFERENCES

(1.) Gurnett, D. A., S. D. Shawhan, N. M. Brice, and R. L. Smith, Ion cyclotron whistlers, J. Geophys. Res., 70, 1665, 1965.

(2.) Gurnett, D. A., and T. B. Burns, The low-frequency cutoff of ELF emissions, J. Geophys. Res., 73, 7437, 1968.

(3.) Rodriguez, P. and D. A. Gurnett, An experimental study of VLF mode coupling and polarization reversal, U. of Iowa Res. Rept., 70-23, March 1970.

(4.) Gurnett, D. A., G. W. Pfeiffer, R. R. Anderson, S. R. Mosier, and D. P. Cauffman, Initial Observations of VLF electric and magnetic fields with the Injun 5 satellite, J. Geophys. Res., 74, 4631, 1969.

NONLINEAR WAVE INTERACTIONS IN THE IONOSPHERE*

by

F. W. Crawford

Institute for Plasma Research
Stanford University
Stanford, California

ABSTRACT

One way in which a VLF signal $(\omega_1, \underset{\sim}{k}_1)$ might be generated in the ionosphere is by the nonlinear mixing of two high frequency waves $(\omega_2, \underset{\sim}{k}_2)$, $(\omega_3, \underset{\sim}{k}_3)$. The interaction can be expected to be strongest when the synchronism conditions $\omega_1 + \omega_2 = \omega_3$, $\underset{\sim}{k}_1 + \underset{\sim}{k}_2 = \underset{\sim}{k}_3$ are satisfied. This presentation considers some possible interactions for which nonlinear coupling coefficients have been evaluated[1]. In particular, the interactions of circularly polarized transverse waves, and longitudinal (Langmuir) waves will be discussed for conditions where $(\omega_3, \underset{\sim}{k}_3)$ is a strong (pump) wave which nonlinearly excites $(\omega_1, \underset{\sim}{k}_1)$ and $(\omega_2, \underset{\sim}{k}_2)$. It is concluded from the analysis and relevant computations that the coupling is too weak to be of any practical importance. Much stronger interactions are possible for other cases, for example excitation of an ion sound wave and a Langmuir wave by a transverse wave pump. It would still be necessary, however, to couple the sound wave to a VLF transverse wave to achieve downlink propagation.

---

* Work supported by the NASA and the NSF.

1. K. J. Harker and F. W. Crawford, J. Appl. Phys. 40, 3247 (1969), J. Geophys. Res. 74, 5029 (1969, and 75,5459 (1970).

EXPERIMENTAL ELECTRIC ANTENNA CHARACTERISTICS IN THE IONOSPHERE AT ELF/VLF

D. P. Cauffman, D. A. Gurnett, and S. D. Shawhan
University of Iowa
Iowa City, Iowa

ABSTRACT

The operation of double-probe type electric antennas flown on the Javelin 8.45 sounding rocket (apogee 760 km) and the Injun 5 satellite (perigee 640 km, apogee 2530 km) is discussed. The dominant impedance measured by the plasma impedance experiment on Injun 5 is that of the ion sheath surrounding each probe. Sheath resistances (F<20 kHz) range from 10^4 to 10^7 ohms, and sheath capacitances vary from 11 to 100 pf. No effects on either the magnitude or phase of the impedance are observed at the plasma resonance frequencies. Impedance changes consistent with Langmuir probe theory and plasma parameters are observed both at the plasmapause and near the magnetic equator.

The impedance measured by Javelin 8.45 shows an inductive perturbation when the sphere axis is aligned with the geomagnetic field. Signals received from a transmitter in the ejected Javelin nosecone are attenuated to a greater extent in the electric channel than in the magnetic channel. It is suggested that for downlink satellite communications applications, electric antennas have nontrivial complications from an engineering viewpoint (their immense research value notwithstanding), and that the use of magnetic loop antennas should not be overlooked.

I. INTRODUCTION

This paper describes the operation of VLF/ELF electric antennas on two University of Iowa spacecraft, the Injun 5 satellite and the Javelin 8.45 sounding rocket. Each experiment measured both the impedance and the potential difference between pairs of spherical probes extended into the ionospheric plasma. In addition, the Javelin rocket nosecone, which separated from the experimental package, transmitted VLF signals, providing a calibrated source of waves whose propagation characteristics could be studied.

II. THE INJUN 5 EXPERIMENT

The NASA/University of Iowa satellite Injun 5 was launched on August 8, 1968, into an elliptical polar orbit with an inclination of 80.66°, an apogee altitude of 2528 km, and a perigee altitude of 677 km. The VLF experiment on board has been discussed by Gurnett et al. [1969].

On December 16, 1968, the Injun 5 satellite achieved magnetic orientation. As illustrated by Figure 1, after magnetic orientation, the (Z) axis of the magnetic loop antenna and the (Y) axis between the electric dipole antenna spheres were both maintained nearly perpendicular (±15°) to the geomagnetic field.

The electric antennas carried by Injun 5 are two spherical aluminum probes 20.3 cm in diameter separated 2.85 meters from center-to-center of the type described by Storey [1965]. The aluminum booms supporting these antenna elements are insulated from the spheres and from the spacecraft body and are coated with a nonconducting paint to insulate the booms from the surrounding plasma.

A small-signal equivalent circuit for one antenna element is shown in Figure 2. The input impedance of the unity gain preamplifiers (located inside the spheres) may be

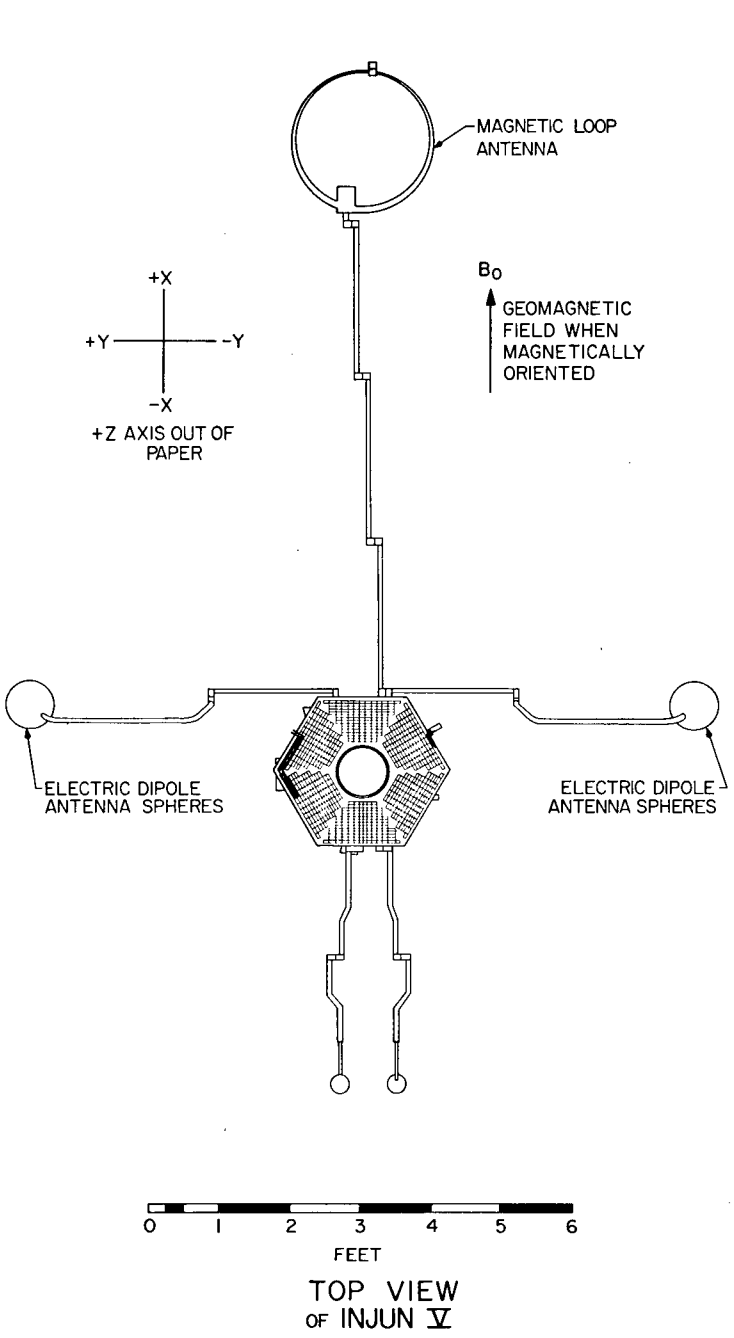

Figure 1. Location and orientation of the VLF antennas on the Injun 5 satellite.

A-G69-166

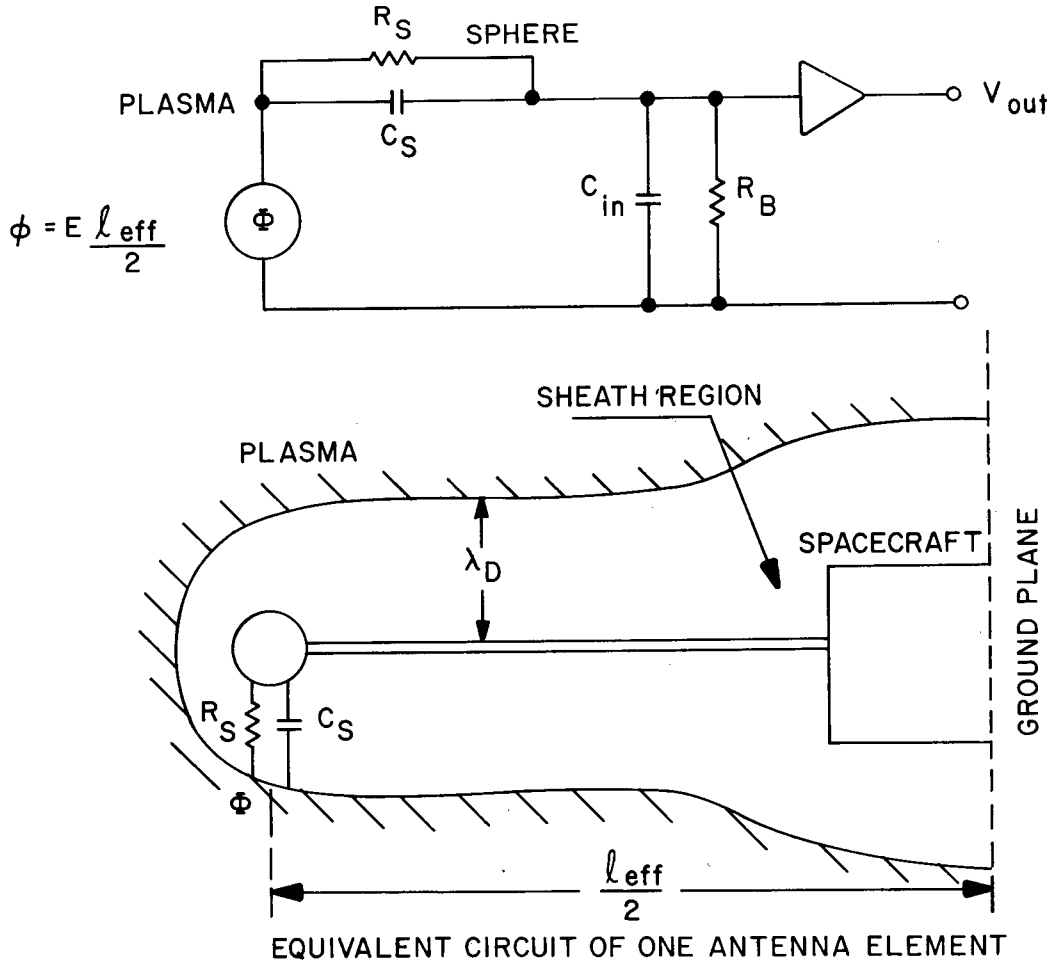

Figure 2. Equivalent circuit of one electric antenna element.

represented by a 20 megohm resistor R_B in parallel with a 10 pf capacitance C_{IN}. The noise level of the unity gain preamplifiers is 10^{-14} volt^2/Hz. These preamplifiers both provide signals to a differential amplifier in the main electronics package, and also drive the aluminum booms supporting the spheres to reduce the sphere-boom capacity. The output of the differential amplifier is proportional to the potential difference between the spheres. The impedance of the electric antenna is measured periodically by differentially driving the spheres with a constant amplitude ac current source (I=0.1 microamp rms), the frequency of which decreases exponentially with time from 20 kHz to 20 Hz. The ratio of the ac potential difference between the spheres to the current I, gives the antenna impedance magnitude $|Z| = V/I$, while the phase ϕ is obtained from a comparison of the voltage and current waveforms. An impedance measurement is made each 30 seconds for a duration of 8 seconds. The dynamic range is 5 kilohms to 10 megohms (magnitude) and $\pm 90°$ (phase).

The theory of operation for a two-sphere electric antenna has been discussed by Storey [1965] and Fahleson [1967]. Langmuir probe theory for a Maxwellian plasma predicts the sheath resistance R_s to be

$$R_s = \frac{kT_e/e}{I_i + I_p}$$

where T_e is the electron temperature, I_i is the ion current incident on the antenna, and I_p is the photocurrent emitted by the antenna.

Typical values of R_s for the Injun 5 orbit and sphere size range from 10^4 to 10^7 ohms. Typical values of sheath capacity vary from 11 pf (the free space capacity of the spheres) at high altitudes to 100 pf in regions of high electron concentration near perigee.

Figure 3 shows a typical impedance measurement. The agreement with the simple resistor-capacitor model for the sheath (Cf. Figure 2) is notable. No effects at the characteristic frequencies of the plasma are observed. Thus the sheath impedance is the dominant impedance measured.

Figure 4 illustrates the rapid change in the sheath resistance ($R_s \simeq |Z|$ at 30 Hz) as the satellite crosses the plasmapause. This characteristic increase in sheath resistance is believed to be due to the increase in electron temperature T_e and the decrease in electron concentration n_e at the plasmapause.

The marked dip in sheath resistance which is commonly observed at low altitudes centered on the magnetic equator is illustrated in Figure 5. This decrease is believed to be due, at least in part, to the electron concentration maximum at the magnetic equator during local daytime. Often the dip has

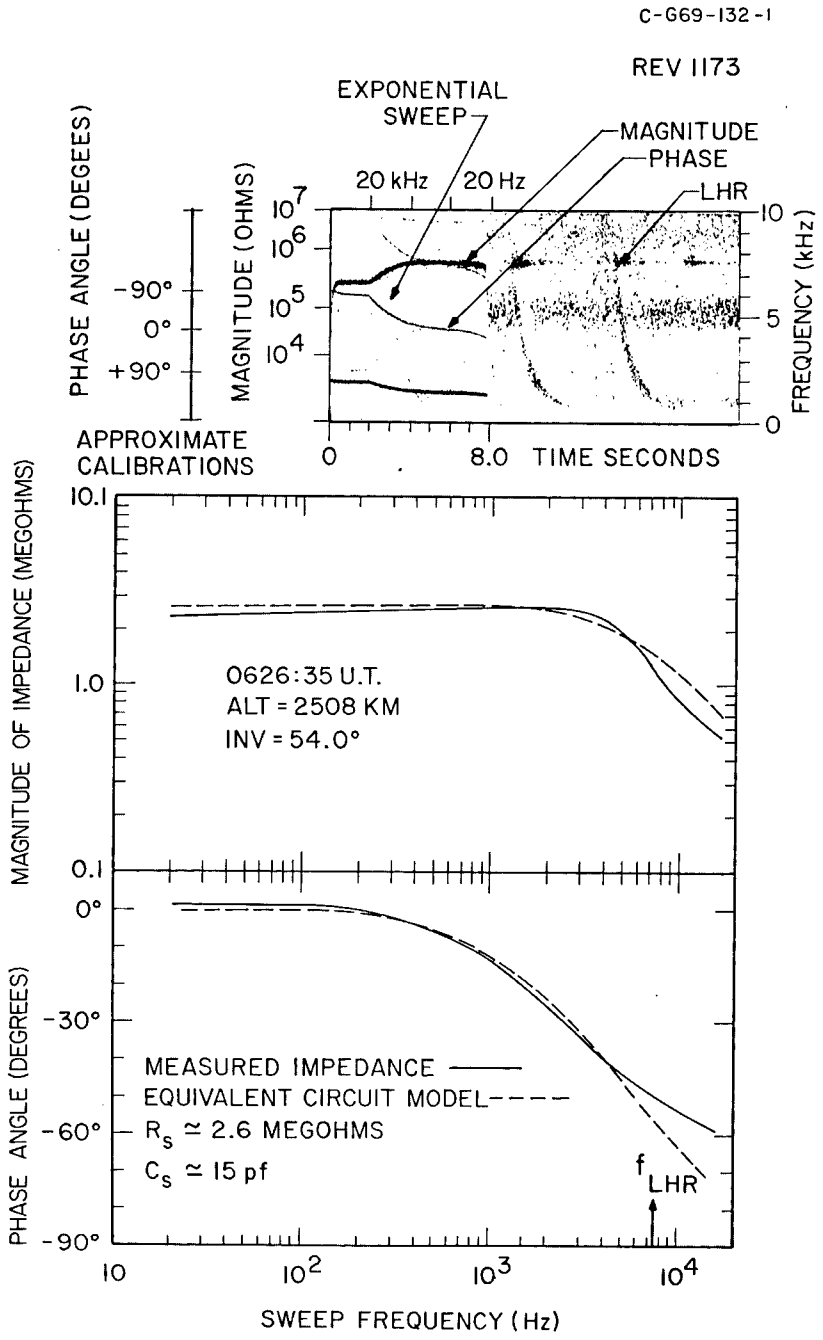

Figure 3. Typical Injun 5 impedance measurement and comparison with equivalent circuit model.

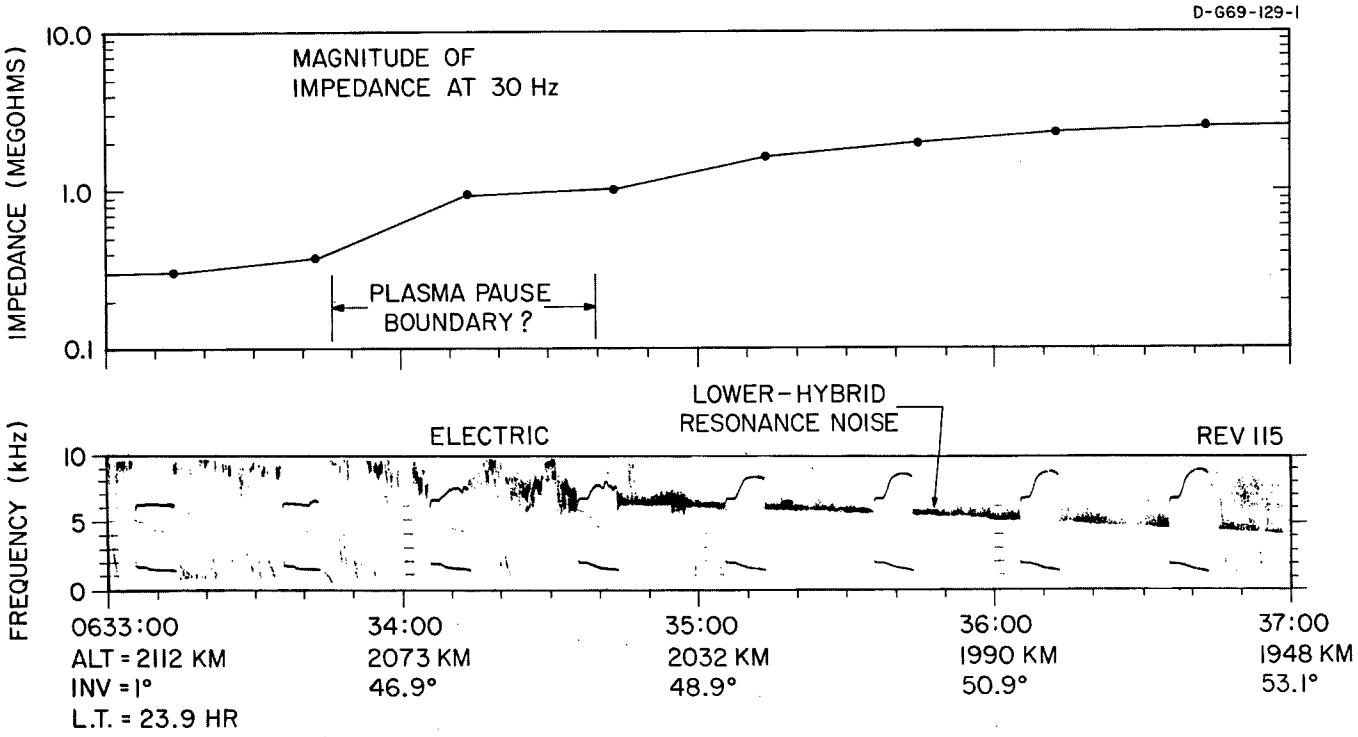

Figure 4. Impedance change across the plasmapause measured with Injun 5.

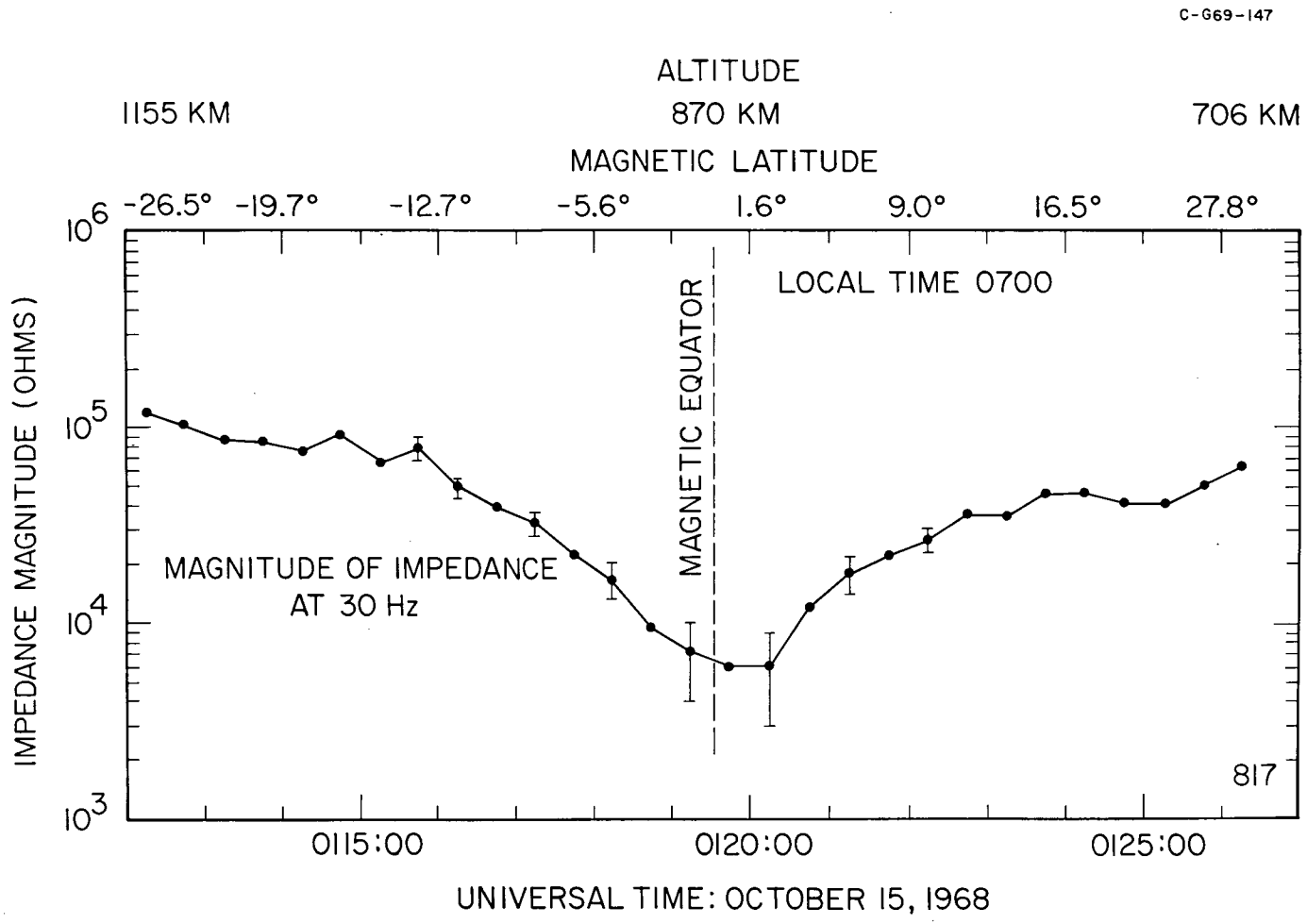

Figure 5. Impedance minimum near the magnetic equator measured with Injun 5.

a very flat bottom, which is believed due to the ion current I_i dominating the photocurrent I_p in the expression $R_s = \frac{kT_e/e}{I_i + I_p}$. Since $I_i \sim n_i \cong n_e$ this allows an estimation of the ratio of electron temperature to electron concentration, or of the square of the Debye length.

III. THE JAVELIN 8.45 EXPERIMENT

On September 21, 1967, at 0338 local time, the Javelin 8.45 rocket flew a VLF electric and magnetic fields experiment to a height of 763 km from Wallops Island, Virginia. Data was provided for 15.5 minutes. The instrumentation is very similar to that flown on the Injun 5 experiment just discussed, [Gurnett et al., 1969] and is described in detail by Shawhan and Gurnett [1968].

Figure 6 shows the location and orientation of the VLF antennas on Javelin 8.45. The electric antenna spheres on Javelin were 15.3 cm in diameter and 3.16 meters apart from center to center. The pair of spherical probes parallel to the Y axis performed an impedance measurement in the same manner as has been described for Injun 5. The rocket payload had a spin period of 5.45 seconds about the Z axis and a precession period of 17.7 seconds about a cone of 27° half angle. Once per precession period the Z axis is nearly perpendicular to the geomagnetic field.

Figure 7 shows a typical impedance measurement sweep made with Javelin 8.45 at 459 km altitude. The impedance generally varies monotonically with frequency, from capacitive (-90° phase angle) at 20 kHz to resistive (0° phase angle)

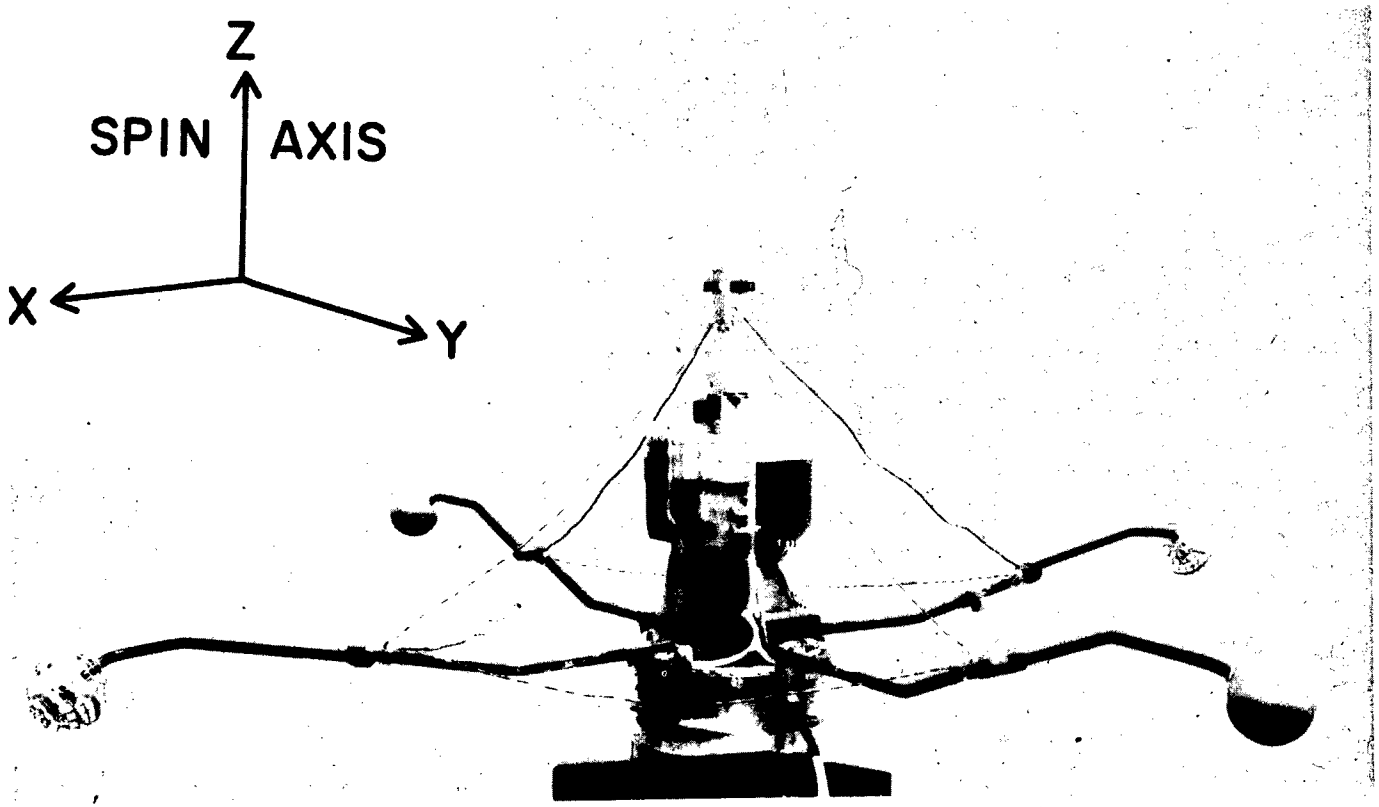

Figure 6. Location and orientation of the VLF antennas on the Javelin 8.45 rocket payload.

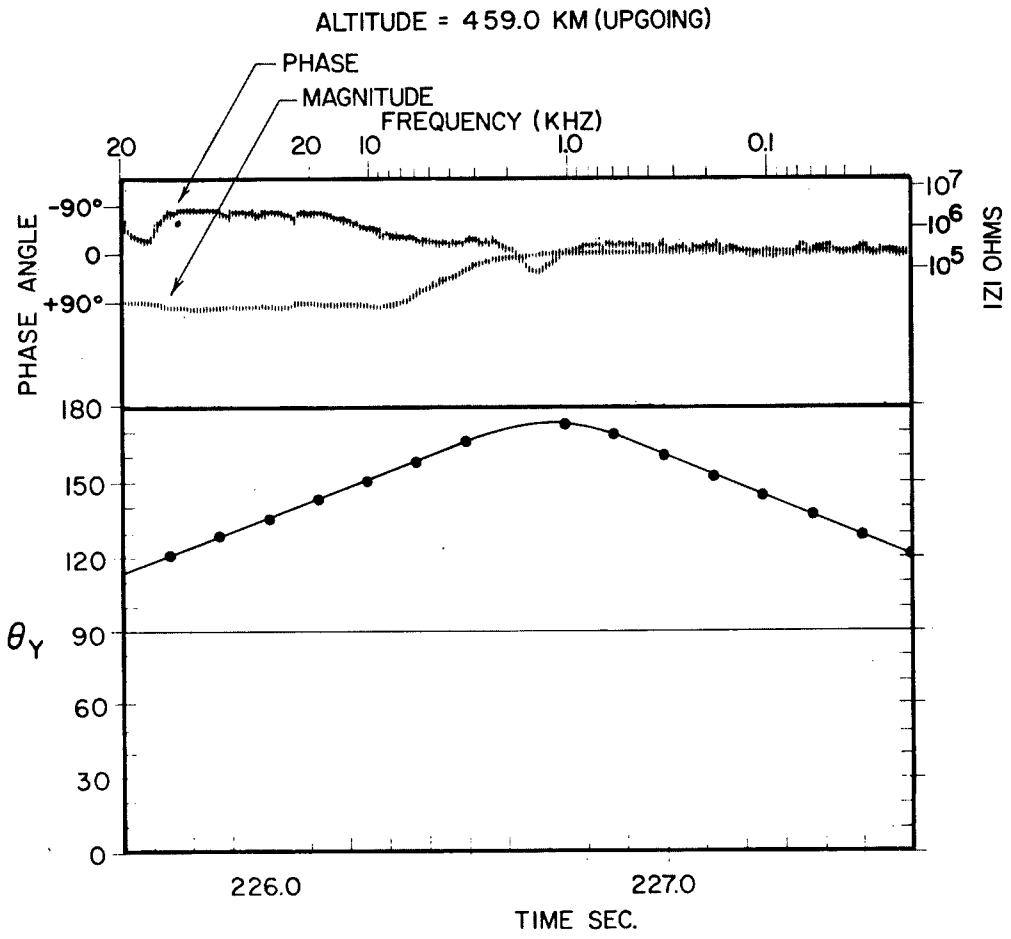

Figure 7. Typical Javelin 8.45 measurement of impedance magnitude and phase. θY is the angle between the electric Y antenna axis and the geomagnetic field.

at about 5 kHz and lower frequencies. The magnitude of impedance varies systematically with altitude with a minimum of about 150 kilohms at 350 km altitude, increasing with increasing altitude to about 600 kilohms at apogee, and reaching values greater than 10 megohms below the ionosphere. Thus at all times the input impedance of the unity gain preamplifiers inside the spheres (20 megohm resistance in parallel with 10 pf capacitance) dominates the resistance across the sheath. The impedance measurement sweep in Figure 7 is unusual due to a large inductive perturbation in the phase angle equivalent to $\Phi \simeq 45°$ just when the angle θY between the electric Y antenna and the geomagnetic field is near 180°. Such phase perturbations occurred primarily at altitudes below 500 km, whenever θY was near 0° or 180°.

To study VLF propagation from a known source, a VLF transmitter was installed in the rocket nosecone. The antennas for the transmitter were a 62-turn loop antenna 0.5 meters in diameter and an electric dipole antenna 1 meter tip to tip. These antennas were pulsed every 2 seconds with a 0.5-second sine wave burst that alternated between 2 and 8 kHz. The peak to peak current in the loop antenna was 4.2 amps, and the peak to peak voltage applied to the electric dipole was 320 volts. Unfortunately the separation velocity indicator ribbon apparently broke, but the nosecone did move away from the payload, as two objects were resolved by the tracking radar, and an upper limit of 2 meters/second can be placed on the separation velocity.

Figure 8 shows frequency-time spectrograms of the electric and magnetic fields from the nosecone transmitter as a function of time from the end of the first pulse at 2 kHz. (Harmonics of 2 kHz are also seen.) The electric antennas and magnetic loops were not fully extended until after 8 seconds in Figure 8. Qualitatively, it is seen that the electric field signal is much more rapidly attenuated than the magnetic field signal. Pulses at 8 kHz can be seen past 28 seconds in the magnetic Y channel, but only to 5 seconds in the electric X channel. The transmitted magnetic signal is, therefore, observed to be less than 5 mγ at a maximum range of 22 meters. No radio noises or instabilities were observed to be stimulated by the nosecone transmitter at any time during the flight.

JAVELIN 8.45 NOSECONE TRANSMITTER

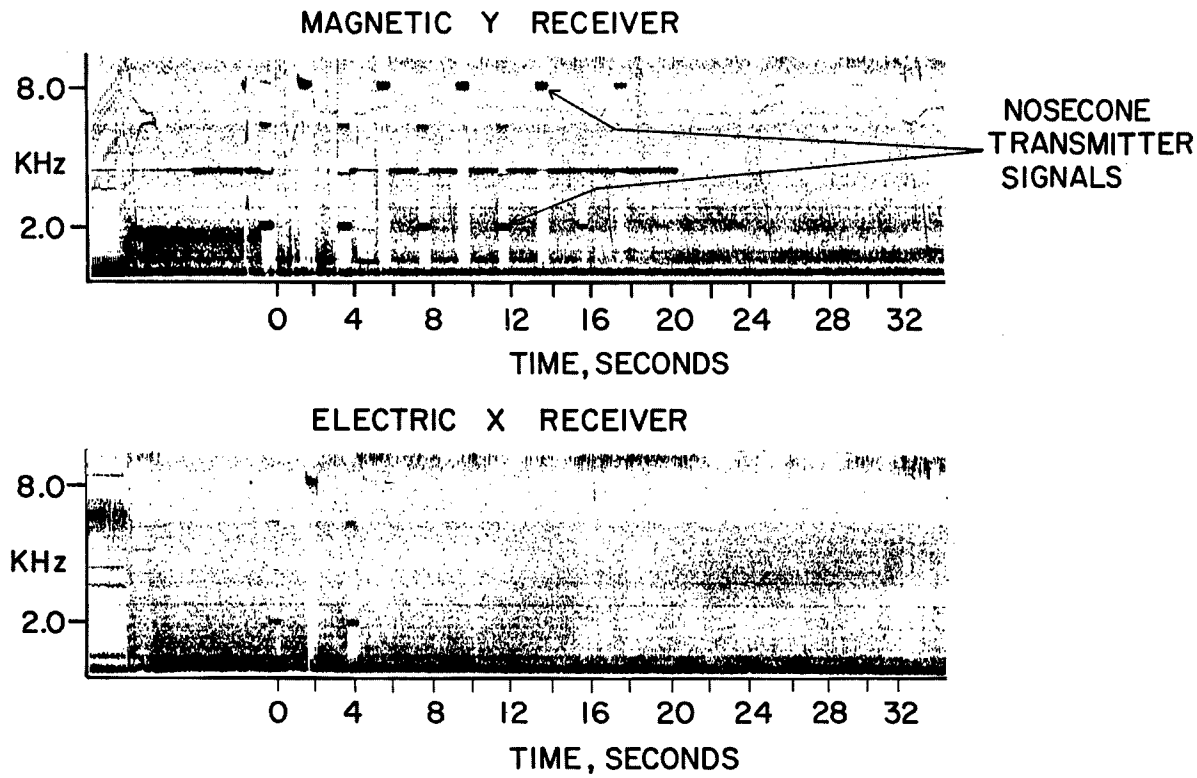

Figure 8. Nosecone transmitter signals detected by the Javelin 8.45 electric and magnetic receivers.

IV. CONCLUSION

The University of Iowa VLF experiments with electric dipoles [Shawhan and Gurnett, 1968; Gurnett et al., 1969; Cauffman and Gurnett, 1970] demonstrate the immense value of electric antennas for ionospheric research due to their sensitivity to a variety of plasma parameters. However, from an engineering standpoint it is precisely this sensitivity to the environment that creates complications when electric antennas are adapted for use in transmission.

The plasma sheath which surrounds the electrodes, and which varies with altitude, latitude, and local time, constitutes an impedance in series with the antenna radiation impedance. We have seen no evidence of any impedance resonances near plasma resonance frequencies such as have been predicted by Storey [1968] and Balmain [1969]. Indications are that the power lost is absorbed in joule heating; the theories neglected collisions. Attempts have been made [Storey, 1965] to bias the sphere potentials in order to eliminate the electric antenna sheaths. This technique has yet to be demonstrated to be possible. The operation of magnetic antennas does not appear to be greatly affected by plasma sheaths.

Electric antennas are also susceptible to wake effects. A spacecraft leaves wakes along the magnetic field vector, as

well as antiparallel to its own velocity vector. The extent of the wakes depends primarily upon the ion thermal velocity, which varies with altitude, latitude, and local time.

In view of these difficulties, we suggest that any attempt to use electric antennas for downlink satellite communications be paralleled by investigations of the feasibility of using magnetic loop antennas. Initial studies of the comparison of electric and magnetic antennas at VLF have been reported by Young (1966).

ACKNOWLEDGMENTS

This research was supported by the NASA under contracts

NSR-16-001-025

NGR-16-001-043

NAS5-10625

NAS1-8141

NAS1-8144 (F),

and NAS1-8150 (F),

and by the Office of Naval Research under Contract

N00014-68-A-0196-0003.

REFERENCES

Balmain, K. G., Dipole Admittance for Magnetoplasma Diagnostics, IEEE Transactions on Antennas and Propagation, AP-17, (3), pp. 389-392, May, 1969.

Cauffman, D. P., and D. A. Gurnett, Initial Injun 5 Measurements of DC Electric Fields, (Paper no. SPM119 delivered at the American Geophysical Union annual meeting in Washington, D. C.) The University of Iowa, Iowa City, Iowa, April, 1970.

Fahleson, U. V., Theory of Electric Field Measurements Conducted in the Magnetosphere with Electric Probes, Space Sci. Rev., 7, 238-262, 1967.

Gurnett, D. A., G. W. Pfeiffer, R. R. Anderson, S. R. Mosier, D. P. Cauffman, Initial Observations of VLF Electric and Magnetic Fields with the Injun 5 Satellite, J. Geophys. Res., 74, (19), pp. 4631-4648, September 1, 1969.

Shawhan, S. D., and D. A. Gurnett, VLF Electric and Magnetic Fields Observed with the Javelin 8.45 Sounding Rocket, J. Geophys. Res., 73, (17), pp. 5649-5664, September 1, 1968.

Storey, L. R. O., Antenna Electrique Dipole pour Reception TBF dans L'ionosphere, L'onde Elec., 45, 1427, 1965.

Storey, L. R. O., M. P. Aubry, and P. Meyer, A Quadrupole Probe for the Study of Ionospheric Plasma Resonances, C.N.E.T. Technical Report GRI/NTP/31, Centre National d'Etudes des Telecommunications, Saint-Maur-des-Fosses, France, April 1968.

Young, C. E., VLF Electric and Magnetic Antenna Impedance Characteristics in the Ionosphere, (Abstract and Manuscript of paper presented 7 December 1966 at URSI Fall Meeting in Palo Alto, California), Naval Research Laboratory, Washington, D. C., 28 November 1966.

A MAGNETOPLASMA FACILITY*

S.Y.K. Tam
RCA Research Laboratories, Montreal, Canada

1. INTRODUCTION

Due to the difficulty in producing large homogeneous plasmas of reasonably high electron densities, experimental work on sources in plasmas was usually performed using plasmas of sizes small or at most comparable to the relevant wavelength. Experiments under such conditions, therefore essentially study a plasma coated source since the whole plasma is in the near field of the source. As an attempt to study antennas and wave propagation in a large plasma, we have developed a magnetoplasma facility (Tam, 1969) which is also useful for studies on electrostatic probes and diffusion processes. In what follows, I will describe the apparatus and the characteristics of a few typical plasmas generated by the same system but useful for different purposes.

2. THE APPARATUS

The magnetoplasma is produced by a discharge in a pyrex glass tube of 22 cm in diameter, and an electrode separation of 35 cm (see Fig. 1). The

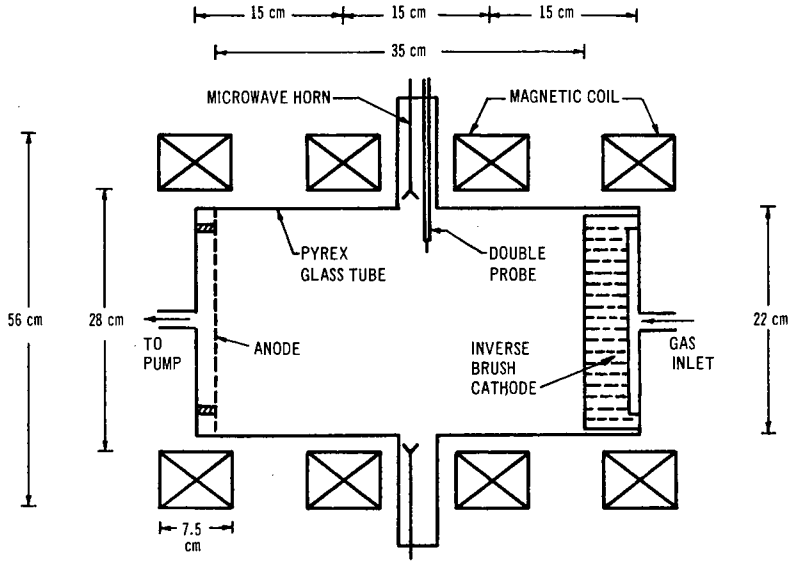

Fig. 1 - Sketch of Apparatus

* This work was supported in part by means of a Defence Industrial Research grant (DRB Grant No. 5501-56) from the Canadian Government and recipients of the research results reported in this document are reminded that under the Terms and Conditions of such grants certain exploitation rights are vested in RCA Limited, Montreal.

anode is made of a perforated sheet of stainless steel while the inverse brush cathode (Musal, 1966) which is the most essential element for producing such a stable plasma, consists of a 5 cm thick stainless steel plate having a large number of 3 mm diameter holes. When the discharge is pulsed, the discharge current is supplied by a condenser bank with a thyratron triggering switch. Under steady state conditions, the electrodes are connected directly to a dc power supply with the same condenser bank acting as a filter. The axial dc magnetic field is provided by four equally spaced plane coils (Magnion D1082-1) and the magnetic flux density may reach a maximum of 0.43 Tesla with a homogeniety within ± 6% over the entire volume of the plasma. Instead of relying on an electrostatic probe to determine the local electron temperature and density, a double probe is used in coordination with two microwave interferometers (at 24 GHz and 75 GH respectively). This allows the double probe to measure the local temperature and relative electron density while the interferometers determine the absolute value of the electron density across the bottle.

3. CHARACTERISTICS OF THE MAGNETOPLASMA

The present magnetoplasma facility has been found to be very versatile. It can be operated under both steady state and pulsed conditions, with crowbarring, over wide ranges of pressures, discharge voltages, discharge currents and magnetic fields. Due to its large volume, homogeneity and suitable electron density, it is particularly useful for experiments on low frequency wave propagation in a large plasma (i.e. the wavelength is much less than the plasma size). In Table 1, we list the characteristics of a few typical plasmas suitable for a wide variety of wave propagation experiments. The steady state plasmas are useful for the X-band and the pulsed plasmas for VLF studies. The homogeneity of a typical plasma as determined from the double probe measurements is shown in Fig. 2. We give the ion saturation currents instead of the relative electron densities as functions of the radial position because the double probe has been working in the transition between the collisionless and collision-dominated regimes (Bienkowski et al., 1968) and a simple theory relating the probe result to the electron density is lacking.

In the density measurements, we find that the double probe ion saturation current remains fairly constant with position until it is about 1 to 3 cm away from the wall depending on the discharge conditions. The bulk plasma therefore is uniform over a fairly large diameter (approximately 16 to 20 cm) and the contribution to the phase shift observed by the microwave interferometer is mainly due to the uniform region. The absolute value of the electron density is now obtained by assuming the plasma to be uniform and extending to a position at which the DP ion saturation current falls to half its value at the center of the plasma.

To determine the electron temperature, we obtain the double probe bias voltage V_{BP} at which saturation of the ion current occurs. The electron temperature T_e is then estimated by the relation $T_e = eV_{BP}/2k$, e being the electronic charge and k the Boltzman constant (Chen 1965, p. 183).

The axial variation of electric potential in the plasma is measured by connecting the double probe to a high impedance voltage probe. The cathode

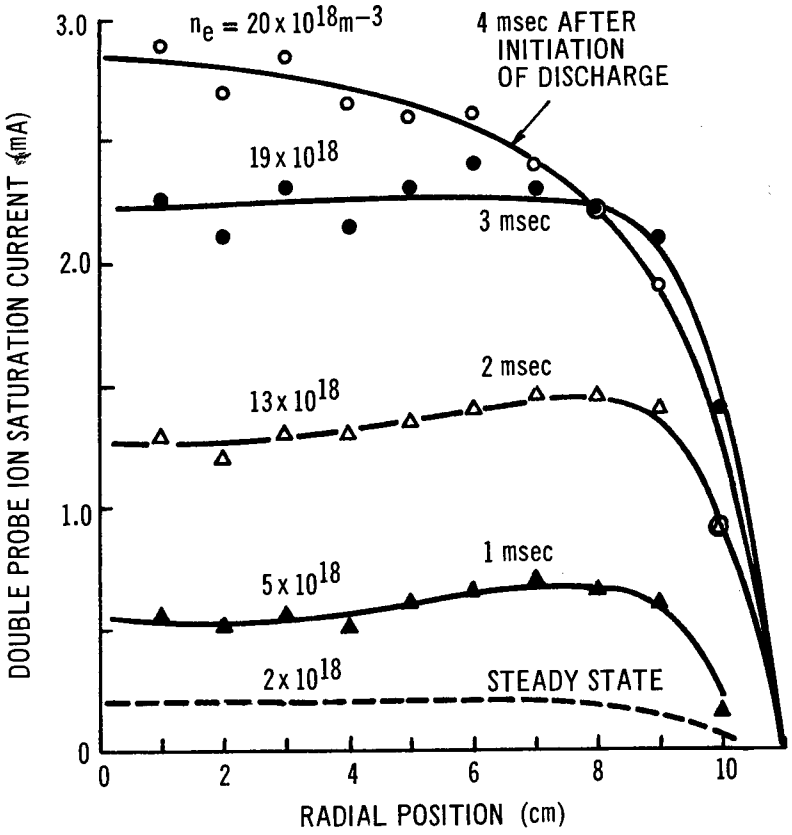

Fig. 2 - Radial variation of double probe ion saturation current.

drop is found to be limited to within 1 cm from the inverse brush cathode while the rest of the bulk plasma shows no detectable variation in potential.

4. CONCLUSIONS

A large volume, highly uniform, quiescent magnetoplasma has been produced with the help of an inverse brush cathode. The plasma produced in a discharge in helium at a pressure of 1 Torr has a length of 35 cm, a diameter of 22 cm and a dc axial magnetic field up to 0.3 T. Under steady dc discharge conditions, the electron temperature T_e is about 0.25 eV and the electron density n_e reaches a value of 2×10^{12} electrons cm^{-3}. At present, the latter is limited by the capacity of the dc power supply. When the discharge is pulsed, $n_e \gtrsim 10^{13}$ electrons cm^{-3} and $T_e \approx 0.35$ eV. The detailed characteristics of a few plasmas suitable for experiments of wave propagation at different frequencies have been given in Table 1.

TABLE 1

CHARACTERISTICS OF TYPICAL MAGNETOPLASMAS

(0.35m long, 0.22 in diameter)

	Pulsed		Steady State dc*	
Filling pressure (Torr)	1.0	0.5	1.0	0.5
Condenser charging voltage (V)	3k	4k	3k	3k
Temperature (^{o}K)				
Neutral T_o	300	300	300	300
Electron T_e	2900	3500	1500	2600
Ion T_i	$\gtrsim 300^{o}$	$\gtrsim 300^{o}$	$\gtrsim 300^{o}$	$\gtrsim 300^{o}$
Densities (particles m^{-3})				
Neutral n_o	3.25×10^{22}	1.6×10^{22}	3.25×10^{22}	1.6×10^{22}
Electron n_e	20×10^{18}	19×10^{18}	2.0×10^{18}	1.5×10^{18}
Ion n_i	20×10^{18}	19×10^{18}	2.0×10^{18}	1.5×10^{18}
Axial dc magnetic field B_o (T)	0.3	0.3	0.3	0.3
Thermal velocities (m sec^{-1})				
Electron V_e	3.6×10^{5}	4×10^{5}	2.6×10^{5}	3.4×10^{5}
Ion V_i	1.4×10^{3}	1.4×10^{3}	1.4×10^{3}	1.4×10^{3}
Collision Cross-Section (m^2)				
Electron-neutral σ_{en}	5×10^{-20}	5×10^{-20}	5×10^{-20}	5×10^{-20}
Electron-ion σ_{ei}	1.1×10^{-15}	0.8×10^{-15}	4.0×10^{-15}	1.6×10^{-15}
Characteristic Lengths (m)				
Cyclotron Radii				
Electron r_{ce}	6.8×10^{-6}	7.5×10^{-6}	4.9×10^{-6}	6.4×10^{-6}
Ion r_{ci}	1.9×10^{-4}	1.9×10^{-4}	1.9×10^{-4}	1.9×10^{-4}

TABLE 1 (continued)

	Pulsed		Steady state dc	
Mean Free Paths				
Electron-neutral λ_{en}	6.4×10^{-4}	12×10^{-4}	6.2×10^{-4}	12×10^{-4}
Electron-ion λ_{ei}	4.4×10^{-5}	6.5×10^{-5}	12.5×10^{-5}	4.2×10^{-5}
Ion-neutral λ_{in}	3.7×10^{-5}	7.4×10^{-5}	3.7×10^{-5}	7.4×10^{-5}
Debye length λ_{Debye}	0.83×10^{-6}	0.93×10^{-6}	1.9×10^{-6}	2.9×10^{-6}
Characteristic Frequencies (rad sec^{-1})				
Electron plasma frequency ω_{pe}	2.5×10^{11}	2.5×10^{11}	0.8×10^{11}	0.7×10^{11}
Electron-neutral collision frequency ν_{en}	5.8×10^{8}	3.3×10^{8}	4.2×10^{8}	2.8×10^{8}
Electron-ion collision frequency ν_{ei}	8.2×10^{9}	6.2×10^{9}	2.1×10^{9}	0.82×10^{9}
Experimental Conditions for the Double Probe				
Probe radius r_p(m)	10^{-4}	10^{-4}	10^{-4}	10^{-4}
Ion neutral mean free path λ_{in}(m)	3.7×10^{-5}	7.4×10^{-5}	3.7×10^{-5}	7.4×10^{-5}
Cyclotron radius for He^+ ion r_{ci}(m)	1.9×10^{-4}	1.9×10^{-4}	1.9×10^{-4}	1.9×10^{-4}
Ion mobility $\mu_o(He^+)(m^2V^{-1}sec^{-1})$ at STP	1.07×10^{-3}	1.07×10^{-3}	1.07×10^{-3}	1.07×10^{-3}
Refraction parameter α_i (Bienkowski et al., 1968)	1.2	1.3	0.9	1.2

REFERENCES

1. Bienkowski, G.K., and Chang, K., "Asymplotic Theory of a Spherical Electrostatic Probe in a Stationary Weakly Ionized Plasma", Phys. Fluids, 11, 784 (1968).

2. Chen, F.F., "Electric Probes", a review article in the book "Plasma Diagnostic Techniques", by Hiddleston, R.H. and Leonard, S.L., Academic Press, New York (1965).

3. Tam, S.Y.K., "A Large Volume Quiescent Magnetoplasma with a High Electron Density", RCA Lab. Report, 7-801-77, May (1969).

SOUNDING THE MAGNETOSPHERE AND IONOSPHERE AT VLF

R. L. Smith, R. A. Helliwell and B. Edgar
Radioscience Laboratory, Stanford University

A common type of whistler observed in the altitude range from 2 to 3 earth radii within 30 degrees of the magnetic equator is the magnetospherically reflected (MR) whistler. Study of the MR whistler has led the the suggestion of a new method of sounding the ionosphere and magnetosphere at VLF. The new mode of propagation is called the "Boomerang" mode since the ray path of the outgoing signal is not the same as the return path, although both rays intersect the satellite. Also, the return ray results not from simple reflection, but rather a refraction. Some of the possible applications of this mode are: (1) density measurements near the magnetic equator; (2) study of asymmetries in the ionosphere and magnetosphere; and (3) experimental determination of the radiation efficiency of a VLF antenna.

NONLINEAR SHEATH CONDUCTANCE AND CAPACITANCE OF A VLF DIPOLE ANTENNA AT HIGH PEAK VOLTAGE IN THE IONOSPHERE

I.P. Shkarofsky
Senior Member of Scientific Staff
RCA Limited, Research Laboratories
Montreal, Quebec, Canada

ABSTRACT

A numerical calculation is performed yielding values of voltage and resistive current distribution, sheath size, and charge per unit length, as a function of distance along the antenna and instantaneous applied voltage. We then illustrate wave forms for the charge and both resistive and displacement current assuming an applied cosine voltage form. Averaging over a cycle yields an average sheath conductance of 2.5×10^{-4} mhos and average sheath capacitance of 3.8 pico-farad at a peak applied VLF voltage of 80 volts at an altitude of 350 km in the ionosphere.

I. INTRODUCTION

If one operates a VLF antenna in the ionosphere at high voltage, non-linear effects are to be expected. The motion of the antennas with velocity v across magnetic field (B) lines induces a further $\underset{\sim}{v} \times \underset{\sim}{B} \cdot \underset{\sim}{l}$ voltage, which combines with the applied voltage. To show their relative effects we pick a maximum $\underset{\sim}{v} \times \underset{\sim}{B} \cdot \underset{\sim}{l}$ voltage across each half antenna length l of 10.4 volts and a peak applied voltage of 80 volts for calculation purposes. These high voltages produce significant sheaths around an uninsulated antenna. The solution here is based on the idea that at any instance, we visualize the VLF applied voltage as a dc effect. The justification is that at frequencies below 10 kHz, the ionosphere equilibrates instantaneously for each applied voltage during its oscillation. This is intuitively obvious for the fast electrons but can also be demonstrated for the ions based on their ram velocity and sheath size.

The calculation for such a non-linear situation is done numerically. We choose an electron density of 8.35×10^{11} m^{-3}, an electron temperature of $1806^{\circ}K$ and ion species O^{+} with a temperature of $825^{\circ}K$, appropriate for an altitude of 350 km. The sheath currents, sizes, and voltage radial variation are all calculated using the theory of Langmuir and Mott-Smith (1924) and Langmuir and Blodgett (1923) for a cylindrical conductor, however as modified by Johnston (1969) to allow for both ion ram energy and photo-electric current. Since due to $\underset{\sim}{v} \times \underset{\sim}{B}$ effects, the voltage, sheath size, etc., vary along the antenna length, we break up the total length into elements each assumed cylindrically symmetric. This is reasonable for a long antenna such as the value of 150 m for each half antenna length adopted here for illustration. The procedure is thus:

(1) calculate the voltage distribution along the antenna for each instantaneous applied voltage;

(2) integrate the differential current obtained from (1) along the length to give the total resistive current at the feed points;

(3) calculate the sheath distribution along the antenna for each applied voltage;

(4) then the distribution of charge per unit length;

(5) integrate (4) along the length to give the total charge at the feed points;

(6) differentiate (5) with respect to voltage to give the total displacement current at the feed points;

(7) average over a cycle (2) and (5) to give the average sheath conductance and capacitance for the particular assumed peak voltage.

Similar efforts in the past are those of Mlodnosky and Garriott (1962), Crawford and Mlodnosky (1964), Grard (1965) and Grard and Tunaley (1968). Here, we extend their work by including $\underset{\sim}{v} \times \underset{\sim}{B}$ effects and an high applied peak voltage with its associated non-linear effects, whereas their theory is a linear formulation valid only if one has both very low peak voltages (of the order of tens of millivolts) and short antennas (less than 5m). Similar remarks apply to Aggson et al (1966) and Koons et al (1970).

II. THEORY

The following relation is used for the current per unit length, i, collected by a cylindrical conductor of radius r_a and with a sheath radius r_s, for an accelerating situation, $q_i V < 0$,

$$i_i = n_i q_i \left[(2\pi r_a v_{si})^2 + (2 r_a v_{ram})^2 \right]^{\frac{1}{2}} \left\{ \frac{r_s}{r_a} \operatorname{erf}\left[\left(\frac{\eta_i r_a^2}{r_s^2 - r_a^2} \right)^{\frac{1}{2}} \right] + e^{\eta_i} \left[1 - \operatorname{erf}\left[\left(\frac{\eta_i r_s^2}{r_s^2 - r_a^2} \right)^{\frac{1}{2}} \right] \right] \right\} \tag{1}$$

where

$$v_{si} = (\kappa T_i / 2\pi m_i)^{\frac{1}{2}}, \quad \eta_i = -q_i V / [\kappa T_i + 2 m_i v_{ram}^2 / \pi]$$

erf is the error function, n_i, q_i, κ, T_i have their usual meaning, v_{ram} is the projected velocity across the antenna diameter $2r_a$, and V is the potential at position x on the antenna. If we set $v_{ram} = 0$, we obtain Langmuir and Mott-Smith's (1924) result. Johnston (1969) provides the simple modifications which include v_{ram}, but he limits himself to the case of $r_s^2 > [(r_s^2 - r_a^2)/\eta_i] > r_a^2$.

For a retarding situation, $q_i V > 0$, we use as given by Johnston (1969)

$$i_i = n_i q_i \left[(2\pi r_a v_{si})^2 + (2 r_a v_{ram})^2 \right]^{\frac{1}{2}} \exp(\eta_i') \tag{2}$$

where

$$\eta_i' = - q_i V / [\kappa T_i + m_i v_{ram}^2 / 2]$$

which again reduces to Langmuir and Mott-Smith's (1924) result for $v_{ram} = 0$.

Photoelectric current per unit length (i_{pe}) is also included by Johnston through the relations

$$i_{pe} = \langle nev \rangle 2r_a \sin\alpha_{sun} \quad \text{if} \quad V < 0$$

$$i_{pe} = \langle nev \rangle 2r_a \sin\alpha_{sun} \exp(-V) \quad \text{if} \quad V > 0$$

where following Bourdeau et al (1961), a typical value of 4×10^{-5} amps/m^2 is assigned to $\langle nev \rangle$. Also $\sin\alpha_{sun}$ allows for the projection of the diameter along the sun direction.

The sheath radius r_s is required in order to use Eq. (1). Following Langmuir and Mott-Smith [5](1924), we use another relation involving i_i, r_s, etc., which involves a function $(-\beta)^2$ of r_s/r_a, tabulated by Langmuir and Blodgett (1923). We have upon summing over the ion species for $V < 0$ or considering only electrons for $V > 0$, the relation

$$\sum_i i_i m_i^{\frac{1}{2}} = 8\pi\varepsilon_0 (2|e|)^{\frac{1}{2}} V^{3/2} / (9 r_a (-\beta)^2) \qquad (3)$$

The actual potential distribution along the antenna at any position x (taking $x = 0$ at the middle of the feed points) is

$$V_{R,L} = V_o \pm V_s/2 + \underset{\sim}{v} \times \underset{\sim}{B} \cdot \underset{\sim}{i}_l \, x$$

where V_s is the applied VLF instantaneous potential across the feed and R denotes right, L is left and the induction voltage is taken to increase towards the right. Also V_o is a reference potential at $x = 0$, determined from the requirement that the total integrated current

$$I(x) = \int_{-l}^{x} (i_e + i_{pe} + \Sigma i_i) dx \qquad (4)$$

is zero at $x = \pm l$ when l is half the antenna length.

A computer program was initially written by Johnston (1969) and extended by the author (using the more complete Eq. (1), for purposes of this paper) to solve Eqs. (1) to (3) for a given V_s and V_o, integrate them and relax the result until $I = 0$ at $x = l$. This yields V_o and subsequently the quantities i, r_s and I. Results are illustrated in the next section. In particular, the value of I at $x = 0$ gives the sheath resistive current at the feed points, a result already displayed by Johnston (1969). Besides plots of r_s, new results calculated here are as follows: The average power dissipated is obtained by integration over a cycle, thus

$$P_{av} = \int_o^{2\pi} I V_s \, d\omega t / 2\pi \qquad (5)$$

and the average conductance is derived from

$$G_{av} = P_{av} / (V_{smax}^2/2) \qquad (6)$$

where V_{smax} is the peak applied VLF voltage.

We also need the displacement current at the feed points and the average capacitance. This additional current is caused by changes in capacitance as the sheath radius is altered. The computer program for this was written by the author and uses again Langmuir and Blodgett's (1924) theory in order to obtain the important quantity $\partial V/\partial r$ at $r = r_a$, namely the radial derivative of potential at the antenna surface. Their theory gives

$$\frac{\partial \ln V}{\partial \ln r} = \frac{2}{3}\left(1 + \frac{\partial \ln \beta}{\partial \ln r}\right) \tag{7}$$

Since $(-\beta)^2$ is tabulated versus r_s/r_a, we can obtain by differentiation $\partial \ln \beta/\partial \ln r$ and consequently $\partial \ln V/\partial \ln r$ at $r = r_a$. Using Poisson's equation, the charge per unit length on the antenna surface is then given by

$$\sigma = \sum_i q_i \int_{r_a}^{r_s} n_i 2\pi r \, dr = 2\pi\varepsilon_o \int_{r_a}^{r_s} \frac{\partial}{\partial r}\left(r \frac{\partial V}{\partial r}\right) dr = 2\pi\varepsilon_o \left(V \frac{\partial \ln V}{\partial \ln r}\right)_{r = r_a} \tag{8}$$

since $\partial V/\partial r$ is zero at $r = r_s$. Knowing $\partial \ln V/\partial \ln r$, we obtain σ. The total charge flowing through the feed points is given by

$$Q = \int_{-1}^{o} \sigma dx - \int_{o}^{1} \sigma dx \tag{9}$$

being aware of changes in the sign of σ, which may occur around zero potential points. Since Q is a function of V_s, we differentiate to obtain $\partial Q/\partial V_s$. Letting $V_s = V_{smax} \cos \omega t$, we consequently derive the displacement current from

$$I_{dis} = \frac{dQ}{dt} = -(\omega V_{smax} \sin \omega t)\partial Q/\partial V_s \tag{10}$$

Of greater interest is the average work done. (Note that the average power is zero since the capacitor is lossless.)

$$W_{av} = \int_0^{2\pi} QV \, d\omega t/2\pi \tag{11}$$

From this, we finally derive the average capacitance

$$C_{av} = W_{av}/(V_{smax}^2/2) \tag{12}$$

The relations in Eqs. (5) to (12) are more exact than those given by Mlodnosky and Garriott (1962) and Crawford and Mlodnosky (1964), since our equations allow for non-linear functions of I and Q versus V_s and also for variations of r_s, σ, etc. along antenna length.

III. RESULTS

The numerical values assumed for various parameters have already

been given above. After having searched and found the condition $I(1) = 0$ in Eq. (4), we also obtain V_o and the voltage distribution along the antenna length for various V_s up to ^{o}80V, as shown in Fig. 1. The slope of the lines is due to the $\underset{\sim}{v} \times \underset{\sim}{B}$ linear voltage variation. When the voltage is above -10.4V (the $-\underset{\sim}{v} \times \underset{\sim}{B}.\underset{\sim}{l}$ voltage), the right hand side is anchored with its outmost edge at a positive potential less than 2V. The applied V_s serves to bias the left-hand arm at a negative potential. The right and left sides reverse for voltages below -10.4V, and the positive potential then occurs near the left hand feed point. This small positive region collects sufficient electrons, balancing the ion collection from everywhere else.

The total current I distribution along the antenna for various V_s is shown in Fig. 2. For positive V_s, the current rises steadily until near the outermost tip where electron collection rapidly starts to cancel the integrated ion current up to there. As the potential goes negative, the current first decreases near the feed point, displaying two maxima, and then for larger negative potentials, the current goes negative near the left hand feed point, where the electrons are mostly collected. It then decreases to zero on the right-hand side as more ions are collected to cancel the surge of electrons previously collected.

The sheath sizes along the antenna for various voltages are shown in Fig. 3. The antenna radius (and thus minimum sheath radius) is taken as 1.6 cm. For voltages near -10.4 volts, the sheath to antenna ratio goes to one on both halves of the antenna. Since the sheath size is small throughout the antenna length, the contribution for these voltages to the total sheath charge is negligible. [The concept of applying a bias equal to $\pm\underset{\sim}{v} \times \underset{\sim}{B}.\underset{\sim}{l}$ between a satellite and each half antenna in order to reduce sheath sizes near the satellite was suggested by Osborne and Kasha (1967) of RCA and this provision is incorporated on ISIS II.] Appreciable charges occur for high voltages with corresponding sheath radii of tens of cms. When V_s is positive, the sheath is located mainly on the left hand side; when V_s is negative, it flips to the right hand side. Over a cycle, the sheath is located half the time on one side and the other half, on the other side. The slopes in these curves are obviously due to the $\underset{\sim}{v} \times \underset{\sim}{B}$ effect.

The charge per unit length, as given in Eq. (8), is next plotted in Fig. 4. Positive charge per unit length always occurs for voltages above -10.4 on the left hand side. For lower voltages, negative charge is allowed to accumulate on this side. Positive charge per unit length always occurs for voltages below -10.4 on the right-hand side and negative charge is allowed for higher voltages. The total charge at the feed terminals, Q, is obtained by subtracting left from right hand net integrated charge.

In Fig. 5, we give Q and in addition its derivative dQ/dV and the resistive current I at the feed terminals. There is nearly a doubling of the slope of Q near the $-\underset{\sim}{v} \times \underset{\sim}{B}.\underset{\sim}{l}$ voltage, and this accounts for the peak in dQ/dV. This peak also causes a "spike" like behaviour in the displacement current (see Eq. (10)), as shown in Fig. 6.

Fig. 6 contains our final results. We assume a cosine waveform for V_s and display the resultant normalized waveforms of Q, and the resistive and displacement components of I. The normalizing constants are given above

the figure. The resultant waveforms are displaced by the $\underset{\sim}{v} \times \underset{\approx}{B} \cdot \underset{\sim}{l}$ equivalent phase. The charge approximates most closely a cosine form. Next the resistive current is most closely related. Both have their negative part chopped. The displacement current is most different, with a spiky behaviour near its maxima. Obviously the average of V_s times I displacement is zero indicating zero net power for this lossless capacitor. [Losses can conceivably occur due to the alternate collapsing of sheaths on each side which may generate an accoustic wave.] The average of V_s times I resistive obviously gives net power dissipation. Using Eq. (6), we derive an average conductance equal to 2.51×10^{-4} mhos. The average of V_s times Q gives average work done and using Eq. (12), the average capacitance turns out to be 3.86×10^{-9} farads for a peak voltage feed of 80V.

CONCLUSION

We have performed what seems to be the first non-linear calculation on average sheath conductance and capacitance of an uninsulated dipole antenna operating at high voltage.

ACKNOWLEDGEMENT

This work was partially sponsored by RCA, Defence Electronic Products, under IR&D funds, Project V001, and partially supported by the Defence Research Establishment, Ottawa, Canada under DIR Project E115, DRB Grant No. 5501-56.

REFERENCES

Aggson, T.L. and C.A. Kapetanakos (1966), NASA Goddard Space Flight Center Report X-612-66-380, August.

Bourdeau, R.E., J.L. Donley, G.P. Serbu and E.C. Whipple, Jr., (1961), J. Astron. Sci., 8, 65.

Crawford, F.W. and R.F. Mlodnosky, (1964), J. Geophys. Res. 69, 2765.

Grard, R.J.L. (1965), Stanford Electronics Lab., Stanford Un., Stanford, Calif., Report No. SU-SEL-65-102, December.

Grard, R.J.L. and J.K.E. Tunaley (1968), Annales de Geophysique, 24, 1.

Johnston, T.W. in M.A. Kasha, J.V. Gore, D.H. McKay and T.W. Johnston (1969), RCA Res. Report 7-801-80, Chapter 6, August.

Koons, H.C., D.A. McPherson and W.B. Harbridge (1970), J. Geophys. Res. 75, 2490.

Langmuir, I., and H. Mott-Smith, Jr., (1924), General Electric Review 17, 449.

Langmuir, I., and K.B. Blodgett (1923), Phys. Rev. 22, 347.

Mlodnosky, R.F. and O.K. Garriott, (1962), Proc. Int. Conf. on the Ionosphere, Inst. Phys. and Phys. Soc., London, p. 484.

Osborne, F.J.F., and M.A. Kasha (1967), Can. J. Phys. 45, 263.

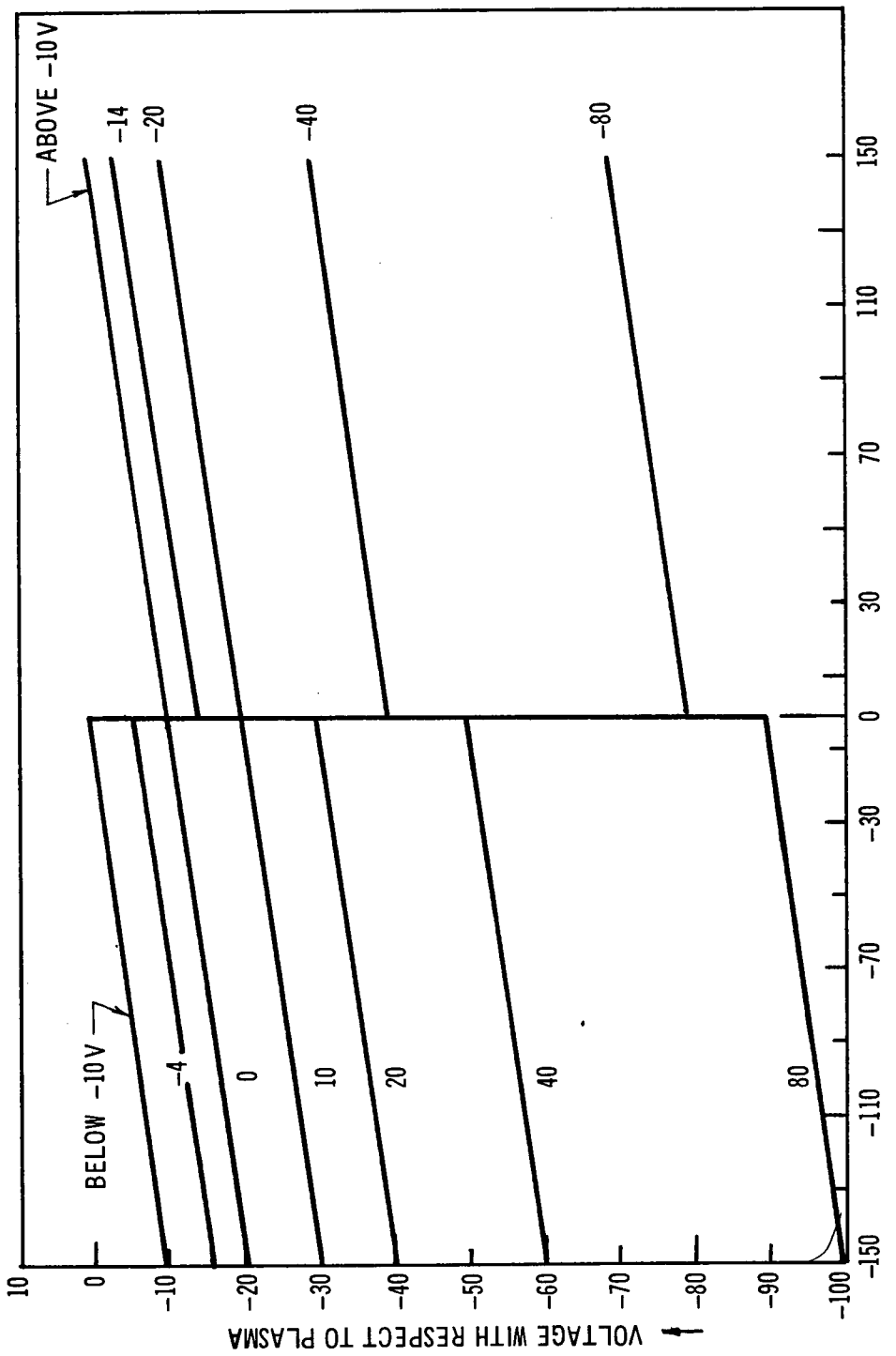

Figure 1 – Voltage distribution along the antennas

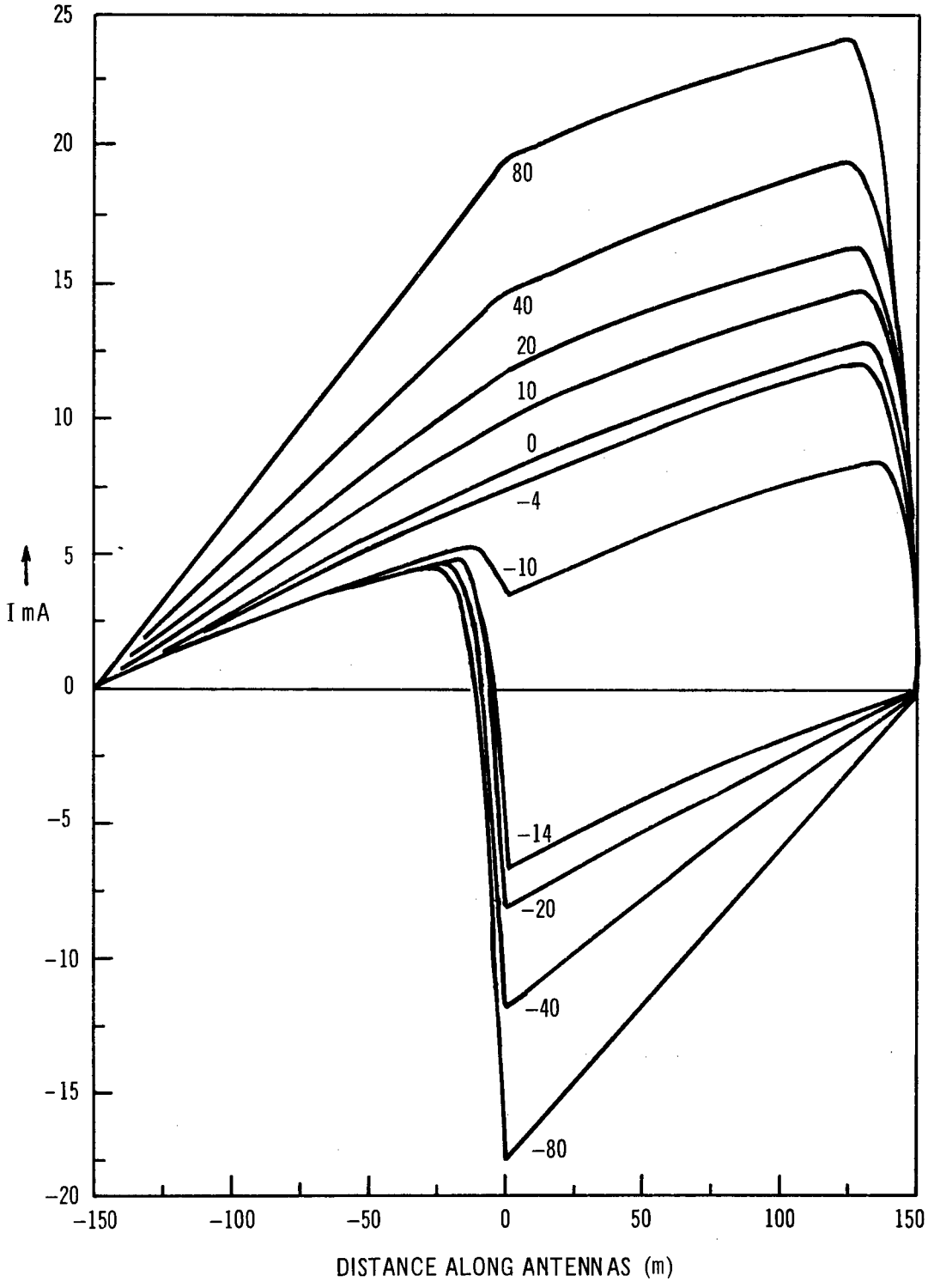

Figure 2 – Integrated resistive current distribution along the antenna for voltages between +80 and −80 volts

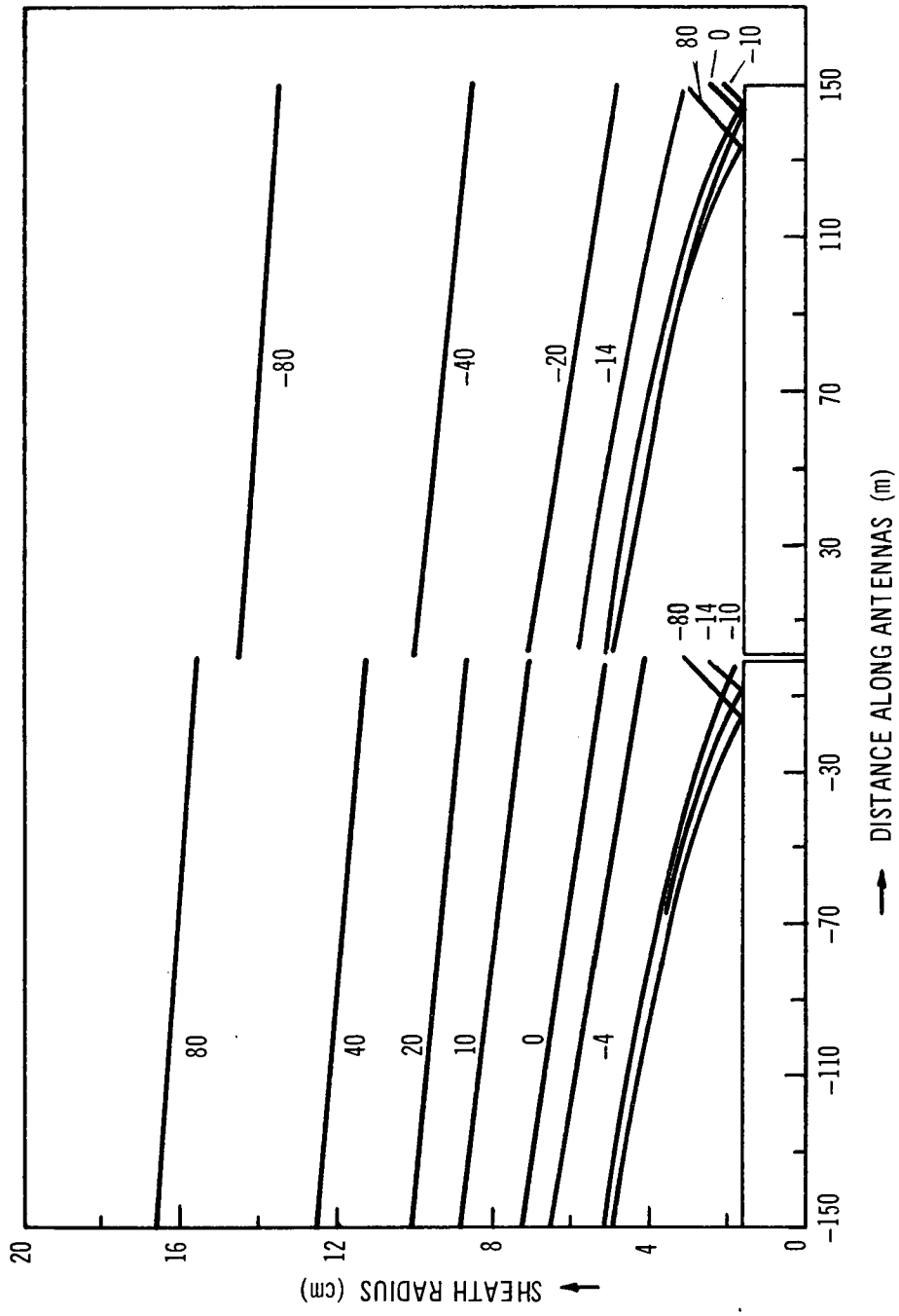

Figure 3 – Sheath sizes along the antenna for voltages between +80 and −80 volts

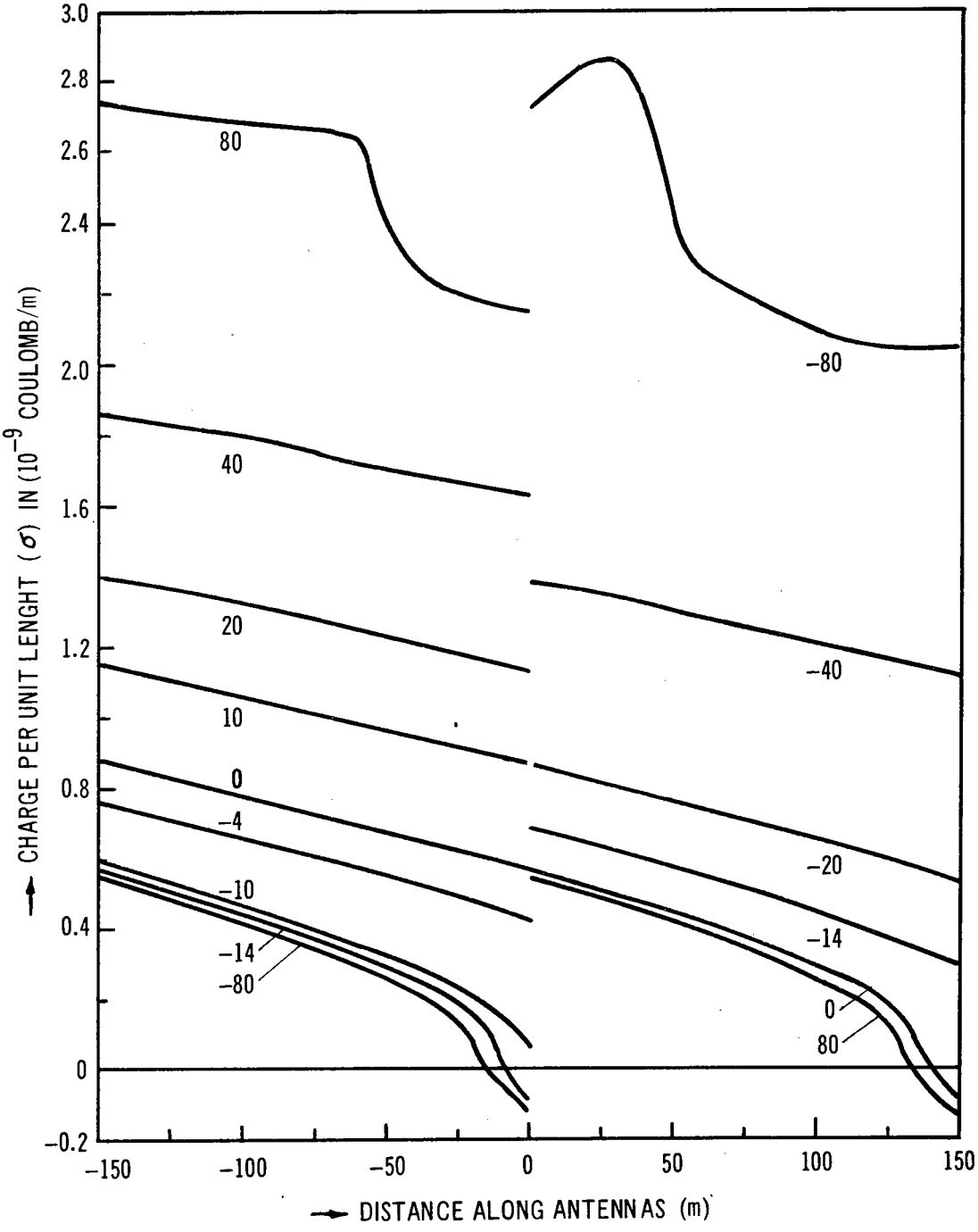

Figure 4 – Distribution of charge per unit length along the antenna for voltages between +80 and −80 volts

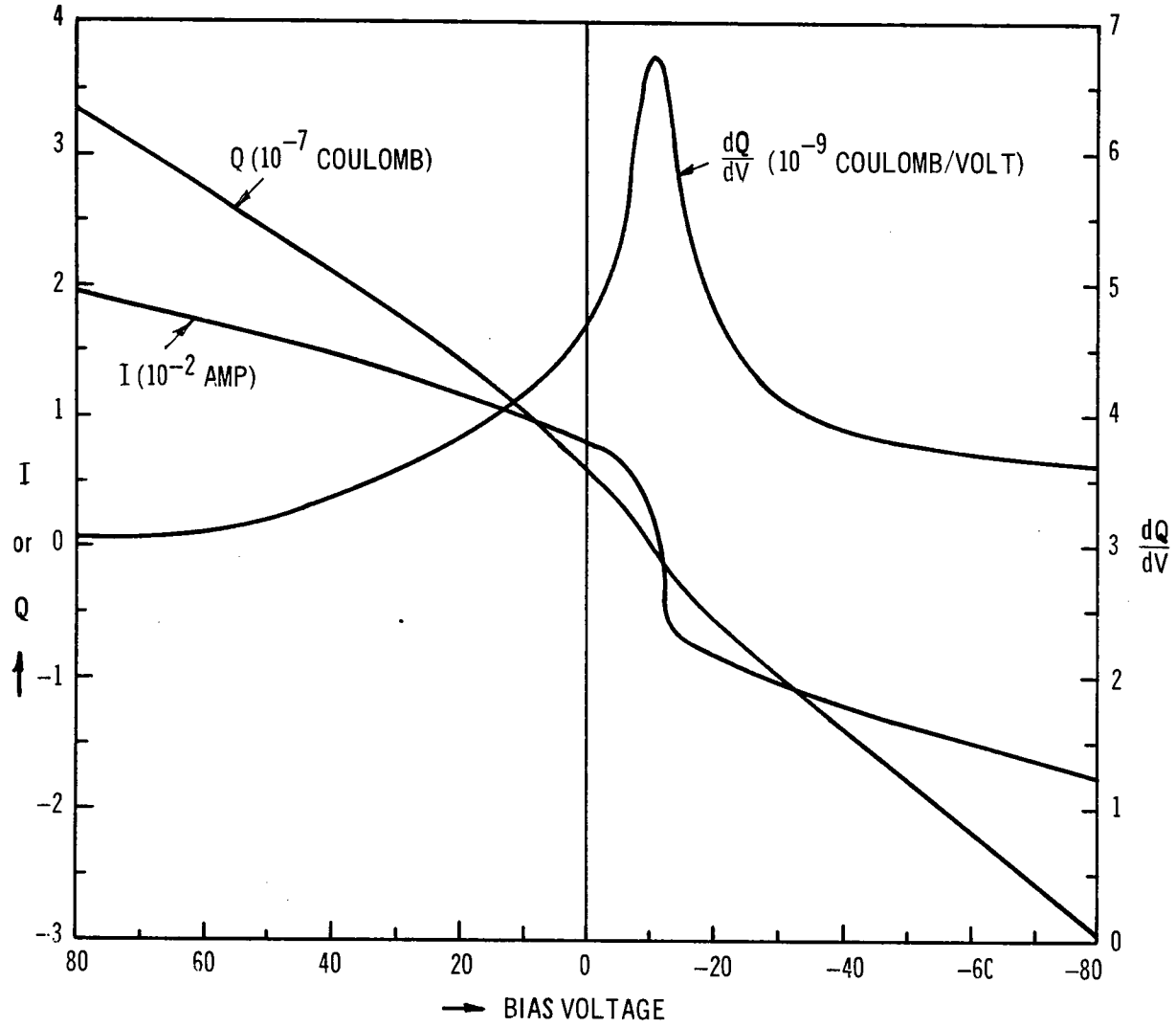

Figure 5 – Values at the antenna feed points of integrated resistive current, integrated charge and its derivative with respect to voltage for voltage bias between +80 and –80 volts

V_{max} = 80 Volt; Q_{max} = 3.33×10^{-7} coulomb;
$I_{resistive\ max} = 1.95 \times 10^{-2}$ amp;
$I_{displacement\ max} = \omega \times 5.4 \times 10^{-7}$ amp

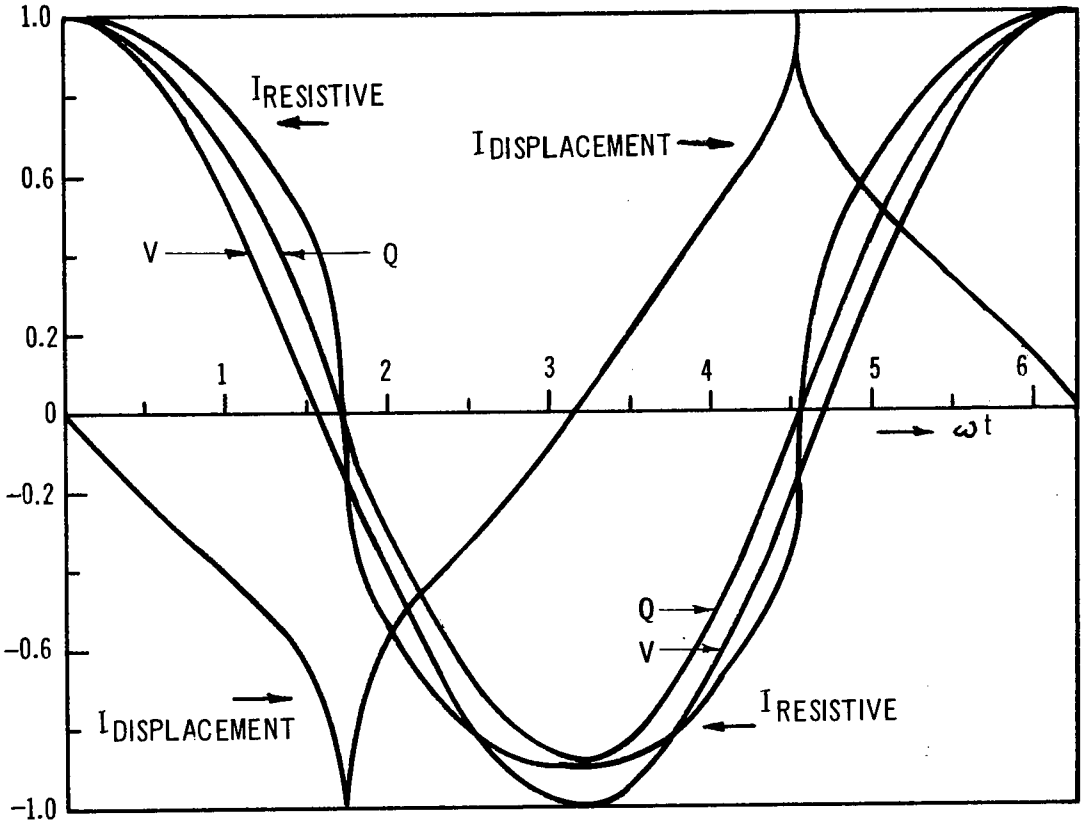

$G_{av} = 2.51 \times 10^{-4}$ mho
$C_{av} = 3.86 \times 10^{-9}$ farad

Figure 6 – Wave forms of the resistive and displacement currents and charge at the feed points for an applied cosine voltage wave form for a peak voltage of 80 volts

TECHNIQUE FOR THE COMPUTATION OF ELECTRICAL CHARACTERISTICS AND SHEATH STRUCTURE OF A LONG ANTENNA IN THE IONOSPHERE

Lee W. Parker
Mt. Auburn Research Associates, Inc.
Cambridge, Massachusetts 02139

and

Elden C. Whipple, Jr.
ESSA Research Laboratories
Boulder, Colorado 80302

ABSTRACT

A numerical method is outlined for the self-consistent solution of the Vlasov and Poisson equations in the case of a long cylindrical antenna moving rapidly through the ionosphere plasma across the geomagnetic field lines. The problem is considered in the frame of reference moving with the antenna. In this frame the Vlasov equation is solved to obtain ion and electron densities and currents by following trajectories backward in time to their points of origin. The boundary conditions for the Poisson equation include a uniform (induction) electric field at infinity and a potential jump between sections of the antenna. A suitable three-dimensional grid defines the electrostatic potential and space charge distributions. The solution of a nonlinear system of difference equations centered on the grid points is obtained by an iteration process, yielding the sheath structure. The net surface charge on and current flow into any section of the antenna may be computed as a function of the potential jump, leading to the antenna impedance. No numerical results are given.

I. INTRODUCTION

The low-frequency impedance or admittance of an antenna immersed in a plasma may be determined theoretically by considering its current-versus-voltage and charge-versus-voltage characteristics under static*conditions [Mlodnosky and Garriott, 1963]. This is related to the theory of the electrostatic probe. Since the calculation of these characteristics involves the simultaneous solution of the Boltzmann equation for both ions and electrons and the Poisson equation, subject to boundary conditions in three dimensions, any analytical approach must rely on enormously simplifying special assumptions. However, the availability of present-day computer facilities makes feasible numerical approaches which have the advantage of applicability to rather general problems. One such problem is that of a long antenna moving rapidly in the ionosphere. This problem is complicated, not only because of the existence of a wake, but also because a large potential drop would be induced by the crossing of geomagnetic field lines (unless the antenna is aligned with the field).

We formulate here a method for the exact numerical calculation of the electrical characteristics and sheath structure of a long antenna in the ionosphere ("long" in the sense that the induction potential drop is important). We consider a static situation at altitudes such that collision effects are negligible. Thus, the Boltzmann equation is replaced by the steady-state Vlasov equation. In particular, the ion and electron densities at any point in the sheath are to be evaluated by detailed Lorentz-force trajectory calculations, using the technique of following trajectories backward in time (for static* or quasi-static*problems such that the transit time for ions is small compared with a time-interval in which the fields change significantly). This technique was developed in order to evaluate the moment integrals for particle density and current density, and is especially useful for arbitrary particle energy distributions [Parker, 1966].

*Steady state

The evaluation of the ion and electron density (or current density) at a point by following trajectories is in effect a process for solving the Vlasov equation when the electric and magnetic fields are given. We call this the "Vlasov problem." The electrostatic potential distribution is, on the other hand, the solution of the Poisson equation when the ion and electron density distributions are given. (The perturbation of the magnetic field due to particle currents is assumed negligible.) Since both the electric field and charge densities are unknown and must be self-consistent, we employ an iteration method for computing the sheath structure. One cycle of the "Poisson-Vlasov" iteration consists of solving the Vlasov problem to obtain the ion and electron density distributions with an assumed potential distribution, and then obtaining a new potential distribution from the solution of the Poisson problem. Probably the earliest self-consistent calculation with iteration in more than one spatial dimension, in which both ion and electron trajectories were followed, was that of Parker [1966] for a flush-mounted probe.

The problem of interest here is that of a dipole antenna of length L and radius a. The two segments are assumed to be connected through a voltage generator which produces a potential jump [Mlodnosky and Garriott, 1963]. It is convenient to consider first a single long cylinder moving perpendicular to its axis with velocity v_o and perpendicular to a magnetic field of intensity B_o in a plasma, as illustrated in Fig. 1. We solve the self-consistent Poisson-Vlasov problem subject to the boundary conditions that the potential vanish at infinity and have the proper variation on the cylinder. For numerical purposes the system is put inside a large box the walls of which represent "infinity." We then compute the ion and electron currents to the cylinder and obtain the net current corresponding to a mean potential V_o. This gives one point on the current-voltage characteristic. The actual floating potential is that for which the net current vanishes. In Fig. 1 the polarization charge separation set up by the v x B induction is indicated. The external plasma space charge density is

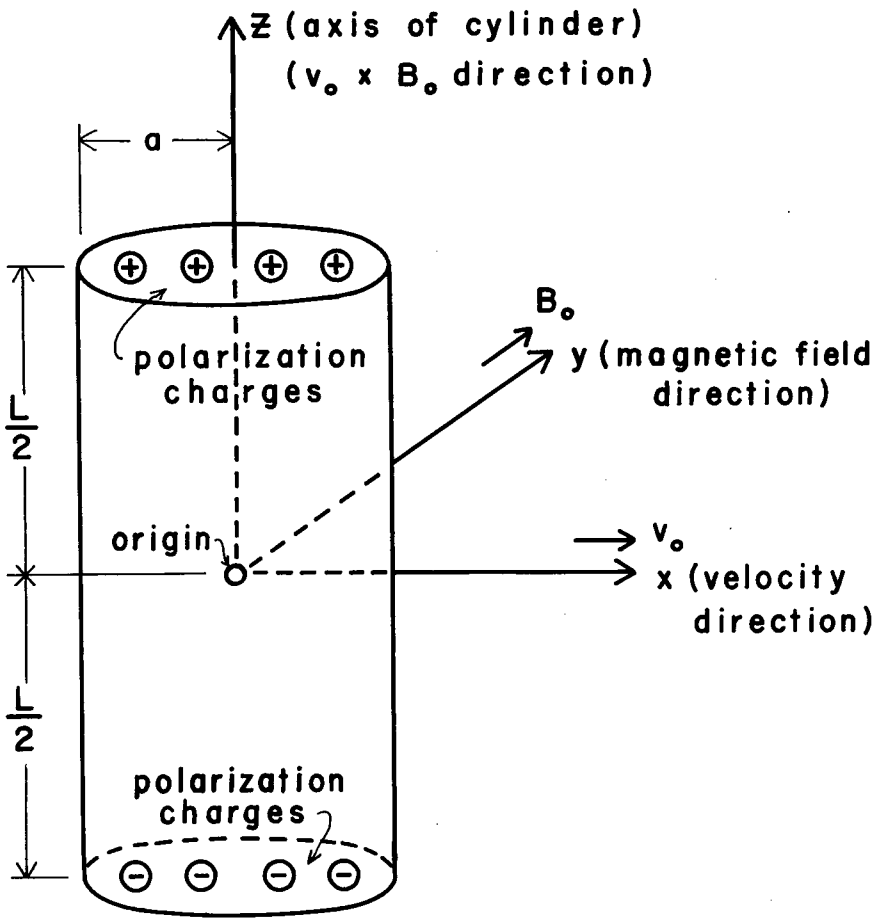

Fig. 1 Geometry of moving cylinder in magnetic field

not shown but would not qualitatively change the picture. The assumption of mutually orthogonal velocity, magnetic field, and axial vectors is not essential. The numerical method to be employed can include arbitrary orientations.

In Sec. II we define the boundary conditions for the frame of reference moving with the cylinder. We then show how the dipole problem is related to the single-cylinder problem. In Sec. III the numerical grid and the trajectory calculations are discussed. In Sec. IV integrals for density and current are presented which go over into quadrature sums over trajectories. In Sec. V the difference analogue of Poisson's equation is discussed, where the charge density consists of the combined ion and electron quadrature sum values. In Sec. VI the iteration method for obtaining self-consistency is presented. We have applied the procedures to be described in the following sections to the case of a probe flush-mounted on a satellite* [Parker, 1966; Parker, 1968; Parker and Whipple, 1967, 1970; Whipple and Parker, 1969a, 1969b]. Sec. VII deals with antenna impedance.

II. BOUNDARY CONDITIONS IN CO-MOVING FRAME

The usual frame of reference is the "laboratory" frame in which the magnetic field is stationary. In this frame, illustrated in Fig. 2, for a single cylinder with no jump in potential, the cylinder surface has a linear potential variation along the side, and the potential V vanishes at infinity (grid boundary). V_o denotes the mean value of the potential. The surface charge produces a uniform field inside the cylinder (opposing the magnetic induction field). The dotted lines outside the cylinder indicate the electric field structure in the absence of plasma (the "Laplace-field problem"). The axis of the cylinder is in the z-direction, the magnetic field B_o is in the y-direction, and velocity v_o is in the x-direction ($v_o \ll c$).

It is more convenient for following trajectories backward in time to be in the (co-moving) frame of reference moving with the

* neglecting magnetic field

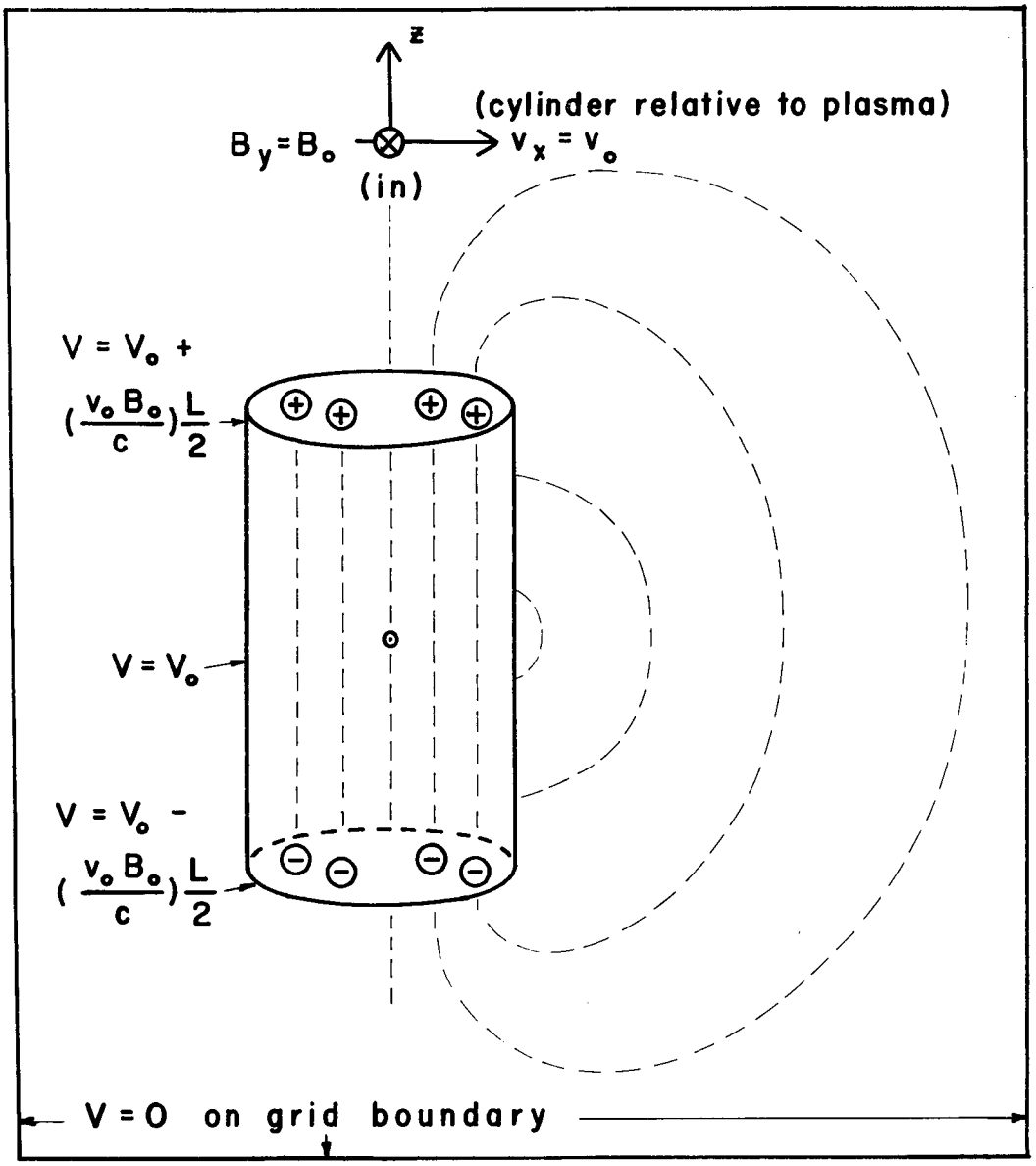

Fig. 2 Laboratory frame boundary conditions

cylinder. The electric field is transformed such that it vanishes inside the cylinder and is imposed as a boundary condition at infinity, as indicated in Fig. 3. The system is effectively put inside a giant condenser, with a stationary magnetic field. The (Laplace) electric field structure is now as shown. The boundary condition of a uniform electric field at infinity of magnitude $v_o B_o/c$ is expressed in terms of the normal derivative of V on the grid boundary.

The dipole problem is a generalization of the single-cylinder problem. There are two essential distinctions between the two problems. One of these distinctions is that in the dipole problem there is a jump in potential at the point where the two sections are joined. The other distinction is that the net current must be considered separately for each section. The distribution of voltages and currents is illustrated in Fig. 4, where the two sections are labelled (1) and (2). The upper portion of the figure shows how the surface voltages change in going from the laboratory frame to the co-moving frame, in the case where there is no voltage jump. The currents I_1 and I_2 denote the net current entering sections (1) and (2), respectively. The current $I_o = I_1 = -I_2$ is defined to be the current passing from section (1) to section (2) (through a generator, which is not shown) when there is no voltage jump produced by the generator. The potential V_o is assumed to be the floating potential. If the generator produces a small voltage jump dV, then an additional current dI flows through the generator, as shown in Fig. 4. In the co-moving frame, the changes in the potentials on the sections are dV/2 and -dV/2, for a symmetric dipole. This assumes that dV is small [Mlodnosky and Garriott, 1963]; for arbitrary values of dV, the voltage partitioning would be in general unsymmetric. Thus, the dipole problem computationally may be considered to be a special case of a single-cylinder problem with an arbitrary surface potential distribution, including an arbitrary jump, which can be handled by the method of the following sections.

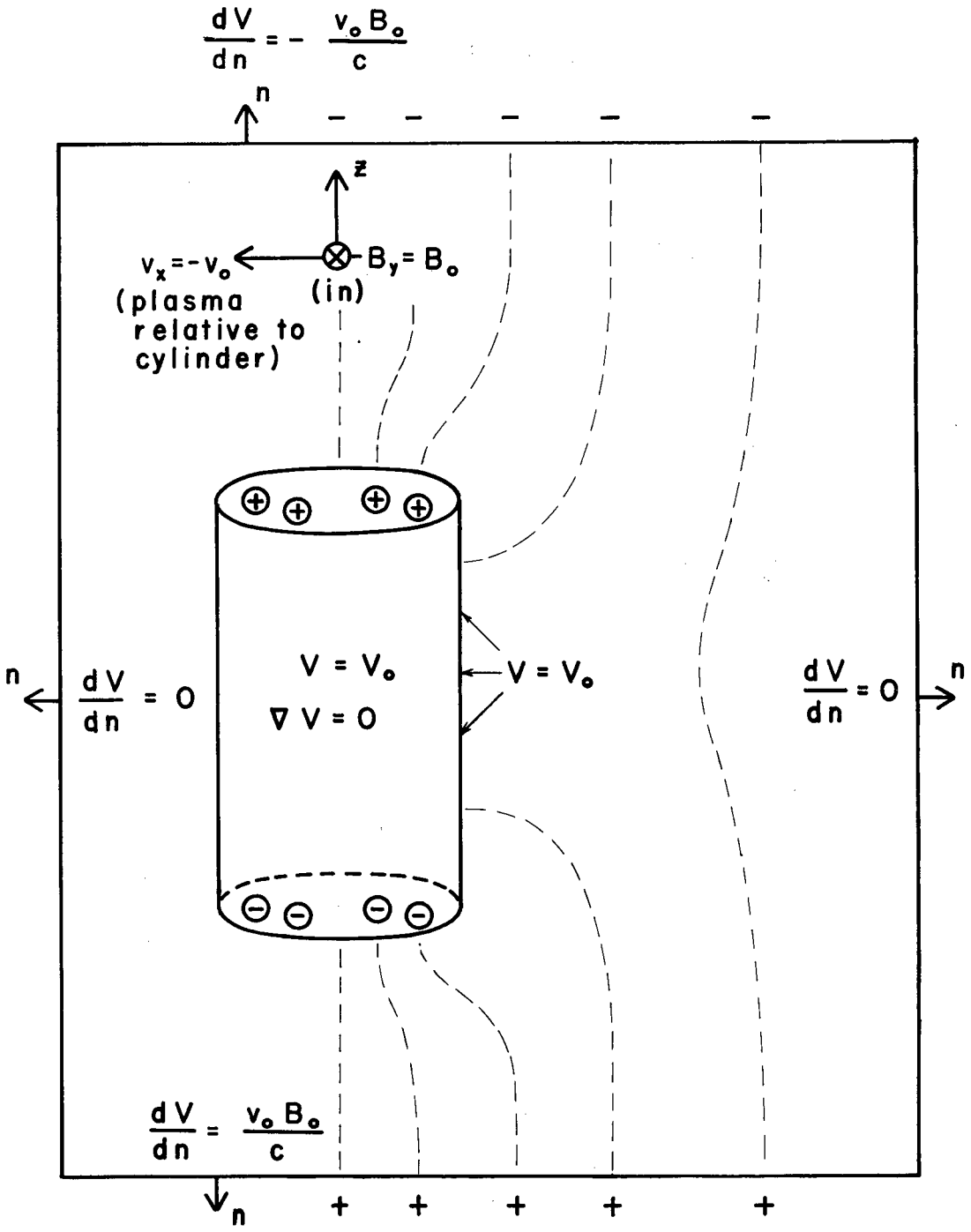

Fig. 3 Co-moving frame boundary conditions

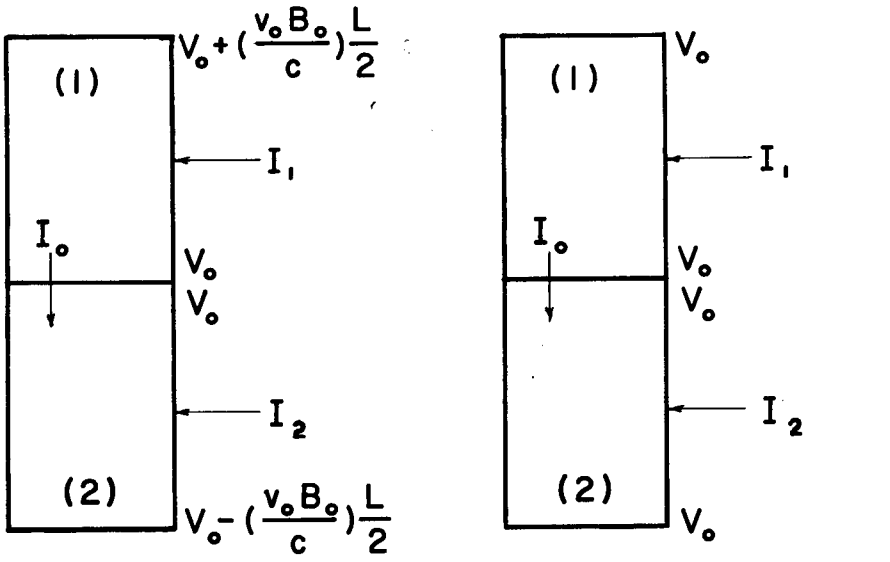

LAB FRAME

CO-MOVING FRAME

$$I_1 + I_2 = 0$$

$$I_o = I_1 = -I_2$$

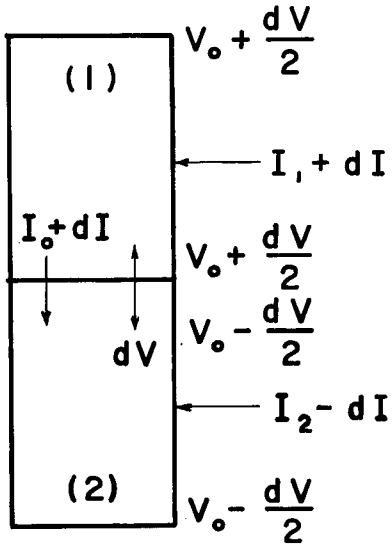

Fig. 4 Dipole antenna currents and voltages

III. NUMERICAL GRID AND TRAJECTORIES

The cylinder is put inside a large cylindrical box which is subdivided by surfaces of constant r, constant θ, and constant z, where r, θ, and z are cylindrical polar coordinates, as in Fig. 5. The cylinder surface coincides with grid surfaces of constant r and z, and is defined by the heavy lines. The electrostatic potential distribution is defined by values at the nodes or grid points. The cylinder radius is a and the grid boundary radius is r_m. The problem is symmetric about the plane of v_o and z, as shown. With the potentials given at the grid points, the ion or electron density at one of these points, say at $\vec{r}$ in Fig. 6, is computed by considering all possible trajectories through the point $\vec{r}$. (Actually a finite number is used, corresponding to the numerical quadrature discussed below.) One of these trajectories, defined by the local velocity vector $\vec{v}$, is followed backward in time to see whether it comes from the cylinder ("non-contributing" in Fig. 6) or from the grid boundary ("contributing" trajectory from infinity), where it has the velocity $\vec{v}_\infty$. The equations of motion under the Lorentz force

$$\frac{d\vec{v}}{dt} = \frac{e}{m}\left(-\nabla V + \frac{\vec{v}}{c} \times \vec{B}_o\right) \qquad (1)$$

are integrated numerically to trace out the trajectory. At each step the components of the potential gradient ∇V are obtained by interpolation among the values of V at the neighboring grid points.

IV. EVALUATION OF DENSITY AND CURRENT

Assume that the unperturbed velocity distribution at infinity is a Maxwellian of temperature T with drift $\vec{v}_o$, for both ions and electrons. The density at a point (r,θ,z) may be expressed in the dimensionless form

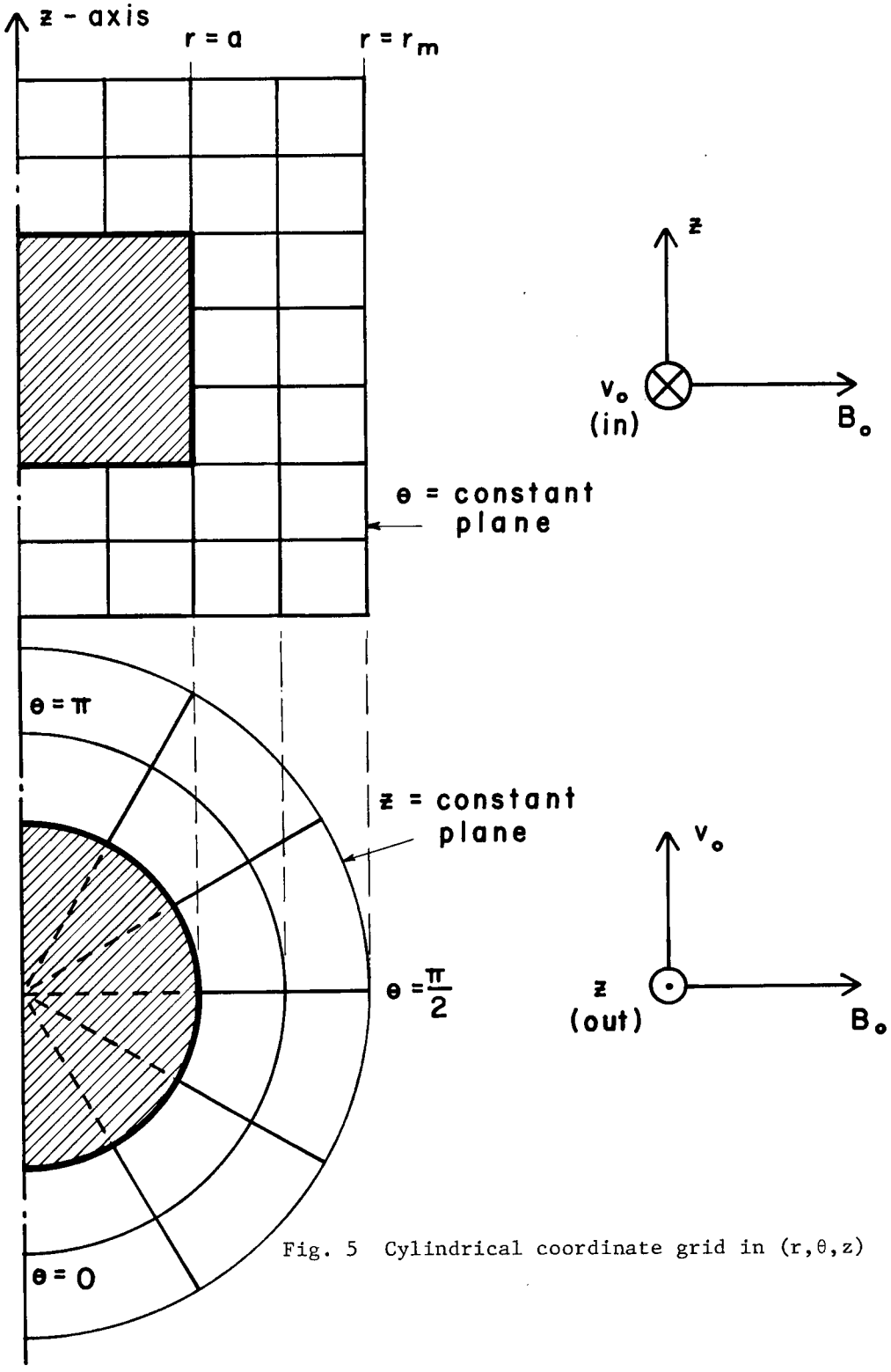

Fig. 5 Cylindrical coordinate grid in (r,θ,z)

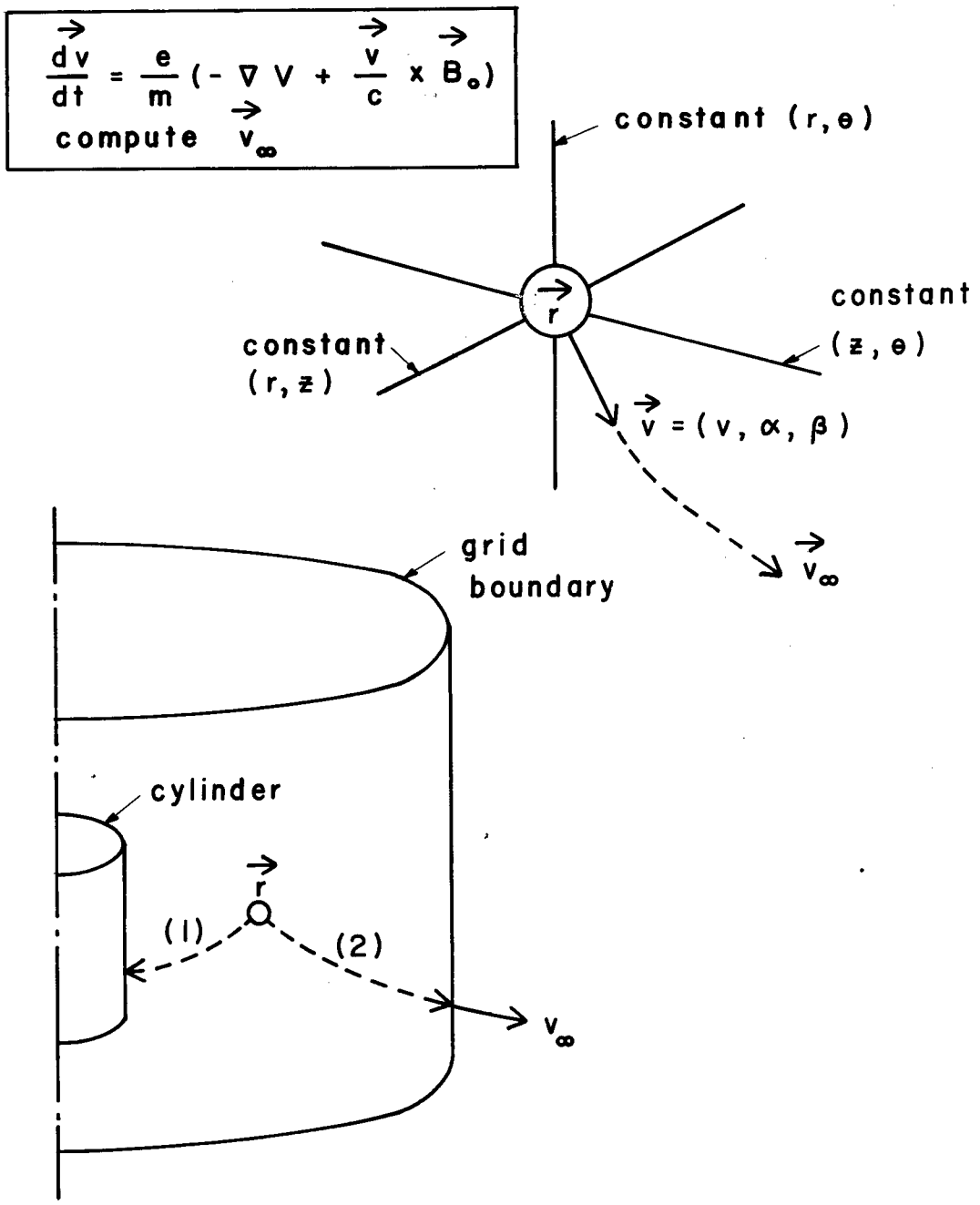

(1) non-contributing trajectory

(2) contributing trajectory

Fig. 6 Trajectories through grid point $\vec{r} = (r,\theta,z)$
Local velocity coordinates (v,α,β)

$$n(r,\theta,z) = \frac{2n_o}{\sqrt{\pi}} \int_{\mathrm{Max}(\phi,0)}^{\infty} dE\ (E-\phi)^{\frac{1}{2}} \iint \delta e^{-u^2} \frac{\sin\alpha\ d\alpha\ d\beta}{4\pi} \qquad (2)$$

where n_o is the density at infinity, and

$$u^2 = E + M^2 - 2ME^{\frac{1}{2}} \cos(\vec{v}_\infty, -\vec{v}_o) \qquad (3)$$

$$E = \frac{mv_\infty^2}{2kT}, \quad M^2 = \frac{mv_o^2}{2kT}, \quad \phi = \frac{eV}{kT} \qquad (4)$$

The angles α and β denote the polar and azimuthal angles for the local velocity vector $\vec{v}$ (Fig. 6). The lower limit on the energy integral is ϕ if $\phi > 0$, and 0 if $\phi < 0$. The factor δ is unity or zero according as the trajectory is contributing or non-contributing (Fig. 6). If it is contributing, the cosine of the angle between $\vec{v}_\infty$ and $-\vec{v}_o$ is employed in (3) to determine the "weight" function $\exp(-u^2)$. The quantity M is the "Mach number." The triple integral (2) may be approximated by a quadrature sum.

The current density at a point (θ,z) on the cylinder side r=a, or at a point (r,θ) on the cylinder end, may be expressed in the dimensionless form

$$j = n_o \sqrt{\frac{kT}{2\pi m}} \int_{\mathrm{Max}(\phi,0)}^{\infty} dE\ (E-\phi) \iint \delta e^{-u^2} \frac{\sin\alpha\ \cos\alpha\ d\alpha\ d\beta}{\pi} \qquad (5)$$

where the various quantities are defined as for (2). The total current is defined by the integral over surface area, comprised of contributions from the cylinder side and ends. These may be expressed as

$$I_{side} = a \iint j(\theta,z)\ d\theta\ dz, \quad I_{end} = \iint j(r,\theta)\ r dr d\theta \qquad (6)$$

The approximation of the foregoing integrals by quadrature sums may be made as in Parker [1968, Ch. V]. The space charge density at a grid point to be used on the right-hand side of the Poisson equation (next section) is obtained by applying (2) first to the ions, and then to the electrons, and subtracting the results.

V. THE POISSON MATRIX EQUATION

The solution of the Poisson problem consists of solving for the potentials at the grid points when the charge density values $\rho(r,\theta,z) = e(n_i - n_e)$ are given at the grid points. In order to obtain a symmetric matrix for the difference form of the Laplacian operator, we apply the Gauss theorem to a box surrounding a grid point, namely,

$$\underset{\text{(box volume)}}{\iiint} \nabla^2 V d\tau = \underset{\text{(box surface)}}{\iint} \frac{\partial V}{\partial n} d\Sigma = -4\pi \underset{\text{(box volume)}}{\iiint} \rho d\tau \qquad (7)$$

where $d\tau$ is a volume element and $d\Sigma$ a surface element. The box is bounded by surfaces of constant r', r", θ', θ", z', and z", as illustrated in Fig. 7. The second equation in (7) may be expressed as

$$A''_z \left(\frac{\partial V}{\partial z}\right)_{z''} - A'_z \left(\frac{\partial V}{\partial z}\right)_{z'} + A''_r \left(\frac{\partial V}{\partial r}\right)_{r''} - A'_r \left(\frac{\partial V}{\partial r}\right)_{r'}$$

$$+ A''_\theta \left(\frac{1}{r}\frac{\partial V}{\partial \theta}\right)_{\theta''} - A'_\theta \left(\frac{1}{r}\frac{\partial V}{\partial \theta}\right)_{\theta'} = -4\pi\tau\rho(r,\theta,z) \qquad (8)$$

where τ is the volume of the box. The A's are the areas of the various surfaces and the expressions in parentheses represent average values of $\partial V/\partial n$ (normal component of gradient) for those surfaces. In practice these average values are taken to be simply the difference of two adjacent potentials divided by the distance between the corresponding grid points. This formulation is convenient for the boundary

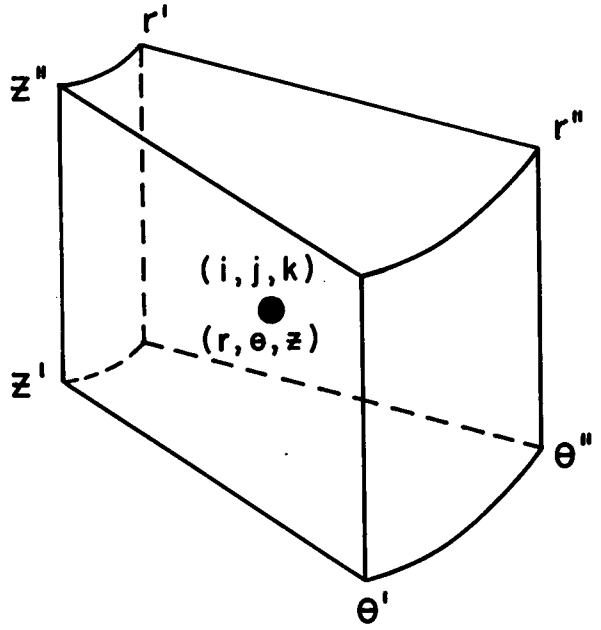

Fig. 7 Geometry for difference equations

conditions of Fig. 3, since for a grid point on the boundary the appropriate term in (8) becomes a given constant [Parker, 1968, Appendix A].

The difference form of (8) constitutes a set of linear equations for the potentials at the grid points. Let V_{ijk} denote the value of the potential at the (i,j,k)-th grid point, and let the constant terms of the (i,j,k)-th equation be lumped into a single constant on the right-hand side denoted by F_{ijk}. Then the system may be expressed in the matrix form

$$L\vec{V} = \vec{F} \tag{9}$$

where $\vec{V}$ and $\vec{F}$ are vectors whose components are the values of V_{ijk} and F_{ijk}, respectively. The Laplacian operator L is a matrix which may be partitioned in block-tridiagonal form. The most common method for solving these equations is that of iteration, for example, by point successive over-relaxation. We designate the iteration employed for these linear equations as the Poisson "inner iteration" to distinguish it from the Poisson-Vlasov "outer iteration" to be discussed in the next section, which deals with the self-consistent solution of the complete non-linear problem.

VI. POISSON-VLASOV ITERATION

Finally, the Poisson (potential output) and Vlasov (charge density output) calculations are successively cycled by successive substitution. If the procedure converges, a self-consistent solution is obtained. The method employed by Parker [1968, Appendix D] introduces a relaxation parameter α which provides artificial damping in the Poisson-Vlasov iteration. Thus, a sequence of linear equations of the form of (9) are solved successively according to the scheme

$$L\vec{V}^{n+1} = \vec{R}^{n+1} = \alpha\, \vec{F}^{n} + (1 - \alpha)\, \vec{R}^{n} \tag{10}$$

where n is the iteration number, $\vec{V}^n$ is the n-th iterate for $\vec{V}$, $\vec{F}^n$ is comprised of the results of the Vlasov calculation with the potential vector $\vec{V}^n$, and $\vec{R}^n$ is an auxiliary right-hand side vector which is a linear combination of all previous $\vec{F}^n$ iterates. When α is small, the earlier iterates are weighted more heavily than the most recent. This provides damping in a sequence of solutions which would tend to diverge as a function of n (with oscillations of increasing amplitude). It can be shown that the tendency for the iteration to diverge (instability) depends on the boundary condition and the dimensions of the boundary of the grid in Debye lengths [Parker and Sullivan, 1969]. When the size of the grid is large, α must be made small for convergence, but this entails many iterations. When α is unity, (10) corresponds to the ordinary Picard method of successive substitutions. The iteration is usually begun by solving the Laplace problem $L\vec{V}^o = \vec{F}^o_o$ for $\vec{V}^o$, where $\vec{F}^o_o$ is the constant vector corresponding to zero charge density. Convergence of the iteration yields the desired self-consistent solution and thus the sheath structure.

VII. ANTENNA IMPEDANCE

Once the solution has been obtained, one may find the net current I into any section of the cylinder through the surface integrals given by (6). The total surface charge Q on any section is a surface integral where the integrand is proportional to the normal component of the potential gradient. Thus, through integrals similar to (6) we have contributions from the side and ends as follows:

$$Q_{side} = -\frac{a}{4\pi}\int\int \frac{\partial V}{\partial r}\, d\theta dz, \quad Q_{end} = -\frac{1}{4\pi}\int\int \frac{\partial V}{\partial z}\, r\, dr d\theta \qquad (11)$$

The impedance at the terminals of a dipole antenna is computed by solving the Poisson-Vlasov problem for the increments in I and Q resulting from changes in applied voltage [Mlodnosky and Garriott, 1963].

REFERENCES

Mlodnosky, R. F., and O. K. Garriott, The VLF admittance of a dipole in the lower ionosphere, Proceedings of the International Conference on the Ionosphere, London, July 1962, p. 484, The Institute of Physics and the Physical Society, London, 1963.

Parker, L. W., A computer program for calculating the charge distribution about a space vehicle, NASA Report CR-401, March 1966.

Parker, L. W., Theory of the circular planar (guardring) Langmuir probe, ESSA Technical Report ERL-100-AL2, 1968. (Available upon request.)

Parker, L. W. and E. C. Whipple, Jr., Theory of a satellite electrostatic probe, Ann. Phys., 44, 126, 1967.

Parker, L. W. and E. C. Whipple, Jr., Theory of spacecraft sheath structure, potential, and velocity effects on ion measurements by traps and mass spectrometers (to be published in the Journal of Geophysical Research), 1970.

Parker, L. W. and E. C. Sullivan, Boundary conditions and iterative procedures for plasma sheath problems, Rarefied Gas Dynamics, Trilling and Wachman, Eds., p. 1637, Academic Press, 1969.

Whipple, E. C., Jr. and L. W. Parker, Theory of an electron trap on a charged spacecraft, J. Geophys. Res., 74, 2962, 1969a.

Whipple, E. C., Jr. and L. W. Parker, Effects of secondary electron emission on electron trap measurements in the magnetosphere and solar wind, J. Geophys. Res., 74, 5763, 1969b.

Report of an Invited Conference on ANTENNAS AND TRANSIONOSPHERIC PROPAGATION AS RELATED TO ELF/VLF DOWNLINK SATELLITE COMMUNICATIONS

at Naval Research Laboratory, Washington, D. C.

June 8 - 10, 1970

T. W. Johnston
Department of Physics
University of Houston

SUMMARY

The Conference discussion indicated a need for further work in the following areas:

a. Dipole moment of actual antenna sheath.

b. Effect of ion sound plasma kinetic linear response to electric dipole excitation.

c. Laboratory experiment to check basic theory of antenna in magnetoplasma.

d. Spacecraft experiments including impedance, waveform, near field study, ground/spacecraft reciprocity.

INTRODUCTION

The general import of the conference was given by the preliminary announcement.

In more specific terms the apparent intent was to record the consensus on the technical problems and appropriate investigations for determining the feasibility of a satellite-to-ground VLF system.

The sponsors hoped that by letting those skilled in the arts involved in predicting the ground reception of signals from VLF satellite sources to come together and interact for three days and by listening carefully to the discussions (including taping the working group interchanges), a coherent picture of the accomplishments, failures, and problem areas would emerge. From this writer's point of vantage the technical situation did become fairly well defined and this will be summarized below.

Questions were asked about the kind of experiments that should be done to test the feasibility of the concept, but lacking any indication of mission requirements and payload or schedule constraints,

the answers were automatically extremely vague and no explicit consensus was reached on a program. For this reason the programs sketched below are simply those which seemed reasonable to the author in the context of the meeting.

TECHNICAL PROBLEMS

The technical approaches to the problem can be conveniently organized as shown in Fig. 1.

THEORY

Although much has been done on the small signal linear theory of waves in plasmas, with or without sources, attempts to run systems at quite modest power levels will usually result in nonlinear effects since the energy of electrons in the ionosphere plasma is typically only 0.25 eV. There is no theory developed for antennas in even the simplest isotropic nonlinear medium. The current approach is to use nonlinear theory close to the antenna (A,B in Fig. 1), to develop linear antenna theory (C) and ionosphere transmission theory (D) and use the former as a source for the latter. There are no conceptual problems with (A) spacecraft engineering or (D) wave transmission, but (B) and (C), the sheath-to-whistler mechanism remains, a formidable roadblock. The discussion below is limited to (B) and (C).

SHEATH/WHISTLER COUPLING THEORY

A useful model for approaching the problem of predicting whistler emission from the antenna current and charge is given in Fig. 2 which is a refinement of (B) and (C) in Fig. 1.

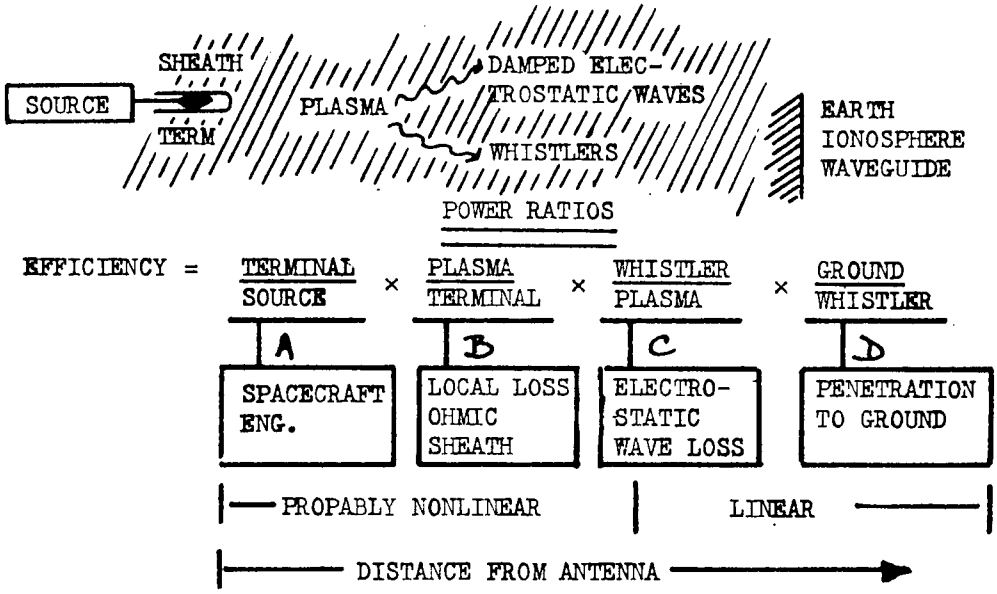

Fig. 1 - Technical Problems in VLF transmission from spacecraft to ground.

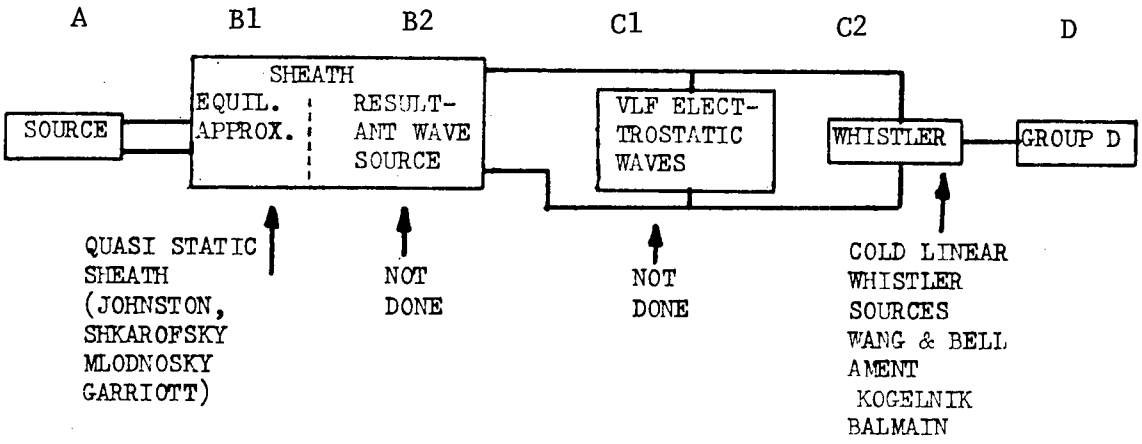

Fig. 2 - Model for VLF Exciter Analysis

Again in this diagram as in Fig. 1, considerable progress has been made in the separated problems of the equilibrium sheath (B1) (Shkarofsky and Johnston, Mlodnosky and Garriott) and the linear source in cold magnetoplasma (C2) (Wang and Bell, Ament, Kogelnik, Balmain etc.).

The equilibrium sheath model (B1) in effect implies that essentially perfect charge cancellation occurs beyond the sheath. This is a good assumption for obtaining the current-voltage characteristics of the sheath itself but would give no radiation. The radiation comes from the lag in the plasma response (B2) due to ion inertia and has yet to be calculated. This omission should be repaired even though the calculation is likely to be far harder than for the basic sheath, because the details of the sheath are now vital. This will be discussed further below under "Further Analysis".

The problem of the short source in a linear cold magnetoplasma presented difficulties at first when the current source was assumed infinitesimal but has been solved (Wang and Bell and earlier work) although the current distribution for a longer source (for which the triangular distribution approximation must fail) is not settled. The general problem of current distribution on a dipole in a birefringent and anisotropic medium is not easy but Miller has some useful results for the isotropic plasma with an infinite antenna.

At VLF frequencies, however, the plasma can also support ion sound oscillations up to roughly the ion plasma frequency. These are, in fact, the nearly shielded average density perturbations of ions and electrons together which probably constitute the main effect of an electrostatic dipole in the plasma (C1 in Fig. 2). These have not been computed at all and yet may start the encouraging emission of whistler waves. Investigation of this problem is essential.

A complication for these waves is that the ion sound wave speed is much less than the satellite speed so satellite velocity must be considered via $\delta(\omega - \underline{k}.\underline{v} - \omega_{source})$ and Doppler shift will be important. The reverse is true for whistler waves. For wave vectors nearly at right angles to the magnetic field the two waves couple near the lower hybrid frequency and can also complicate the analysis.

To sum up, there are three main theoretical problems on the sheath/whistler coupling chain where more effort is needed; in order in toward the antenna and in order of difficulty and nonlinearity, they are:

(1) The kinetic Debye shielding (ion sound) thermal plasma response to electric dipole must be included in the theory (which must now recognize source motion): cold plasma theory may well be quite misleading.

(2) The problem of a useful current distribution model for the longer antenna should be considered further (this is not so urgent, but probably can be done without an inordinate effort).

(3) The analysis of incomplete shielding of large signal nonlinear antennas should be pursued so as to establish the connection with problem (1) and complete the chain from terminal to whistler.

EXPERIMENTS

Ionosphere

Only a small number of relevant ionosphere VLF experimental results were available at the conference: LOFTI IIA, a calibration rocket experiment for ISIS I, ISIS I itself (and inferences from Alouette data), Javelin 8.45 rocket experiment, FR-1 and supporting Aerobee experiments.

The data from these is quite meagre and most conclusions must be drawn from inadequate data or the very short runs from rocket experiments.

Plasma impedance effects on the output from the coil on the short lived LOFTI IIA satellite appears to have been negligible. The 40 foot electric dipole output did show noticeable effects but not the orders of magnitude change predicted by most theories, perhaps because the ideal orientation of theory was not sufficiently accurately obtained and/or because of antenna bending from a 15 rpm spin rate.

The verbal report from the crossed dipole rocket experiments of Barrington and Palmer show transfer impedances probably characteristic of sheaths and nonlinear effects (like saturation), no noticeable lower hybrid resonance effects, and some definite orientation effects. Nonlinearity can be seen at 1 volt excitation or less on ISIS I. Some Alouette/ISIS passive VLF data indicate occasional strong orientation effects on reception.

The Iowa University experiments on floating electric dipole spheres on a satellite indicate that only the sheath impedance is measured and a crude two-station rocket experiment showed qualitatively that near field electric signals decreased faster than magnetic signals. No satellite stimulated emissions were observed (in agreement with ISIS I observations) and no lower hybrid resonance. They feel that in view of sheath problems that magnetic loops should be pursued further.

The French group under Storey have also performed several experiments aimed more at understanding the problem, detecting lower hybrid resonance phenomena, etc. than at transmission. Results from these experiments are few and indicate findings somewhat similar to the Iowa group unless the sheath is collapsed by use of electron emitters.

There are also a large number of satellite receiver experiments which report reception of ground transmitter VLF emissions on occasion and one might be tempted to draw conclusions from reciprocity. However, the plasma sheath nonlinearity is likely to result in considerable saturation and probably results in over-optimism. Also reciprocity really involves the far fields, which are not yet properly known for satellite transmitters even theoretically.

Laboratory

With the difficulty and cost of satellite experiments laboratory verification of the theory would seem worthwhile. To give any hope of simulating far field electromagnetic effects, the plasma must be large compared with c/ω_p; most plasma systems which fit this restriction are really aimed at thermonuclear fusion plasma studies and are usually short lived or unstable.

One steady state system - Tam's - was reported as suitable, but has been so far only used at higher frequencies near or above the gyro frequency and in a wide range about the plasma and upper hybrid frequency. Difficulties of end wall reflections and collisions probably prevent investigation of lower hybrid resonance effects, but the whistler region corresponding to 50-200 kHz in the ionosphere could probably be adequately investigated by using 1 GHz equipment in the system.

Near field electrostatic investigation in a smaller plasma (size $\sim c/\omega_p$) by Fisher and Gould were not discussed at the conference but are in the literature: these laboratory results are the only ones which show the $(K_\perp \cos^2\theta + K_{\parallel} \sin^2\theta)$ field pattern cone angles predicted by theory and are the only really solid confirmation of the theory.

Need for More Tests

Evidently even the theory developed so far, limited as it is to cold lossless plasmas with small stationary sources, requires more experimental checks including those in the laboratory before it can be trusted. Both single site (i.e. impedance, current waveforms at antenna) and double site (field and radiation patterns) are required. The latter

although more difficult are more essential for VLF downlink analysis and also can check theory more reliably (in the far field).

To expand on this last point: a far-field pattern feature measurement can check cold whistler emission theory even though numerical details may be incorrect due to sheaths, plasma, nonlinearities and the like. The input impedance measurement may well be quite dominated by these effects and give no guide at all to whistler radiation (see Figs. 1, 2).

FURTHER WORK

The next steps follow naturally from the summary given and are listed below.

Theory: The nonlinear sheath model should be extended to allow for ion inertia to calculate the effective dipole strength (B2 in Fig. 2). The small supersonic dipole problem should be done for the linear warm plasma with sound waves (C1 in Fig. 2).

Experiment: Any laboratory experiment that can provide confirmation of theory in the way that Fisher and Gould have for resonant angles would be invaluable since there is no other good confirmation of theory: determined efforts should be made on these lines, since quite elaborate setups impossible in spacecraft can easily be obtained.

Space: Space experiments are so expensive that one wishes to extract as much as possible from those that are still operating in particular from the Alouette/ISIS series. For instance, a near conjunction between Alouette II and ISIS 1 would provide a dramatic possibility of VLF excitation from ISIS 1 and reception by the Alouette: a space first. Lessons learned from omissions and failures of earlier experiments should be applied to the design of future experiments.

In the absence of any detailed mission specifications a few points are to be noted.

(1) Essential overall requirements apart from the actual VLF experiment configuration are as follows:

   (a) Frequency coverage: should be close and detailed; small steps best, ~ 300 Hz (below proton gyrofrequency) up to 20 kHz.

   (b) Amplitude range from definitely linear to highly nonlinear (e.g. in volts ~ .01 to 10 volts or more).

(c) Complete attitude information not just magnetic sensors with attendant ambiguity.

(d) Auxiliary plasma diagnostics: electron density (resonance relaxation most reliable, bottom, topside sounding useful), ion density and composition (spherical ion trap); electron temperature (and density check) (Brace whip probe);

(2) Desirable VLF experiments models (with level and frequency as noted in (1) above) roughly in order of complexity:

(a) Impedance: probably dominated by sheath unless collapsed, can check sheath theory but probably not whistler emission.

(b) Waveform: actual waveforms telemetered to ground required for appreciation of nonlinearity.

(c) Near field: either a double package separating on injection into orbit or rendezvous between satellites again either (a) and/or (b).

(d) Ground spacecraft transmission reception: transmit swept frequency and amplitude to ground on VLF reception at satellite (check reciprocity etc.).

(3) Desirable VLF antennas

(a) Dipole (b) circular phased crossed dipole.

(b) Loop.

Many of the essential features can be crammed into a simple experiment, particularly for a feasibility trial, but a good reliable test will require a full test.

Without more specific mission definition it seems pointless to construct detailed experiment plans.

PROPOSED SATELLITE OBSERVATIONS OF ELF EMISSIONS

David R. Criswell
Harold B. Killen
Houston, Texas

INTRODUCTION

This report describes an early effort at Rice University to develop a satellite which would monitor electromagnetic and hydromagnetic activity in the magnetosphere.

The program was initiated at Rice in 1964 by Dr. B. J. O'Brien and one of the authors (D.R.C.). The Office of Naval Research expressed an early interest in the proposed research. Funds were provided for development of one detector type and a satellite feasibility study. Program activity was essentially completed by early 1968.

The three primary research objectives were: Exploration, precision observations of waves in situ, and reception of man made signals for controlled propagation experiments. The three frequency ranges of interest were:

(1) VLF - approximately 1 to 10 KHz associated with whistlers;

(2) ELF - approximately 10 Hz to 1 KHz associated with irregular emissions, lower frequency whistlers, and extreme ionospheric adsorption; and

(3) the ULF range from .1 Hz to 10 Hz associated with hydromagnetic activity such as pearl pulsations.

Many factors justify satellite-borne observations. The signals originate in the magnetosphere, thus the propagation, amplitude behaviour, and origin of the activity are best studies there. Ground based observations are hampered by variable ionospheric attenuation, ducting, mode conversion, and reflection. Conversely, the ionosphere tends to shield satellite detectors from both natural and artifical terrestrial activity. In addition, satellite instrumentation should detect activity more frequently and over greater ranges of latitude,

longitude, and altitude than comparable terrestrial networks while affording greater response uniformity (i.e., standardization) and simpler logistics.

By 1964 it was apparent that two different orbits were necessary to study the full range of wave phenomenon. A low, circular orbit for ionospheric interface effects or an extended, eccentric orbit, 3 Re-perigee and 10 Re-apogee, for studies of propagation effects and location of source regions. Economics of launch precluded an extended orbit. Thus a slightly eccentric trajectory which varied in altitude between 500 and 3-4,000 kilometers was considered desirable. Wave activity both in and outside the ionosphere could be observed.

AURORA II

The authors (DRC,HBK) developed the general scientific and engineering requirements for the satellite, which was designated Aurora II. These ground rules are presented in Table 1. The basic objective was to perform simultaneous measurements of both the varying electric and magnetic fields. Telemetry bandwidth was the dominant factor limiting detector resolution and maximum frequency. The three magnetic field ranges reflect detector restrictions. A limited project scope, items 2 and 3, was required because of budgetary restrictions, difficulty of the electric field measurements, and a desire to minimize system noise or electrical interference onboard the satellite. Limitations of the magnetometer required a slowly rotating satellite. Item 5 was not a restriction. The Owl Satellite was an active program at Rice and the structure was available and understood.

DETECTORS

Table 2 specifies the detector complement.

VARIABLE-MU MAGNETOMETER

The variable-mu magnetometer is the device which is least familar to most geophysicsts. It is suited for satellite-borne observation of .1 - 10 Hz magnetic activity at the 1 - 10 milligamma level or greater. The device utilizes a ferrite rod as the core of the inductance coil in an oscillator circuit. The ferrite permeability varies with the strength of the magnetic field along the core. Changes in field strength modify the coil inductance and

TABLE 1

1. Simultaneous measurements of $\vec{E}$ and $\vec{B}$

   a. $0.1\ \text{Hz} \lesssim f \leq 10\ \text{KHz}$

   b. $1\ \frac{\mu\text{volt}}{\text{meter}} < E < 1\ \frac{\text{volt}}{\text{meter}}$

   c. (1) $10^{-4}\ \gamma \lesssim B\ (100\ \text{Hz} - 10\ \text{KHz}) \lesssim 10\ \gamma$

      (2) $10^{-3}\ \gamma \lesssim B\ (.1\ \text{Hz} - 100\ \text{Hz}) \lesssim 10\ \gamma$

      (3) $100\ \gamma \lesssim B\ (\text{D.C.} - .1\text{Hz}) < 5 \cdot 10^{+4}\ \gamma$

2. Limited Scope

   a. Primary $\vec{E}$ and $\vec{B}$ observations

   b. Housekeeping and attitude data

   c. No plasma or particle detectors

3. Data System

   a. Prefer a PCM system

   b. Real time only - no onboard recorder

   c. Control of onboard processing

4. Orientation

   a. Very long spin period ($T \gtrsim 100$ seconds)

   b. No attitude control

5. Utilize an "Owl" structure

TABLE 2

DETECTOR COMPLEMENT

DETECTOR	MEASUREMENT	PARAMETERS
1. Variable-Mu Magnetometer	Magnetic Field (Three Axis)	Freq. - 0.1 Hz - 100 Hz Sensitivity - .01γ - 100γ
2. Loop Antennas	Magnetic Field (Three Axis)	Freq. - 100 Hz - 10 KHz Sensitivity - .0001γ - 10γ
3. Dipoles	Electric Field (Three Axis)	Freq. - 0.1 Hz - 10 KHz Sensitivity - 1 μ volt/meter - 1 volt/meter
4. Impedance	Dipole Impedance	Freq. - 1 Hz - 10 KHz

thus the resonant frequency of the oscillator circuit. The basic device outputs an FM signal in response to a time variable field. Analog conversion is possible.

A prototype, orthogonal, three-axis magnetometer was produced by the Electro Mechanics Company, for Aurora II. Test indicated that the flight version, after incorporating a few modifications, would be compatible with the 10^{-3} - 10 gamma (.1 Hz - 100 Hz) requirements for observation of hydromagnetic waves.

The remaining technical descriptions are extracted from the feasibility study conducted by Develco, Inc.

LOOP ANTENNAS

For higher frequencies, three mutually orthogonal loop antennas were to be placed inside the satellite. Placing the loops inside the satellite avoided shadowing solar cell strings. Very little loss in sensitivity was expected. The loop terminals were connected through RFI filters to the electronics package where they were coupled by means of balanced transformers to the low noise preamplifiers. Magnetic field measurements were to be made over the range of 15 Hz to 10 KHz, overlapping the variable-mu magnetometer between 15 and 100 Hz. Sensitivity of the loops was adjustable by changing the impedance match of the matching transformers.

ELECTRIC FIELD SENSORS

Measurement of the electric field was to be accomplished by using electric dipoles. In order to make accurate measurements with a dipole, the potential between two elements of known separation must be measured. Each end of the dipole will be surrounded by a plasma sheath; both ends will acquire a potential different from the plasma. As a consequence, equally shaped electrodes with similar characteristics must be used. Errors are introduced if the probes interact by screening each other or suffer screening by the satellite structure. It is unavoidable that at times one or more of the probes will be affected. The satellite geometry must be chosen to enable removal of some of those effects during data analysis.

Initial estimates for the boom lengths is on the order of 5 feet to avoid embedding the electric field sensors in the stabilization magnetic field of the alignment magnet. This requires shielded preamplifiers in the probes with sufficient current capacity to overcome the capacity of wires leading to VLF amplifiers located in the main structure.

Accurate measurements using a probe system dictate high input impedance pre-amplifiers to avoid loading the probes. A pre-amplifier utilizing a FET transistor is suitable for this purpose. Projected sensor sensitivities range from a few μ-volts at 0.1 Hz to less than one μ-volt at 10 KHz. The variation in sensitivity is controlled primarily by the frequency dependent characteristics of the source impedance and plasma noise.

IMPEDANCE MEASUREMENT

Electric dipole impedance must be measured in order to estimate local plasma densities. This measurement would be accomplished by inserting a constant current into the antenna and sweeping the frequency. The resulting voltage would be measured by the normal data channels. A slow sweep would be used so that high Q resonances could be resolved. Figure 1 illustrates the placement of the detectors and antennas.

MECHANICAL FEATURES

The physical structure of the satellite is made up largely of a central support column with a surrounding shell indicated by the dashed lines. This arrangement allows the major portion of the instrumentation to be placed inside the support column with a corresponding reduction of the RFI problem.

SATELLITE STABILIZATION AND ASPECT

Prior to payload ejection a satellite spin period of greater than 100 seconds would be established. Stabilization of the space-craft was expected to be accomplished using a bar magnet and damping rods as in Injun III and Aurora I. Orientation was expected to be achieved in a period of two to three weeks. The roll rate would then be reduced to zero and the pitch rate reduced to two revolutions per orbit. This technique might disturb operation of the variable-μ magnetometer. However, it would have prevented acceleration of satellite rotation due to sunlight or gravity gradient effects.

D. C. feedback from the variable-mu magnetometer could provide reference with respect to the geomagnetic field. A sun sensor signal or alternatively, current measurements on the various solar cell arrays could be telemetered for information on aspect about the spin axis.

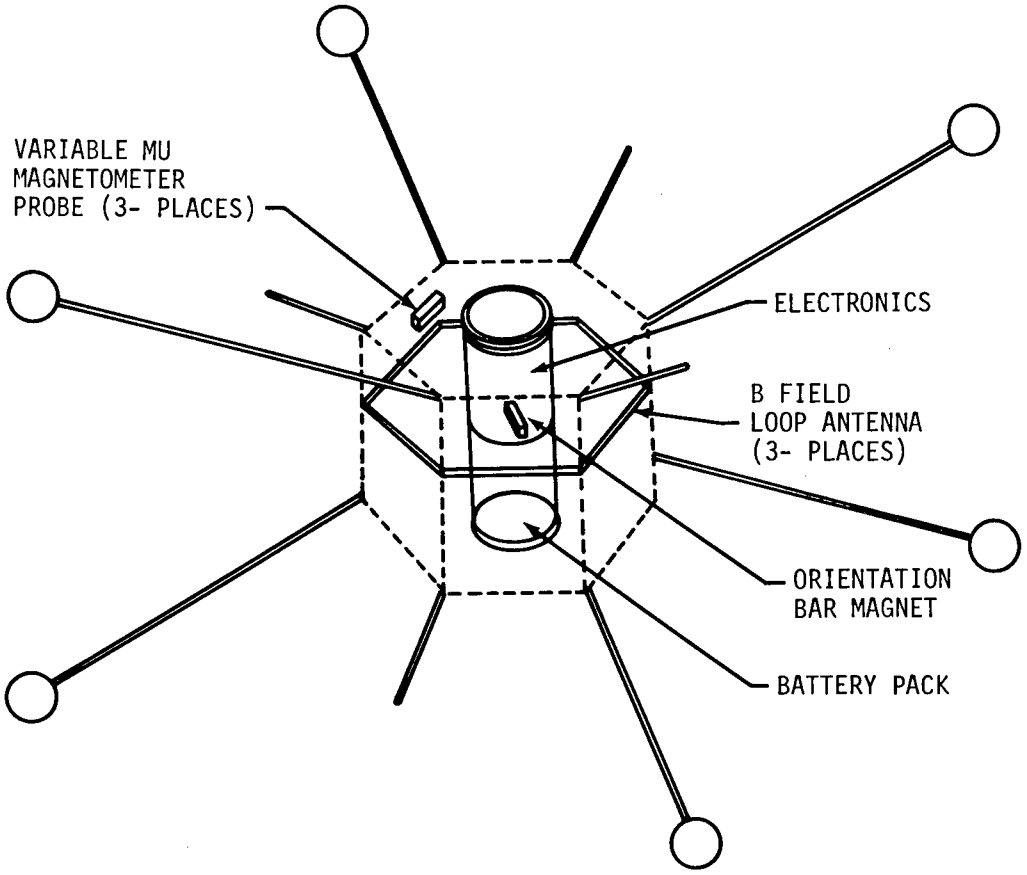

SATELLITE EXPLODED VIEW

FIGURE 1

DATA SYSTEM

During the early phases of the design study it became apparent that a formidable communications problem was involved in transmitting real time the large quantities of data. A PCM system, desired from the viewpoint of data accuracy, would required a S-band rf system. However, Goddard indicated that S-band coverage would not be adequate by the expected launch data. Accordingly, a 400 MHz, FM telemetry system was designed. Data formatting was to employ band splitters consisting of multipliers followed by band pass filters to translate the data to another part of the spectrum in order to achieve orthogonality. Transmitted pilot tones would allow translation of the data back to the baseband for data reduction. The rf link was designed for a signal/noise ratio of approximately 30 db.

A number of design features were included to give the system added flexibility. A tone sequential command system was chosen since it would be less costly to implement. Operational commands included the ability to change gains of individual VLF amplifiers and the low frequency limit of the variable-mu magnetometer. Linear amplifiers were specified rather than logarithmic compression because of the higher order product interference terms the latter generate. Another command feature was operation of the electric field probes either differentially or single ended and thus using the spacecraft body as a reference to determine the effects of a probe trailing in the satellite's "wake". Also, the use of two telemetry transmitters with different rf power levels was considered. Switching transmitters test for interaction between the transmission system and the sensor probes. These techniques would have materially extend the capability of the satellite to make definitive measurements.

PROBLEM AREAS - SUGGESTIONS

Telemetry and data recording, difficulty of the electric field observations, and extremely slow satellite rotation constituted the major problem areas in the Aurora II project. Technology, and preset concepts prevented the circumvention of these problems.

The Aurora II work was performed in the 1964-1967 time frame. Even though only three years have passed there has been sufficient development, especially in integrated circuitry, to warrant a different approach. The use of small programmable computers may be feasible for some onboard data processing. For example, active filter techniques would improve the ultimate sensitivity of the variable-mu magnetometer. A second possibility is to place the sensors and data systems in separate but close satellites, as illustrated in Figure 2. In this manner a completely adequate data

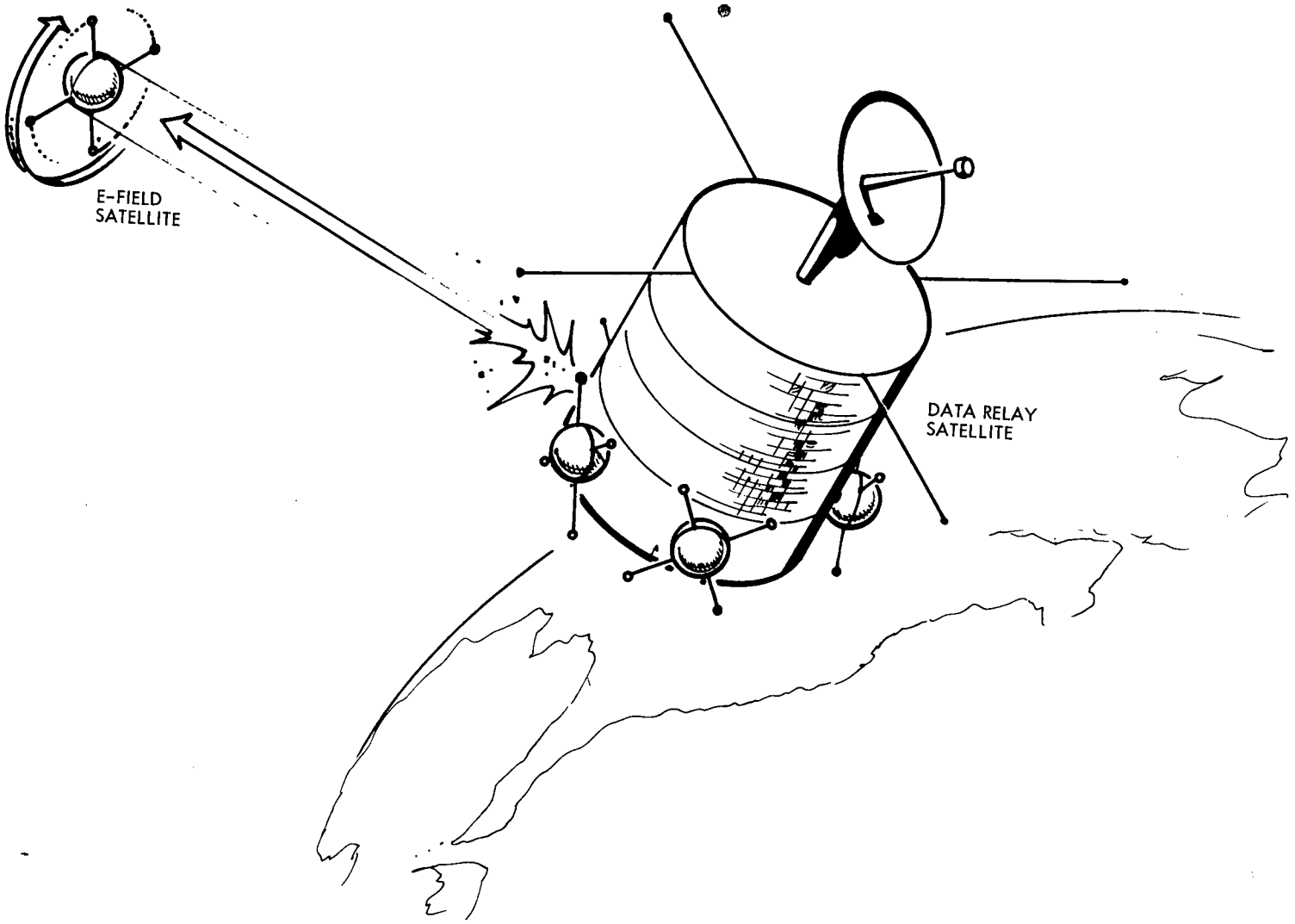

Figure 2

system could be provided. Additionally, the sensor platforms could be designed for minimum noise levels, simplicity, and minimum interaction with the environment.

A somewhat speculative approach to E-field observations is suggested in Figure 2. The E-field satellite would be composed of two electrically separated but conductive hemispheres. The sphere would contain, as integrated circuitry, a FET amplifier which would directly modulate a small FM or AM transmitter for relay of data to the mother satellite. Low power usage would allow batteries to provide 2 - 6 months lifetimes. The basic advantage provided by this technique is that the E-field satellite could have a diameter less than the local Debye length in many regions of the magnetosphere. Thus, the satellite would be decoupled from several strong plasma effects such as the plasma sheath. Preliminary studies indicate that electric fields with magnitudes greater than 10 microvolts per meter might be detected by this technique.

Analysis of the Excitation of the Earth-Ionosphere Waveguide by a Satellite-borne Antenna

by

F. Einaudi and J. R. Wait

Cooperative Institute for Research in Environmental Sciences
University of Colorado
Boulder, Colorado 80302

Abstract

An analytical approach is outlined to obtain the fields near the earth's surface for a long wave transmitting antenna on a satellite. The medium is divided in slabs, each of which is characterized by a dielectric tensor. To simplify the calculations, a planar model is considered in which the d-c magnetic field is vertical. An explicit derivation is given for a three-layer planar model: the lowest layer, up to ca. 70 km, represents the earth-ionosphere waveguide, the second layer may represent the D-region; and the third layer is the one containing the satellite, which is idealized by a vertical electric dipole. Emphasis is placed on the relative launching efficiency of a satellite-borne antenna as compared with a ground-based antenna of the same strength.

I. Introduction

Several authors have derived Green's functions for the problem of antennas radiating in an anisotropic medium. Bunkin (1957), Kogelnik (1960), Meecham (1961), Kuehl (1962), Mittra and Deschamps (1963) have solved the dipole problem with different techniques, for a cold plasma. Arbel and Felsen (1963) have also treated the problem of radiation in anisotropic media, with special emphasis on stratified media. Wait (1964) has reviewed some of these methods and has also given a direct derivation of the electromagnetic field due to a dipole in a cold anisotropic plasma.

An interesting example of a source immersed in an anisotropic magneto-ionic medium is a radiating dipole antenna on a satellite. For any stable orbit, it is necessary that the satellite be at a height above the earth's surface, where there is an appreciable density of charged particles. Then because of the presence of the terrestrial magnetic field, the antenna's environment is anisotropic in its electrical properties for long radio waves.

In the present paper, we outline the mathematical approach to calculate the electromagnetic fields at a receiving antenna on or near the earth due to a transmitting antenna on a satellite. Although the formulae are valid for any frequency range, the model has been chosen having in mind frequency below 15 kHz. For such frequencies, the various parameters characterizing the ionosphere below about 300 km experience substantial variations over distances comparable to the local wavelengths; under such

circumstances, the propagation is dominated by internal reflections, coupling between different modes of propagation and by collisional absorption. A W.K.B.-type of solution or ray-methods are not feasible (Wait 1962); thus we resort to obtain a full-wave solution.

The geometry is indicated in Fig. 1. The transmitting antenna is located at $z = z_o$ and the receiving antenna at $z = 0$ on the earth's surface. Media 1, 2, and 3 are individually homogeneous, but otherwise arbitrary. For example, medium 2 could be taken to simulate the D region, and medium 1 would be the earth-ionosphere waveguide. The model is obviously very crude, and its validity will depend on the frequency of the transmitting antenna. A vertical d-c magnetic field is present, so that the validity of the model applies best in the polar regions. We also assume that the antenna is represented by a vertical electric dipole. As indicated, the earth curvature is neglected.

II. General Equations

The equations governing the propagation of the electromagnetic fields in each medium are the Maxwell equations; for time factor $\exp(i\omega t)$, these can be written

[1a] $$\nabla \times \vec{H} = i\omega\vec{D} + \vec{J}$$

[1b] $$\nabla \times \vec{E} = -i\omega\mu_o \vec{H}$$

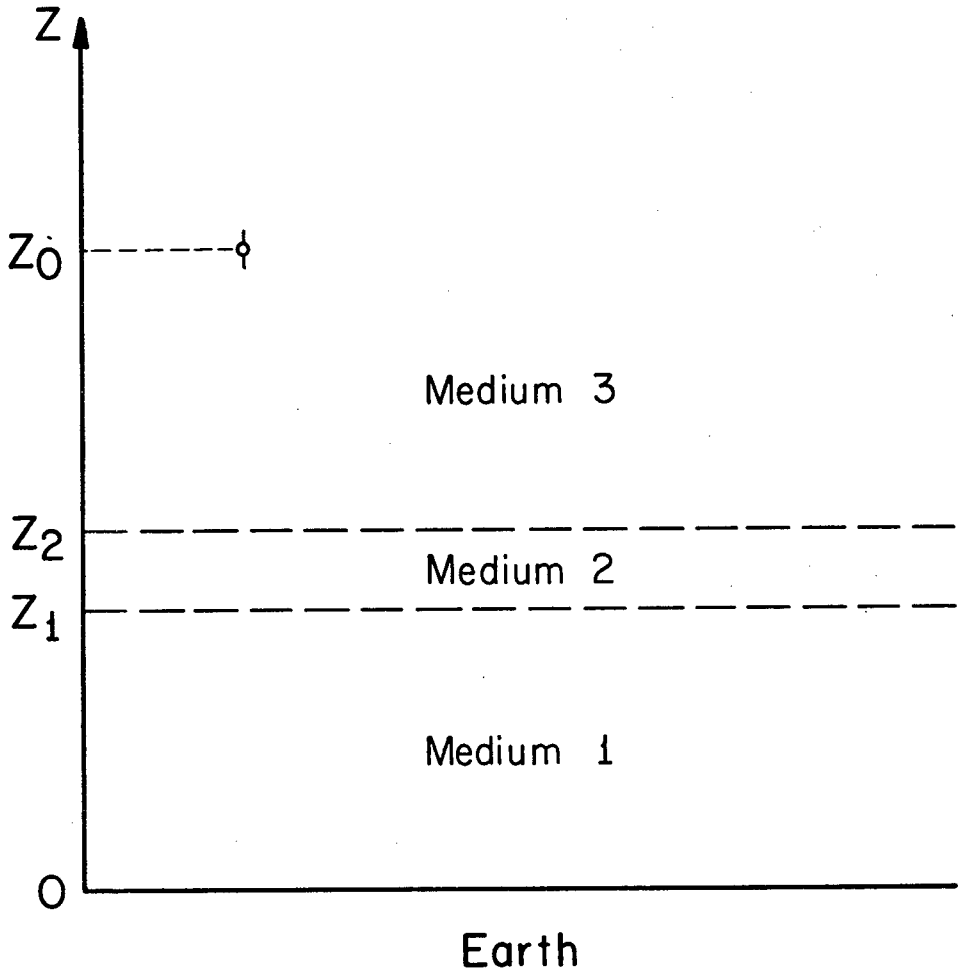

Figure 1 - The geometry of the system (not to scale).

Figure 1

Here μ_o is the permeability of free space which we assume constant throughout the system; $\vec{J}$ is the current flowing in the dipole, while currents due to electron and ion motion are included in the displacement $\vec{D}$. $\vec{D}$, in turn, is related to the electric field $\vec{E}$ via the dielectric tensor $\tilde{\epsilon}$ which, for the present cold-plasma model, is given by

$$[2] \quad \tilde{\epsilon} = \begin{pmatrix} \epsilon & -ig & 0 \\ ig & \epsilon & 0 \\ 0 & 0 & \hat{\epsilon} \end{pmatrix}; \quad \vec{D} = \begin{pmatrix} D_\rho \\ D_\varphi \\ D_z \end{pmatrix} = \begin{pmatrix} \epsilon & -ig & 0 \\ ig & \epsilon & 0 \\ 0 & 0 & \hat{\epsilon} \end{pmatrix} \begin{pmatrix} E_\rho \\ E_\varphi \\ E_z \end{pmatrix}$$

The dielectric tensor, in the linear approximation which we adopt, is independent of the magnitude of the field components. For a two component plasma with neutrals included, the components for $\tilde{\epsilon}$ are given by [e.g., Hines (1953), Stix (1962), Wait (1962) and Galejs (1964)]:

$$\epsilon/\epsilon_o = 1 - i\frac{\omega_e^2}{\omega^2}\,\frac{\nu_e/\omega + i}{\Omega_e^2/\omega^2 + (\nu_e/\omega + i)^2} - i\frac{\omega_i^2}{\omega^2}\,\frac{\nu_i/\omega + i}{\Omega_i^2/\omega^2 + (\nu_i/\omega + i)^2}$$

$$[3] \quad \hat{\epsilon}/\epsilon_o = 1 - i\frac{\omega_e^2/\omega^2}{\nu_e/\omega + i} - i\frac{\omega_i^2/\omega^2}{\nu_i/\omega + i}$$

$$g/\epsilon_o = -\frac{(\Omega_e/\omega)(\omega_e^2/\omega^2)}{\Omega_e^2/\omega^2 + (\nu_e/\omega + i)^2} - \frac{(\Omega_i/\omega)(\omega_i/\omega)^2}{\Omega_i^2/\omega^2 + (\nu_i/\omega + i)^2}$$

where

ν_e (ν_i) is the collision frequency of electrons (ions) with the neutral particles; ω_e (ω_i) and Ω_e (Ω_i) are the electron (ion) plasma and gyro-frequencies respectively:

$$\omega_e^2 = N_o e^2/\epsilon_o m_e \; ; \qquad \omega_i^2 = N_o e^2/\epsilon_o m_i \; ;$$

$$\Omega_e = -\mu_o H_o e/m_e \; ; \qquad \Omega_i = \mu_o H_o e/m_i \; .$$

The quantities m_e and m_i are the mass of the electrons and ions respectively, N_o is the electron and ion density, -e is the charge of the electrons and ϵ_o is the dielectric constant of free space. Several approximations are involved in deriving [3], which we do not discuss here, except to say that we consider media macroscopically neutral, and we neglect collisions between ions and electrons [e.g. see Hines (1953)].

In each layer, we can reduce Maxwell equations to a system of two coupled equations in the vertical components E_z and H_z. Because of the symmetry of the problem (vertical dipole and vertical d-c magnetic field) it is useful to introduce cylindrical coordinates, with the z-axis vertical. In this case $\frac{\partial}{\partial \varphi} = 0$.

From the z-component of [1b] we get:

$$[4] \qquad \frac{1}{\rho} \frac{\partial}{\partial \rho} (\rho E_\varphi) - \frac{1}{\rho} \frac{\partial}{\partial \varphi} E_\rho = -i\omega\mu_o H_z$$

Using the divergence equation

$$[5] \qquad \nabla \cdot \vec{D} = \bar{\rho} = \frac{i}{\omega} \nabla \cdot \vec{J}$$

and equation [4] we obtain

$$[6] \qquad \epsilon \left(\frac{1}{\rho} \frac{\partial}{\partial \rho} \rho E_\rho + \frac{1}{\rho} \frac{\partial}{\partial \varphi} E_\varphi \right) = g \omega \mu_o H_z + \bar{\rho} - \hat{\epsilon} \frac{\partial}{\partial z} E_z .$$

Taking the curl of [1a] and then taking the z-component and using [4] and [6], we find that

$$[7] \qquad \nabla_t^2 H_z + \frac{\partial^2 H_z}{\partial z^2} + H_z \frac{k_o^2}{\epsilon \epsilon_o} (\epsilon^2 - g^2) + \frac{\hat{\epsilon}}{\epsilon} \omega g \frac{\partial E_z}{\partial z} = - [\nabla \times \vec{J}]_z + \frac{\bar{\rho}}{\epsilon} \omega g$$

where

$$[8] \qquad k_o^2 = \omega^2 \epsilon_o \mu_o , \qquad \nabla_t^2 = \frac{1}{\rho} \frac{\partial}{\partial \rho} \rho \frac{\partial}{\partial \rho} + \frac{1}{\rho^2} \frac{\partial^2}{\partial \varphi^2}$$

Taking the z-component of [1a]:

$$[9] \qquad \frac{1}{\rho} \frac{\partial}{\partial \rho} \rho H_\varphi - \frac{1}{\rho} \frac{\partial}{\partial \varphi} H_\rho = i \omega \hat{\epsilon} E_z + J_z$$

Taking the z-component of $\nabla \times \nabla \times \vec{E}$ and using [6] and [9], we obtain

$$[10] \quad \nabla_t^2 E_z + \frac{\hat{\epsilon}}{\epsilon} \frac{\partial^2 E_z}{\partial z^2} + k_o^2 \frac{\hat{\epsilon}}{\epsilon_o} E_z - \mu_o \omega \frac{g}{\epsilon} \frac{\partial H_z}{\partial z} = i\omega \mu_o J_z + \frac{1}{\epsilon} \frac{\partial \bar{\rho}}{\partial z}$$

Equations [7] and [10] form a system of coupled equations which hold for any piecewise homogeneous region: one simply has to use, for each homogeneous slab, the appropriate values of ϵ_n, $\hat{\epsilon}_n$ and g_n. It is interesting to note that,if we neglect the earth's magnetic field, $\tilde{\epsilon}$ becomes a diagonal matrix, i.e. $\epsilon = \hat{\epsilon}$ and $g = 0$, and equations [7] and [10] become uncoupled. In such a case,two independent solutions exist: TE waves with $E_z = E_\rho = H_\varphi = 0$, and TMwaves with $H_z = H_\rho = E_\varphi = 0$. The effect of the magnetic field is that of coupling together these two waves. From E_z and H_z, we obtain the expression for the transverse components of E and H whose matching at each interface allows the determination of the fields everywhere.

III. The Primary Field

We now calculate the primary field due to a dipole, of current moment p_o, located at $z = z_o$: this is the field that would exist if the dipole were radiating in an infinite medium. The current density of the dipole has the form

$$[11] \quad J_z = i\omega p_o \delta(z-z_o) \frac{\delta(\rho)}{2\pi\rho} .$$

Using the following spectral representation of Dirac delta functions

$$\delta(z-z_o) = \frac{1}{2\pi}\int_{-\infty}^{\infty} e^{iv(z-z_o)}\,dv, \quad \frac{\delta(\rho)}{\rho} = \int_0^{\infty} J_o(\lambda\rho)\,\lambda\,d\lambda,$$

the current density J_z and the density $\bar{\rho}$ given by [5] can be written as

$$[12] \quad J_z = \frac{i\omega p_o}{(2\pi)^2}\int_0^{\infty}\int_{-\infty}^{\infty} J_o(\lambda\rho)e^{iv(z-z_o)}\,\lambda\,d\lambda\,dv$$

$$[13] \quad \bar{\rho} = -\frac{ip_o}{(2\pi)^2}\int_0^{\infty}\int_{-\infty}^{\infty} J_o(\lambda\rho)e^{iv(z-z_o)}\,\lambda v\,d\lambda\,dv.$$

$J_p(\lambda\rho)$ is the first kind Bessel function.

Because of the form of [12] and [13], we write the primary fields E_z^p and H_z^p (the superscript p refers thereafter to the primary fields) as follows:

$$E_z^p = \frac{p_o}{(2\pi)^2}\int_0^{\infty}\int_{-\infty}^{\infty} A(\lambda, v)\, J_o(\lambda\rho)\, e^{iv(z-z_o)}\,d\lambda\,dv$$

$$[14] \quad H_z^p = \frac{p_o}{(2\pi)^2}\int_0^{\infty}\int_{-\infty}^{\infty} B(\lambda, v)\, J_o(\lambda\rho)\, e^{iv(z-z_o)}\,d\lambda\,dv$$

Substituting [14] into [7] and [10], using [12] and [13] and making the change of variable $u = -iv$, we obtain

$$A = \lambda \left\{ -u^4 - u^2 [s_1^2 + k_o^2 (\epsilon/\epsilon_o)] - k_o^2 (\epsilon/\epsilon_o)(s_1^2 - k_o^2 g^2/\epsilon\epsilon_o) \right\} / \epsilon\Delta$$

$$[15] \quad B = -\lambda\, \omega g (\hat{\epsilon}/\epsilon)(k_o^2/\epsilon_o - s_2^2/\epsilon)\, u / \Delta = -\lambda^3 \omega g u / \epsilon\Delta$$

$$\Delta = (\hat{\epsilon}/\epsilon)[u^4 + u^2(s_1^2 + s_2^2) + s_1^2 s_2^2 - s_2^2 k_o^2 g^2/\epsilon\epsilon_o]$$

where

$$s_1^2 = k_o^2 \epsilon/\epsilon_o - \lambda^2; \qquad s_2^2 = (\epsilon/\hat{\epsilon})(k_o^2 \hat{\epsilon}/\epsilon_o - \lambda^2)$$

Using the above expressions for A and B, the integration over $v = iu$ in [14] can be carried out easily by applying the method of contour integration, this yields

$$E_z^p = \int_o^\infty \lambda^3 J_o(\lambda\rho)[e_1 e^{-u_1 |z-z_o|} - e_2 e^{-u_2 |z-z_o|}]\, d\lambda$$

$$[16] \quad H_z^p = -[(z-z_o)/|z-z_o|] \int_o^\infty \lambda^3 h J_o(\lambda\rho)[e^{-u_1 |z-z_o|} - e^{-u_2 |z-z_o|}]\, d\lambda$$

where

$$e_1 = (p_o/4\pi)\left\{\epsilon u_1(u_1^2+s_1^2)/[(\hat{\epsilon})^2 s_2^2(u_2^2-u_1^2)]\right\}$$

[17] $$e_2 = (p_o/4\pi)\left\{\epsilon u_2(u_2^2+s_1^2)/[(\hat{\epsilon})^2 s_2^2(u_2^2-u_1^2)]\right\}$$

$$h = (p_o/4\pi)\omega g/[\hat{\epsilon}(u_2^2-u_1^2)]$$

The quantities u_2 and u_1 are the solutions, with $R_e u_1 > 0$ and $R_e u_2 > 0$, of the equation

[18] $$\Delta = 0.$$

In order to express the transverse components of the electric and magnetic fields, we introduce the following quantities.

$$p_1 = igs_2^2/[\epsilon(s_2^2+u_1^2)] = i(s_1^2+u_1^2)/\omega^2 g\mu_o$$

[19]

$$\eta_1 = iu_1/\omega\mu_o; \qquad r_1 = \lambda^2/u_1; \qquad \xi_1 = -i\omega\epsilon u_1/s_2^2; \qquad q_1 = -\epsilon\lambda^2 u_1/\hat{\epsilon}s_2^2.$$

Similarly p_2, η_2, r_2, ξ_2 and q_2 will be defined by [19] in which, however, u_1 will be replaced by u_2. Physically, the quantities p, q, r, ξ and η are related to the ratios E_ρ / E_φ, E_z / E_ρ, H_z / H_ρ, H_φ / E_ρ and H_ρ / E_φ respectively.

The transverse components can now be written as follows

$$E_\varphi^p = -(z-z_o)/(|z-z_o|) \int_0^\infty \lambda^4 J_1(\lambda\rho)[E_1^p e^{-u_1|z-z_o|} + E_2^p e^{-u_2|z-z_o|}]d\lambda$$

$$E_\rho^p = -(z-z_o)/(|z-z_o|) \int_0^\infty \lambda^4 J_1(\lambda\rho)[p_1 E_1^p e^{-u_1|z-z_o|} + p_2 E_2^p e^{-u_2|z-z_o|}]d\lambda$$

[20]

$$H_\rho^p = -\int_0^\infty \lambda^4 J_1(\lambda\rho)[\eta_1 E_1^p e^{-u_1|z-z_o|} + \eta_2 E_2^p e^{-u_2|z-z_o|}]d\lambda$$

$$H_\varphi^p = -\int_0^\infty \lambda^4 J_1(\lambda\rho)[\xi_1 p_1 E_1^p e^{-u_1|z-z_o|} + \xi_2 p_2 E_2^p e^{-u_2|z-z_o|}]d\lambda$$

where

[21] $E_1^p = h/r_1\eta_1, \qquad E_2^p = -h/r_2\eta_2.$

The actual values for u_1 and u_2 will depend on the parameters of the medium in which the dipole is located. We shall use the notation $u_1^{(j)}$, $u_2^{(j)}$, $p_1^{(j)}$, $p_2^{(j)}$ etc., to indicate quantities within the jth medium. We shall use the subscript zero for quantities within the earth-ionosphere wave guide.

It is interesting to note that when the vertical electric dipole is located in the earth-ionosphere wave guide, the primary field is purely TM whose components can be obtained from [16] and [20]. Thus, in this case,

$$E_z^p = \int_0^\infty \lambda^3 J_o(\lambda\rho)\, e_o e^{-u_o |z-z_o|}\, d\lambda; \qquad H_z^p = 0$$

$$[22] \quad E_\rho^p = \frac{(z-z_o)}{|z-z_o|} \int_0^\infty \lambda^4 J_1(\lambda\rho) \frac{e_o}{q_o} e^{-u_o |z-z_o|} d\lambda; \qquad E_\varphi^p = 0$$

$$H_\varphi^p = \int_0^\infty \lambda^4 J_1(\lambda\rho) \frac{\xi_o}{q_o} e_o e^{-u_o |z-z_o|}\, d\lambda; \qquad H_\rho^p = 0$$

here

$$u_o = (\lambda^2 - k_o^2)^{\frac{1}{2}}, \qquad e_o = p_o/4\pi\epsilon_o u_o$$

and q_o and ξ_o are given by [19] in which u_o replaces u_1 and the remaining quantities are those for free space. Finally, it is simple to show that E_z^p, given in [22], can be written as

$$E_z^p = \frac{p_o}{4\pi\epsilon_o}\left(k_o^2 + \frac{\partial^2}{\partial z^2}\right)\frac{e^{-ik_o R_o}}{R_o}; \qquad R_o = [\rho^2 + (z-z_o)^2]^{\frac{1}{2}}$$

which is the form most often encountered in the literature (e.g. see Stratton (1941) and Wait (1962)). In this case, we see that $p_o = Ids/i\omega$ where I is the current in the dipole of length ds. This is consistent with [11].

IV. The Secondary Fields

Taking a clue from the expression of the primary field, we write the electromagnetic fields in the media with no sources and the secondary field in the medium containing the source in the following form:

$$E_{\varphi}^{(j)} = \int_0^{\infty} \lambda^4 J_1(\lambda\rho)[E_1^{(j)} e^{-u_1^{(j)}z} + E_2^{(j)} e^{u_1^{(j)}z} + E_3^{(j)} e^{-u_2^{(j)}z} + E_4^{(j)} e^{u_2^{(j)}z}]d\lambda$$

$$E_{\rho}^{(j)} = \int_0^{\infty} \lambda^4 J_1(\lambda\rho)[(E_1^{(j)} e^{-u_1^{(j)}z} + E_2^{(j)} e^{u_1^{(j)}z})p_1^{(j)} + (E_3^{(j)} e^{-u_2^{(j)}z} + E_4^{(j)} e^{u_2^{(j)}z})p_2^{(j)}]d\lambda$$

[23]

$$H_{\rho}^{(j)} = \int_0^{\infty} \lambda^4 J_1(\lambda\rho)[(E_1^{(j)} e^{-u_1^{(j)}z} - E_2^{(j)} e^{u_1^{(j)}z})\eta_1^{(j)} + (E_3^{(j)} e^{-u_2^{(j)}z} - E_4^{(j)} e^{u_2^{(j)}z})\eta_2^{(j)}]d\lambda$$

$$H_{\varphi}^{(j)} = \int_0^{\infty} \lambda^4 J_1(\lambda\rho)[(E_1^{(j)} e^{-u_1^{(j)}z} - E_2^{(j)} e^{u_1^{(j)}z})\xi_1^{(j)} p_1^{(j)} + (E_3^{(j)} e^{-u_2^{(j)}z} - E_4^{(j)} e^{u_2^{(j)}z})\xi_2^{(j)} p_2^{(j)}]d\lambda$$

The vertical components in jth medium can be written similarly as:

$$E_z^{(j)} = \int_0^{\infty} \lambda^3 J_o(\lambda\rho)[(E_1^{(j)} e^{-u_1^{(j)}z} - E_2^{(j)} e^{u_1^{(j)}z})q_1^{(j)} p_1^{(j)} + (E_3^{(j)} e^{-u_2^{(j)}z} - E_4^{(j)} e^{u_2^{(j)}z})q_2^{(j)} p_2^{(j)}]d\lambda$$

[24]
$$H_z^{(j)} = \int_o^\infty \lambda^3 J_o(\lambda\rho)[\,(E_1^{(j)} e^{-u_1^{(j)} z} + E_2^{(j)} e^{u_1^{(j)} z}) r_1^{(j)} \eta_1^{(j)} + (E_3^{(j)} e^{-u_2^{(j)} z} + E_4^{(j)} e^{u_2^{(j)} z}) r_2^{(j)} \eta_2^{(j)}]\,d\lambda$$

From the two above sets of equations, we deduce that each slab introduces 4 unknowns, $E_1^{(j)}$, $E_2^{(j)}$, $E_3^{(j)}$ and $E_4^{(j)}$. The number of unknowns reduces to two in the slabs which limit the system from above and below: this is because of the radiation condition at $z = \pm\infty$. For the case described in figure 1, we have a total of 12 unknowns: we also have 12 equations corresponding to imposing the continuity of the transverse components of $\vec{E}$ and $\vec{H}$ at the three interfaces.

In the earth-ionosphere wave guide the fields are a superposition of TM and TE fields:

[25]
$$E_\varphi^{(1)} = \int_o^\infty \lambda^4 J_1(\lambda\rho)[E_1^{(1)} e^{-u_o z} + E_2^{(1)} e^{u_o z}]\,d\lambda$$

$$E_\rho^{(1)} = \int_o^\infty \lambda^4 J_1(\lambda\rho)[E_3^{(1)} e^{-u_o z} + E_4^{(1)} e^{u_o z}]\,d\lambda$$

$$H_\rho^{(1)} = \int_o^\infty \lambda^4 J_1(\lambda\rho)[E_1^{(1)} e^{-u_o z} - E_2^{(1)} e^{u_o z}]\eta_o\,d\lambda$$

$$H_\varphi^{(1)} = \int_o^\infty \lambda^4 J_1(\lambda\rho)[E_3^{(1)} e^{-u_o z} - E_4^{(1)} e^{u_o z}]\xi_o\,d\lambda$$

where $\eta_o = iu_o/\omega\mu_o$ and $\xi_o = i\omega\epsilon_o/u_o$. If the earth is perfectly conducting, $E_2^{(1)} = -E_1^{(1)}$ and $E_4^{(1)} = -E_3^{(1)}$.

V. The Boundary Conditions

At the boundary between layers, the transverse components of the electric and magnetic fields must be continuous. A convenient method of matching boundary conditions involves coefficient matrices, the elements of which depend on the field ratios introduced in part III. Let us consider the continuity of the transverse components at the boundary $z = z_{\quad}$ between layer i and (i+1), neither of which

[28]

$$b_{ji} = \begin{pmatrix} e^{-u_1^{(j)} z_{ji}} & 0 & 0 & 0 \\ 0 & e^{u_1^{(j)} z_{ji}} & 0 & 0 \\ 0 & 0 & e^{-u_2^{(j)} z_{ji}} & 0 \\ 0 & 0 & 0 & e^{u_2^{(j)} z_{ji}} \end{pmatrix}$$

In equation [26] the equalities between the first, second, third and fourth rows in each column matrix correspond to imposing the continuity of E_φ, E_ρ, H_ρ, and H_φ respectively. If the (j+1)th layer contains the source, then we have to add, on the right of [26], a second term corresponding to the primary field. Coefficient matrices similar or equivalent to the above ones have been used by several authors, often in connection with numerical calculations done by computer (see, for example, Price (1964, 1967), Swain (1965), Galejs (1967, 1968), Wait (1968), Holden and Bostick (1968)). We now apply the above considerations to the model described in figure 1, and we treat two possible cases; a): $z_o > z_2$; b): $0 < z_o < z_1$. In both cases, the purpose of the calculations is to determine the fields on the earth surface. Assuming that the earth is perfectly conducting and thus $E_\rho^{(1)} = E_\varphi^{(1)} = 0$ at $z = 0$, we look for a non-homogeneous system of four equations in the following four unknowns: $E_1^{(1)}$, $E_3^{(1)}$, $E_1^{(3)}$ and $E_3^{(3)}$. We obtain such a system

by matching the transverse fields across the upper boundary of the earth-ionosphere waveguide.

Case a: $z_o > z_2$.

Imposing the boundary conditions at $z = z_2 = z_{23}$, we get:

[29] $$t_2 b_{23} \Phi^{(2)} = t_3 b_{32} [\Phi^{(3)} + \Phi^p]$$

where

[30] $$\Phi^{(3)} = \begin{pmatrix} E_1^{(3)} \\ 0 \\ E_3^{(3)} \\ 0 \end{pmatrix} \quad ; \quad \Phi^p = \begin{pmatrix} 0 \\ E_1^p e^{-u_1^{(3)} z_o} \\ 0 \\ E_2^p e^{-u_2^{(3)} z_o} \end{pmatrix}$$

Let F_+ be the column matrix whose elements are the integrands which appear in [23], calculated at $z = z_{1+}$ proceeding downward from medium 3. We can write:

[31] $$F_+ = \begin{pmatrix} \mathcal{E}_\varphi^{(2)} \\ \mathcal{E}_\rho^{(2)} \\ \mathcal{H}_\rho^{(2)} \\ \mathcal{H}_\varphi^{(2)} \end{pmatrix}_{z = z_{1+}} = t_2 b_{21} \Phi^{(2)} = t_2 b_{21} b_{23}^{-1} t_2^{-1} t_3 b_{32} [\Phi^{(3)} + \Phi^p] =$$

$$= \begin{pmatrix} q_{11} S_1 + q_{13} S_3 \\ q_{21} S_1 + q_{23} S_3 \\ q_{31} S_1 + q_{33} S_3 \\ q_{41} S_1 + q_{43} S_3 \end{pmatrix} + \begin{pmatrix} q_{12} S_1^p + q_{14} S_3^p \\ q_{22} S_1^p + q_{24} S_3^p \\ q_{32} S_1^p + q_{34} S_3^p \\ q_{42} S_1^p + q_{44} S_3^p \end{pmatrix}$$

where

$$S_1 = E_1^{(3)} e^{-u_1^{(3)} z_2}, \qquad S_3 = E_3^{(3)} e^{-u_2^{(3)} z_2},$$

[32]

$$S_1^p = E_1^p e^{u_1^{(3)}(z_2 - z_o)}, \qquad S_3^p = E_2^p e^{u_2^{(3)}(z_2 - z_o)}$$

and q_{ij} are the elements of the matrix $Q = t_2 b_{21} b_{23}^{-1} t_2^{-1} t_3$.

The field components at $z = z_1$ calculated proceeding upward from the earth can be written as:

[33] $$F_- = \begin{pmatrix} \mathcal{E}_\varphi^{(1)} \\ \mathcal{E}_\rho^{(1)} \\ \mathcal{H}_\rho^{(1)} \\ \mathcal{H}_\varphi^{(1)} \end{pmatrix}_{z = z_{1-}} = t_1 b_{12} \Phi^{(1)} = \begin{pmatrix} E_1^{(1)} m_o \\ E_3^{(1)} m_o \\ E_1^{(1)} n_o \eta_o \\ E_3^{(1)} n_o \xi_o \end{pmatrix}$$

where

$$t_1 = \begin{pmatrix} 1 & 1 & 0 & 0 \\ 0 & 0 & 1 & 1 \\ \eta_o & -\eta_o & 0 & 0 \\ 0 & 0 & \xi_o & -\xi_o \end{pmatrix}$$

$$m_o = e^{-u_o z_1} - e^{u_o z_1}$$

$$n_o = e^{-u_o z_1} + e^{u_o z_1}$$

The above equation is obtained making use of [25] and of the condition that the earth is perfectly conducting. Finally, equating F_+ to F_- we obtain the system

$$\begin{aligned} m_o E_1^{(1)} - q_{11} S_1 - q_{13} S_3 &= q_{12} S_1^p + q_{14} S_3^p = N_1 \\ m_o E_3^{(1)} - q_{21} S_1 - q_{23} S_3 &= q_{22} S_1^p + q_{24} S_3^p = N_2 \\ n_o \eta_o E_1^{(1)} - q_{31} S_1 - q_{33} S_3 &= q_{32} S_1^p + q_{34} S_3^p = N_3 \\ n_o \xi_o E_3^{(1)} - q_{41} S_1 - q_{43} S_3 &= q_{42} S_1^p + q_{44} S_3^p = N_4 \end{aligned} \qquad [34]$$

in the four unknown quantities $E_1^{(1)}$, $E_3^{(1)}$, S_1 and S_3. We discuss the solution of [34] in the next section.

Case b: $0 < z_o < z_1$.

One can proceed in much the same manner for this case, which we consider namely for comparing it with the previous one. The primary field is now a TM mode and the new system can be readily obtained

$$
\begin{aligned}
& m_o E_1^{(1)} - q_{11} S_1 - q_{13} S_3 = 0 \\
& m_o E_3^{(1)} - q_{21} S_1 - q_{23} S_3 = -(T_1 + T_2) = M_2 \\
& n_o \eta_o E_1^{(1)} - q_{31} S_1 - q_{33} S_3 = 0 \\
& n_o \xi_o E_3^{(1)} - q_{41} S_1 - q_{43} S_3 = \xi_o (T_1 - T_2) = M_4
\end{aligned}
\qquad [35]
$$

where

$$
T_1 = (e_o / q_o) e^{u_o (z_1 - z_o)}, \qquad T_2 = (e_o / q_o) e^{-u_o (z_1 - z_o)}
$$

VI. Analytical Results and a Numerical Example

We can solve systems [34] and [35] for the unknown $E_1^{(1)}$ and $E_3^{(1)}$, which we write in the form:

$$
\begin{aligned}
& E_1^{(1)} = f_1(\lambda) / g(\lambda) ; \qquad E_3^{(1)} = f_3(\lambda) / g(\lambda) \qquad \text{for } z_o > z_2 \\
& E_1^{(1)} = \ell_1(\lambda) / g(\lambda) ; \qquad E_3^{(1)} = \ell_3(\lambda) / g(\lambda) \qquad \text{for } 0 < z_o < z_1
\end{aligned}
\qquad [36]
$$

where the functions f_1, f_3, ℓ_1, ℓ_3 and g can be derived readily if we apply Kramer's rule in solving systems [34] and [35]. Using the fact that f_1, f_3, ℓ_1, ℓ_3 and g are even functions of λ and introducing the Hankel functions $H_1^{(1)}$ and $H_1^{(2)}$:

$$J_1(x) = \tfrac{1}{2}\left[H_1^{(1)}(x) + H_1^{(2)}(x)\right], \quad H_1^{(1)}(-x) = H_1^{(2)}(x),$$

we derive from [25]:

[37]

$$H_\rho^{(1)} = \int_{-\infty}^{\infty} \lambda^4 H_1^{(2)}(\lambda\rho)\, \eta_o (f_1/g)\, d\lambda \qquad \text{for } z_o > z_2$$

$$H_\varphi^{(1)} = \int_{-\infty}^{\infty} \lambda^4 H_1^{(2)}(\lambda\rho)\, \xi_o (f_3/g)\, d\lambda$$

$$H_\rho^{(1)} = \int_{-\infty}^{\infty} \lambda^4 H_1^{(2)}(\lambda\rho)\, \eta_o (\ell_1/g)\, d\lambda \qquad \text{for } 0 < z_o < z_1$$

$$H_\varphi^{(1)} = \int_{-\infty}^{\infty} \lambda^4 H_1^{(2)}(\lambda\rho)\, \xi_o (\ell_3/g)\, d\lambda$$

We are left then with the calculation of integrals of the form

[38] $$\int_{-\infty}^{\infty} H_1^{(2)}(\lambda\rho)\, f(\lambda)\, d\lambda$$

where $f(\lambda)$ is a rather complex function. The evaluation of the above integral by using asymptotic expansions would, at the frequencies we are considering, severely limit the range of applicability of the results. Aside from the use of a computer in evaluating the integrals, we can follow the method of contour integration and locate the poles of the integrands. Such poles, λ_s, are the solution of the equation

[39] $$g(\lambda) = 0 .$$

Equation [39] is the modal or resonance equation of the system. We should note that the only contribution derives from the poles in the fourth quadrant, i.e., from those for which $\mathrm{Im}(\lambda_s) < 0$ and $\mathrm{Re}(\lambda_s) > 0$. In addition, in calculating [38], one has a contribution from the branch points associated with the slabs bounding the system from above and below. They are responsible for the appearance of lateral waves which, however, are highly attenuated for lossy media and we shall neglect them here. We can write, for simple poles λ_s and for a unitary dipole moment p_o:

$$H_\rho^{(1)} = -2\pi i \sum_{s=0}^{\infty} \left[\lambda^4 H_1^{(2)}(\lambda\rho)\, \eta_o f_2 \left| \frac{dg}{d\lambda} \right. \right]_{\lambda=\lambda_s} = \left[H_1^{(2)}(\lambda_o^M \rho)\, A_\rho^{(0)} + \right.$$

$$\left. + H_1^{(2)}(\lambda_1^E \rho)\, A_\rho^{(1,E)} + H_1^{(2)}(\lambda_1^M \rho)\, A_\rho^{(1,M)} + \cdots \right]$$

[40] $z_o = z_s > z_2$

$$H_\varphi^{(1)} = -2\pi i \sum_{s=0}^{\infty} \left[\lambda^4 H_1^{(2)}(\lambda\rho)\, \xi_o f_3 \left| \frac{dg}{d\lambda} \right. \right]_{\lambda=\lambda_s} = \left[H_1^{(2)}(\lambda_o \rho)\, A_\varphi^{(0)} + \right.$$

$$\left. + H_1^{(2)}(\lambda_1^E \rho)\, A_\varphi^{(1,E)} + H_1^{(2)}(\lambda_1^M \rho)\, A_\varphi^{(1,M)} + \cdots \right].$$

Here λ_s^M or λ_s^E refer to the ordering of the roots as well as to the nature of the modes, TM or TE, in the limiting case in which the earth and the ionosphere are both perfectly conducting. In the actual situation, one may call such modes as quasi-TM or quasi-TE modes. Similar expressions can be written for $H_\rho^{(1)}$ and $H_\varphi^{(1)}$ when $z_o = 0$, i.e., when the antenna is on the earth's surface: we simply have to replace f_1, f_3 and the A's by ℓ_1, ℓ_3 and the B's, respectively.

The above analytical development has been applied to a particularly simple case in which a simple plasma slab is considered at a height of 70 km and of 10 km thickness. It simulates the D-region in the ionosphere where, due to the high collisions, the attenuation of the waves is maximum. The relevant parameters have been chosen as follows:

$$N_o = 10^4 \text{ electrons/cm}^3; \qquad B_o = \mu_o H_o = 0.5 \text{ gauss};$$

$$\nu_e = \nu_i = 10^7 \text{ collisions/sec}; \qquad z_o - z_a = 150 \text{ km}.$$

The medium above $z = z_2$ is taken to be free space. In addition, the conductivity of the earth is taken to be infinite.

The dispersion equation [39] has been solved numerically: in figure 2, the attenuation factors are plotted versus frequency up to 12 kHz; this is about the value of frequency above which the earth curvature becomes very important. In the ELF range only the TM zero order mode is important, whereas for higher frequencies, the TE, n=1 mode reveals the lowest attenuation. In figure 3, the excitation factors for the lowest mode $n = 0$, are plotted versus frequency, together with the ratio $R^{(0)} = A_\varphi^{(0)} / B_\varphi^{(0)} = A_\rho^{(0)} / B_\rho^{(0)}$. In figure 4a, b, the same quantities are plotted for $n = 1$, for the quasi-TE and quasi-TM modes, respectively.

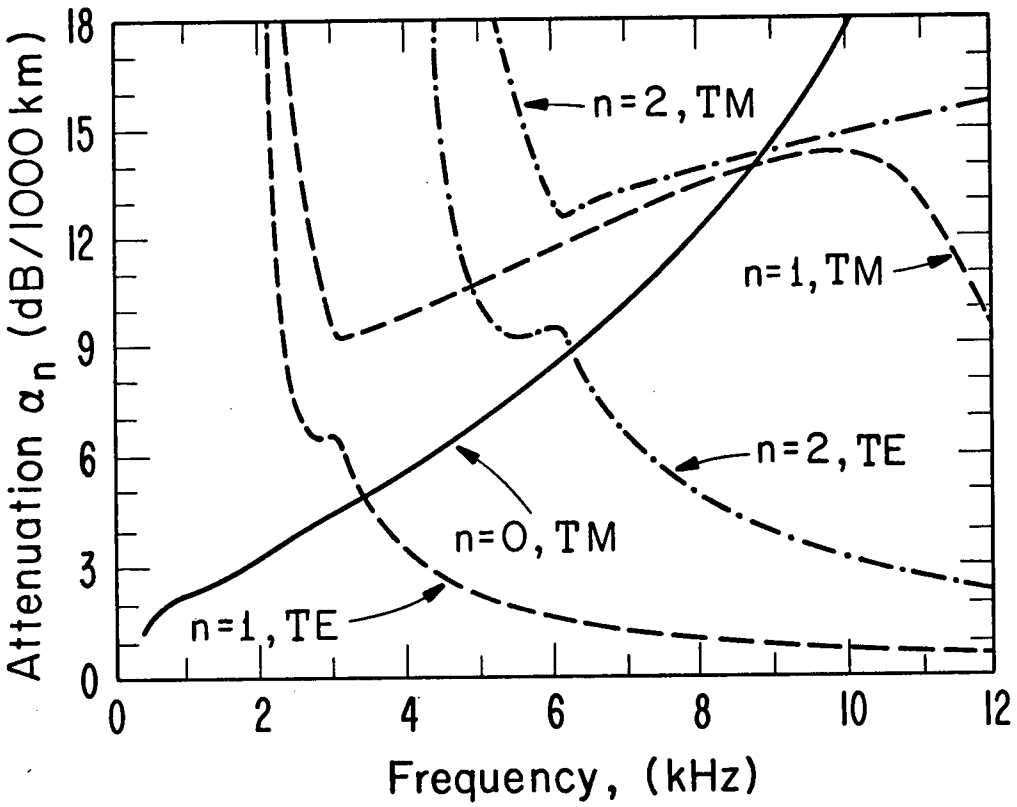

Figure 2 - The attenuation factor in decibels per 1000 km of path length as a function of the frequency in kiloHertz. The mode number is indicated on each curve. The conductivity, σ, of the ground is taken to be infinite and the height of the ionospheric reflective layer is $H_1 = 70$ km. The ratio ω_r = electron plasma frequency square/electron collision frequency = $3.18\ 10^6$ rad/sec.

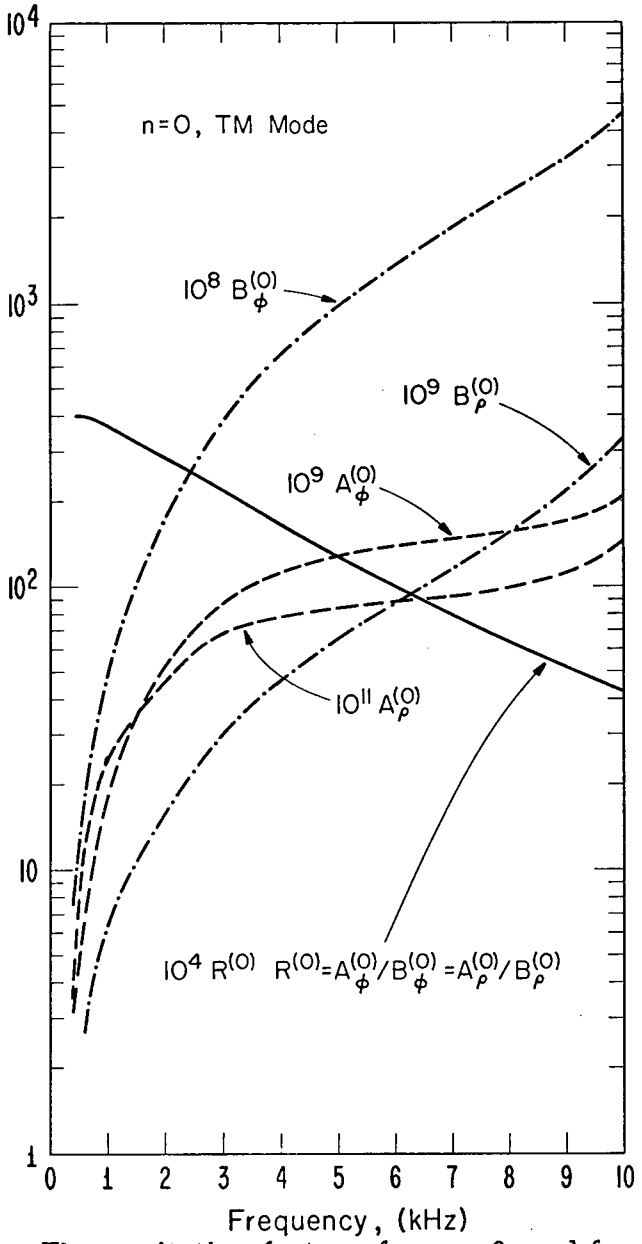

Figure 3 - The excitation factors for $n = 0$ and for the ρ and φ components of the magnetic fields at the earth surface are given as functions of frequency in kiloHertz. The A's refer to the dipole at 230 km, and the B's to the dipole located at the earth surface.

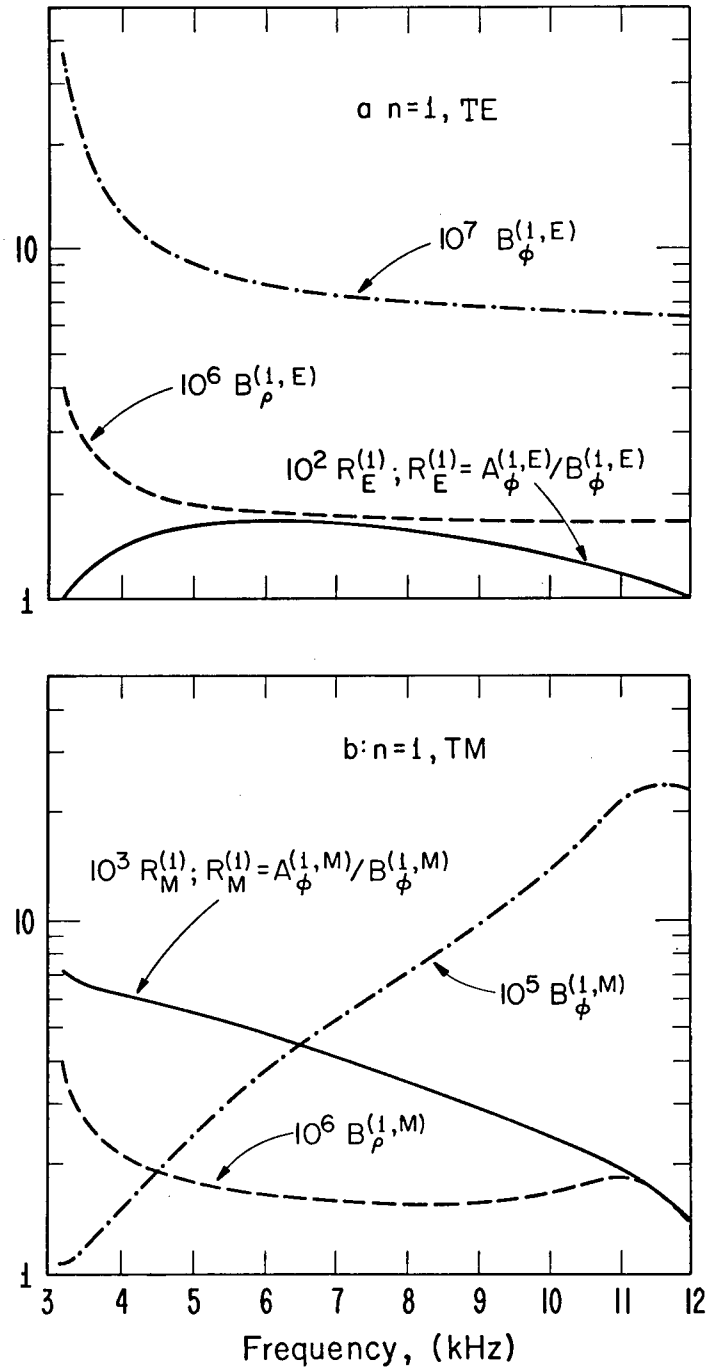

Figure 4 - As in Figure 2, but for the mode n = 1. Part (a), on the top half, refers to the TE mode, and part (b), below, to the TM mode.

VII. Conclusions

The efficiency of the coupling into the earth-ionosphere waveguide is estimated for ELF/VLF waves emitted from an antenna at satellite heights. The model adopted is crude, for only a planar slab simulating the D-region is included, and only a vertical geomagnetic field is considered parallel to a short electric dipole which simulates the transmitting antenna. The dipole is located at 230 km above the earth, i.e., just about at the peak of the F_2 layer. The effectiveness of such an ionosphere source appears to be small. For the entire ELF range, the mode of interest is $n = 0$ and this has a quasi-TM character. In this case, for 500 Hz, the magnetic fields at the earth's surface are about 5% of those for a ground-based source. At 10 kHz, this relative efficiency between satellite-borne and ground-based dipoles reduces to 0.5%. Similar values apply for the quasi-TE, $n = 1$ mode; over the frequency range 3 - 12 kHz, the relative effectiveness is of the order of 1%. The excitation of a quasi-TM, $n = 1$ mode is even less efficient.

It is recommended that the present method be used to calculate the fields in the earth-ionosphere waveguide for satellite-borne dipoles (both electric and magnetic) not aligned with the geomagnetic field. In such cases, as Galejs (1970) has suggested, the effectiveness of the launching may be increased greatly. No new principles in the method are needed for such calculations.

Finally, we should indicate that the present formulation is appropriate for studying the impedance properties of the dipole in the ionospheric plasma. Subject to the validity of the linearized cold-plasma description, we can use the integral representations of the field components to compute a value for the driving point impedance of the dipole. Using this information in conjunction with the launching efficiencies discussed above, we will be in a position to predict the overall efficiency of the satellite-borne dipole as a source for global communication using ELF and VLF electromagnetic waves.

Acknowledgment

We are grateful to Loren Bearce of the U. S. Naval Research Laboratory who stimulated our interest in this problem.

REFERENCES

Arbel, E. and Felsen, L. B. 1963. Electromagnetic Waves, E. C. Jordan, Ed. (Pergamon Press, Inc.).

Budden, K. G. 1966. Radio Waves in the Ionosphere (Cambridge Univ. Press), Chapter 7.

Bunkin, F. V. 1957. Sov. Physics JETP 5, 277.

Galejs, J. 1964. Radio Sci. J. Res. NBS 68D, 693.

Galejs, J. 1967. Radio Sci. 2, 1497.

Galejs, J. 1968. J. Geophys. Res. 73, 339.

Galejs, J. 1970. Excitation of the terrestrial waveguide by sources in the lower ionosphere, paper presented at the Conference on Antennas and Tranionospheric Propagation as Related to ELF/VLF Downlink Satellite Communications, Washington, D.C.,

Hines, C. O. 1953. Proc. Camb. Phil. Soc. 49(2), 299.

Holden, H. D. and Bostick, F. X. 1968. The Univ. of Texas at Austin, Elect. Eng. Res. Lab. Rept. No. 146.

Kogelnik, H. 1960. Radio Sci. J. Res. NBS 64D, 515.

Kuehl, H. H. 1962. Phys. of Fluids 5, 1095.

Meecham, W. C. 1961. Phys. of Fluids 4, 1517.

Mittra, R. and Deschamps, G. A. 1963. Electromagnetic Waves, E. C. Jordan, Ed. (Pergamon Press, Inc.).

Price, G. H. 1964. Radio Sci. J. Res. NBS 68D, 407.

Price, G. H. 1967. Radio Sci. 2, 607.

Stix, T. H. 1962. The Theory of Plasma Waves (McGraw-Hill Book Co.), Chapter 1.

Stratton, J. A. 1941. Electromagnetic Theory (McGraw-Hill Book Co.), Chapter 8.

Swain, G. R. 1965. Univ. of New Mexico, Bureau of Eng. Research Rep. No. EE - 126.

Wait, J. R. 1962. Electromagnetic Waves in Stratified Media (Pergamon Press, Oxford). [Second revised edition 1970].

Wait, J. R. 1963. Can. J. Phys. 41, 299.

Wait, J. R. 1964. Radio Sci. J. Res. NBS 68B, 119.

Wait, J. R. 1968. Electromagnetics and Plasmas (Holt, Rinehart and Winston, New York).

FULL WAVE SOLUTION FOR THE TRANSMISSION OF ELF WAVES THROUGH THE IONOSPHERE

Mr. D. Lynn Shaeffer
University of Pittsburgh
506 Langley Hall
Pittsburgh, Pa. 15213
U.S.A.

Dr. Yuji Inoue, Associate Professor
University of Pittsburgh
403 Space Research Coordination Center
Pittsburgh, Pa. 15213
U.S.A.

INTRODUCTION

Various full-wave methods have been proposed for the solution of the problem of electromagnetic wave propagation in a horizontally stratified magneto-ionic medium. These include Budden (1955, 1961), Barron and Budden (1959), Johler and Harper (1962), Pitteway (1965) and more recently, Walsh (1967) and Altman and Cory (1969a, b). The advantages and disadvantages of the different methods are discussed in the cited literature. The present investigation utilizes a technique developed by Inoue and Horowitz (1966a, b) and is adapted to obtain numerical solutions to the full-wave equations for cases of ELF and ULF waves originating in the magnetosphere and propagating through the ionosphere to the Earth's surface. The ultimate aim is to determine the modification of these waves as they propagate and the effect of reflection at the ground surface.

Briefly, the numerical procedure is as follows. The Earth's environment is considered to be horizontally stratified with a vertical magnetic field. The necessary condition that the electric and magnetic fields be continuous across the boundary separating two strata is guaranteed by the matricant method of solution. All field quantities are assumed to vary in the manner

$$e^{-iwt}\, e^{ik_gLX + ik_gMY}$$

where

$$k_g = \frac{1}{R_e}$$

$$R_e = \text{Earth's radius}$$

The disturbance function is represented by the above double Fourier series with L = M = 0 for the plane wave case and L = M = 10 for the localized disturbance case. Only one component of the Fourier spectrum is considered at a time. The horizontal components of the wave fields may be cast into the convenient matrix form

$$\frac{d}{dz}\begin{bmatrix} E_x \\ E_y \\ H_x \\ H_y \end{bmatrix} = ik_g \overline{\overline{T}} \begin{bmatrix} E_x \\ E_y \\ H_x \\ H_y \end{bmatrix}$$

$\overline{\overline{T}}$ is the propagation tensor and is a function of the dielectric tensor and the Fourier numbers L and M. It is this equation which we integrated numerically from -400 km out to 5000 km. A model ionosphere at midlatitudes for midday and sunspot minimum conditions was compiled from published data and used in the numerical computations. An average ion was defined at each altitude from the model ionosphere and a two component plasma was considered. The cold plasma approximation was made but with temperature dependent collision frequencies included in the equations of motion. The results for the localized disturbance case at 100 c/s and 3.0 c/s will be presented.

ION CYCLOTRON RESONANCE

Figure 1 depicts the ion cyclotron resonance profile, i.e., the L = infinity surface on the CMA diagram (Stix, 1962), for the particular model ionosphere used in this work. The ions primarily responsible for each portion of the curve are indicated. That part of the profile which tails off to the left above 2000 km is due to the constancy of the ion mass (H^+) and the r^{-3} dependence of the magnetic field. Between approximately 50 c/s and 300 c/s both the fast and slow modes (i.e., the R and L modes, respectively) are propagating above the resonance level, i.e., to the left of the curve. Below this level only the R mode propagates and the L mode is evanescent. Between 20 c/s and 50 c/s the effect on a disturbance originiating to the left of the resonance profile and crossing the L = infinity surface in the downward direction is not so clear because this crossing takes place at altitudes where collisions become important and tend to wash out resonance effects.

Disturbances between 50 c/s and 300 c/s generated at distances beyond 1.4 earth radii and to the right of the resonance curve must encounter the resonance condition twice as they propagate to ground level. Thus the slow mode (i.e., the L mode) may become trapped in the region between the two resonance levels. This region will then serve as a waveguide for the L mode. The width of the waveguide varies with frequency. At 50 c/s the waveguide walls are located at 900 and 9000 km whereas at 300 c/s the waveguide walls are located at 1900 and 2400 km. Also, any observation of the L mode at ground level implies that the disturbance was generated at altitudes below the ion resonance level, varying from about 900 km at 50 c/s to 1200 km at 300 c/s.

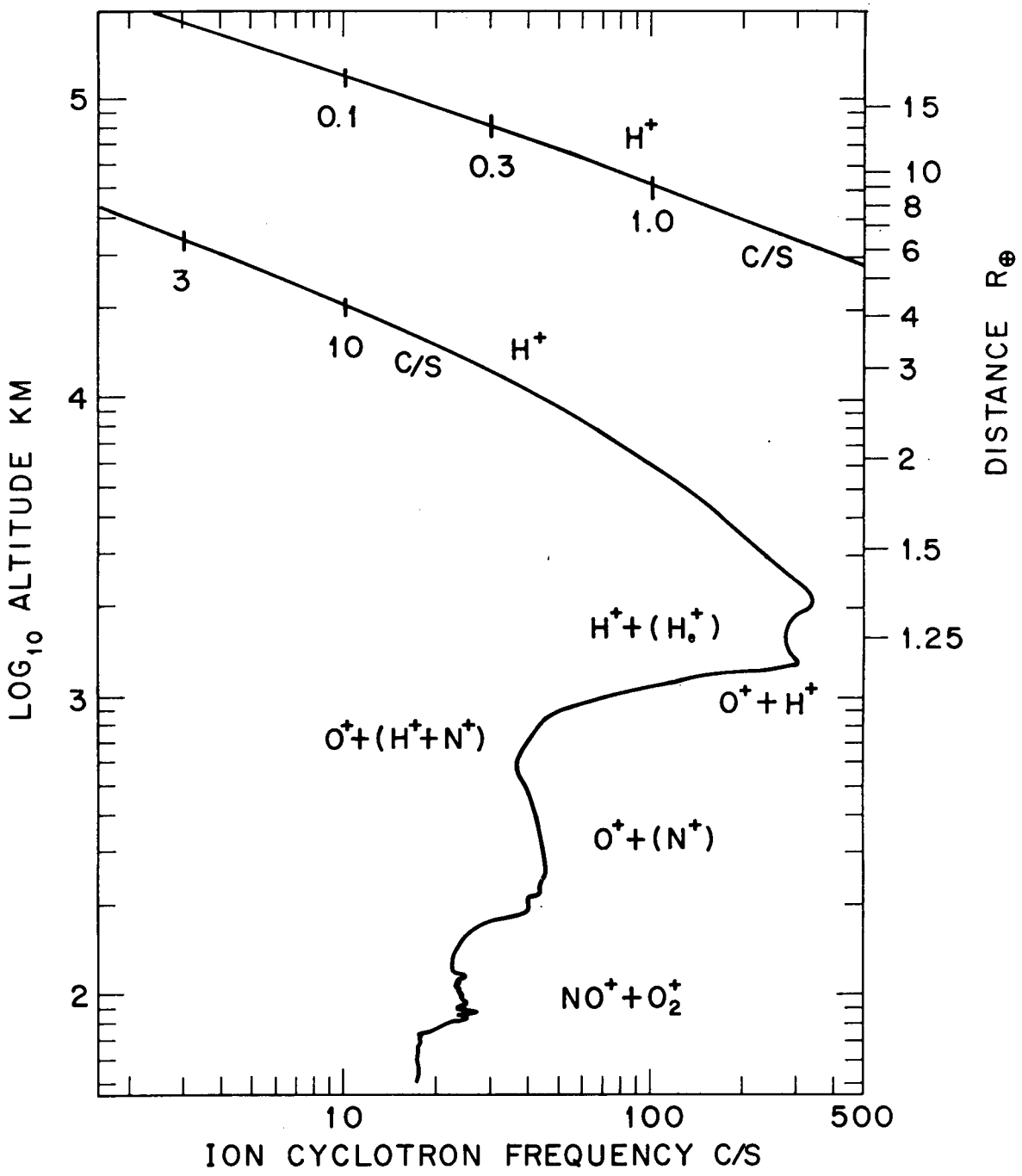

Figure 1

LOCALIZED DISTURBANCE AT 100 C/S

Booker Quartic Roots

Figure 2 shows the altitude dependence of the Booker quartic roots for the slow (S) and fast (F) waves. The abbreviations QR and QI stand for real parts and imaginary parts of the quartic roots, respectively. The index of refraction for propagation in the Z-direction is obtained by multiplying the QR and QI values by a factor of .075. Downgoing and upgoing waves are represented by the same curves and differ only by a minus sign.

The Booker quartic roots reveal that the indices of refraction are almost entirely real in the region above 1070 km. The slow and fast waves are quite similar in this region and are both propagating. At 1070 km the ion cyclotron resonance is encountered. Below this level the slow and fast waves are interchanged and the fast wave is evanescent. This resonance condition corresponds to a crossing of the L = infinity surface in parameter space on the CMA diagram. The magneto-ionic quantity Y_i is equal to one. As we shall see later from the mixing ratios and coupling coefficients this resonance causes the L mode to be almost completely reflected back to the magnetosphere. The slow mode is highly propagating down to the neutral atmosphere. Thus, above the resonance level the ionosphere is slightly anisotropic. Below the resonance level the ionosphere is highly anisotropic.

In the neutral atmosphere the quartic roots are pure imaginary and both modes are evanescent. This effect is due to the presence of a horizontal component in the propagation vector. In the neutral atmosphere the electron and ion densities are zero. Therefore, in Stix' notation:

$$R = L = P = S = 1$$

$$A = C = 1$$

$$B = 2$$

The dispersion relation then becomes

$$n^4 - 2n^2 + 1 = 0$$

or

$$(n^2-1)^2 = 0$$

$$n^2 = 1 = n_x^2 + n_z^2$$

thus

$$n_z^2 = 1 - \frac{c^2}{v_x^2}$$

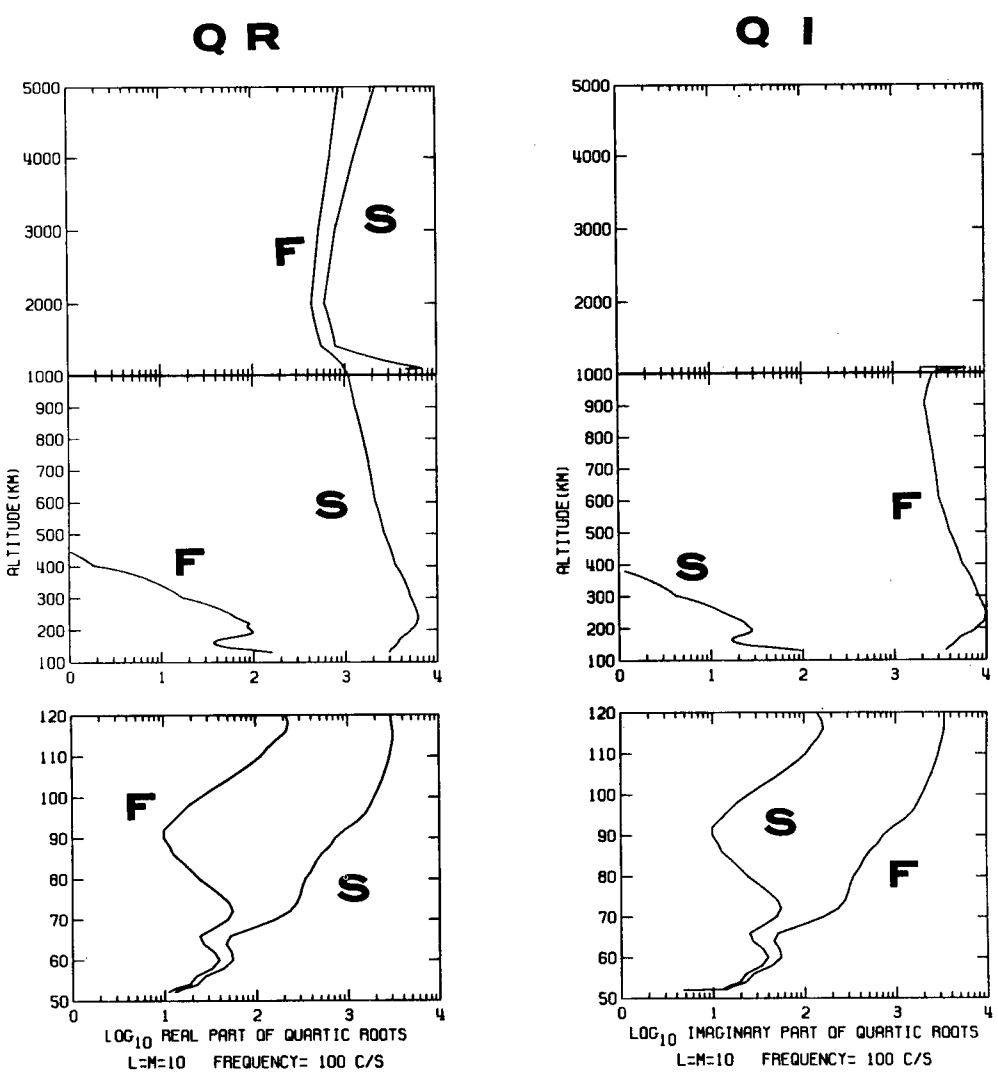

Figure 2

If $v_x^2 < c^2$, then

$$n_z^2 < 0$$

and hence n_z is pure imaginary. Thus the neutral atmosphere acts as an elastic medium for the vertically propagating component of the particular localized disturbance being considered. If v_x had been greater than c then n_z is greater than or equal to zero but less than one and the neutral atmosphere would have been dispersive for the vertically propagating component.

Inside the Earth the magnitudes of the real and imaginary parts of the quartic roots are all equal. Thus the Earth's interior is isotropic and "dense resistive," i.e., behaves like a metal.

Magneto-ionic Coupling Coefficients

Figure 3 shows the magneto-ionic coupling coefficients for the localized disturbance at 100 c/s. The abbreviations S, F, M, R stand for slow, fast, mode coupling and reflection, respectively. Thus RS means reflection of the slow wave. M means generation of a downgoing slow wave from a downgoing fast wave or an upgoing fast wave from an upgoing slow wave, etc. MR means generation of an upgoing fast wave from a downgoing slow wave or an upgoing slow wave from a downgoing fast wave, etc.

Reflection is the dominant type of coupling at almost all heights. At 1070 km reflection type coupling for the slow wave becomes very large because of the ion cyclotron resonance. For the fast wave below this level the magnitude of the coupling is larger than or comparable to the quartic roots. For the slow wave below the resonance level coupling is of less importance than the quartic roots down to the D region. In the lower D region coupling becomes very large for the slow and fast modes. Mode reflection type coupling also appears. The plane wave case produces no mode reflection type coupling in the lower D region. Therefore this effect is due to the localized nature of the disturbance.

Reflection type coupling occurs within the surface layer of the Earth and is a maximum at a depth of about 2.5 km. This reflection region corresponds to the rapid change in the earth conductivity. In this region the coupling coefficients are smaller than the quartic roots but are of comparable magnitude at a depth of 2.5 km.

Characteristic Wave Mixing Ratios

The mixing ratios for the incident fast wave are given in Figure 4 and show that above 1070 km the resultant wave fields consist primarily of a downgoing fast wave (DF) but with some partial reflection occurring as may be seen by the presence of a small amount of the

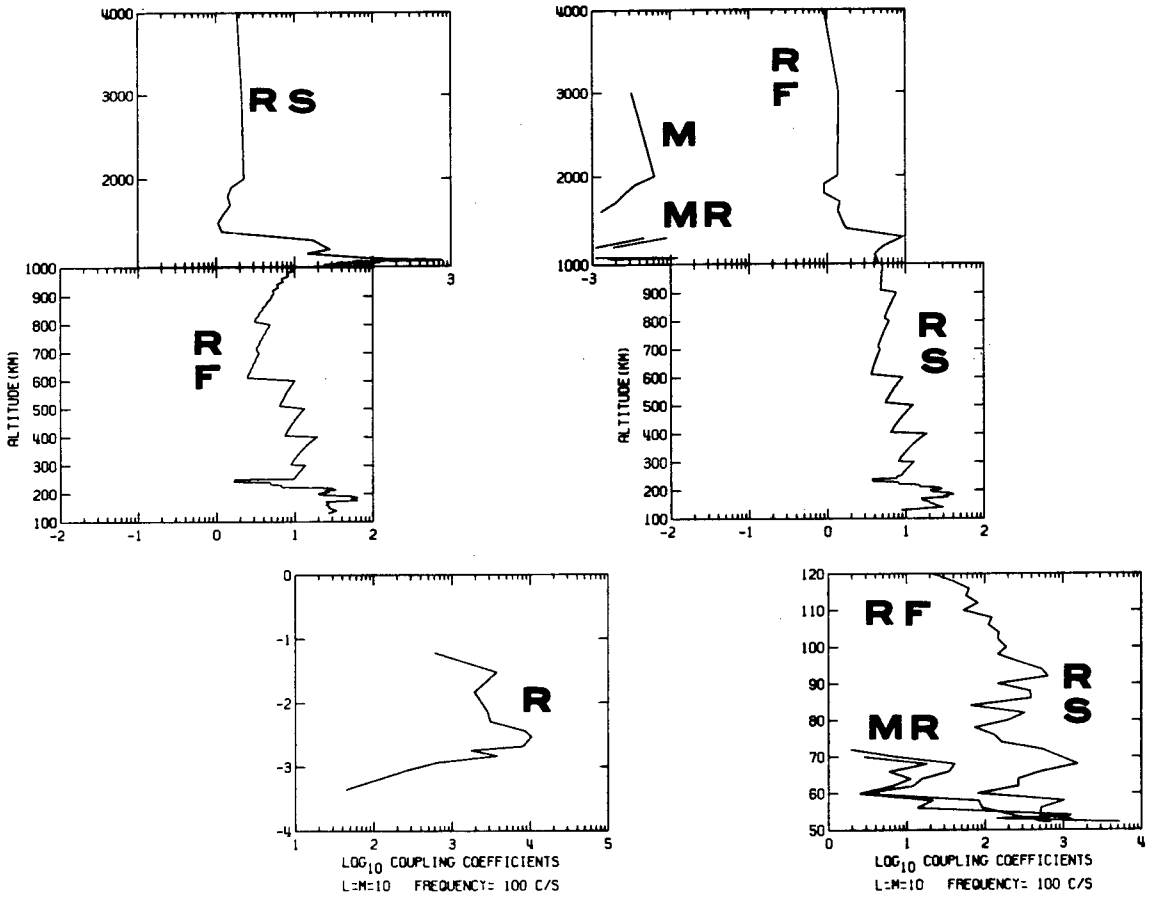

Figure 3 **MAGNETO-IONIC COUPLING**

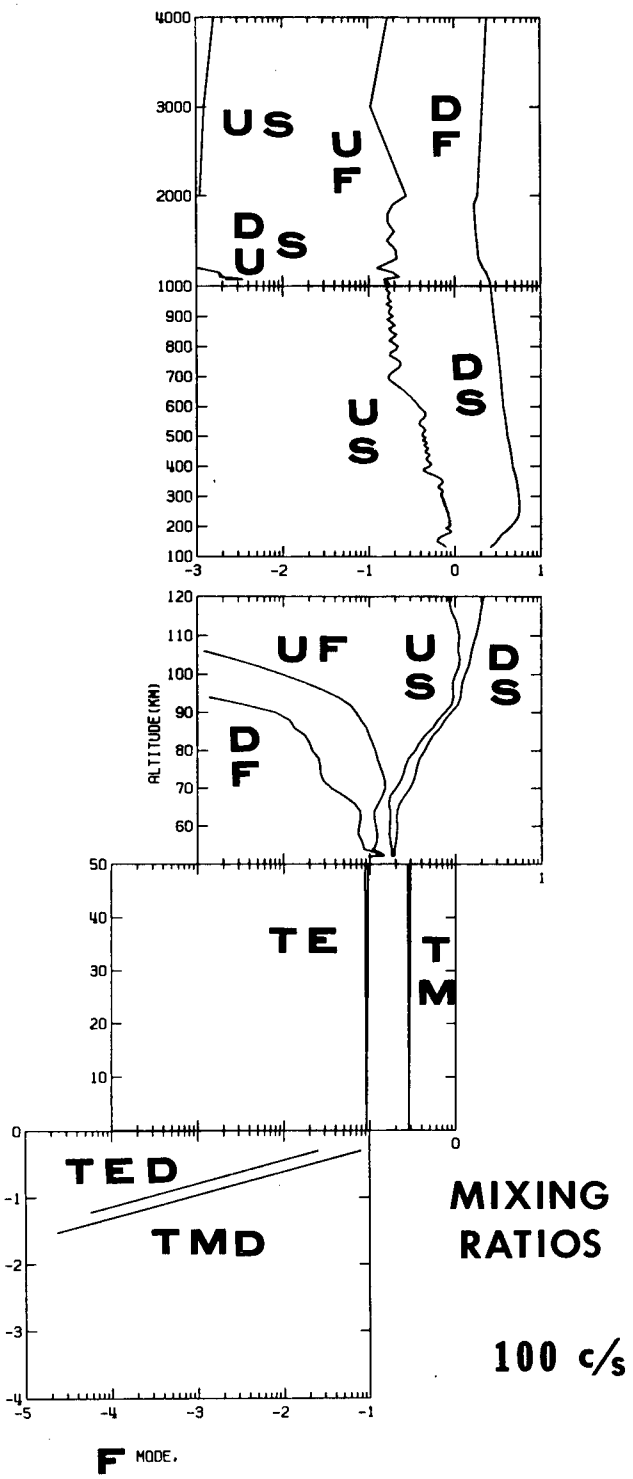
US
UF
DF
DU
DS
US
DS
UF
US
DS
DF
TE
TM
TED
TMD
MIXING
RATIOS
100 c/s
ALTITUDE(KM)
F MODE.

Figure 4

upgoing fast wave (UF). The mixing ratio for the upgoing fast wave exhibits a standing wave nature due to reflection from the ion cyclotron resonance level. The downgoing slow wave (DS) is generated by mode coupling, which may also be seen in the coupling coefficients in Figure 3. The upgoing slow (US) wave is generated by mode reflection type coupling, again also seen in Figure 3. However, these last two waves offer only a small contribution to the total wave field.

From 1070 km down through the D region the dominant mixing ratio is that of the downgoing slow wave. (Remember that below the critical reflection layer the R mode becomes a slow wave.) Some partial reflection is seen throughout this altitude range as evidenced by the mixing ratio for the upgoing slow wave. Between 700 and 1000 km there is a standing wave due to the ion mass changing very rapidly. The standing wave between 300 and 600 km is caused by the upper slope of the F maximum electron density. There is also a standing wave centered on the F region maximum.

In the D region the mixing ratios for the downgoing and upgoing fast waves grow rapidly as a consequence of the mode reflection type coupling already seen in Figure 3. This effect is due to the localized nature of the disturbance.

In the neutral atmosphere and in the ground the transverse magnetic (TM) wave is larger than the transverse electric (TE). The earth acts as a good conductor and almost complete reflection occurs as seen from the approximate equality of the downgoing and upgoing parts of the TM and of the TE waves. The mixing ratios are attenuated logarithmically in the ground and only downgoing waves are present. Although the coupling coefficients indicate that reflection occurs for both the transverse magnetic and transverse electric modes between about 1 and 3 km depth this process has negligible effect on the resultant mixing ratios and wave fields due to the fact that the quartic roots are larger than the coupling coefficients and are therefore more important in determining the final wave field characteristics.

The mixing ratios for the incident slow wave may be seen in Figure 5. The equality of the mixing ratios for the downgoing slow and upgoing slow waves indicates that complete reflection takes place at 1070 km, the ion cyclotron resonance level. Thus the slow mode (i.e., the L mode) is completely nonpenetrating below this level. This result is in agreement with the prediction of the CMA diagram that the wave normal surface for the L mode disappears upon crossing the L = infinity surface from lower to higher frequencies.

Wave Fields

The wave fields of the incident fast wave are shown in Figure 6. The magnitudes of the electric and magnetic fields are all relative to the values at 4000 km. If the magnetic field values are multiplied

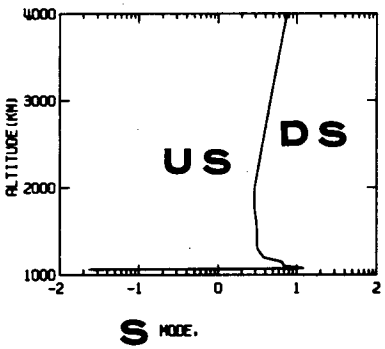

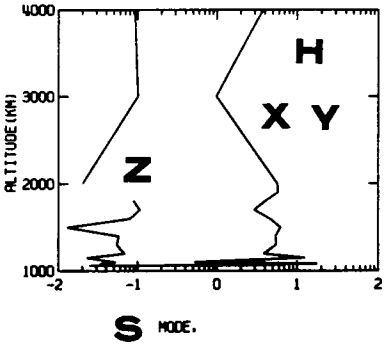

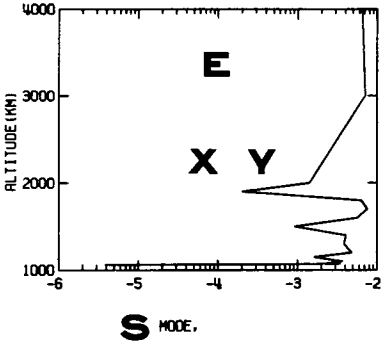

MIXING RATIOS

WAVE FIELD

100 c/s

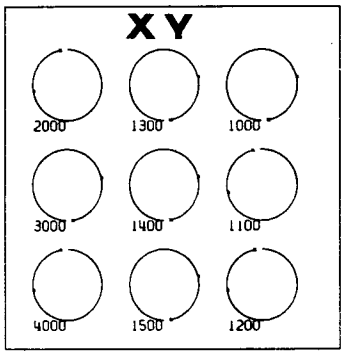

H S MODE.

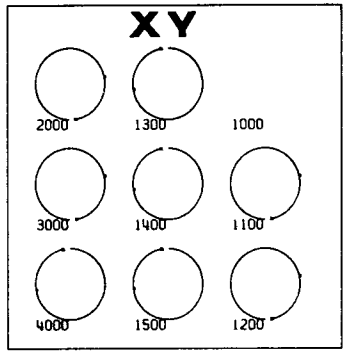

E S MODE.

POLARIZATION

Figure 5

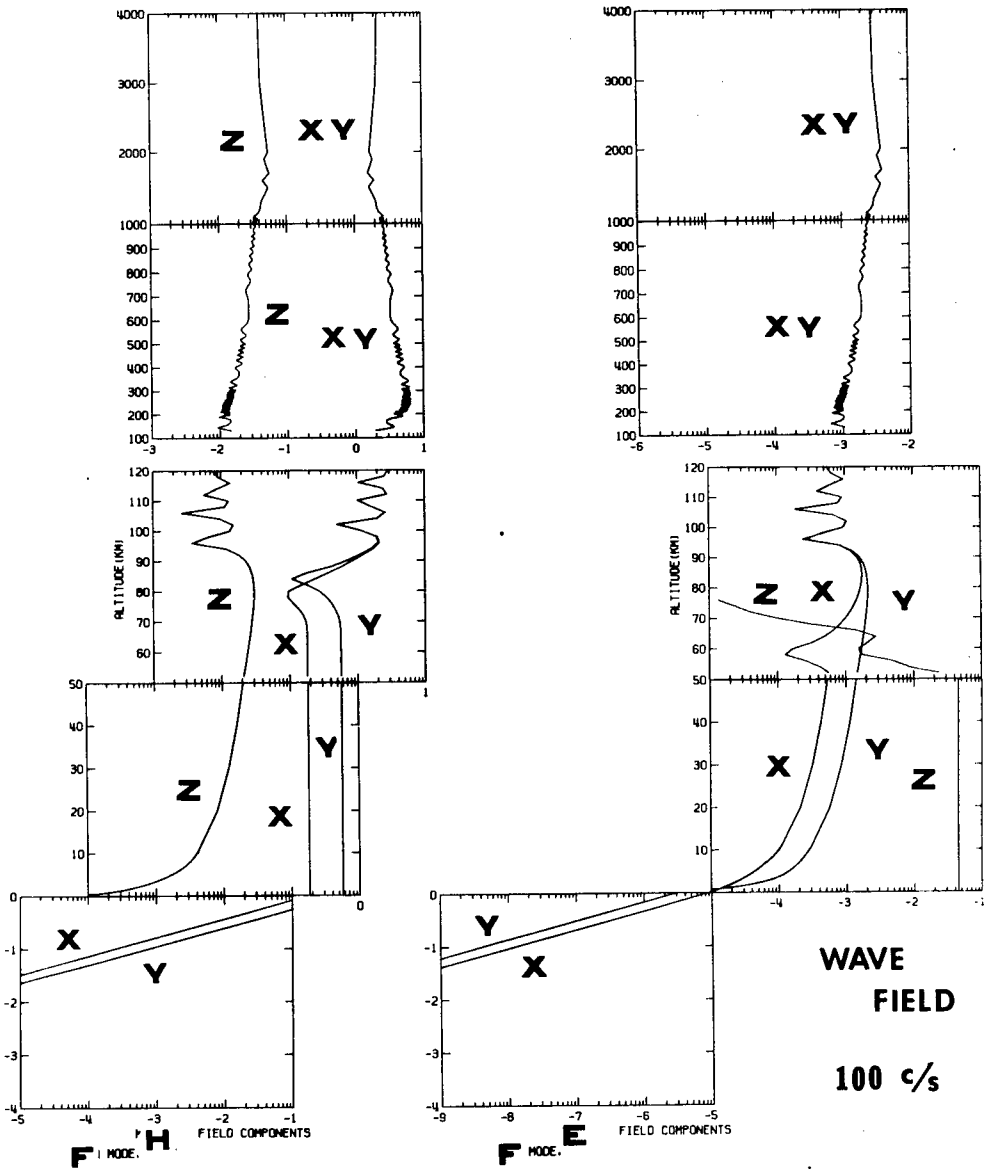

Figure 6

by a factor of 0.25 the B field is then obtained in gammas (1 gamma = 10^{-5} gauss). The electric field is read directly in volts/meter. The letters X, Y, Z stand for the X, Y, and Z components of the field quantities.

The wave fields exhibit the same standing wave characteristics as the mixing ratios in the F region. The standing wave above 1070 km is due to partial reflection at the ion cyclotron resonance level. The standing wave between 700 and 1000 km is due to the rapid change in the average ion mass. The standing wave between 300 and 600 km is caused by partial reflection from the upper slope of the F maximum electron density. A standing wave is also centered on the F layer maximum. Standing waves are visible in the wave fields down through the E region but are less obvious in the D region and neutral atmosphere. In the D region mode coupling produces the separation in the X and Y components of the electric and magnetic fields and an increase in the Z-component of the electric field. The electric field remains essentially vertical throughout the neutral atmosphere and must cause charge separation to occur between the Earth's surface and the lower ionosphere. In the ground the fields are attenuated logarithmically.

The wave fields for the incident slow wave (see Figure 5) display a standing wave effect above 1070 km due to reflection from the ion cyclotron resonance level. The fields are completely zero below this level and further substantiate the fact that the L mode is nonpenetrating beyond the ion resonance level.

Wave Field Polarization

The polarizations of the electric and magnetic wave fields for the incident fast wave are given in Figure 7. The labelling at the top of each diagram specifies the plane in which the polarization is plotted. For example, "YZ" implies that the Y component of the field quantity is plotted along the horizontal direction and the Z component is plotted along the vertical direction. The number under each polarization curve represents the altitude in km for which that polarization plot is valid. The Earth's magnetic field is directed inward and rotation in the clockwise direction represents right-handed polarization. To obtain the direction of rotation the gap in the polarization curve must first be found. That side of the gap which is marked with an "X" represents the beginning point. At 90^{o} to the "X" is a dot and the rotation sense is obtained by proceeding from the "X" to the dot. At each altitude the plot is normalized to the larger of the two components being plotted. Thus in order to determine the relative sizes of plots at different altitudes one must determine the wave field magnitudes from Figure 6.

In the X-Y plane the electric and magnetic fields are right circularly polarized down to the D region. Due to the mode coupling

POLARIZATION

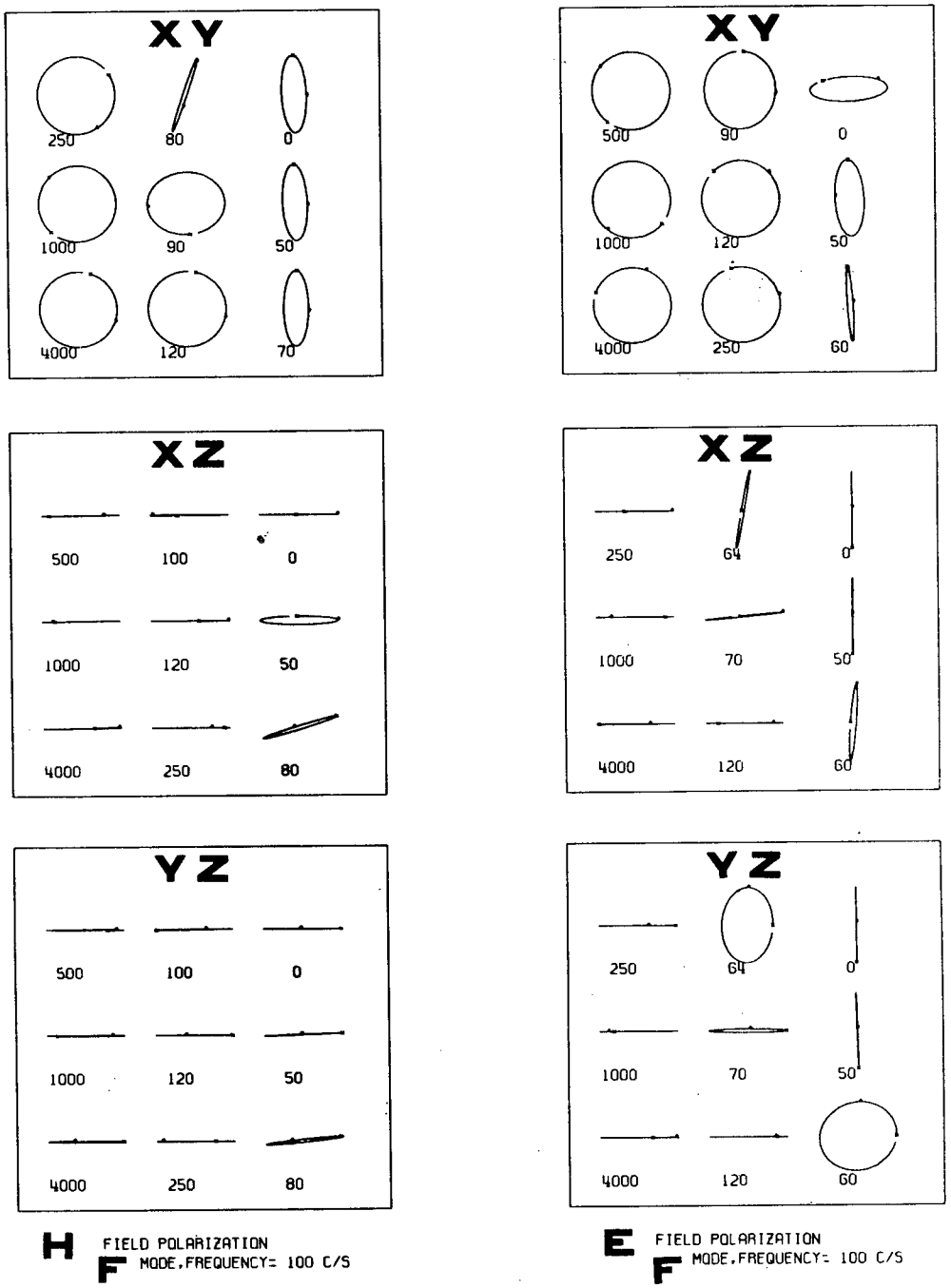

H FIELD POLARIZATION
F MODE,FREQUENCY= 100 C/S

E FIELD POLARIZATION
F MODE,FREQUENCY= 100 C/S

Figure 7

which produces a separation in the X and Y components of the electric and magnetic fields in the D region the fields become elliptically polarized in the lower ionosphere. At 50 km the electric field becomes left elliptically polarized and then changes back to right elliptically polarized at ground level. Thus the fast mode which is polarized in the right hand sense at 4000 km is also right handed polarized at ground surface.

However, on the Earth's surface the X and Y components of the electric field are smaller than the Z component by three and four orders of magnitude respectively. Thus the XZ and YZ planes are more important than the XY plane. In these planes the electric field on the ground is linearly polarized.

The incident slow mode is left circularly polarized throughout the region above the ion cyclotron resonance level.

COMPARISON OF PLANE WAVE AND LOCALIZED DISTURBANCE CASES AT 100 C/S

Comparison of the effects of the plane wave and localized disturbance shows very little difference between the incident slow modes. Both are nonpenetrating below about 1070 km and in both cases the downgoing slow wave is reflected in the form of an upgoing slow wave. The major difference seems to be that the wave fields of the plane wave are pi out of phase with those of the localized disturbance. However, comparison of the incident fast modes does reveal some differences. Because there is no propagation in the horizontal direction the plane wave propagates vertically through the neutral atmosphere with a phase velocity equal to the speed of light. Thus the neutral atmosphere behaves like free space for the plane wave but appears as an elastic evanescent region to the localized disturbance.

Also, mode coupling and mode reflection type coupling appear for the localized disturbance in the lower D region but no such coupling appears for the plane wave. Reflection of the slow mode however still occurs throughout the ionosphere for the plane wave just as it does when the localized disturbance effect is introduced. The Z components of the electric and magnetic fields are zero everywhere for the plane wave and the electric field polarization in the XY plane remains right circularly polarized throughout the ionosphere and the neutral atmosphere. In contrast the localized effect produces a Z component of the magnetic field throughout the ionosphere and atmosphere and a Z component of the electric field in the lower D region and neutral atmosphere. The Z components are due to the additive interference of the upgoing and downgoing waves. Therefore only the localized disturbance gives rise to charge separation between ground level and the lower ionosphere. Also the localized disturbance wave field polarizations changed considerably in the lower D region due to strong coupling.

Within the Earth the horizontal components for both the electric and magnetic fields are equal in the plane wave case but the localized disturbance gives rise to an inequality in these components.

LOCALIZED DISTURBANCE AT 3.0 C/S

Booker Quartic Roots

The Booker quartic roots are presented in Figure 8. The labelling used in this figure is the same as that used in Figure 2. The actual values of the index of refraction for propagation in the vertical direction are obtained by multiplying the values read from the curves in Figure 8 by a factor of 2.50.

Comparison of the real and imaginary parts of the quartic roots reveals that both the slow and fast modes are propagating down to about 150 km. The region above 1000 km is slightly anisotropic. At 1000 km mode switching occurs and the incident slow wave becomes a fast wave and the incident fast wave becomes a slow wave. At 150 km mode switching again occurs with the slow mode changing back to the fast mode and vice versa. Later we shall see that the wave fields undergo a polarization reversal at 1000 km but not at 150 km. This region between 1000 km and 150 km is quasi-isotropic. Between 220 km and 160 km the slow and fast waves are indistinguishable and this region is completely isotropic. The fast wave is evanescent between 150 km and the Earth's surface. The slow wave is propagating down to about 70 km at which point it becomes evanescent and remains as such down to ground level. The lower D region between about 70 km and 50 km is quasi-isotropic. The phase velocities of the fast and slow waves reach their maximum values around 250 km and 120 km, respectively.

The neutral atmosphere is isotropic and the quartic roots for this region are pure imaginary due to the localization of the disturbance. The interior of the Earth is also isotropic and behaves as a metal.

Magneto-ionic Coupling Coefficients

Figure 9 reveals the altitude dependence of the magneto-ionic coupling coefficients for the localized disturbance at 3.0 c/s. These curves have the same nomenclature attached to them as that used in Figure 3.

Reflection type coupling is dominant down to about 1000 km. At this altitude there is a strong mode coupling layer caused by the equality of the fast and slow wave quartic roots, i.e., the medium rapidly approaches isotropic conditions. Reflection type coupling for both the slow and fast modes once again becomes the major coupling process below about 900 km and remains dominant down to the lower D

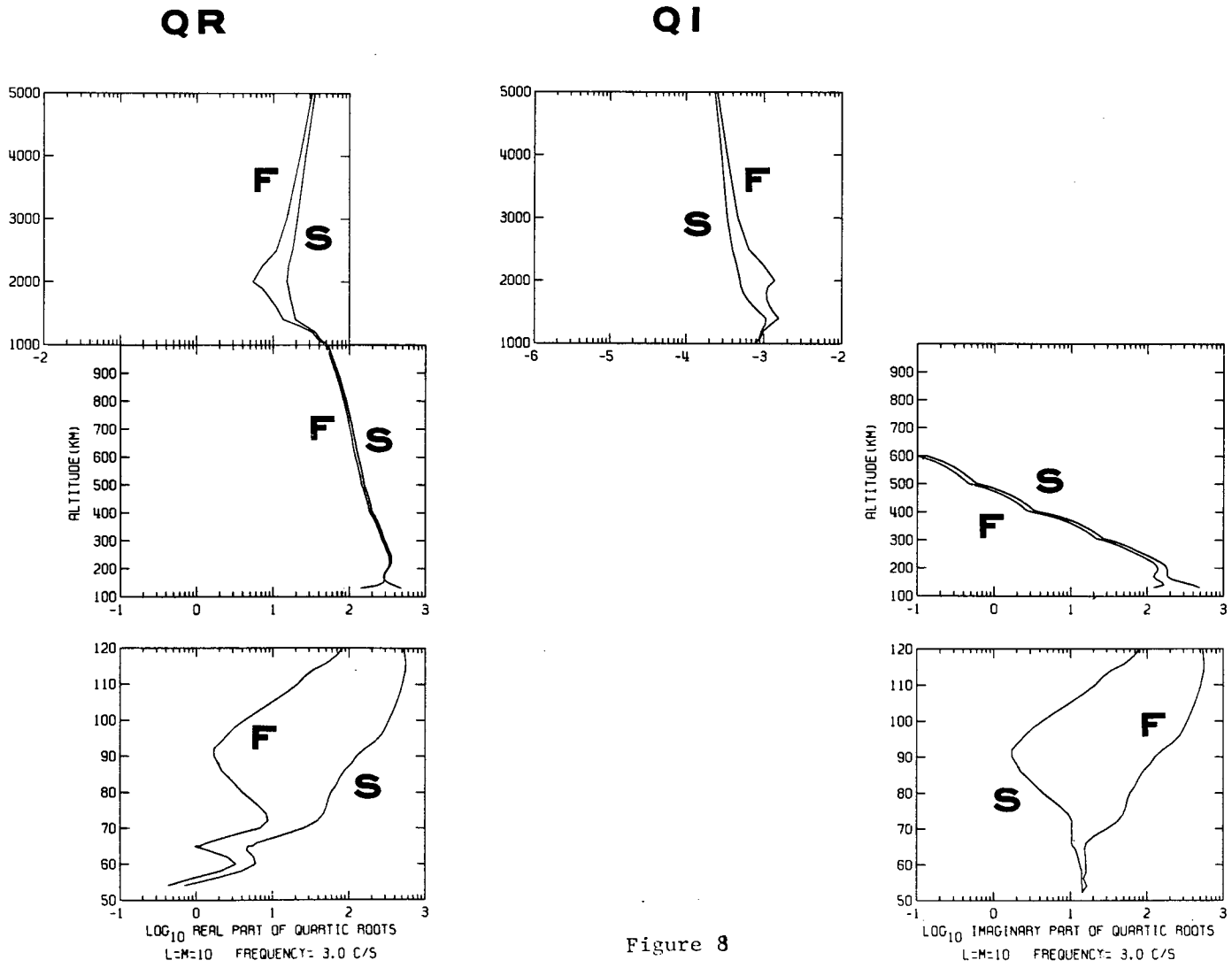
QR
QI
F
S
ALTITUDE(KM)
LOG10 REAL PART OF QUARTIC ROOTS
LOG10 IMAGINARY PART OF QUARTIC ROOTS
L=M=10 FREQUENCY= 3.0 C/S

Figure 8

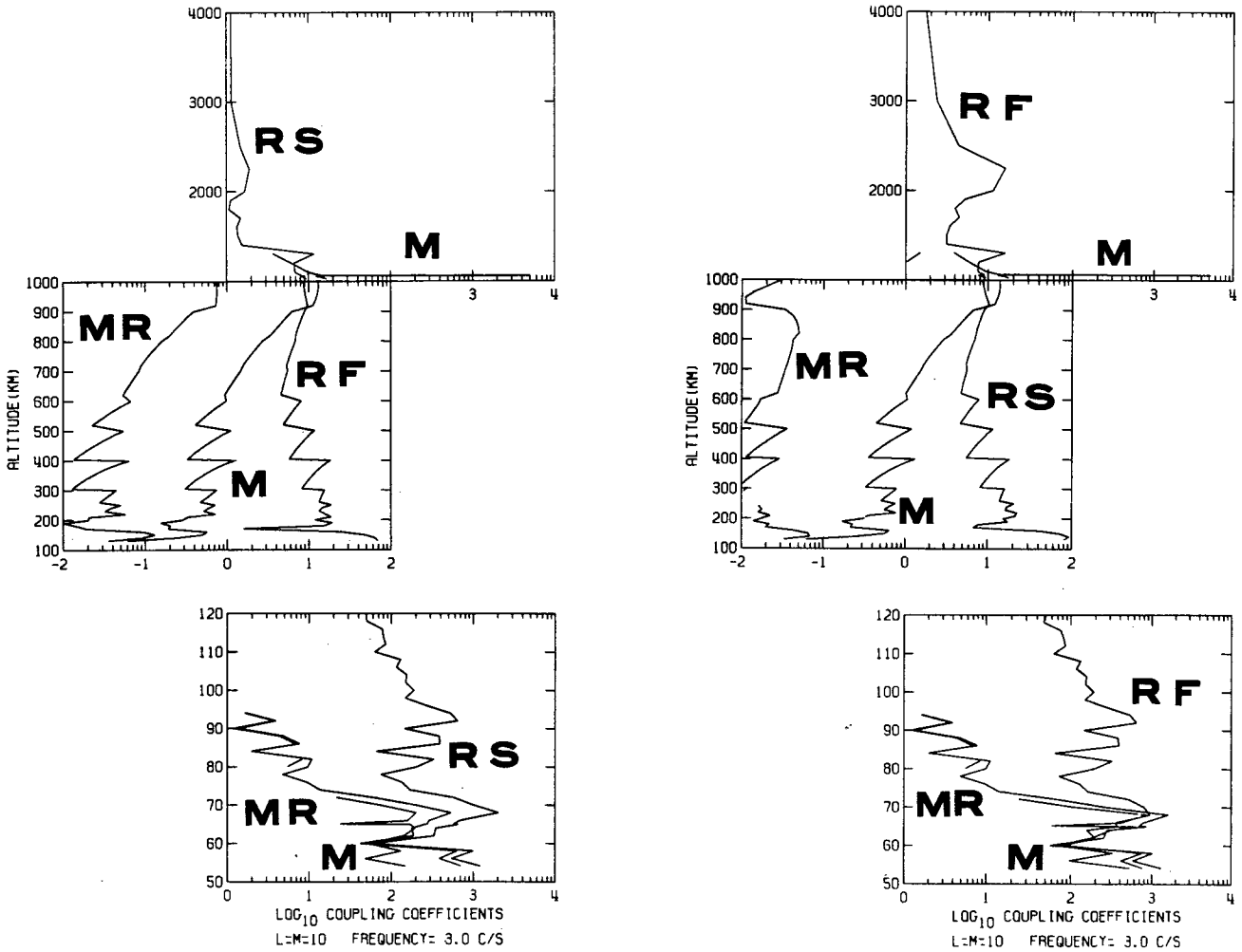

Figure 9 **MAGNETO - IONIC COUPLING**

region. In the F region mode coupling and mode reflection type coupling are also present due to the quasi-isotropic nature of the F region. These coupling processes become small in the E region because the medium is anisotropic and reappear in the lower D region due to the localized disturbance. Thus coupling is of importance in the D and F regions but not in the E region. The quartic roots are larger than the coupling coefficients throughout the F region except for the region around 1000 km where mode coupling becomes very large. The fast wave quartic roots are smaller than the coupling coefficients throughout the D and E regions. The coupling coefficients become larger than the slow wave quartic roots below about 95 km. Coupling in the neutral atmosphere is, of course, zero.

As with the 100 c/s case, reflection type coupling occurs in the surface layer of the Earth and reaches a maximum at a depth of about 2.5 km. This reflection process corresponds to the rapid change in the ground conductivity. The coupling coefficients in this region are smaller than the quartic roots but become of similar magnitude around a depth of 2.5 km. The medium inside the Earth is isotropic and behaves as a metal.

Characteristic Wave Mixing Ratios

The characteristic wave mixing ratios for the incident slow and fast waves at 3.0 c/s are depicted in Figure 10. The labelling used for these curves is identical to that used in Figure 4.

In the region above 1000 km the resultant wave for the incident slow mode consists primarily of the downgoing slow wave. The presence of the upgoing slow wave is indicative of reflection taking place throughout the region. The downgoing and upgoing fast waves are also present and are generated by mode coupling and mode reflection type coupling. In the F region below 1000 km the downgoing fast and downgoing slow waves are nearly equal in magnitude due to the strong coupling associated with this quasi-isotropic region. The upgoing fast and upgoing slow waves are also present due to reflection from the F region maximum. The standing wave formation in these upgoing waves is quite obvious. Around 200 km the real and imaginary parts of the quartic roots are equal as in a conductor. Therefore this level will behave as the upper conducting wall of a cavity with the other conducting wall being the Earth's surface. This fact is borne out when we look at the standing wave formation observed in the wave fields in the next section. Below this level in the D and E regions the downgoing slow and upgoing slow waves are almost equal, indicating that reflection is continuously taking place. In the neutral atmosphere the incident slow wave is comprised of both transverse electric and transverse magnetic waves with the transverse electric being dominant. Both the TE and TM modes are reflected quite well at ground surface. Reflection of the transverse electric wave is also seen to take place within the Earth and the maximum of the reflected wave occurs at a depth of about two km, near the conductivity maximum.

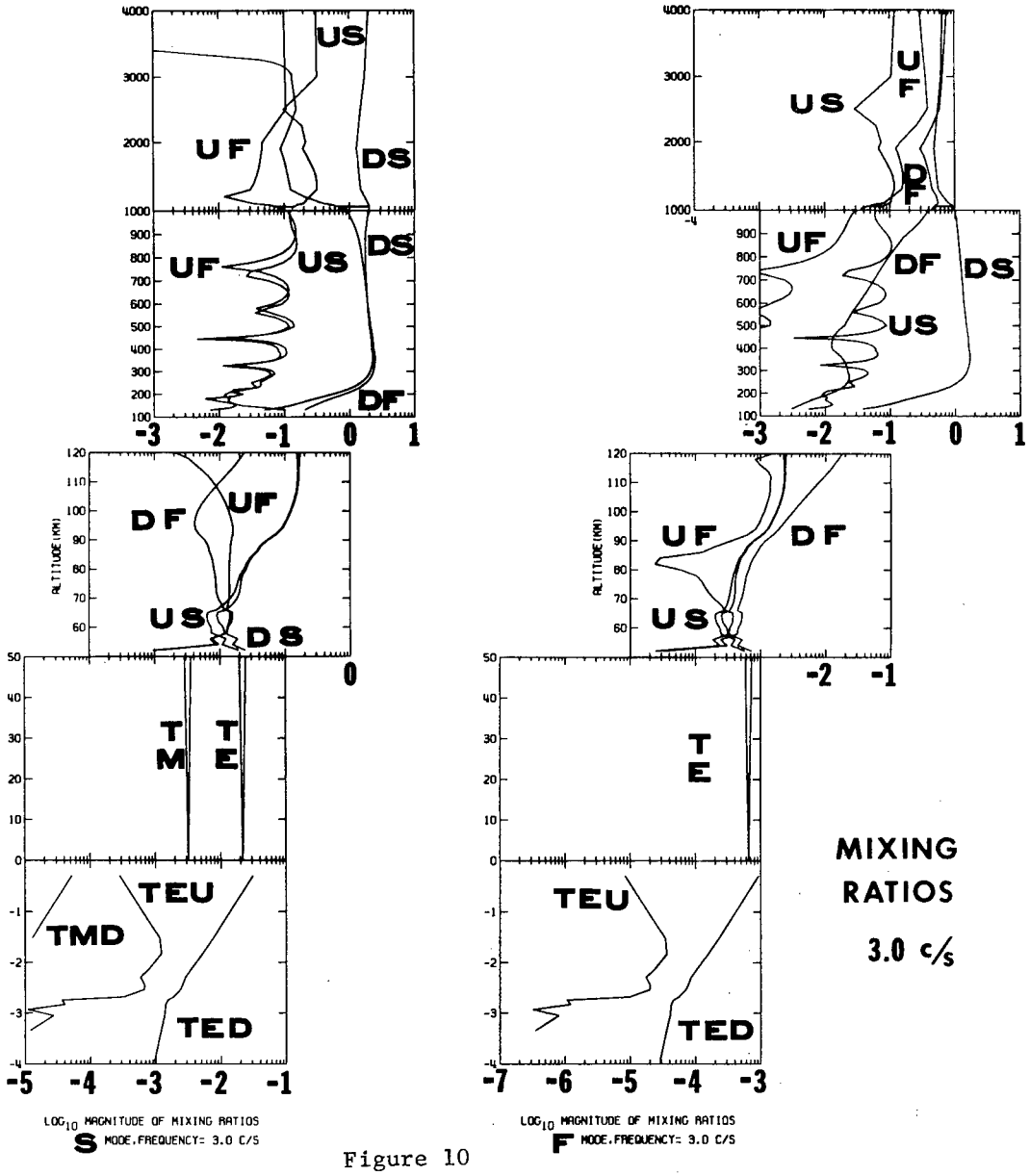
US
UF
DS
UF
US
DS
DF
DF
UF
TMD
TEU
TED
T M
T E
ALTITUDE (KM)
LOG10 MAGNITUDE OF MIXING RATIOS
S MODE, FREQUENCY= 3.0 C/S
US
UF
DF
UF
DF
DS
US
UF
DF
US
T E
TEU
TED
LOG10 MAGNITUDE OF MIXING RATIOS
F MODE, FREQUENCY= 3.0 C/S
MIXING RATIOS
3.0 c/s

Figure 10

For the incident fast wave above 1000 km all of the characteristic waves are of the same order of magnitude. The upgoing waves are generated by reflection and mode reflection type coupling. Although this region is anisotropic it is sufficiently close to being isotropic that mode coupling and mode reflection type coupling are important. In fact the downgoing slow wave is at times larger than the downgoing fast wave. In the F region below 1000 km, where the slow wave becomes a fast wave and vice versa, the downgoing slow wave is dominant and a standing wave formation occurs in the reflected upgoing slow wave. The downgoing fast and upgoing fast waves are also present due to mode coupling and mode reflection type coupling, respectively, resulting from the quasi-isotropic nature of this region. In the D and E regions the reflected upgoing fast wave is smaller than the downgoing and upgoing slow waves, which are generated by mode coupling and mode reflection type coupling, respectively. Thus the D and E regions will not act to store energy for the incident fast wave as readily as for the incident slow wave. This fact will be easily seen from inspection of the wave fields. In the neutral atmosphere the incident fast wave is transverse electric and is reflected quite well at the Earth's surface. Inside the Earth the incident fast wave is primarily comprised of the downgoing transverse electric mode. However reflection produces a small amount of the upgoing transverse electric mode which reaches a maximum at a depth of about two km, near the conductivity maximum.

Wave Fields

The wave fields of the incident slow wave are shown in Figure 11. The magnitudes of the electric and magnetic fields are all relative to the values at 4000 km. If the magnetic field values are multiplied by a factor of 8.33 the B field is then obtained in gammas. The electric field is read directly in volts/meter.

The incident slow wave disturbance is primarily transverse magnetic at the top of the ionosphere and becomes transverse electric in the ground. In the region above 1000 km a standing wave character is exhibited and is due to reflection from the interface separating the anisotropic region above 1000 km from the quasi-isotropic region below 1000 km. Standing waves are also seen in the region between 150 and 1000 km and are due to reflection within this isotropic region.

Standing waves are still discernible down through the D region and neutral atmosphere but are of considerably longer wavelengths than were seen in the F region. The Y component of the magnetic field decreases and the Z component of the electric field increases through the D region due to coupling caused by the localized disturbance. In the neutral atmosphere the Z component of the electric field persists and must result in charge separation between the lower ionosphere and ground level.

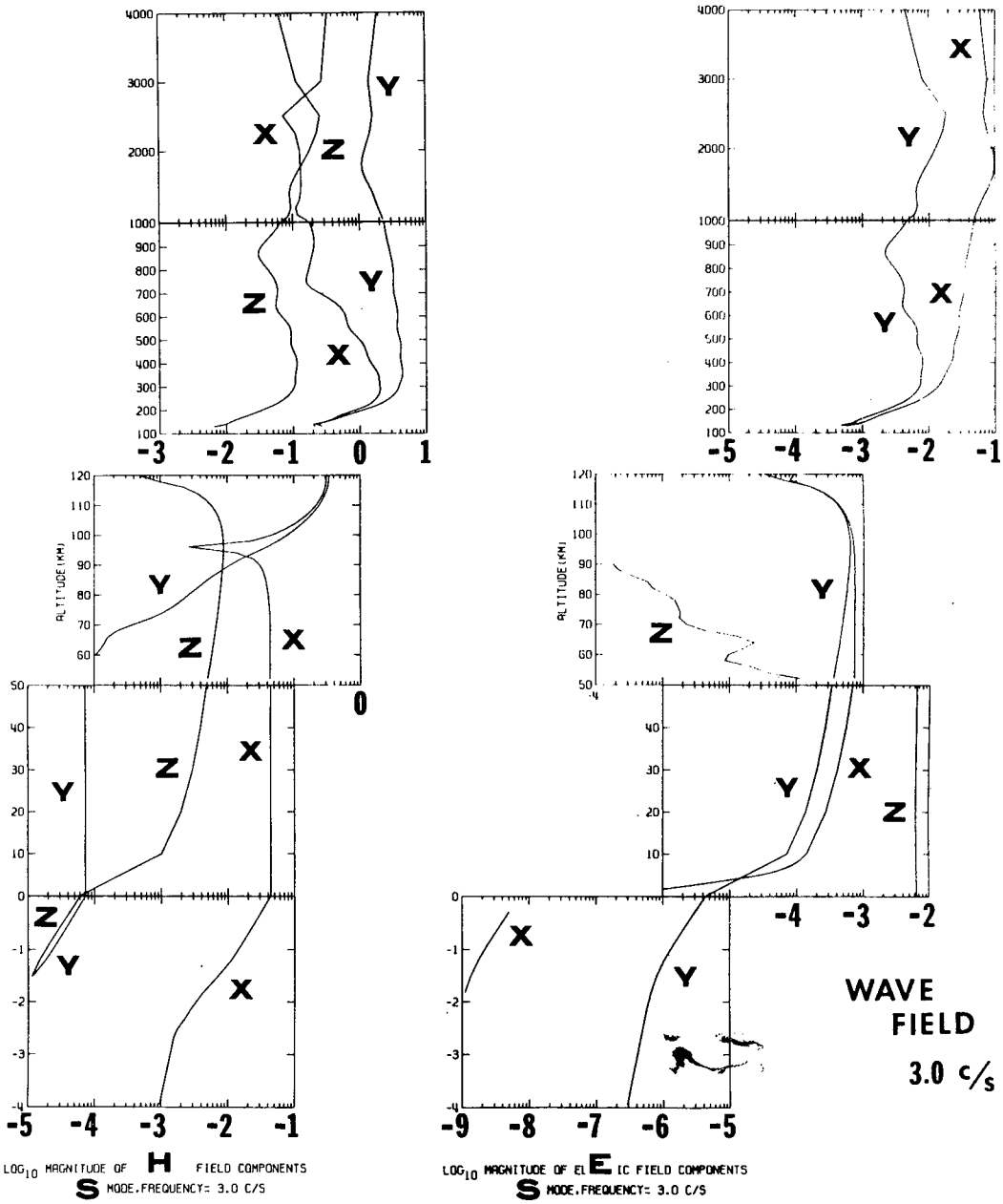
ALTITUDE (KM)
WAVE
FIELD
3.0 c/s
LOG10 MAGNITUDE OF H FIELD COMPONENTS
S MODE, FREQUENCY= 3.0 C/S
LOG10 MAGNITUDE OF ELECTRIC FIELD COMPONENTS
S MODE, FREQUENCY= 3.0 C/S

Figure 11

The X component of the magnetic field grows gradually throughout the F region and becomes nearly equal to the Y component in the E region. The X and Y magnetic field components are again separated in the D region due to coupling. The X component is dominant at ground level and implies that the Y component is dominant at 4000 km.

The electric field has a similar behavior with the X and Y components being well separated in the D and F regions because of coupling. In the E region the X and Y electric field components are nearly equal.

Within the Earth the electric and magnetic fields are horizontal. The skin depth for these fields within the Earth's surface is less than one km.

The wave fields for the incident fast wave are depicted in Figure 12. At the top of the ionosphere the disturbance is neither transverse magnetic nor transverse electric. However, the disturbance is transverse electric at all altitudes below 110 km. As was true of the incident slow wave, standing waves are observed above 150 km with the magnetic field envelope reaching a maximum around the F region electron density maximum. The field components become well separated in the D region due to mode coupling. At ground level the magnetic field is primarily in the X direction and the electric field is in the Y direction. Unlike the incident slow wave no electric field Z component is generated in the neutral atmosphere. Therefore the incident fast wave will not generate charge separation between the ground and the lower ionosphere. Also, the electric field is attenuated by five orders of magnitude between 4000 km and the ground. Therefore the electric field of a disturbance generated at 4000 km may be difficult to observe on the ground.

The disturbance within the Earth is transverse electric and the skin depth is less than one km.

Wave Field Polarization

The wave field polarizations for the incident slow and fast waves are given in Figures 13 and 14, respectively. The labelling of these graphs is the same as that used in Figure 7.

The electric field of the incident slow wave is left elliptically polarized in the XY plane at 4000 km with the major axis in the X direction. The electric field of the incident fast wave is also elliptically polarized at 4000 km but in the right hand sense. Thus the slow and fast waves at 4000 km may be discriminated by observation of the electric field polarization. The slow and fast modes at 4000 km may also be differentiated by observing the magnetic field polarization, which is left elliptically polarized for the incident slow wave and right elliptically polarized for the fast wave. However, on

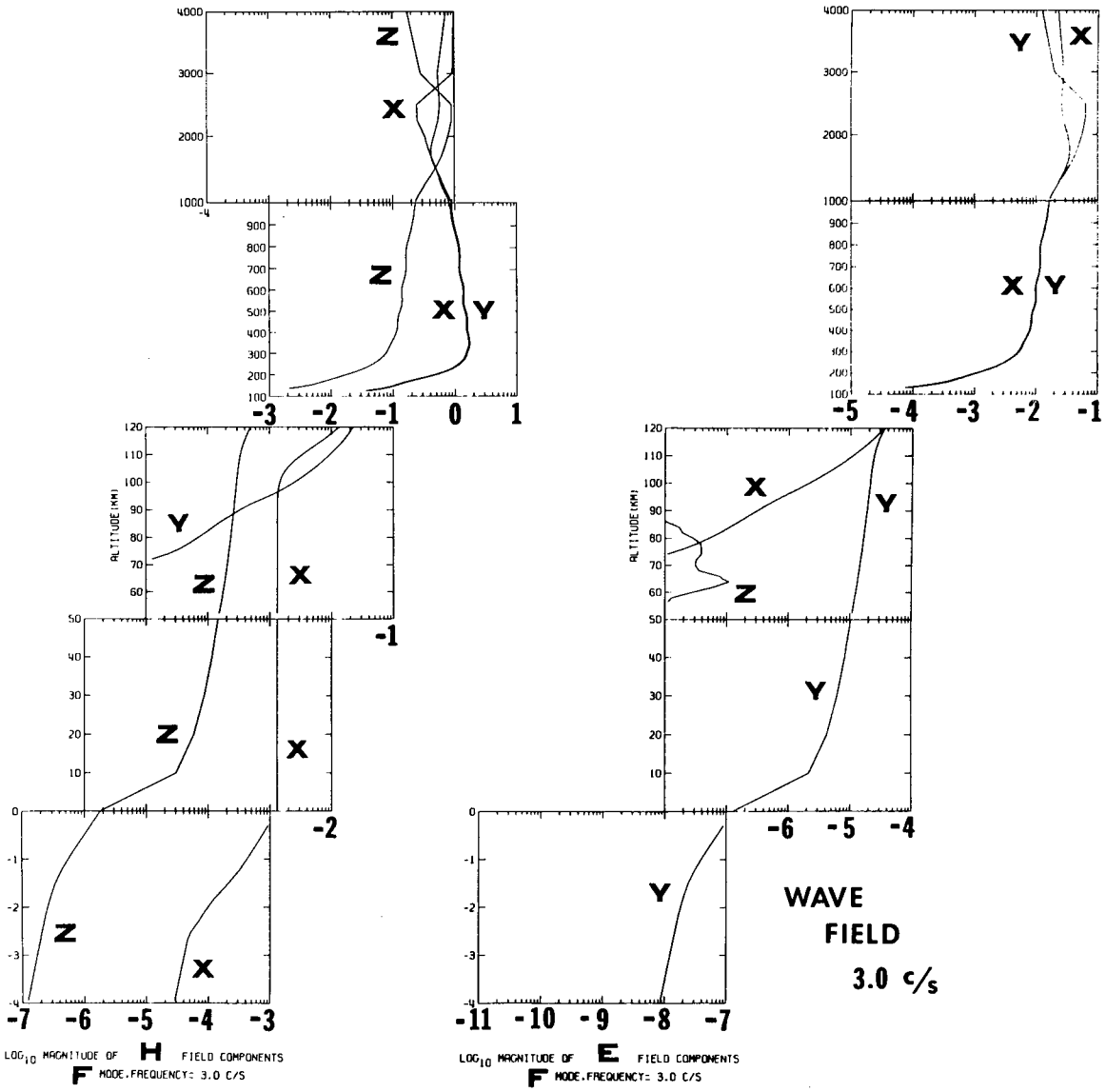
ALTITUDE (KM)
Z
X
Y
-3 -2 -1 0 1
-5 -4 -3 -2 -1
-1
-2
-7 -6 -5 -4 -3
-6 -5 -4
-11 -10 -9 -8 -7
WAVE
FIELD
3.0 c/s
LOG10 MAGNITUDE OF H FIELD COMPONENTS
F MODE. FREQUENCY= 3.0 C/S
LOG10 MAGNITUDE OF E FIELD COMPONENTS
F MODE. FREQUENCY= 3.0 C/S

Figure 12

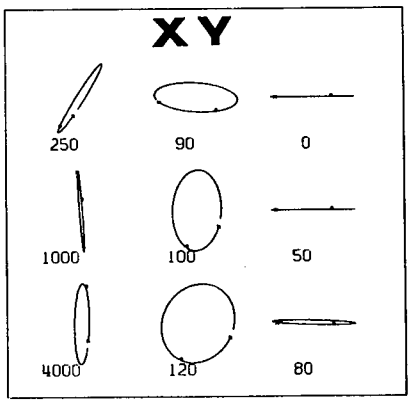

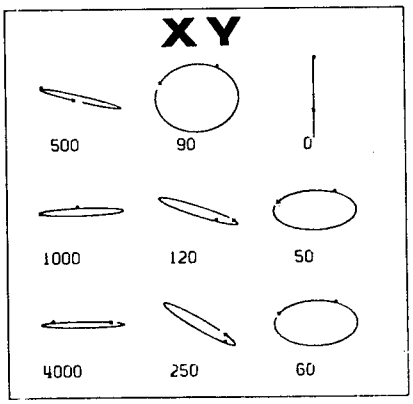

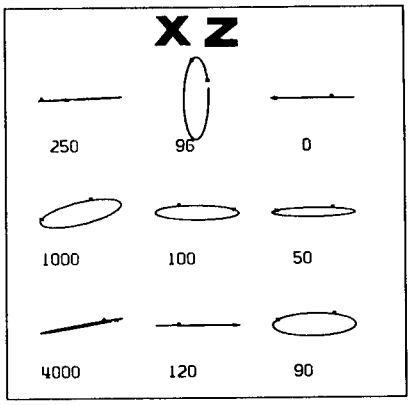

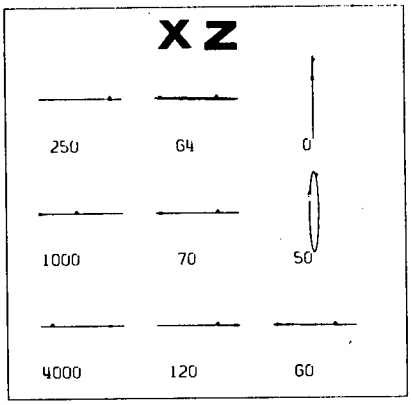

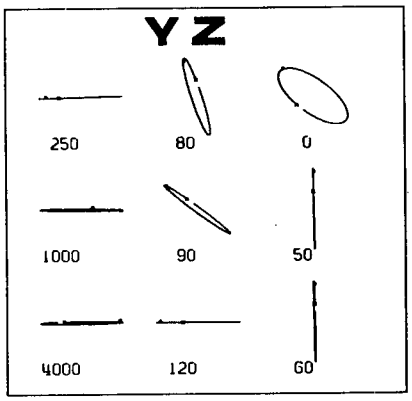

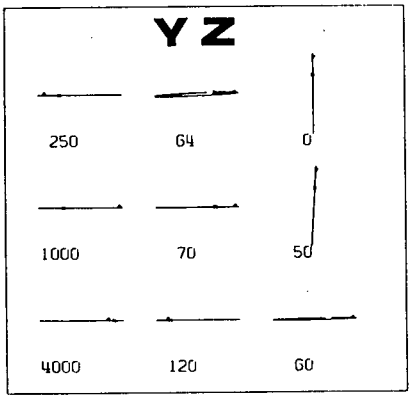

H FIELD POLARIZATION
S MODE,FREQUENCY= 3.0 C/S

E FIELD POLARIZATION
S MODE,FREQUENCY= 3.0 C/S

Figure 13

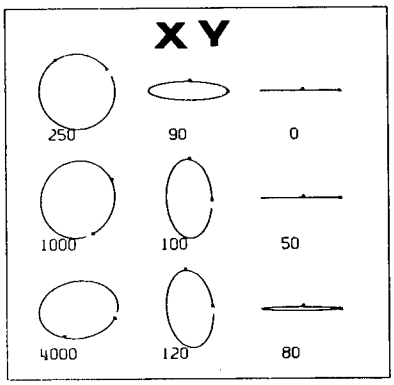

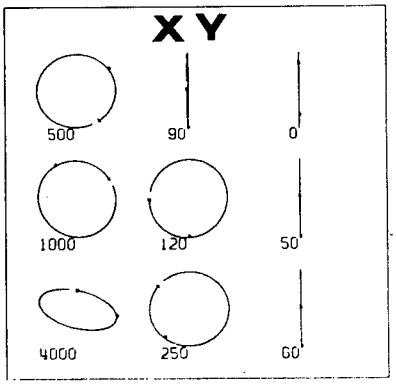

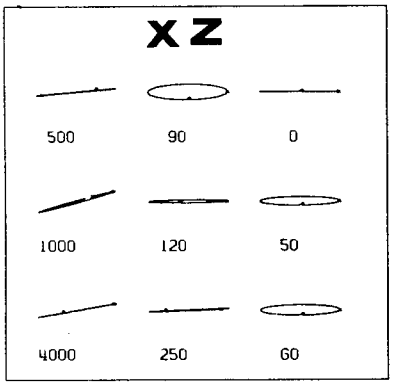

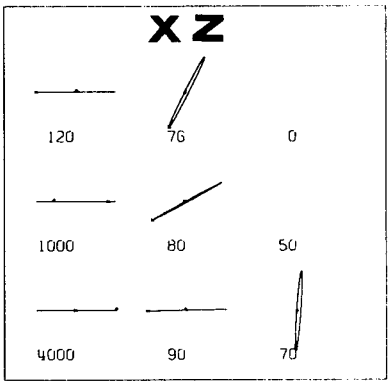

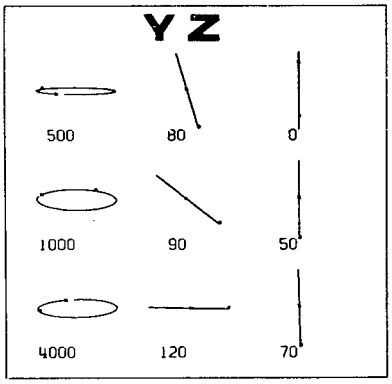

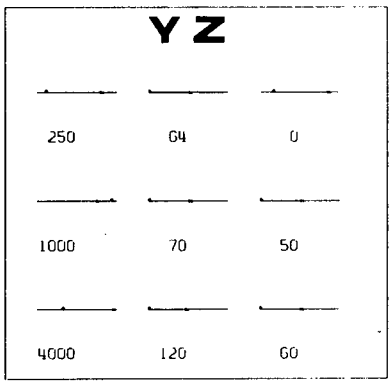

H FIELD POLARIZATION
F MODE,FREQUENCY= 3.0 C/S

E FIELD POLARIZATION
F MODE,FREQUENCY= 3.0 C/S

Figure 14

the ground the electric and magnetic field polarizations in the XY plane are linear in the same fashion for both the incident slow and incident fast waves. The two disturbances may be identified on the ground only by observation of the Z component of the electric field, which is zero for the incident fast wave and nonzero for the incident slow wave.

The electric and magnetic fields of both the incident slow and fast waves undergo a polarization reversal in the XY plane at approximately 1000 km. This polarization reversal is due to the sudden change of the medium from anisotropic above 1000 km to quasi-isotropic below 1000 km. Also the magnetic field of the incident slow wave changes back to left elliptically polarized in the XY plane at 90 km, which corresponds to the point at which the X component of the magnetic field becomes larger than the Y component.

The incident fast wave electric field is left circularly polarized between 1000 km and 100 km and then becomes linearly polarized in the Y direction. The incident slow wave electric field is right elliptically polarized between 1000 km and ground surface, at which point it becomes linearly polarized in the Y direction in the XY plane.

REFERENCES

Altman, C., and H. Cory, The simple thin-film optical method in electromagnetic wave propagation, Radio Sci., 4, 449-457, 1969a.

Altman, C., and H. Cory, The generalized thin-film optical method in electromagnetic wave propagation, Radio Sci., 4, 459-470, 1969b.

Barron, D. W., and K. G. Budden, The numerical solution of differential equations governing the reflexion of long radio waves from the ionosphere, 3, Proc. Roy. Soc. London, A, 249 (1258), 387-401, 1959.

Budden, K. G., The numerical solution of differential equations governing ~~the~~ reflexion of long radio waves from the ionosphere, 1, Proc. Roy. Soc. London, A, 227 (1171), 516-537, 1955.

Inoue, Y., and S. Horowitz, Magneto-ionic coupling in an inhomogeneous anisotropic medium, Radio Sci., 1, 427-440, 1966a.

Inoue, Y., and S. Horowitz, Numerical solution of full-wave equation with mode coupling, Radio Sci., 1, 957-970, 1966b.

Johler, J. R., and J. D. Harper, Reflection and transmission of radio waves at a continuously stratified plasma with arbitrary magnetic induction, J. Res. NBS, 66D (1), 81-99, 1962.

Pitteway, M. L. V., The numerical calculation of wave-fields, reflection coefficients and polarizations for long radio waves in the lower ionosphere, 1, Phil. Trans. Roy. Soc. London, A, 257 (1079), 219-241, 1965.

Stix, T. H., The Theory of Plasma Waves, McGraw-Hill Book Company, Inc., New York, N. Y., 1962.

Walsh, E. J., Full-wave solutions in terms of coupled vacuum modes, Radio Sci., 2, 913-925, 1967.

Acknowledgment:

This work has been supported by the Air Force Cambridge Research Laboratories, Bedford, Mass., under contract no. F 19628-67-C-0109.

TRANSMISSION OF ELECTROMAGNETIC WAVES THROUGH NORMAL AND DISTURBED IONOSPHERES

H. G. Booker*
C. M. Crain
E. C. Field

The RAND Corporation
1700 Main Street
Santa Monica, California

*Professor Booker's permanent address is the University of California at San Diego, La Jolla, California.

I. INTRODUCTION

In this paper we will present the results of an analysis of the transmission of electromagnetic waves through the ionosphere. The objective of the calculations is to provide estimates of the propagation losses to be expected on communication links between satellites and the ground. A wide range of frequencies, 10^{-3} Hz - 10^{10} Hz, is considered and normal and disturbed night-time and day-time conditions are analyzed. The models and computational methods are summarized briefly in Section II, extensive numerical results for the total transmission loss and height dependence of ionospheric attenuation are presented in Section III and the conclusions are given in Section IV.

II. MODEL IONOSPHERES AND COMPUTATIONAL METHODS

Calculations were made for four profiles of electron and ion density identified in Figure 1 as ambient night (AN), ambient day (AD), disturbed night (DN) and disturbed day (DD). The first two are nominal models of the undisturbed ionosphere and are representative of models in current use. The DN and DD models represent either a moderate nuclear environment or a very strong polar cap absorption event. The ion and electron collision frequency profiles used are essentially as given by Ginzburg,[1] a mass number of 29 was assumed for the ions, and the ground level electron gyrofrequency was taken as 1.7×10^6 Hz.

The major approximation is the use of WKB methods to compute the transmission loss. This, of course, neglects the effects of gradient reflection, thereby underestimating the transmission loss on a given link. Gradient reflection should be significant only when the wavelength in the ionosphere is comparable with or larger than the characteristic distance over which the medium changes substantially, i.e., a few kilometers. Thus, for frequencies above, say, 100 Hz, the transmission curves to be given should provide quite reliable estimates. However, as the frequency is lowered much below 100 Hz, the curves should be taken as order of magnitude lower bounds on the transmission loss. For example, the well known transmission resonances associated with geomagnetic micropulsation (freq $\lesssim$ 1 Hz) cannot be predicted without recourse to full-wave solutions. Rand has, in fact, run full-wave solutions to spot check some of the results to be given presently and, even for frequencies as low as a few Hz. the agreement was found to be better than within an order of magnitude.

The calculations have been done for waves travelling vertically, and for waves having propagation vectors at an angle of 80°, with respect to the vertical at the base of the ionosphere. The geomagnetic field was taken to be vertical, and longitudinal propagation was assumed. Strictly speaking this limits the analysis to polar regions although, as a practical matter, quasi-longitudinal propagation obtains even at temperate latitudes. We have also run calculations for vertical equatorial propagation, whence the geomagnetic field is transverse to the direction of propagation.

These results will not be given in detail here. We note, however, that the transmission losses for transverse propagation tend to be (at VLF/ELF) much more severe than for longitudinal propagation.

The earth's curvature has been neglected in the calculations as has the curvature of the geomagnetic field lines. The height-dependent strength of the geomagnetic field has been included, however.

III. NUMERICAL RESULTS

The computed transmission losses in decibels are plotted versus frequency in Figures 2-9. Results are shown for four model ionospheres and the two propagation modes, O (right-hand polarized) and X (left-hand polarized). Two incidence (or emergence) angles, 0^{o} and 80^{o}, are also shown for those cases where the loss difference between the two is of any consequence. The curves show the total loss incurred between a height of 1000 km and the base of the ionosphere. However, in all cases where the losses are small enough that a mode is of practical interest, almost all of the absorption occurs below about 200 km at ELF and below about 100 km at VLF. Thus, for reasonable ELF/VLF communication links, Figures 2-9 are applicable provided the satellite is above about 200 km/100 km.

For the undisturbed night and day cases, the O-mode has two passbands. One is the hydromagnetic band below the ion gyrofrequency (i.e., below a few tens of Hz) and the other is above the critical frequency, appropriately interpretated in the case of nonvertical incidence. Thus, for frequencies between a few or a few tens of Hz and several MHz, the O-mode does not penetrate the ionosphere. For the X-mode, there is again an upper transmission band above the critical frequency, namely, above 5 or 10 MHz. However, the low frequency transmission band extends into the whistler range, reaching about 1 MHz at night and nearly 10 KHz in the daytime. Thus, the entire ELF/VLF spectrum is readily transmitted through the undisturbed night-time ionosphere, as are the ELF and lower VLF bands through the undisturbed day-time ionosphere.

As seen in Figures 6-9, the transmission losses are much more severe for the disturbed conditions than for the ambient ones. For both the day-time and night-time models, the entire frequency range between a few Hz and 10 MHz is forbidden as far as the O-mode is concerned. The X-mode fares only somewhat better since the anomalous ionization causes the absorption in the whistler range to become prohibitively high. In order to make use of the lower passband, one must use frequencies below a few hundred Hz in the disturbed night and below a few tens of Hz in the disturbed day. The situation is summarized in Table 1. Two possible ways of alleviating the very unfavorable propagation under disturbed conditions are evident. One is to use a sufficiently low frequency, provided such a low frequency can be effectively radiated. Another

is to employ enough satellites such that at least one will be transmitting at local night or, better, under locally undisturbed conditions. The propagation path would then be vertically under the satellite and then around the world in the earth-ionosphere cavity. These possibilities require further study.

The height dependences of the attenuation for the two modes, four model ionospheres and frequencies in the LF/VLF/ELF/ULF bands are illustrated in Figures 10-19. For ambient conditions and hydromagnetic frequencies ($\lesssim$ 10 Hz), most of the attenuation is due to ion-neutral collisions and occurs near the altitude where the ion-neutral collision frequency is about equal to the ion-gyro frequency; i.e., around 120 km. Under disturbed conditions attenuation due to electron heating, which occurs at lower altitudes, is important even in the hydromagnetic band. This behavior is shown in Figures 10-13. Figures 16-19 show some attenuation profiles in the ELF/VLF/LF bands. As indicated by Figure 17, the O-wave is evanescent at altitudes above about 150 km and is thus of little practical interest. The X-wave attenuation occurs in an altitude layer a few tens of km thick centered around 75 km for the parameters used here. This attenuation is almost entirely due to Ohmic heating of the electrons. The small amount of attenuation shown to occur below about 50 km for the disturbed cases in Figures 16, 18, and 19 is due mainly to ion heating, since the conductivity is dominated by the relatively numerous ions at these low altitudes. The very severe anomalous attenuation which can be caused by ionospheric disturbances is evident from Figures 10-19.

IV. CONCLUSIONS

Under undisturbed conditions and for quasi-longitudinal propagation, the ionosphere is relatively transparent to electromagnetic waves having frequencies lower than about 10 KHz. For certain classes of artificially or naturally disturbed ionospheres, frequencies less than a few tens of Hz must be used to insure reliable transmission. A working system should be configured so as to maximize the probability that at least one satellite is transmitting under undisturbed ionospheric conditions, and reliance thus placed upon part of the propagation path being in the earth ionosphere cavity. More study is needed on these aspects.

REFERENCE

1. Ginzburg, V. L., Propagation of Electromagnetic Waves in Plasma, Gorden and Breach Science Publishers, New York, 1961.

Table I

IONOSPHERIC TRANSMISSION BANDS IN HERTZ
(VERTICAL INCIDENCE)

Wave	Ambient Night	Ambient Day	Disturbed Night	Disturbed Day
Ordinary	$f < 30$, $f > 4 \times 10^6$	$f < 1.4$, $f > 8 \times 10^6$	$f < 3$, $f > 1.4 \times 10^7$	$f < 0.5$, $f > 4 \times 10^7$
Extraordinary	$f < 1.1 \times 10^6$, $f > 7 \times 10^6$	$f < 10^4$, $f > 1.3 \times 10^7$	$f < 200$, $f > 1.8 \times 10^7$	$f < 30$, $f > 5 \times 10^7$

Table II

IONOSPHERIC TRANSMISSION BANDS IN HERTZ
(GLANCING INCIDENCE, $i = 80^o$)

Wave	Ambient Night	Ambient Day	Disturbed Night	Disturbed Day
Ordinary	$f < 30$, $f > 3 \times 10^7$	$f < 1.4$, $f > 6 \times 10^7$	$f < 3$, $f > 4 \times 10^7$	$f < 0.5$, $f > 1.1 \times 10^8$
Extraordinary	$f < 5 \times 10^5$, $f > 3 \times 10^7$	$f < 5 \times 10^3$, $f > 6 \times 10^7$	$f < 200$, $f > 5 \times 10^7$	$f < 10$, $f > 1.3 \times 10^8$

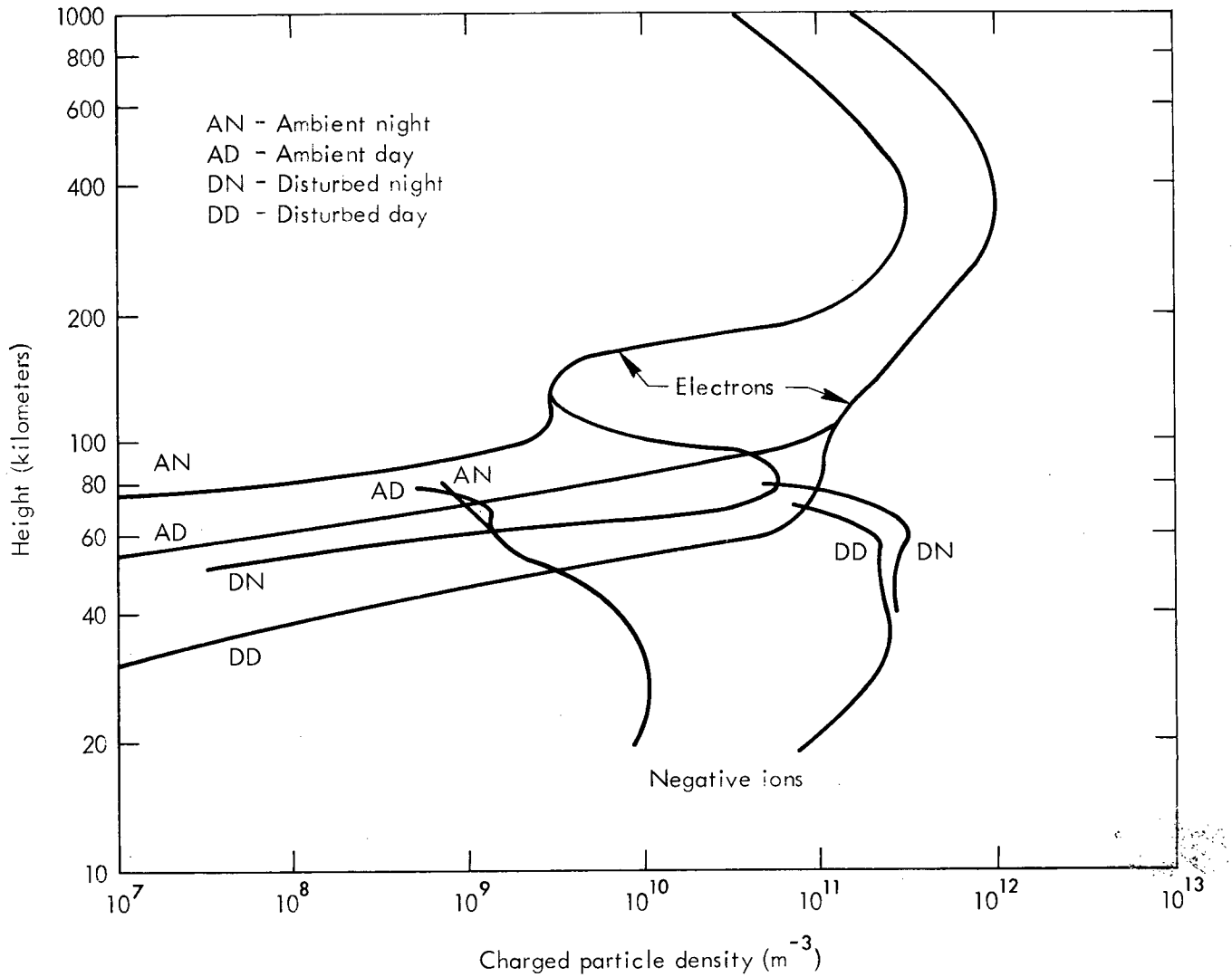

Figure 1

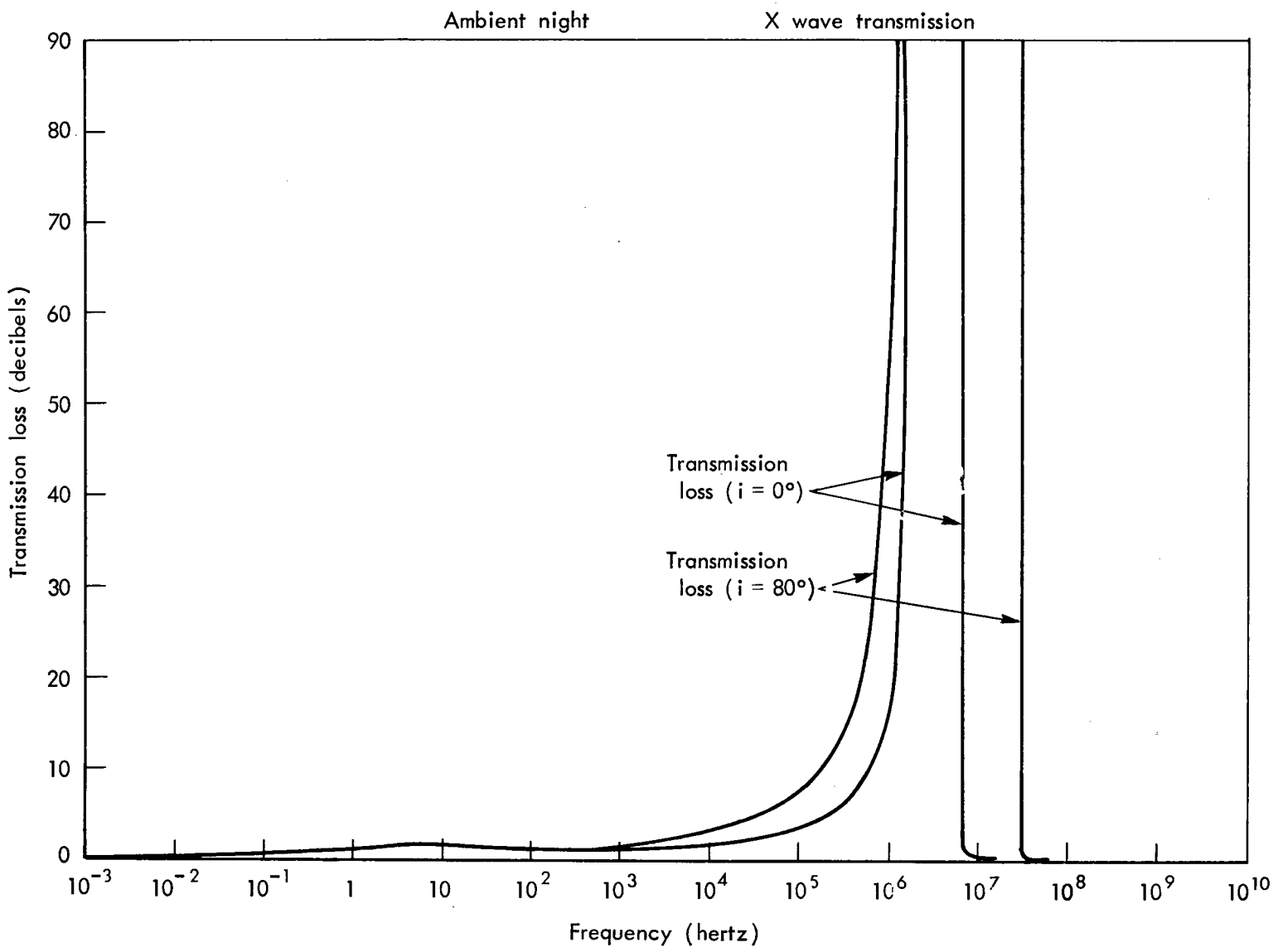
Ambient night
X wave transmission
Transmission loss (decibels)
90
80
70
60
50
40
30
20
10
0
Transmission loss (i = 0°)
Transmission loss (i = 80°)
10^{-3}
10^{-2}
10^{-1}
1
10
10^{2}
10^{3}
10^{4}
10^{5}
10^{6}
10^{7}
10^{8}
10^{9}
10^{10}
Frequency (hertz)

Figure 2

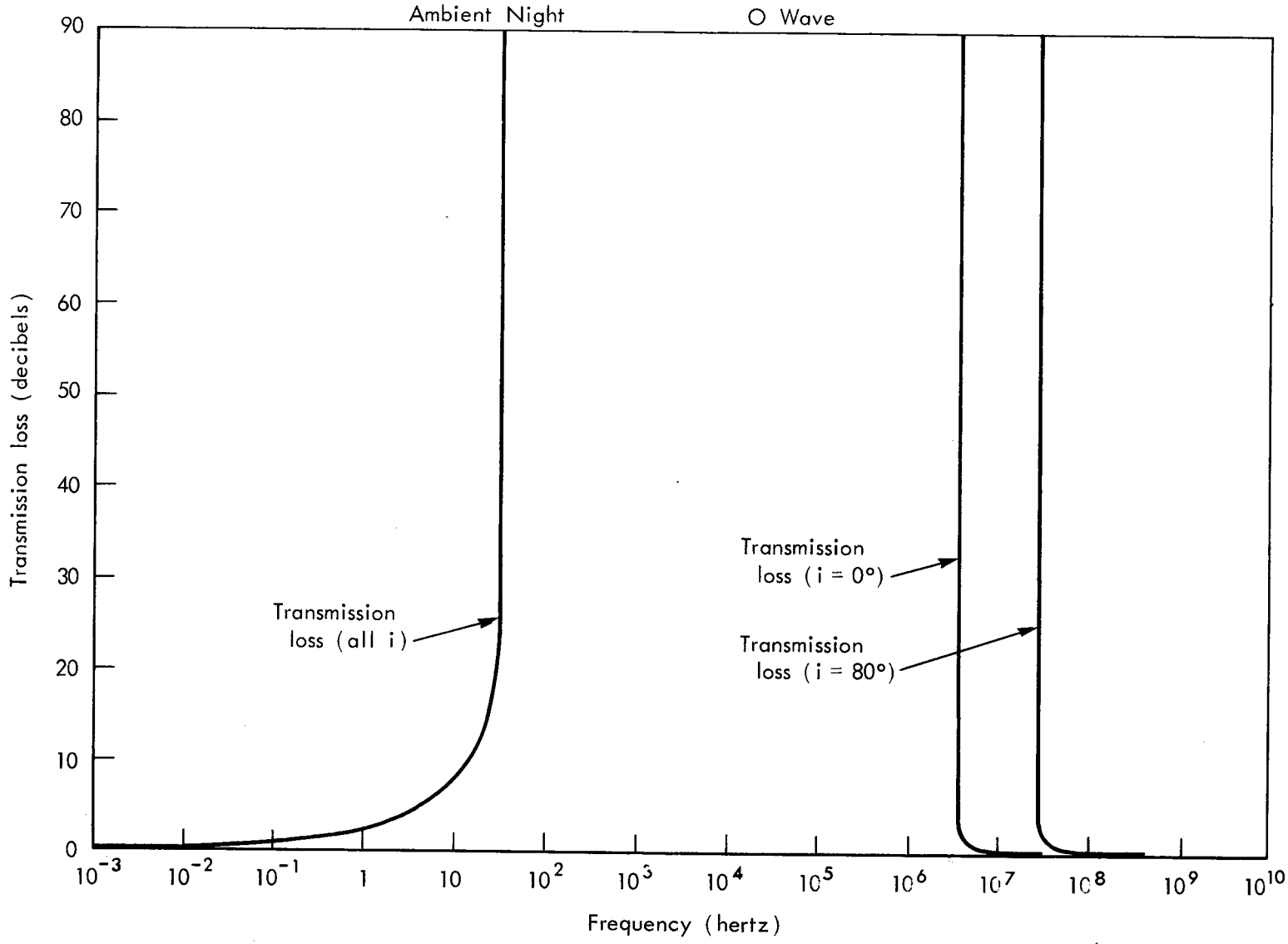

Figure 3

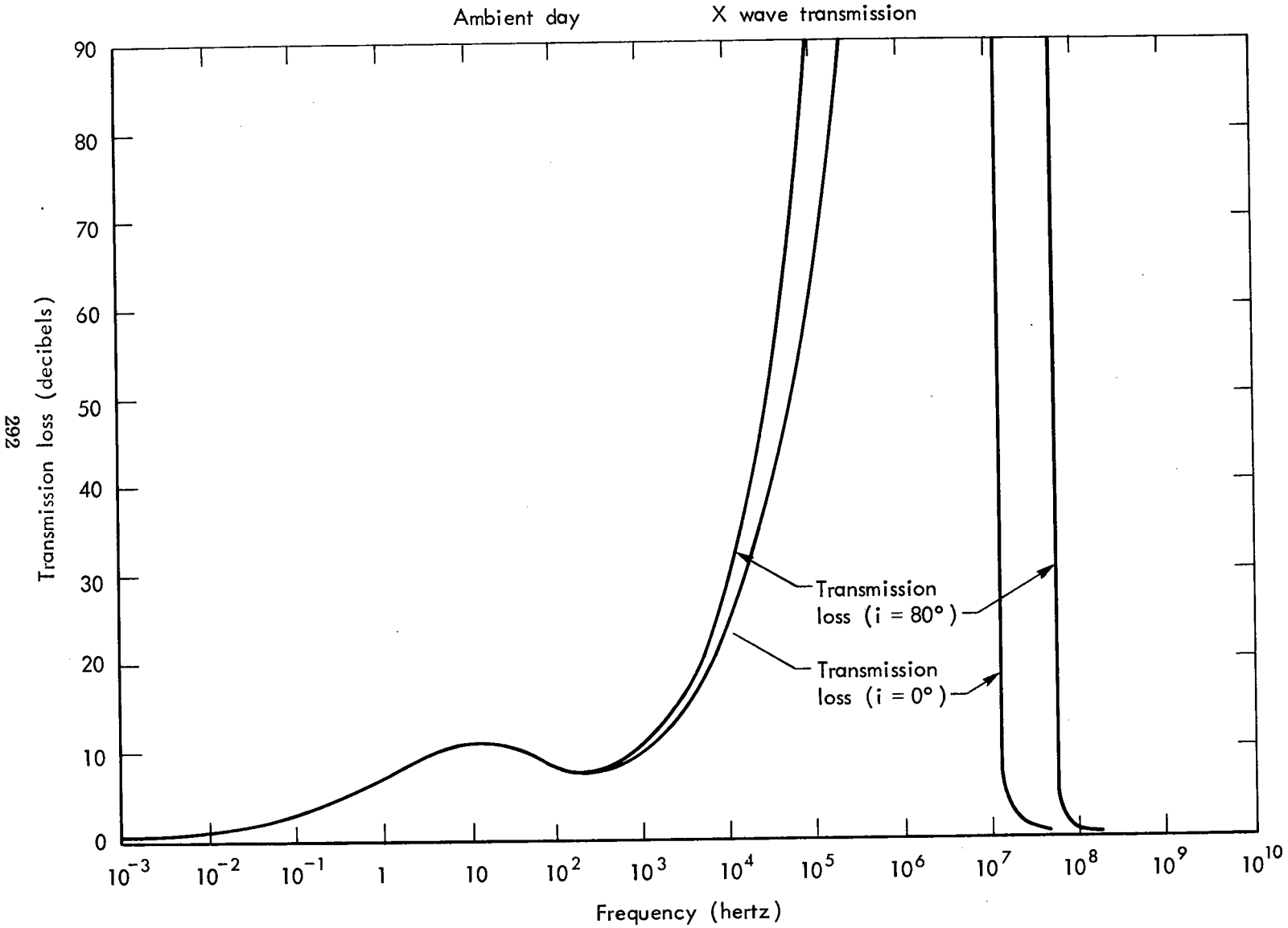
Ambient day
X wave transmission
Transmission loss (decibels)
90
80
70
60
50
40
30
20
10
0
Transmission loss (i = 80°)
Transmission loss (i = 0°)
10^{-3}
10^{-2}
10^{-1}
1
10
10^{2}
10^{3}
10^{4}
10^{5}
10^{6}
10^{7}
10^{8}
10^{9}
10^{10}
Frequency (hertz)

Figure 4

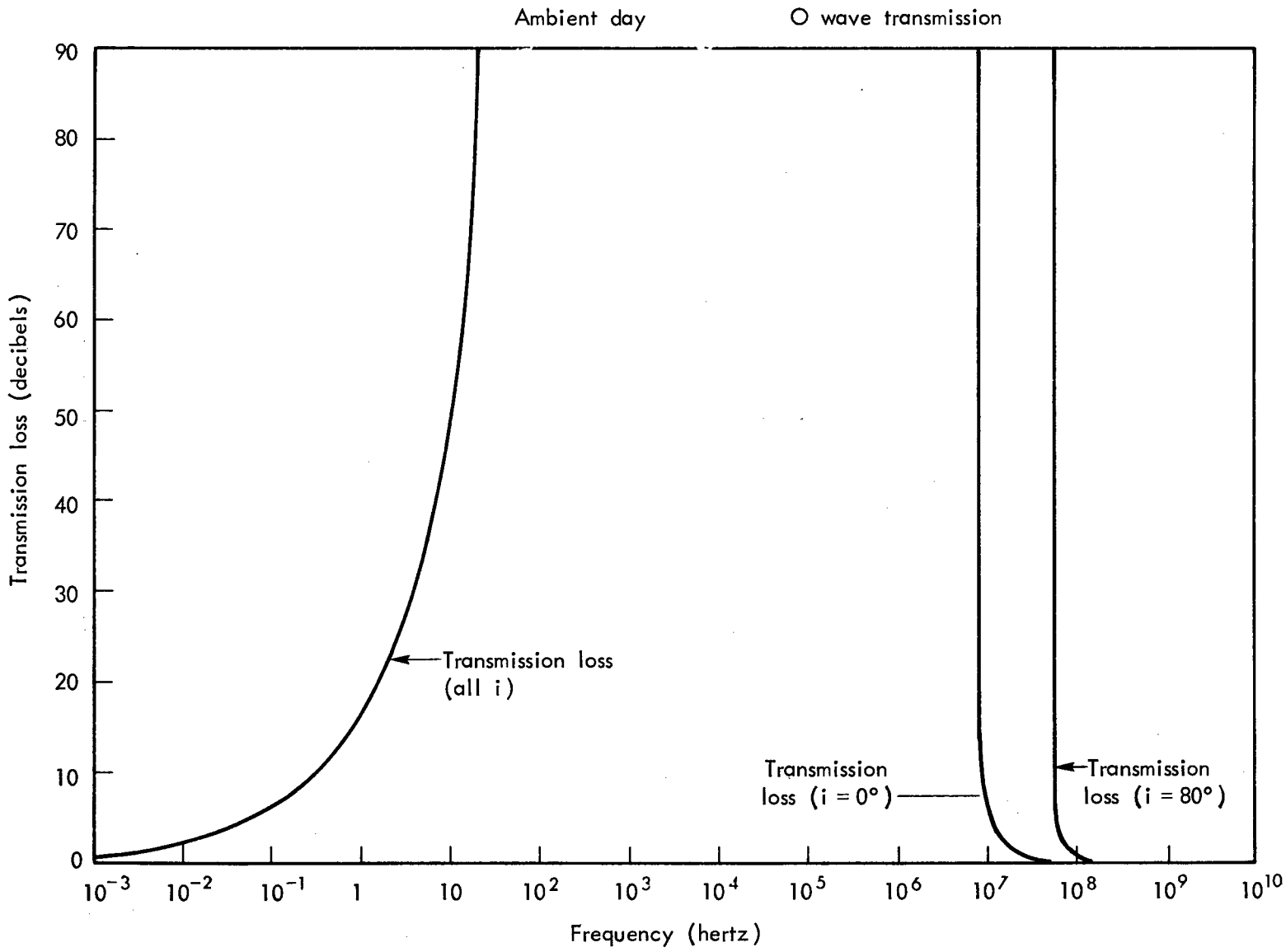

Figure 5

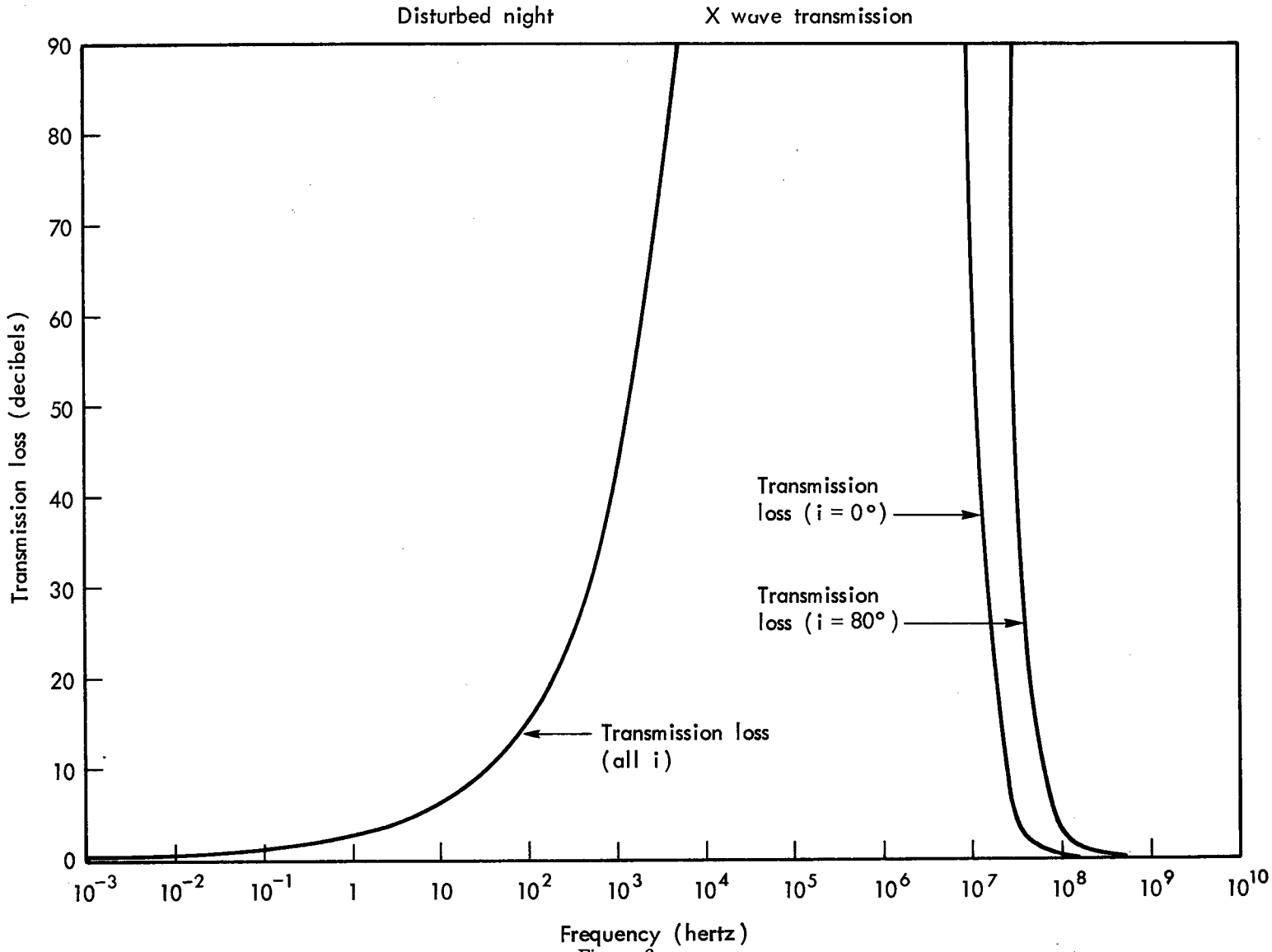
Disturbed night
X wave transmission
Transmission loss (decibels)
90
80
70
60
50
40
30
20
10
0
Transmission loss (i = 0°)
Transmission loss (i = 80°)
Transmission loss (all i)
10^{-3}
10^{-2}
10^{-1}
1
10
10^{2}
10^{3}
10^{4}
10^{5}
10^{6}
10^{7}
10^{8}
10^{9}
10^{10}
Frequency (hertz)

Figure 6

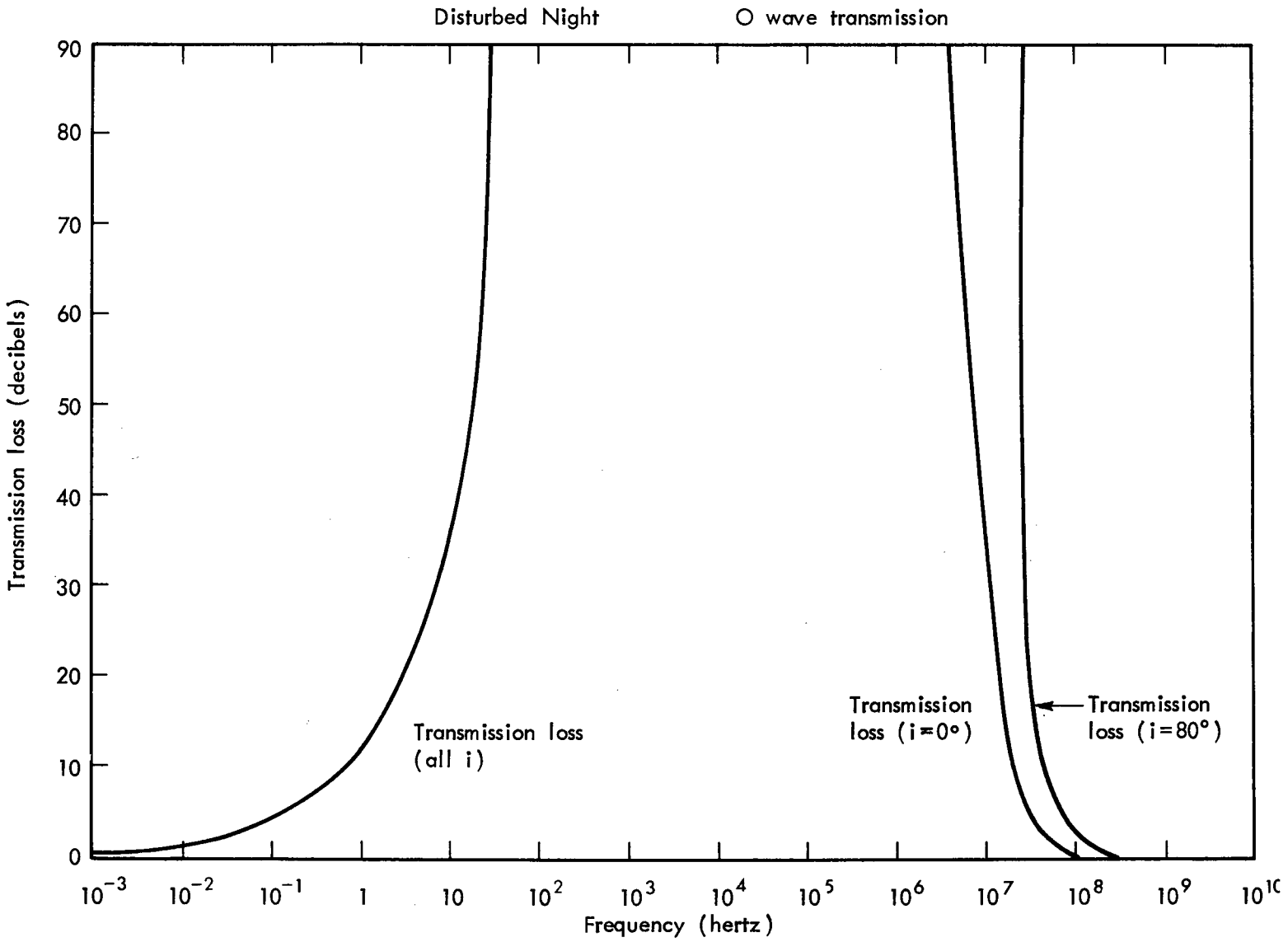

Figure 7

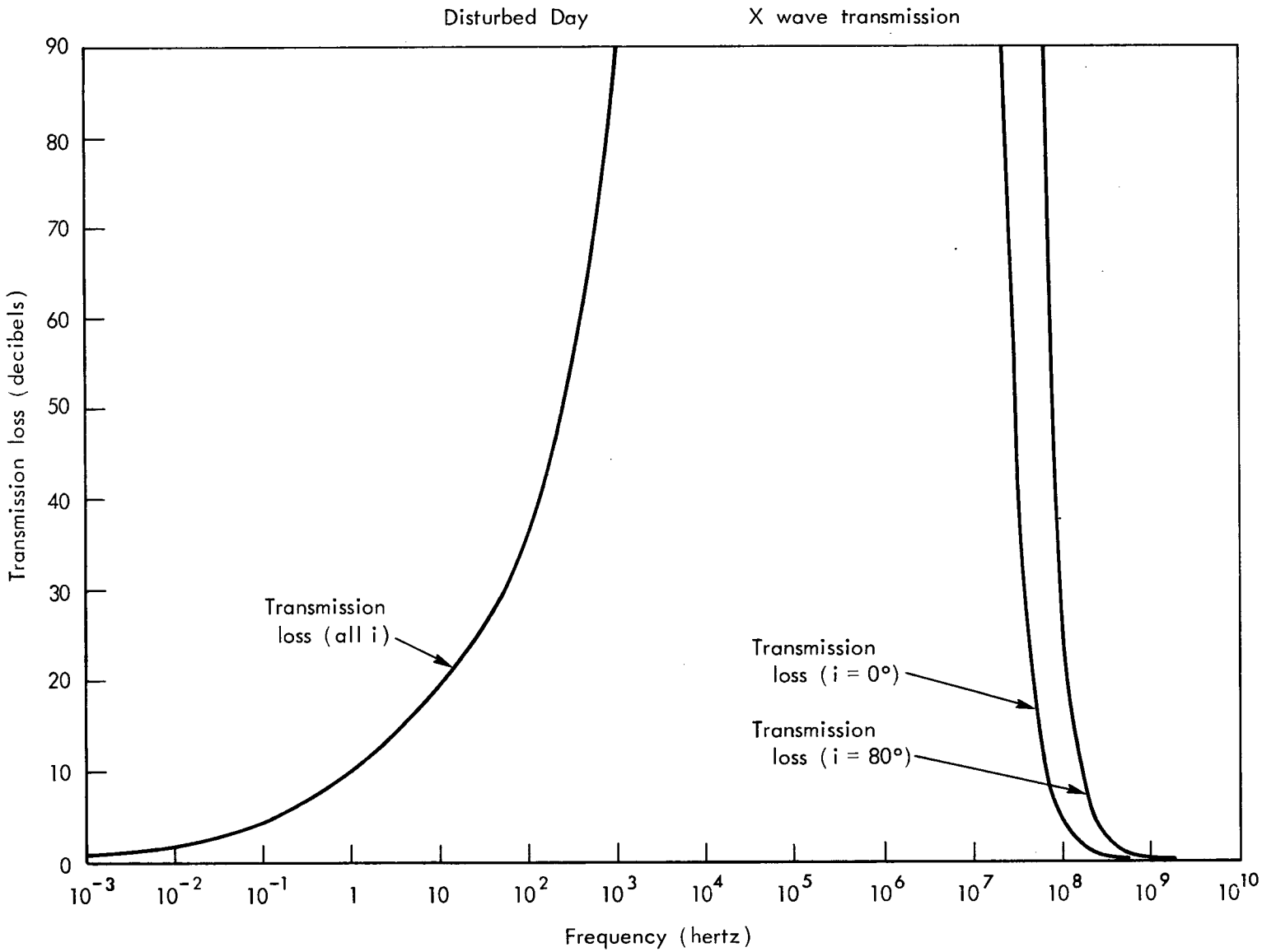
Disturbed Day
X wave transmission
Transmission loss (decibels)
90
80
70
60
50
40
30
20
10
0
Transmission loss (all i)
Transmission loss (i = 0°)
Transmission loss (i = 80°)
10^{-3}
10^{-2}
10^{-1}
1
10
10^{2}
10^{3}
10^{4}
10^{5}
10^{6}
10^{7}
10^{8}
10^{9}
10^{10}
Frequency (hertz)

Figure 8

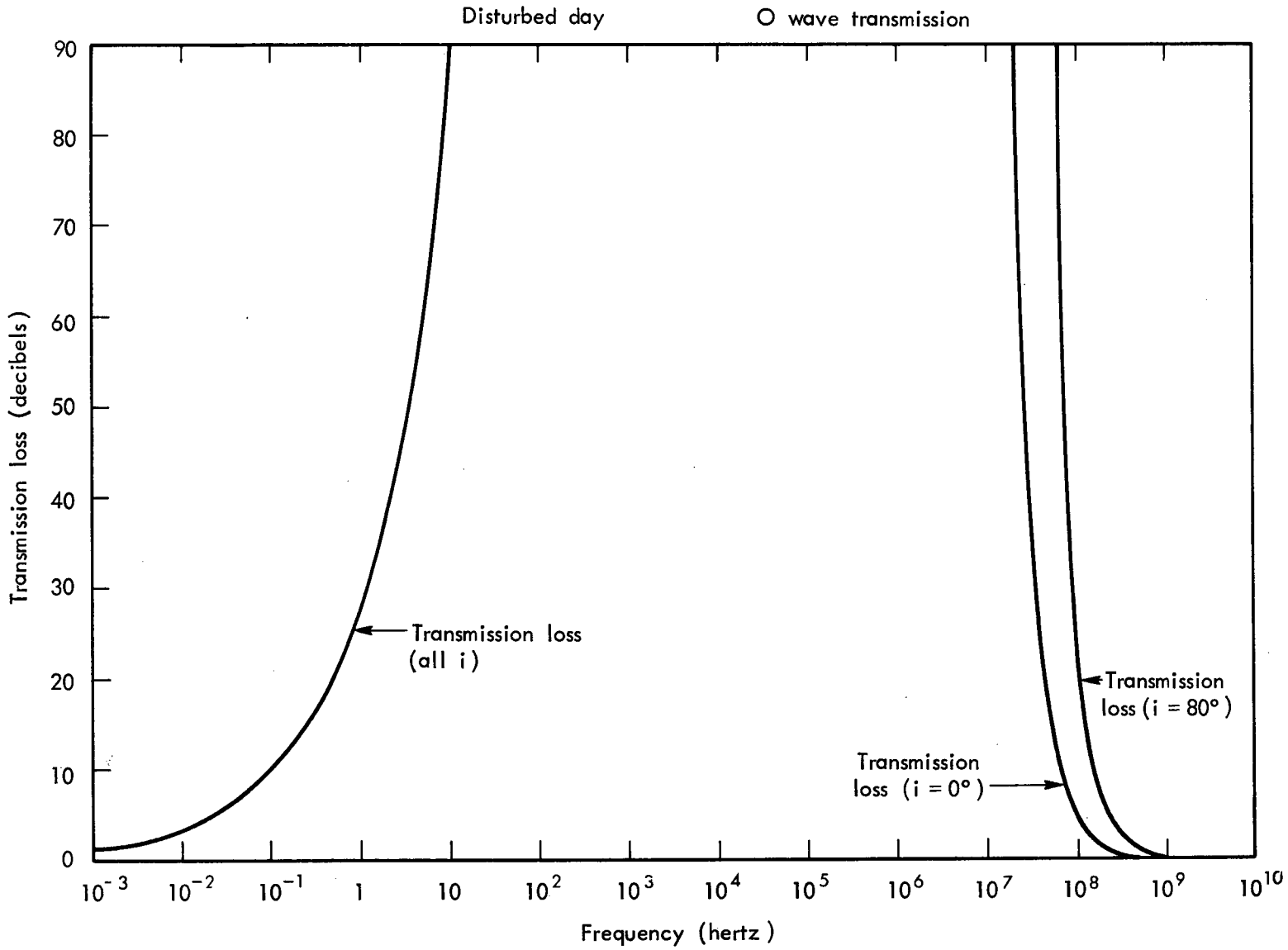

Figure 9

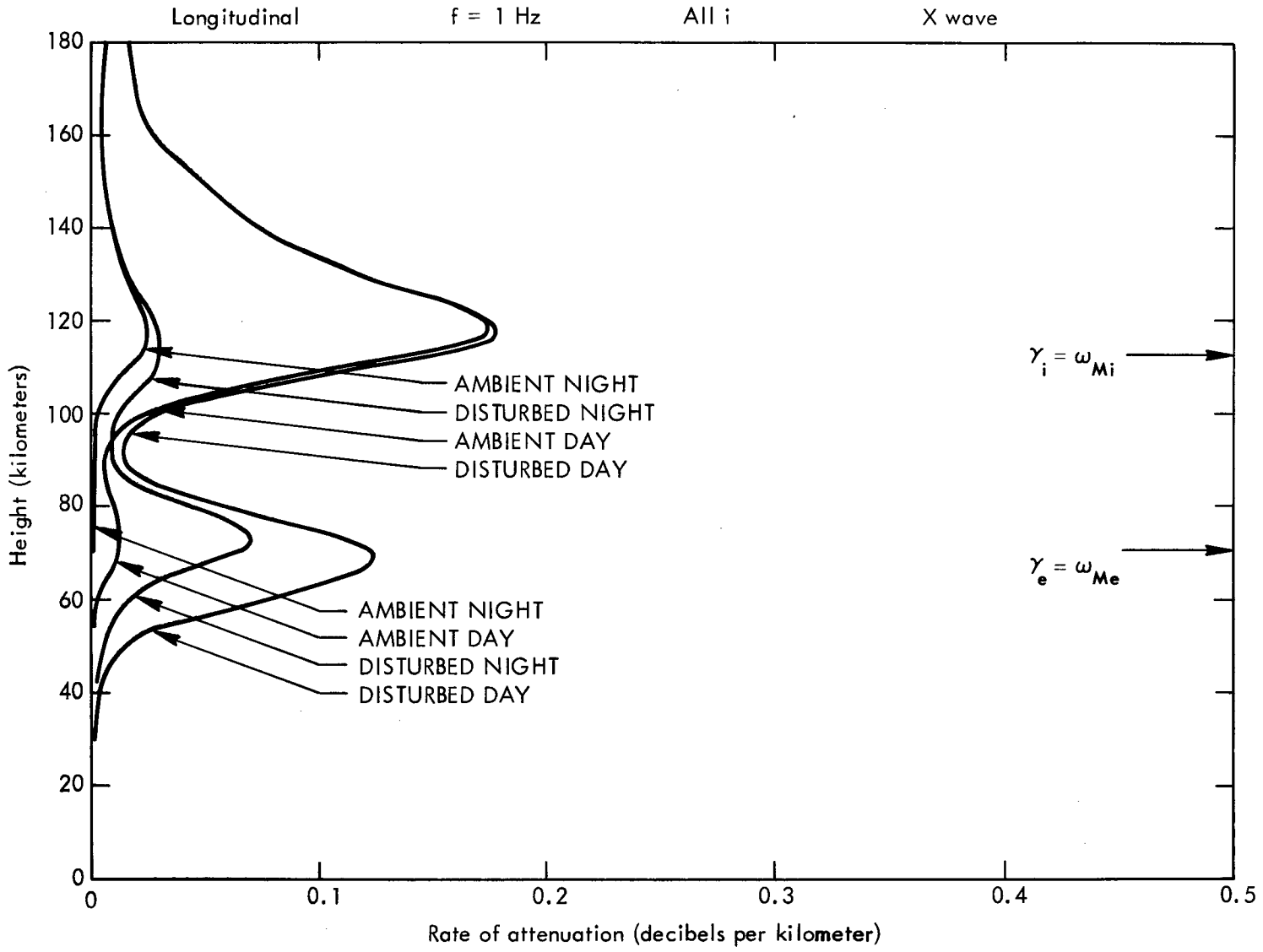
Longitudinal
f = 1 Hz
All i
X wave
Height (kilometers)
180
160
140
120
100
80
60
40
20
0
0
0.1
0.2
0.3
0.4
0.5
Rate of attenuation (decibels per kilometer)
AMBIENT NIGHT
DISTURBED NIGHT
AMBIENT DAY
DISTURBED DAY
AMBIENT NIGHT
AMBIENT DAY
DISTURBED NIGHT
DISTURBED DAY
$\gamma_i = \omega_{Mi}$
$\gamma_e = \omega_{Me}$

Figure 10

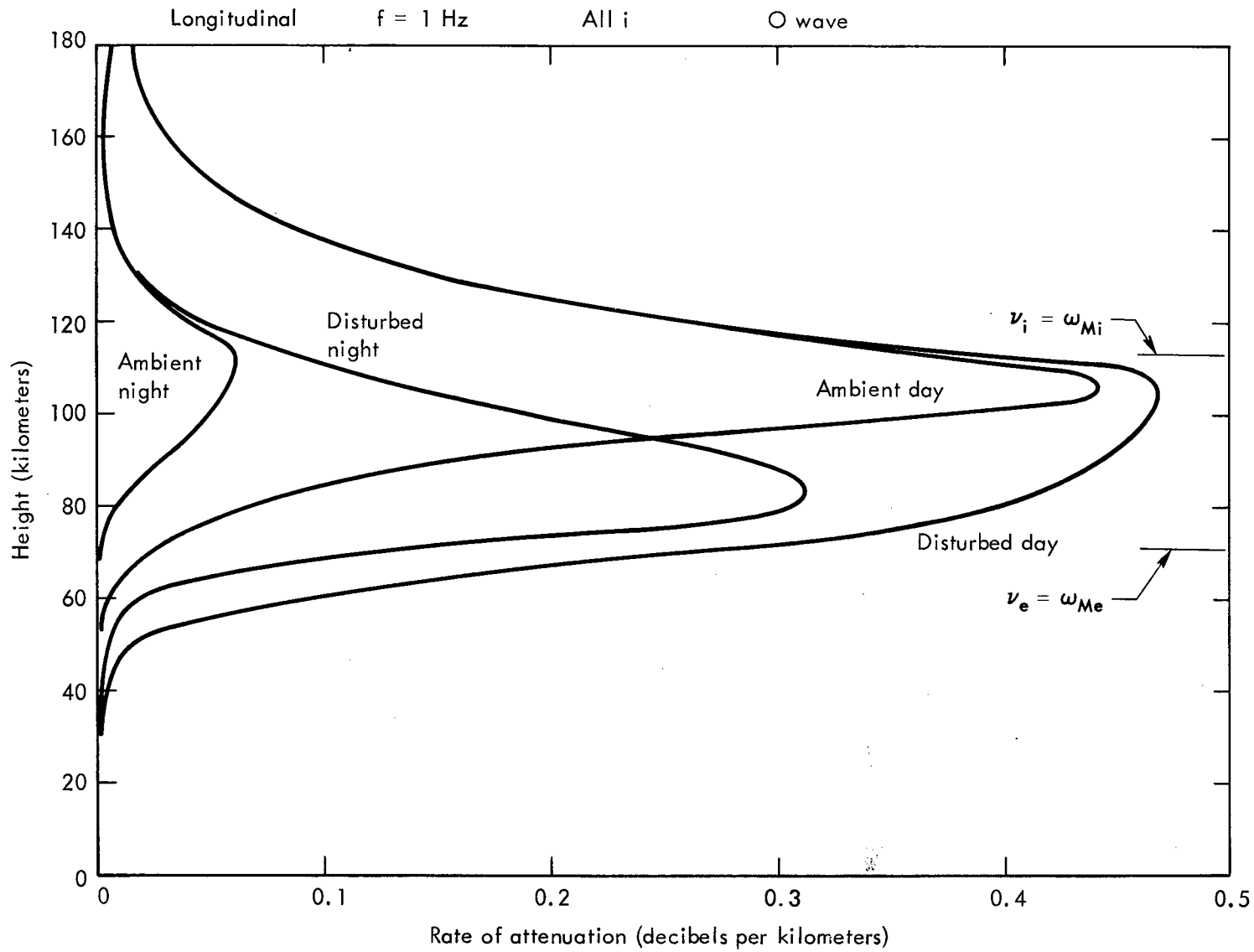

Figure 11

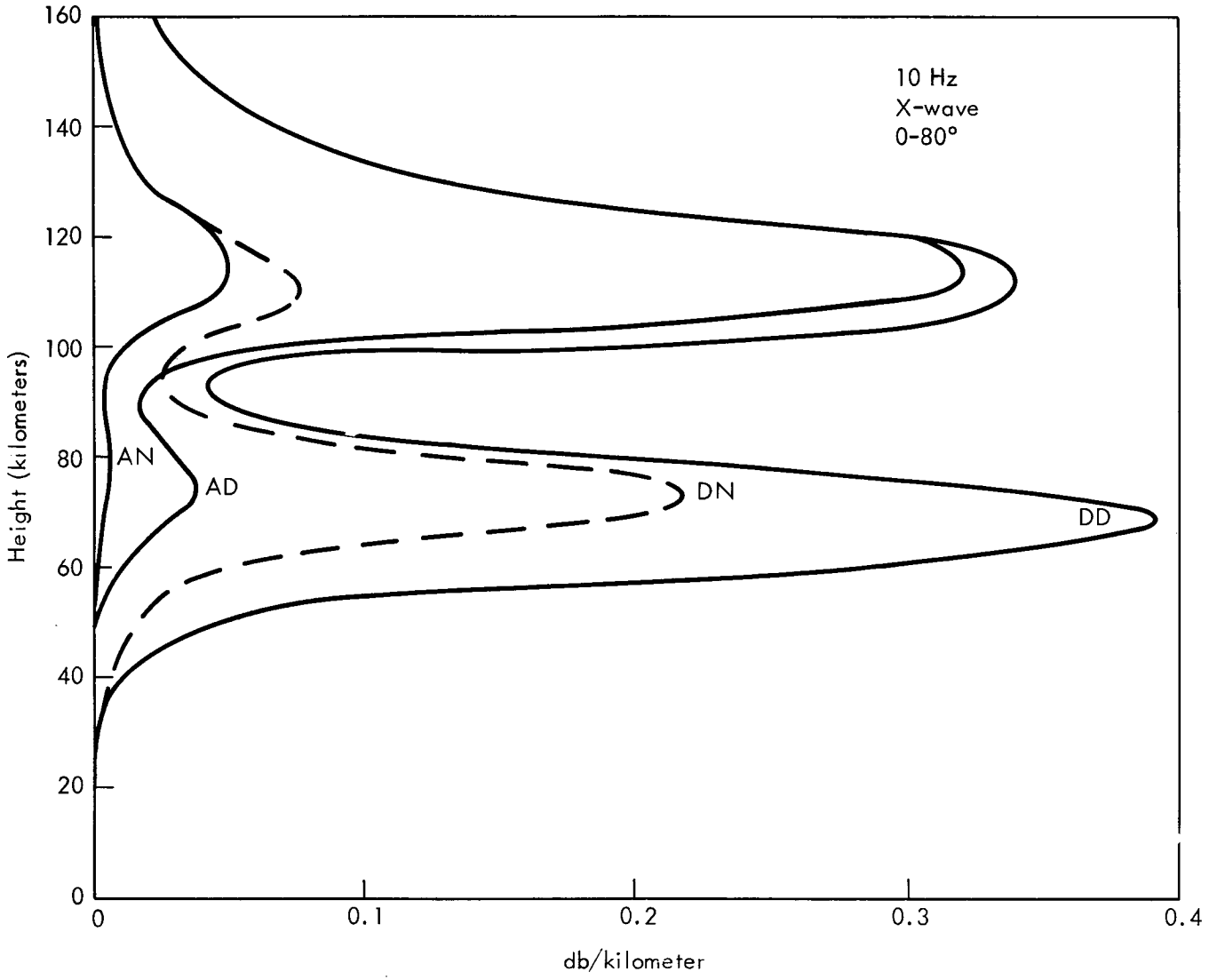
160
140
120
100
80
60
40
20
0
Height (kilometers)
10 Hz
X-wave
0-80°
AN
AD
DN
DD
0
0.1
0.2
0.3
0.4
db/kilometer

Figure 12

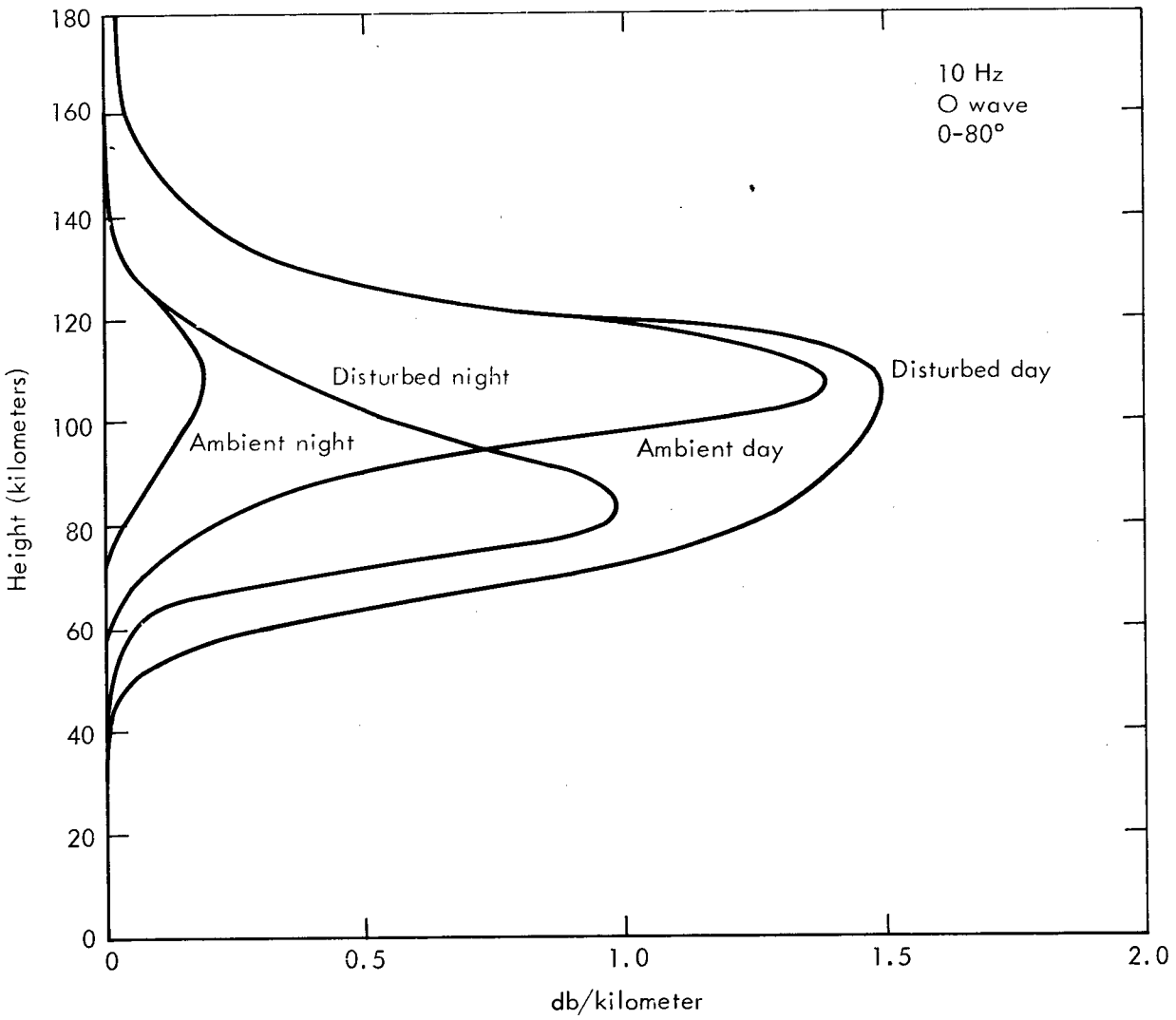

Figure 13

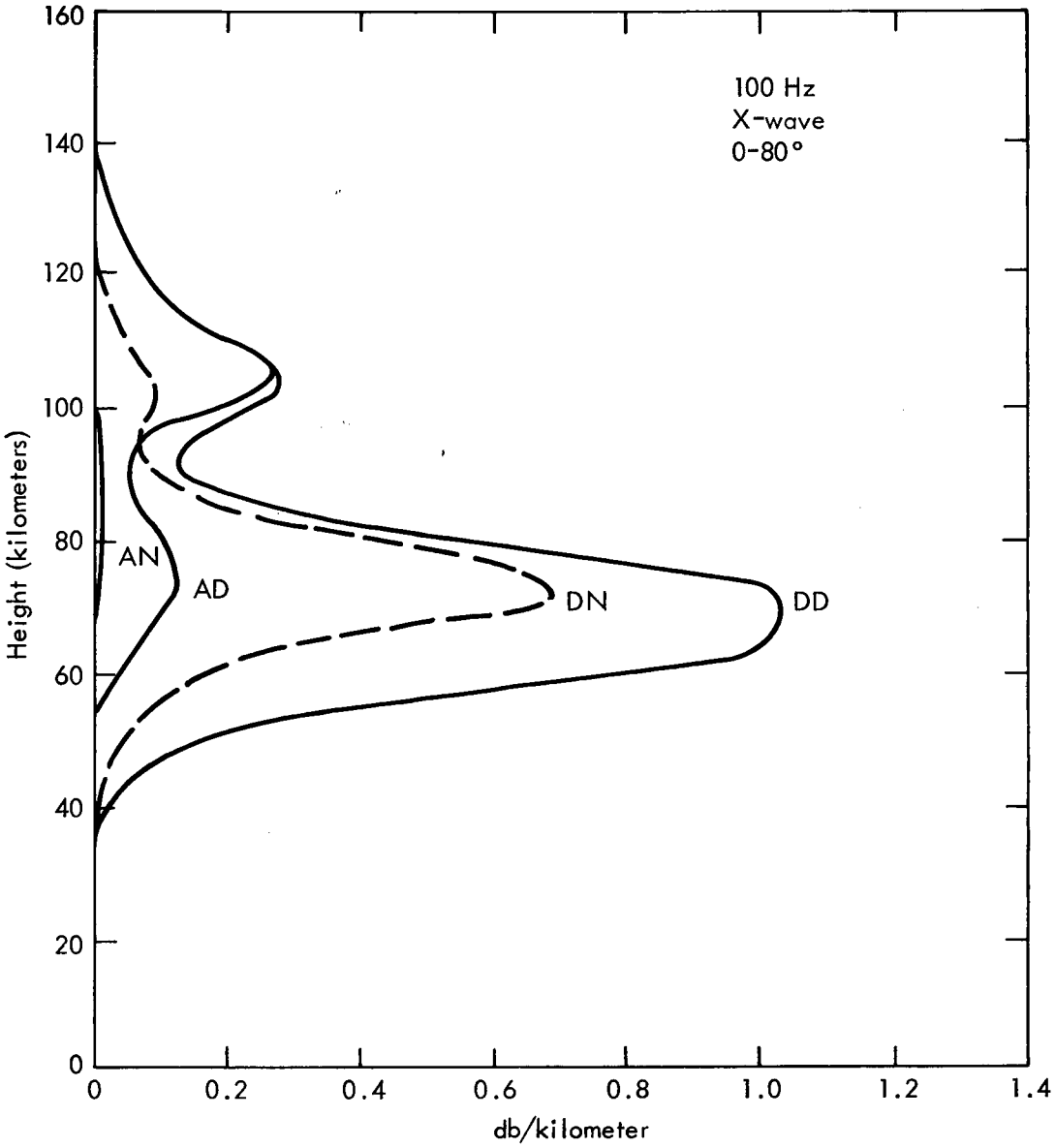
100 Hz
X-wave
0-80°
AN
AD
DN
DD
Height (kilometers)
db/kilometer
160
140
120
100
80
60
40
20
0
0
0.2
0.4
0.6
0.8
1.0
1.2
1.4

Figure 14

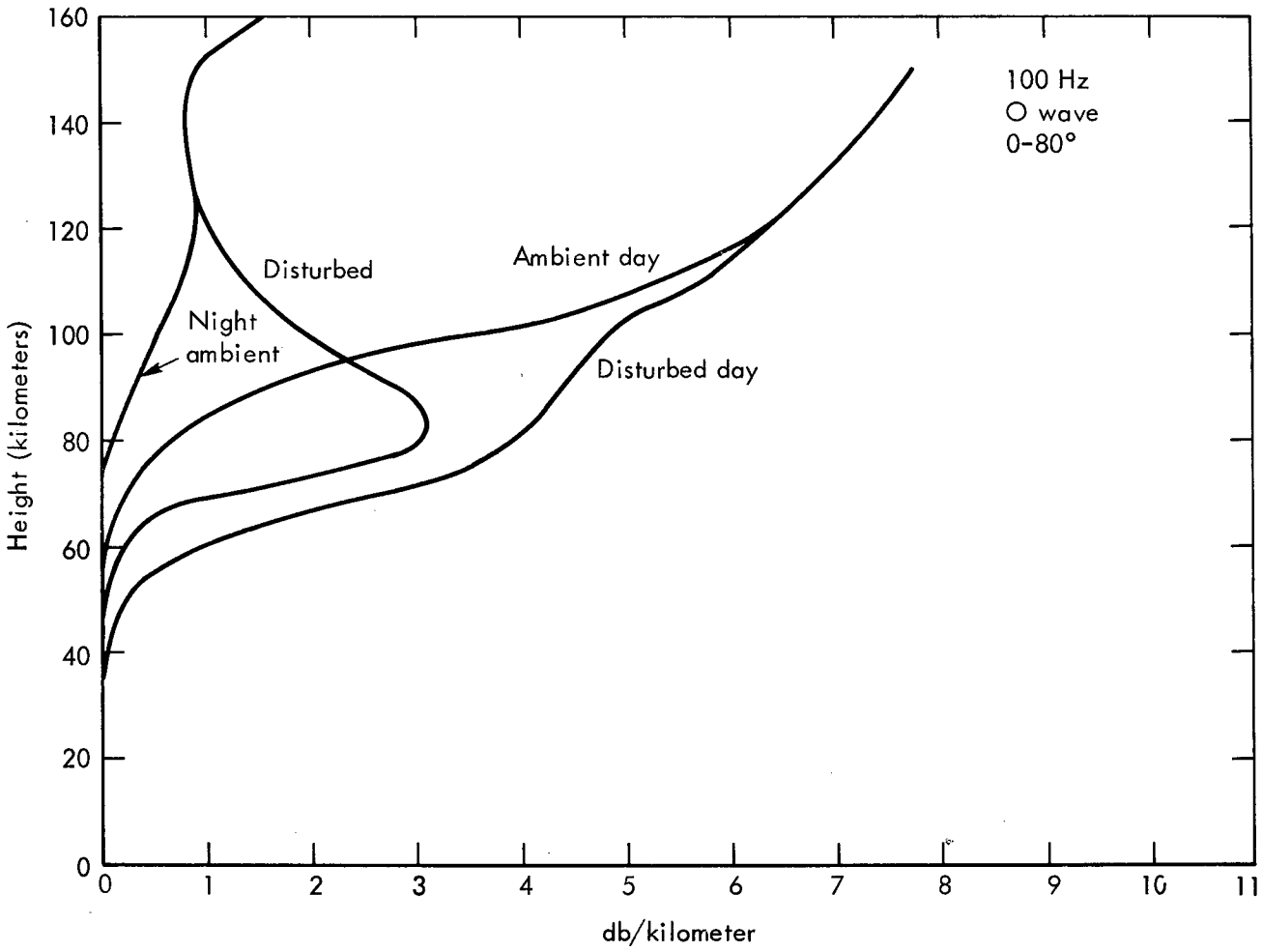

Figure 15

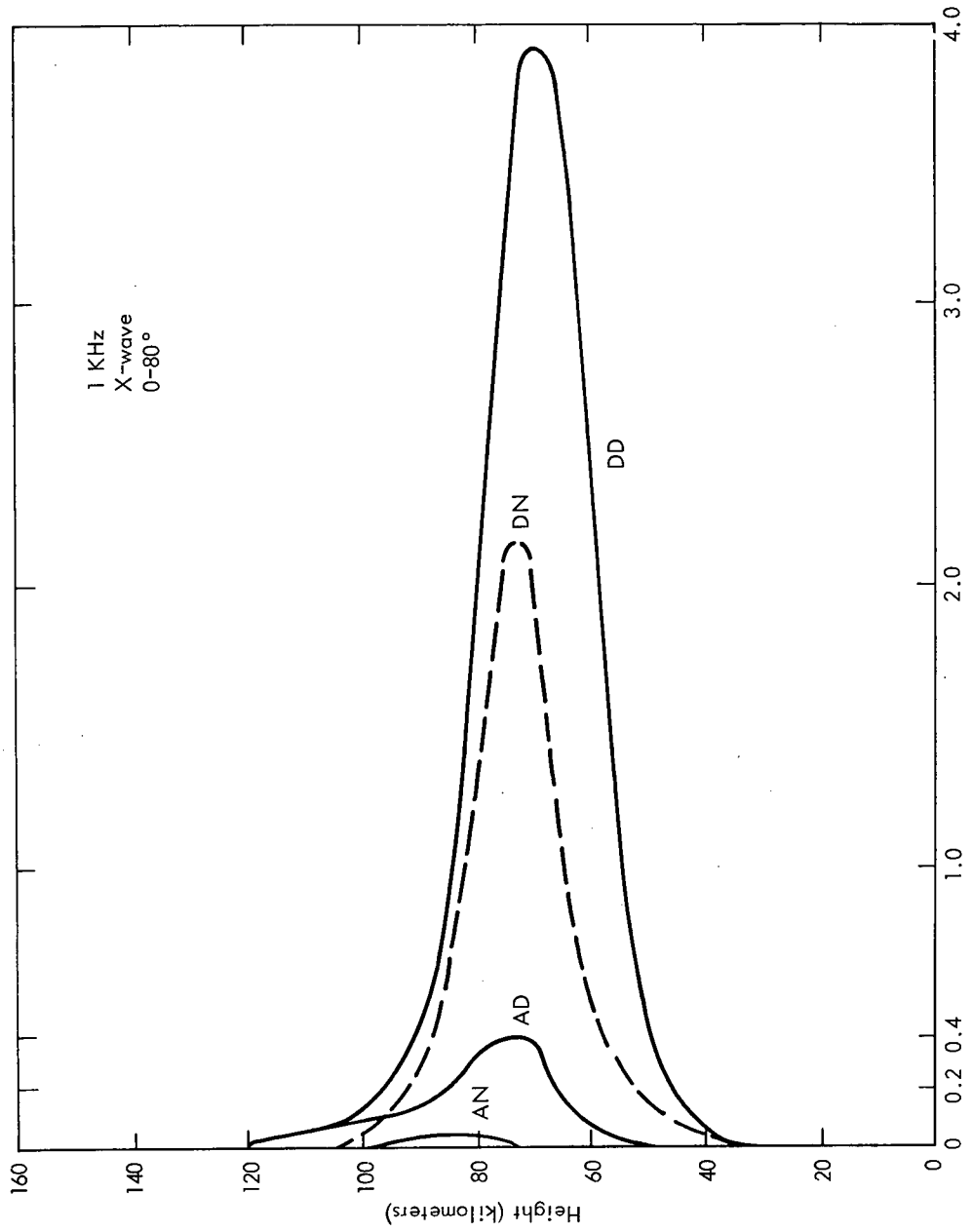
1 KHz
X-wave
0-80°
DD
DN
AD
AN
Height (kilometers)
160
140
120
100
80
60
40
20
0
0 0.2 0.4
1.0
2.0
3.0
4.0
db/kilometer

Figure 16

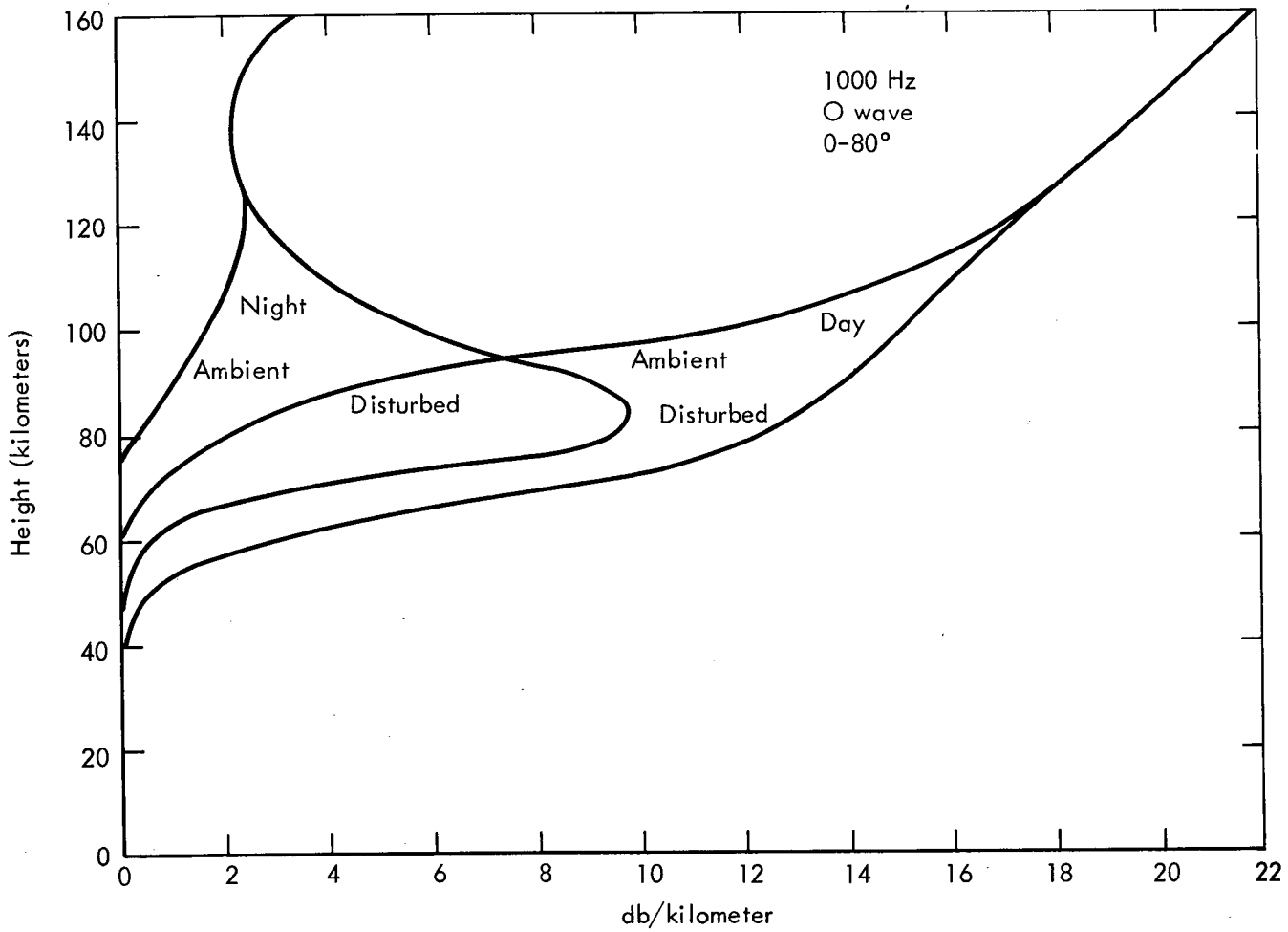

Figure 17

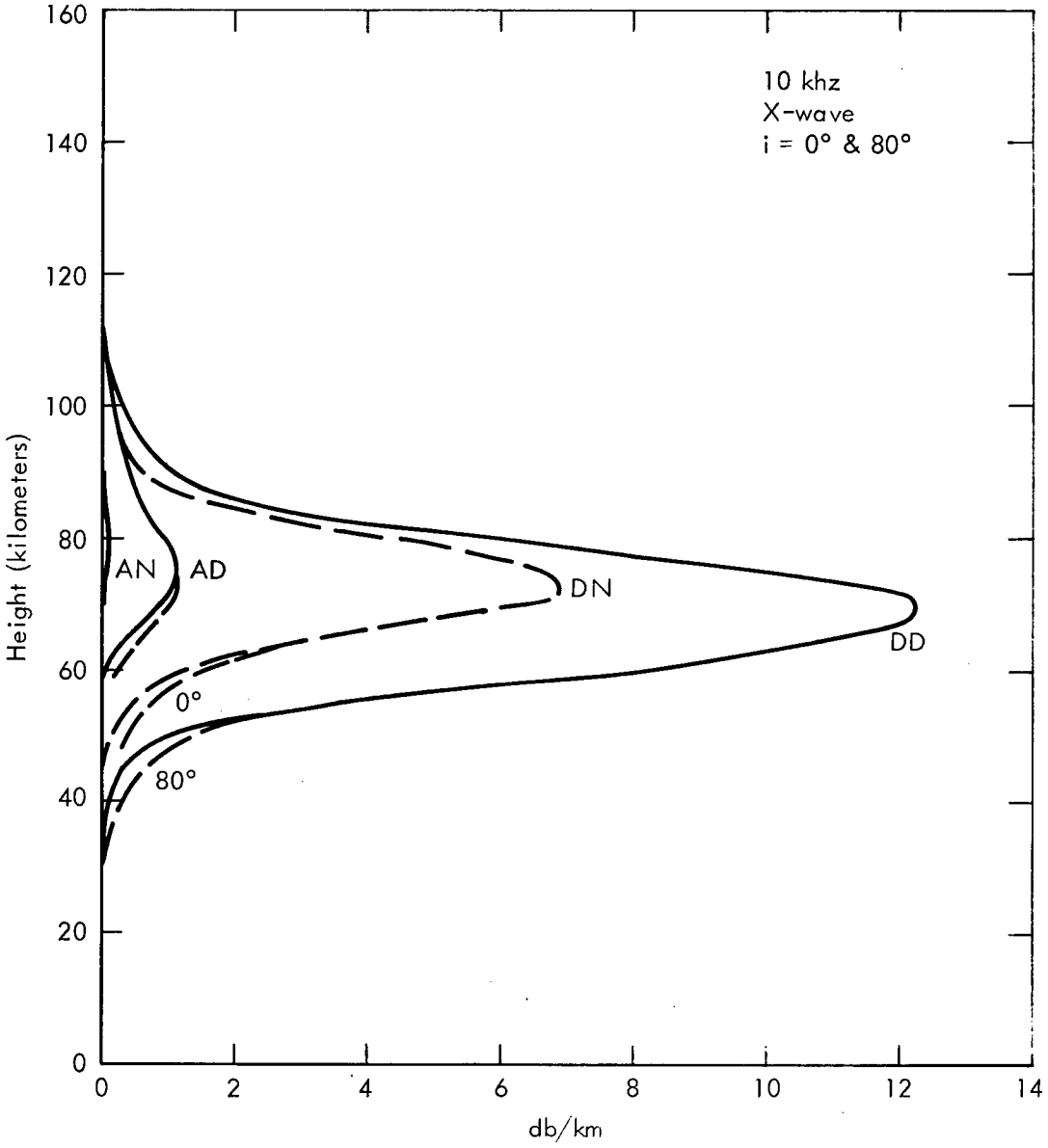
10 khz
X-wave
i = 0° & 80°
Height (kilometers)
160
140
120
100
80
60
40
20
0
AN
AD
DN
DD
0°
80°
0
2
4
6
8
10
12
14
db/km

Figure 18

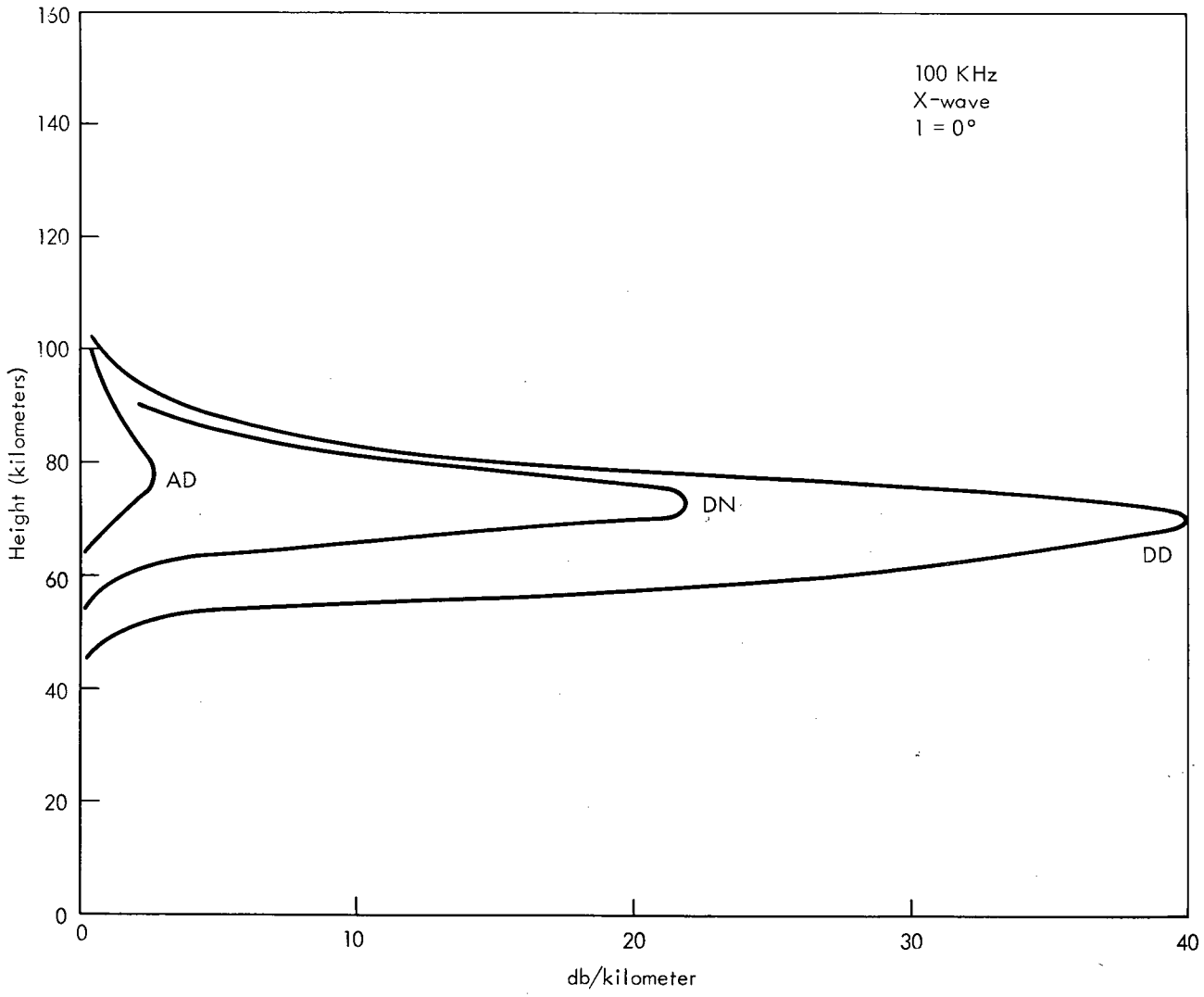

Figure 19

EXCITATION OF THE TERRESTRIAL WAVEGUIDE BY SOURCES IN THE LOWER IONOSPHERE

by

Janis Galejs

Sylvania Electronic Systems Eastern Division
An Operating Group of Sylvania Electric Products Inc.
77 "A" Street, Needham Heights, Massachusetts 02194

Abstract

The effectiveness of a dipole source within the ionosphere is determined relative to a groundbased source of same dipole moment. Electric and magnetic dipoles should be oriented with their axes transverse to the geomagnetic field and axial electric dipoles are particularly ineffective. The dipangle of the geomagnetic field should exceed 15 to 20^{o}. For frequencies in the VLF range the relative effectiveness of a ionospheric source is about 10% at nighttime and 1% at daytime. In the ELF range the relative effectiveness is from 20 to 100%.

1. Introduction

Groundbased VLF transmissions can be received in satellites and transmissions have been proposed from sources within the ionosphere (Leiphart etal, 1962). In the treatment of satellite born antennas the near-field problem or impedance formulation provide an estimated relation between the dipole moment and the power applied to the antennas. A number of impedance formulations have been reviewed by Galejs (Chapter 12,1969c) and among the more recent contributions one may mention the work of Wang and Bell (1969a,1970)and Duff and Mittra (1970). The problem of radiation patterns (Wang and Bell, 1969b; Gia Russo and Bergeson, 1969) and of coupling into the earth-to-ionosphere cavity may be treated subsequently. However, it is also possible to obtain a direct relation between the dipole moment of the antenna and of the various mode amplitudes in the terrestrial waveguide (Einaudi and Wait, 1970).

There exist formulations for calculating the various field amplitudes that penetrate in the ionosphere from groundbased sources (Galejs, 1968), and one may apply the appropriate reciprocity relations for estimating the effectiveness of dipole sources at satellite altitudes. In such a reciprocal geometry it is readily possible to treat ionospheric stratifications, curvature effects of the waveguide and arbitrary orientations of the dipole, of the geomagnetic field and of the direction of propagation for the waves below the ionosphere. The proper consideration of all these factors would require an extensive analytical effort in a direct formulation of radiation from ionospheric sources. The excitation factors are relatively sensitive to changes of the effective complex incidence angle that distinguishes between the various waveguide modes. Available data on field penetration for oblique plane wave incidence (real incidence angles) are not directly applicable for estimating the excitation factors of the various waveguide modes.

In the calculations of this paper the effectiveness of sources at satellite altitudes will be estimated in relation to ground based sources of equal dipole moments. No attempt will be made to investigate the impedance properties of the antennas and the calculated curves can not be directly translated into comparisons for equal powers applied to the two antenna configurations. The principal reflection and absorption loss of transmissions to and from satellites occurs in the altitude range between the D and E - layer. Although most of the calculations will be reported for altitudes near 100 km, comparable results may be anticipated for altitudes below the F-layer.

2. Reciprocity Relations

For sources decomposed in a sum of electric ($\underline{p}$) and magnetic ($\underline{m}$) point dipoles the reciprocity theorem of a magnetoionic medium (equation (29.33) of Ginzburg, 1964) states that

$$\underline{p}_1 \cdot \underline{E}_2 (1, \underline{H}_o) - \underline{m}_1 \cdot \underline{H}_2 (1, \underline{H}_o) = \underline{p}_2 \cdot \underline{E}_1 (2, -\underline{H}_o) - \underline{m}_2 \cdot \underline{H}_1 (2, -\underline{H}_o) \tag{1}$$

where $\underline{F}_i (j, \underline{H}_o)$ refers to fields (F = E or H) of a source i of dipole moments $\underline{p}_i$ and $\underline{m}_i$ observed at the location j in the presence of a geomagnetic field $\underline{H}_o$. The fields $\underline{F}_2(1, \underline{H}_o)$ are related by (1) to fields $\underline{F}_1(2, -\underline{H}_o)$ in the presence of a reversed geomagnetic field. This relation will be applied to sources consisting of two electric dipoles and to a combination of an electric and magnetic dipole.

Application of (1) to part A of Figure 1 shows that

$$\underline{p}_1 \cdot \underline{E}_2(1, \underline{H}_o) = \underline{p}_2 \cdot \underline{E}_1 (2, -\underline{H}_o) \tag{2}$$

$$\underline{p}_1 \cdot \underline{E}_3 (1, \underline{H}_o) = \underline{p}_3 \cdot \underline{E}_1 (3, -\underline{H}_o) \tag{3}$$

Assumming equal dipole moments $\underline{p}_2$ and $\underline{p}_3$, (2) and (3) are rearranged into

$$\frac{\underline{E}_2 (1, \underline{H}_o)}{\underline{E}_3 (1, \underline{H}_o)} = \frac{\underline{E}_1 (2, -\underline{H}_o)}{\underline{E}_1 (3, -\underline{H}_o)} \tag{4}$$

Fields on the ground $\underline{E}_2(1)$ excited by a source 2 in the ionosphere are related to the fields on the ground $\underline{E}_3$ (1) of a groundbased source 3 in the same way as the fields in the ionosphere $\underline{E}_1(2)$ are related to the fields on the ground surface $\underline{E}_1(3)$ for a groundbased source 1 with a reversed direction of the geomagnetic field. The relative effectiveness $\underline{E}_2$ (1)/$\underline{E}_3(1)$ of a source ($\underline{p}_3$) raised into the ionosphere ($\underline{p}_2$) is the same as the relation between fields in the ionosphere $\underline{E}_1$ (2) and the fields on the ground surface $\underline{E}_1(3)$ of a groundbased source ($\underline{p}_1$). The analysis of the geometry A1 will provide the same information as the geometries A2 and A3.

The equivalence of the geometries A1 and A2 of Figure 1 can be also established by a direct solution of the two problems. The mathematical complexity of these two formulations is greatly reduced by assuming a planar two dimensional geometry with a horizontal geomagnetic field $\underline{H}_o$, as indicated in Figure 8. The developments of the Appendix lead to a verification of the reciprocity relation (2).

Application of (1) to part B of Figure 1 shows that

$$\underline{p}_1 \cdot \underline{E}_2\,(1,\underline{H}_o) = -\,\underline{m}_2 \cdot \underline{H}_1\,(2, -\underline{H}_o) \tag{5}$$

$$\underline{p}_1 \cdot \underline{E}_3\,(1,\underline{H}_o) = -\,\underline{m}_3 \cdot \underline{H}_1\,(3, -\underline{H}_o) \tag{6}$$

Assuming that the dipole moments $\underline{m}_2$ and $\underline{m}_3$ are the same, (5) and (6) are rearranged into

$$\frac{\underline{E}_2\,(1,\underline{H}_o)}{\underline{E}_3(1,\underline{H}_o)} = \frac{\underline{H}_1\,(2, -\underline{H}_o)}{\underline{H}_1\,(3, -\underline{H}_o)} \tag{7}$$

The relative effectiveness $\underline{E}_2$ (1)/$\underline{E}_3(1)$ of a magnetic dipole source ($\underline{m}_3$) raised into the ionosphere ($\underline{m}_2$) is the same as the relation between the fields in the ionosphere $\underline{H}_1$ (2) and the fields on the ground surface $\underline{H}_1(3)$ of a groundbased electric dipole source ($\underline{p}_1$). The analysis of the geometry B1 will provide the same information as the geometries B2 and B3.

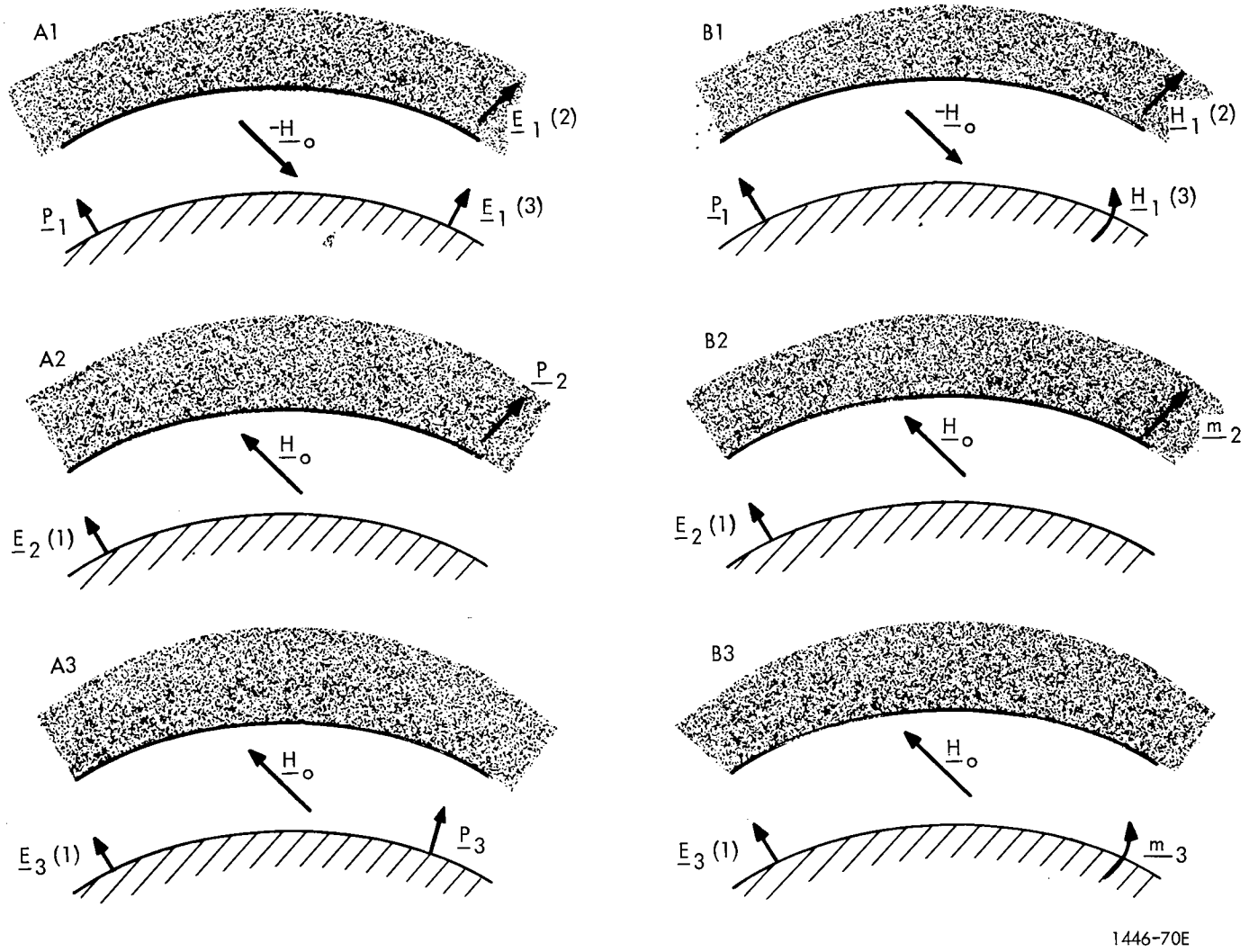

Figure 1. Reciprocal Geometries

Penetration of terrestrial waves in the ionosphere (A1 and B1 of Figure 1) provides information about the excitation of the terrestrial waveguide by ionospheric sources (A2 and B2). Detailed treatments of the geometries A1 and B1 are available (Galejs 1968, 1969a) and there is no need to go through the laborious mathematics for a direct formulation of the problem in geometries A2 and B2.

3. Discussion

The excitation of the earth-to-ionosphere waveguide will be considered in cylindrial (r, ϕ, z) coordinates, where r is in the radial (or vertical) direction, ϕ in the direction of propagation below the ionosphere, and z is transverse to this direction. The distant vertical electric fields $E_2(1)$ excited at the ground surface by an electric (or magnetic) dipole source oriented along the r, ϕ or z axis at an altitude y within the ionosphere will be estimated relative to the vertical electric fields $E_3(1)$ of a vertical electric (or a horizontal z-directed magnetic) dipole located at the earth's surface. Following (4) and (5) this ratio is the same as the ratio of the fields $E_r(y)/E_r(o)$, $E_\phi(y)/E_r(o)$ or $E_z(y)/E_r(o)$ or $H_r(y)/H_z(o)$, $H_\phi(y)/H_z(o)$ or $H_z(y)/H_z(o)$ excited by a groundbased vertical electric dipole.

The initial calculations are restricted to a z-directed horizontal magnetic dipole. The nighttime data of Figures 2 and 3 are based on the estimated electron density profile shown in Figure 2 of Galejs (1968), where the electron density is changed from 10 to 500 cm^{-3} at an altitude of 80 km.

Variations of the dip-angle I of a geomagnetic field of 0.5 gauss are illustrated in Figure 2 for propagation in East-to-West and West-to-East directions. Ionospheric sources become inefficient for $I < (15 \text{ to } 20^\circ)$. For propagation towards East the quasi - TE modes m=1 and m=2 are excited more effectively than the quasi - TM modes n=1,2 and 3. However, for propagation towards West the quasi - TM mode becomes relatively more effective.

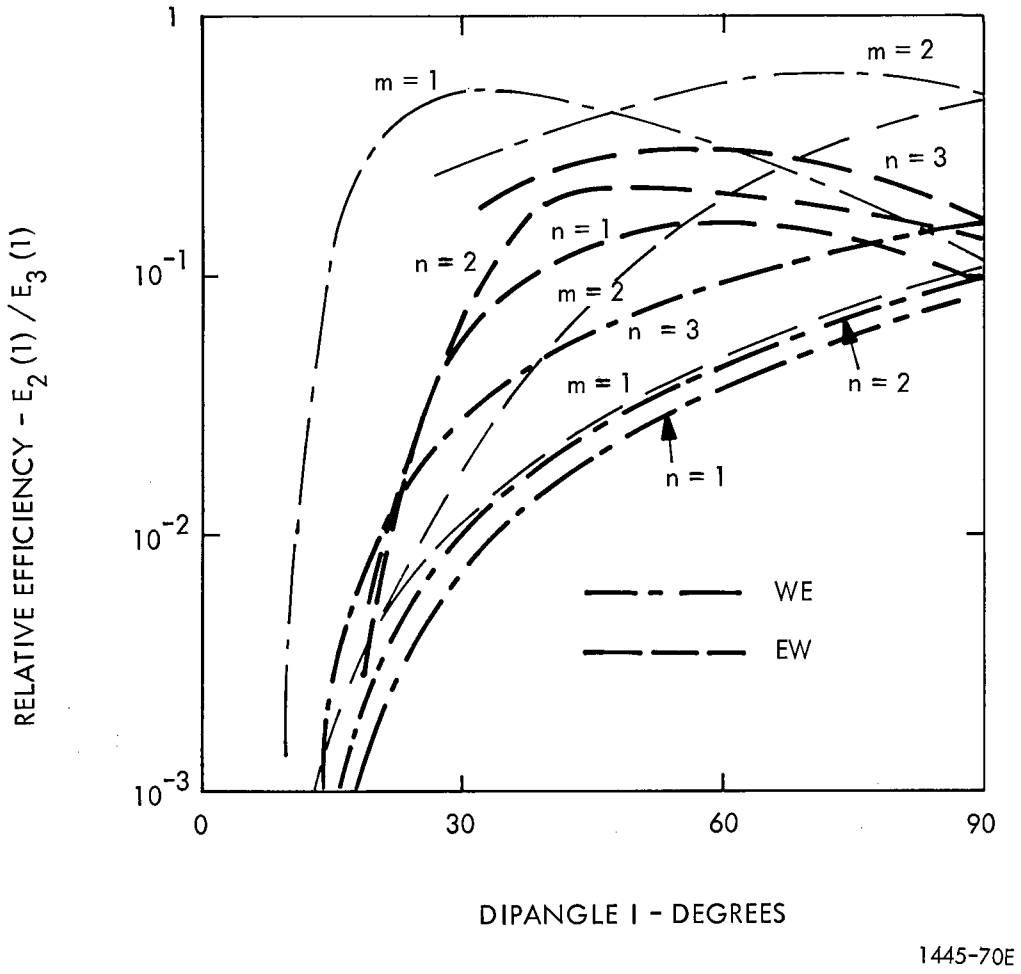

Figure 2. Relative Efficiency of a Horizontal Magnetic Dipole In a Nighttime Ionosphere

F = 20 kc/s, y_o = 100 km

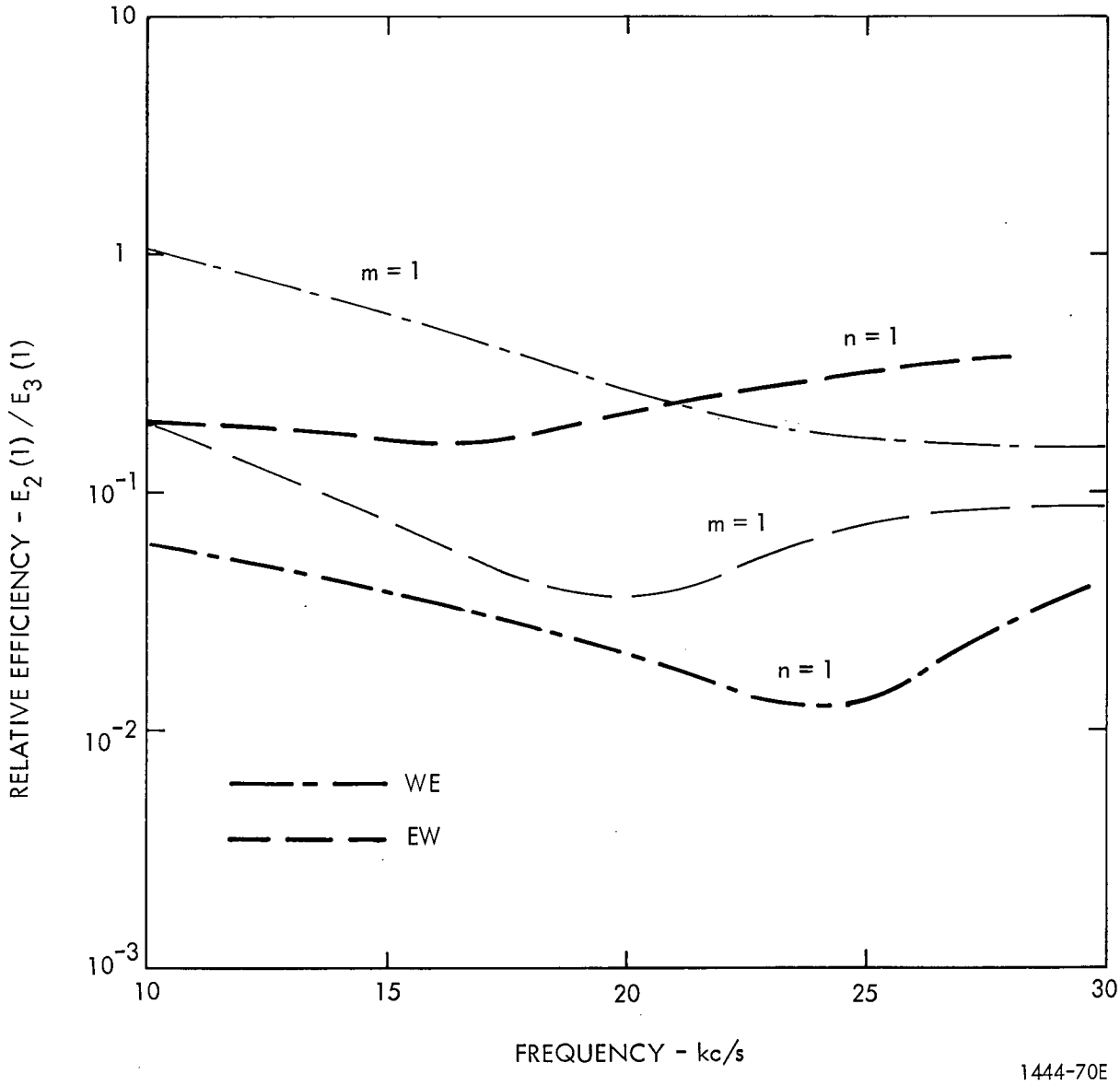

Figure 3. Relative Efficiency of a Horizontal Magnetic Dipole In a Nighttime Ionosphere

$I = 45^{\circ}$, $y_o = 100$ km

Figure 3 indicates the frequency dependence of the relative effectiveness for the dip-angle I = 45^{o}. The m modes are more effective at the lower frequencies, but in the n modes the relative effectiveness tends to increase also for the higher frequencies. The m=1 mode is excited more effectively for propagation towards East, but the n=1 mode for propagation towards West.

The characteristics of other sources are summarized in Table 1 using the winter nighttime ionosphere model of Deeks (1966). Electric and magnetic dipoles are designated by E and H, and the orientation of the dipole is along the r, ϕ or z axis. For a purely radial geomagnetic field of a dip-angle I=90^{o} a vertical electric dipole (ER) is about 100 times less efficient than the horizontal electric (Eϕ and EZ) or vertical magnetic dipole (HR). The horizontal magnetic dipoles (Hϕ and HZ) are the most effective radiators in the ionosphere. For a dipangle I=45^{o} the sources ER,Eϕ,EZ and HR exhibit about the same efficiency, which is somewhat less than one half of the efficiency of Hϕ and HZ. In the n=1 mode the efficiency is higher for the EW direction of propagation, which was also noted in Figure 3 for a different ionosphere model.

At a given altitude y the values of ER, Eϕ, EZ, HR, Hϕ and HZ are interrelated by the local characteristics of ionized medium. Based on the formulation for a radial geomagnetic field (Galejs, 1965) it can be readily shown that for I = 90^{o} ER/HZ $\approx 1/\epsilon_3$. The permittivity element is computed as $|\epsilon_3| \approx \omega_p^2/\omega^2 = 3.185 \times 10^9 N_e/\omega^2$; for $N_e = 10^3$ cm^{-3} and f = 20 kc/s this gives $|\epsilon_3| \approx 200$. It can be also shown that $|HR/EZ| \approx 1$ and that $|HZ/HR| \approx (\epsilon_2)^{0.5}$; with $|\epsilon_2| \approx \omega_p^2/(\omega\,\omega_c)$, the latter ratio is 1.7 for $N_e = 10^3 cm^{-3}$, f = 20 kc/s and the gyro frequency $|\omega_c| = 8.8 \times 10^6 sec^{-1}$. The above examples explain the relative magnitudes of ER and HZ, HR and EZ, or HZ and HR shown in Table 1 for I = 90^{o}.

For I = 45^{o} the component of the electric dipole transverse to the geomagnetic field is the same for dipoles oriented along r, ϕ and z-axes, and ER, Eϕ and EZ are of comparable magnitudes. However for magnetic dipoles the ratio HZ/HR remains about the same for I = 90^{o} and 45^{o}.

I	DIR.	ER	E_ϕ	EZ	HR	H_ϕ	HZ
90°		0.0005	0.058	0.050	0.050	0.099	0.115
45°	WE	0.0069	0.0073	0.0067	0.0066	0.0161	0.0159
45°	EW	0.095	0.101	0.092	0.091	0.224	0.218

1431-70E

TABLE 1 Relative efficiency $E_2(1)/E_3(1)$ of electric (E) and magnetic (H) dipole sources oriented along R, ϕ and Z axes. Winter nighttime ionosphere of Deeks. f = 20 kc/s, n = 1, y_o = 100 km, B = 0.5 Gauss.

The plots of Figure 4 illustrate the frequency variations of the relative efficiency in the n=1 and m=1 modes for $I=45^{o}$. ER, Eϕ, EZ and HR sources exhibit about the same efficiency and only the plot of EZ is shown. Also Hϕ curves are nearly the same as the plotted HZ curves. The relative efficiency of Hϕ and HZ sources is about 2 times higher than the efficiency of ER, Eϕ , EZ and HR sources and the curves are functionally similar to the HZ plots of Figure 3.

The relative effectiveness of a z-directed horizontal magnetic dipole is shown in Figure 5 for the summer daytime ionosphere model of Deeks (1966). For the lower frequencies an ionospheric source excites the quasi-TE m=1 mode nearly as effectively as a groundbased source. However, a groundbased source is an ineffective exciter of TE modes (see Figure 10 of Galejs (1969b)). Using E_3 (1) in mode n of a groundbased source as a reference, the ratio $E_2(1)\big|_m / E_3(1)\big|_n$ will be less than $E_2(1)\big|_n / E_3(1)\big|_n$ in magnitude.

In the ELF range the daytime conditions are illustrated using the electron density profiles of Deeks (1966) and Bain and May (1967) in conjunction with ion contributions as discussed by Galejs (1970). The calculations of Figure 6 refer to ϕ and z-directed horizontal magnetic dipole sources at altitudes of y_o=90 or 95 km. At the lower frequencies the source should be oriented in the direction of propagation below the ionosphere (ϕ), but at higher frequencies the waves are circularly polarized at this altitude and the source effectiveness is nearly the same for ϕ and z orientations. One may anticipate that the dependence on source orientation will disappear for larger altitudes h also at the lower frequencies.

The nighttime conditions are discussed with ionosphere models that are based on Deeks (1966) electron density profiles for altitudes below 100km; there is also a residual nighttime E-layer, a simulated semi-infinite F-layer for altitudes above h_F and ion effects are considered as shown by Galejs (1970). The calculations of Figure 7 are made for the composite electron density profiles C and CD of Figure 2 by Galejs (1970), the propagation data of which are shown in Figure 9 of the same paper. The relative source effectiveness at the altitudes y_o=200 or 240 km is in the range between 0.2 and 1. The sources are most effective at frequencies that correspond to absorption peaks of waves in the earth-to-ionosphere waveguide, which have been attributed to standing waves between E and F layers in the propagating magneto-ionic mode

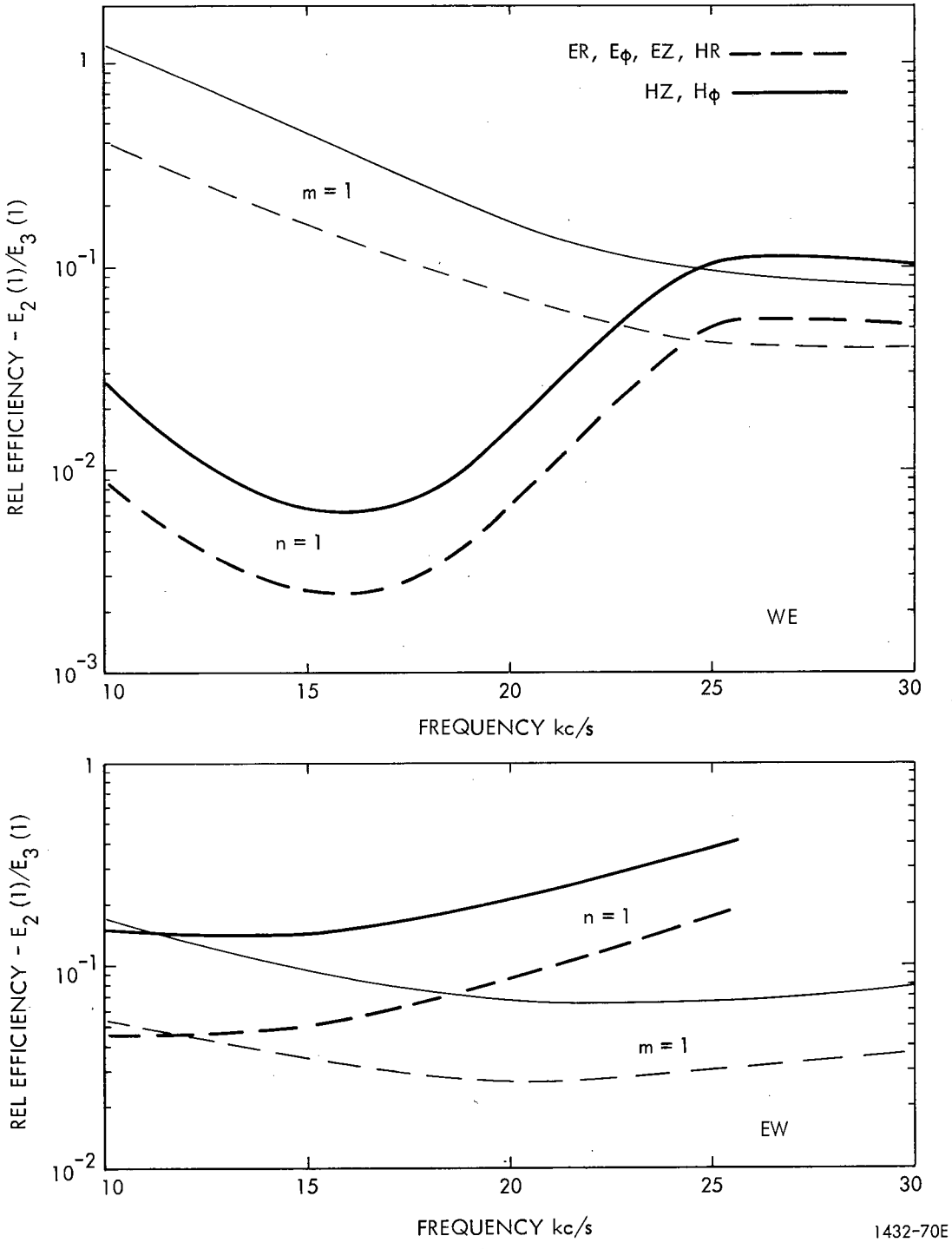

Figure 4. Relative efficiency of electric (E) and magnetic (H) dipole sources oriented along R, ϕ and Z axes. Winter nighttime ionosphere of Deeks. y_o = 100 km; B = 0.5 Gauss; I = 45°

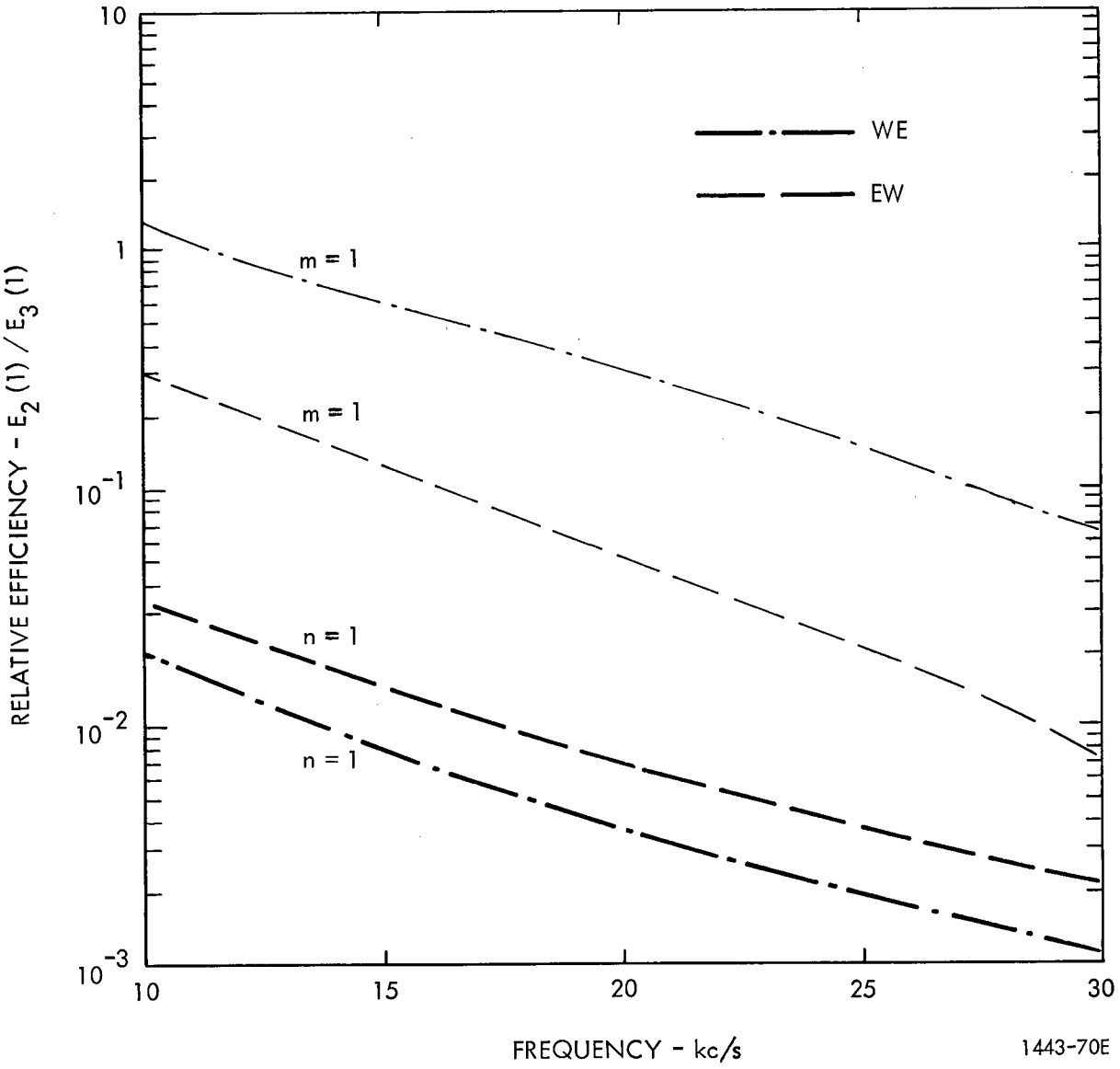

Figure 5. Relative Efficiency of a Horizontal Magnetic Dipole In a Daytime Ionosphere
$I = 45^{\circ}$, $y_o = 90$ km

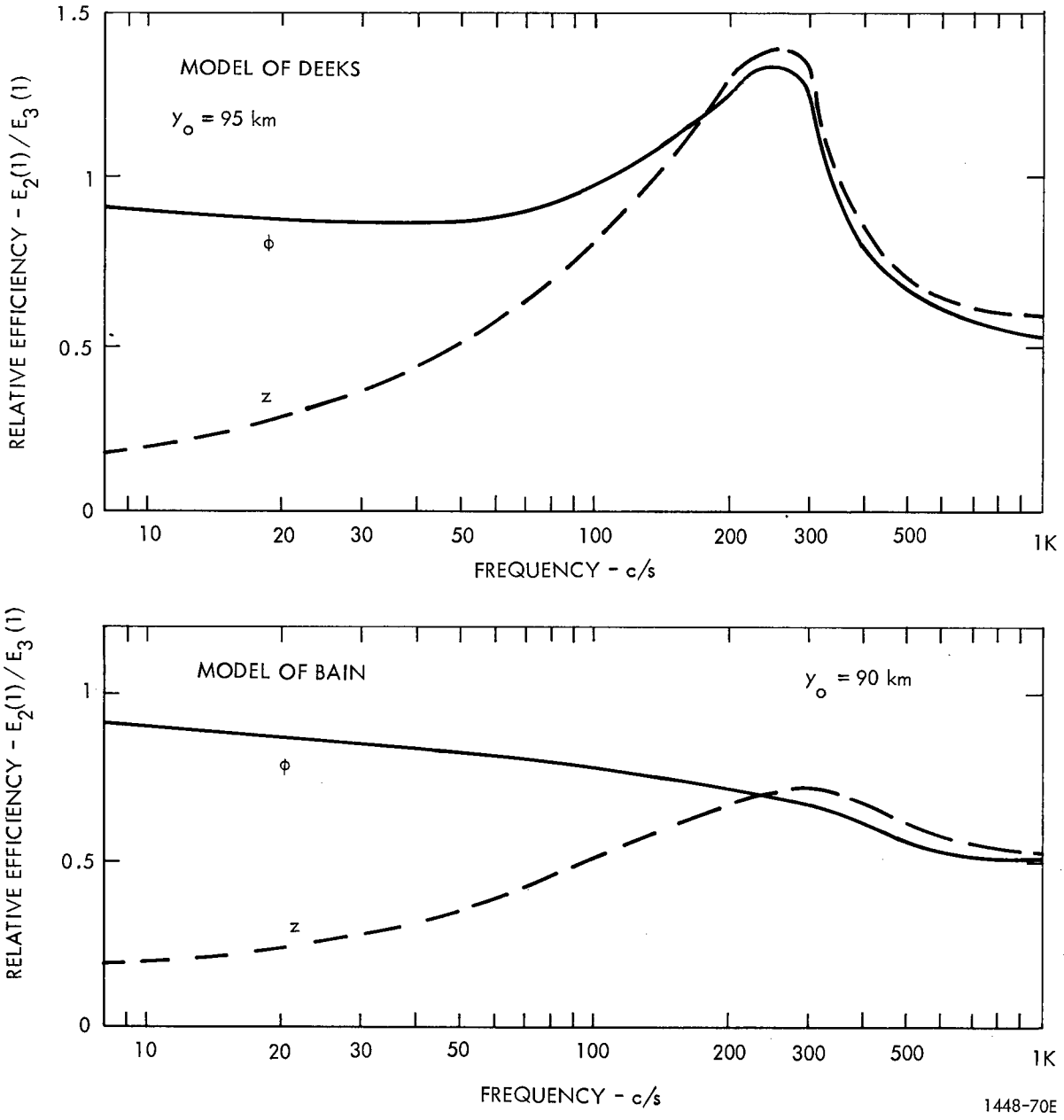

Figure 6. Relative Efficiency of a Horizontal Magnetic Dipole Source Oriented Along ϕ and z Axes In a Daytime Ionosphere. $I = 90^o$, $B_o = 0.3$ Gauss.

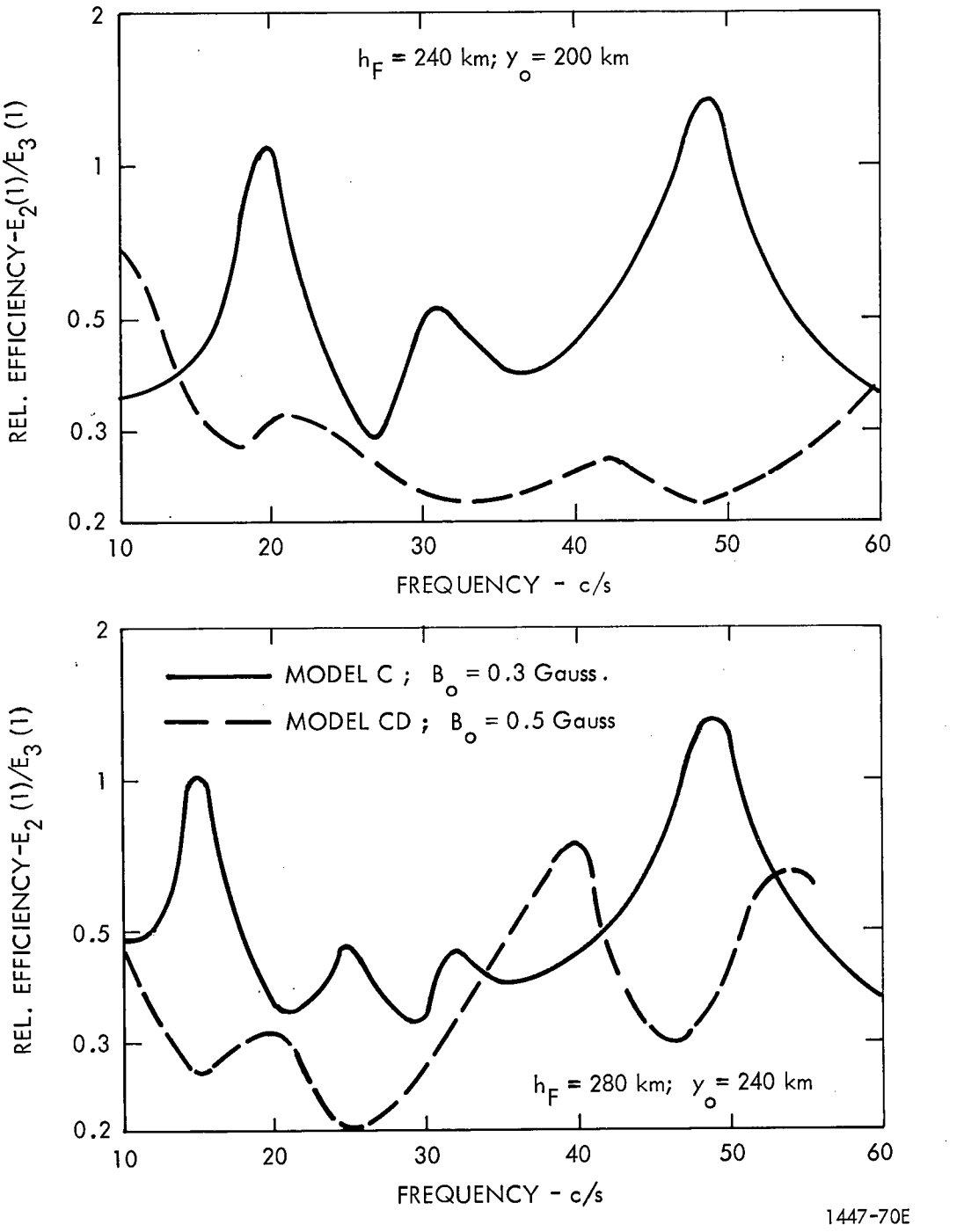

Figure 7. Relative Efficiency of a Horizontal Magnetic Dipole Source Located Below The F-Layer of Nighttime Ionosphere Models. $I = 90^o$.

(Galejs, 1970). Effective coupling from an altitude near the F-layer to ground surface corresponds by reciprocity to strong fields excited at this altitude and above by groundbased sources. The large absorption peaks in the waveguide fields occur under conditions when strong fields are observed near the altitude of the F-layer.

4. Summary of Results

Data on field penetration in the ionosphere are used in conjunction with the appropriate reciprocity relations to determine the effectiveness of dipole sources within the ionosphere relative to sources near the surface of the earth. In this formulation the orientation of the magnetic or electric dipole sources, the direction of the geomagnetic fields and the direction of propagation below the ionosphere are arbitrary; ionospheric stratifications and curvature of the geometry is allowed for.

Electric dipoles oriented along the direction of the geomagnetic field are ineffective exciters of the terrestrial waveguide, and a transverse orientation is preferable. For magnetic dipoles the transverse orientation is also preferable, but the fields of an axial orientation are of the same order of magnitude. An effective penetration to the earth-to-ionosphere cavity requires dip angles of the geomagnetic field in excess of 15 to 20^{o}. Under nighttime conditions VLF TE modes are excited more effectively for West-to-East direction of propagation and the TM modes - for East-to-West direction. During daytime ionospheric sources excite TE modes more effectively than groundbased sources; still TM modes appear to dominate. The effectiveness of a ionospheric source is about 10% at nighttime and 1% at daytime relative to groundbased sources of same dipole moment in the VLF range.

In the ELF range the relative effectiveness is from 20 to 100%. During nighttime the largest efficiencies are observed under conditions when strong terrestrial fields are observed near the F-layer or when the terrestrial waves are highly attenuated.

In this formulation ion sheath effects can be considered by placing the antenna in a layer of free space. The net fields excited by ionospheric sources may be estimated after developing mode summations similarly as by Galejs, (1969a).

5. Appendix - Fields of Reciprocal Configurations

The reciprocity relations will be illustrated by analyzing the planar geometries of Figure 8, where the z- directed geomagnetic field is purely horizontal. The waveguide of Figure 8a is excited by a vertically polarized line source of dipole moment $J_{sey}\,dy$ per unit length in the z- direction, and the horizontal electric field component E_x is observed at altitude $y = y_o$ in the ionosphere. In Figure 8b, the x and z coordinate axes are reversed and the fields are excited by a horizontally polarized line source of dipole moment $J_{sex}dx$ per unit length in z- direction; the vertical electric fields E_y are observed at the ground surface. Noting the differences between the x-axis orientations of Figures 8a and b, the reciprocity relation (2) leads to

$$E_y(o)\, J_{sey}dy = -E_x(y_o)\, J_{sex}dx \tag{A.1}$$

This relation will be verified after deriving the appropriate field expressions.

1. Fields of the Ionosphere

In a plasma with a z- directed magnetic field, the Maxwell's equations may be written as

$$\nabla \times \underline{H} = -i\omega\epsilon_o \left[\epsilon\right] \cdot \underline{E} \tag{A.2}$$

$$\nabla \times \underline{E} = i\omega\mu_o \underline{H} \tag{A.3}$$

where the relative permittivity tensor $\left[\epsilon\right]$ is of the form

$$\left[\epsilon\right] = \begin{bmatrix} \epsilon_1 & -\epsilon_2 & 0 \\ \epsilon_2 & \epsilon_1 & 0 \\ 0 & 0 & \epsilon_3 \end{bmatrix} \tag{A.4}$$

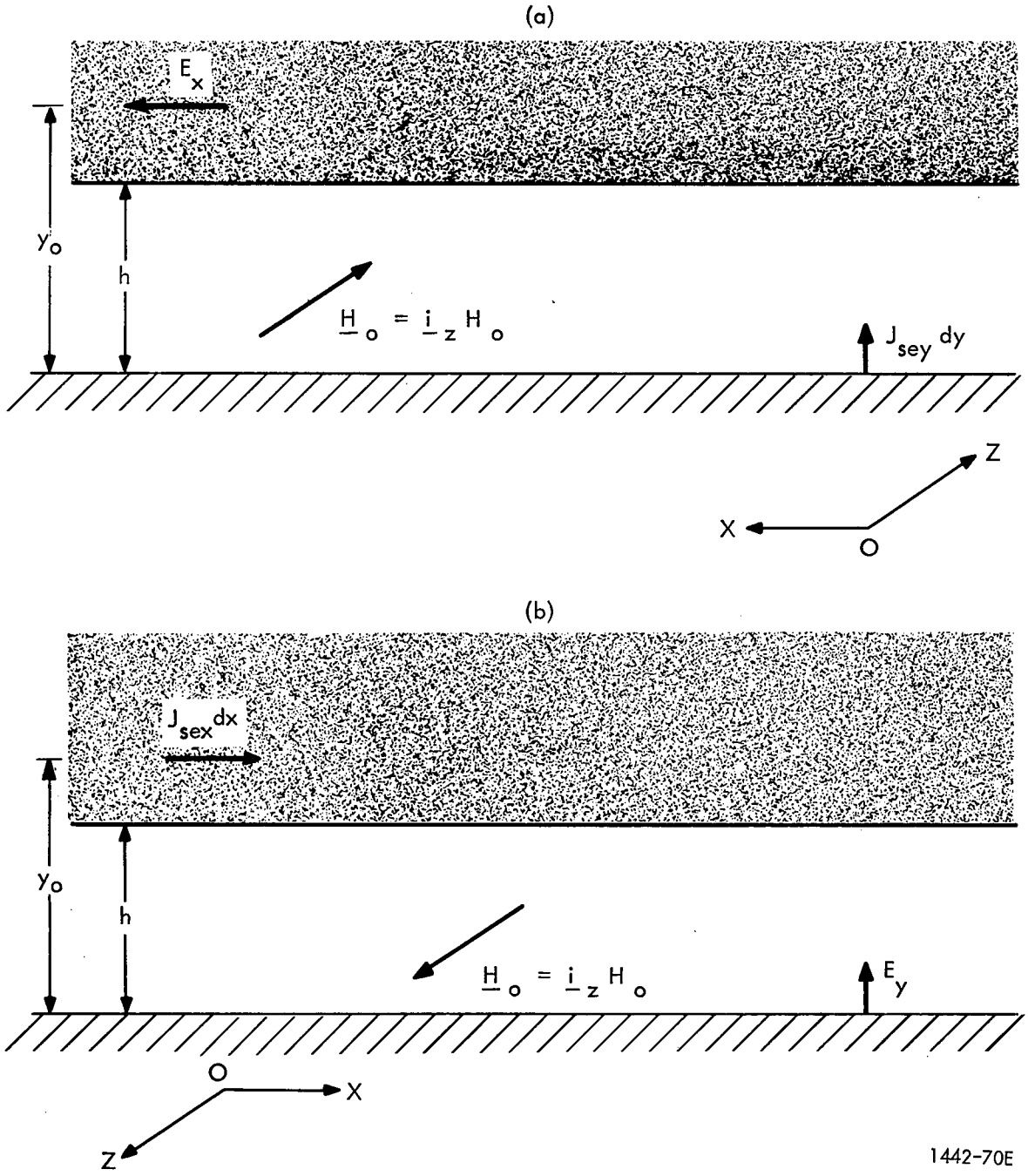

Figure 8. Excitation of a Planar Waveguide

With no z-variations of the fields, the TM field components (E_x, E_y, H_z) are uncoupled from the TE components (E_z, H_x, H_y) and E_x is related to H_z as

$$E_x = \frac{1}{i\omega\epsilon_o(\epsilon_1^2 + \epsilon_2^2)} \left[-\epsilon_1 \frac{\partial H_z}{\partial y} + \epsilon_2 \frac{\partial H_z}{\partial x}\right] \tag{A.5}$$

H_z satisfies the differential equation

$$\frac{\partial^2}{\partial x^2} H_z + \frac{\partial^2}{\partial y^2} H_z + k_o^2 \frac{\epsilon_1^2 + \epsilon_2^2}{\epsilon_1} H_z = 0 \tag{A.6}$$

For an assumed $\exp(ik_o Sx)$ x-dependence of the fields H_z of the ionsphere ($y>h$) will be of the form

$$H_z = A \exp(ik_o Sx + i K_i y) \tag{A.7}$$

where

$$K_i/k_o = \sqrt{\frac{\epsilon_1^2 + \epsilon_2^2}{\epsilon_1} - S^2} \tag{A.8}$$

with $\mathrm{Im}\ K_i > 0$. Substitution of (A.7) in (A.5) shows that the normalized surface impedance of the ionosphere becomes

$$\Delta_e = -\frac{1}{\eta} \frac{E_x}{H_z} = \frac{\epsilon_1 K_i - \epsilon_2 S k_o}{k_o(\epsilon_1^2 + \epsilon_2^2)} \tag{A.9}$$

where $\eta = \sqrt{\mu_o/\epsilon_o} = 120\pi$ is the characteristic impedance of free space.

2. Groundbased Vertical Source

For a groundbased vertically polarized source the fields of the air space ($0 \le y \le h$) are obtained from (59) of Galejs (1969a) as

$$E_x(y) = \frac{\eta J_{sey}\, dy}{h} \sum_n \Lambda_n G_n(y) \Delta_n(y) e^{ik_o S_n x} \tag{A.10}$$

In the limit of a flat and perfectly conducting earth (radius $a \to \infty$ and impedance $\Lambda_g = 0$) the functions Λ_n, G_n, Δ_n are derived from (17) to (20) of Galejs (1969b) as

$$\Lambda_n = \left[1 + \frac{\sin 2 K_o h}{2 K_o h} \right]^{-1} \tag{A.11}$$

$$G_n(y) = \cos K_o y \tag{A.12}$$

$$\Delta_n(y) = \frac{iK_o}{k_o} \tan K_o y \tag{A.13}$$

where $K_o^2 = k_o^2 (1 - S_n^2)$. The parameters S_n are computed from the solution of

$$D = k_o \Delta_e \cos K_o h - iK_o \sin K_o h = 0 \tag{A.14}$$

E_x of the ionosphere follows from (A.5) and (A.7). Continuity of E_x for $y = h$ shows that for a given mode of $S = S_n$ the ionospheric fields are given by

$$E_x(y) = \frac{\Delta_e \eta}{h} \int J_{sey}\, dy \; \frac{\cos K_o h}{1 + \frac{\sin 2 K_o h}{2 K_o h}} \; e^{ik_o S_n x + iK_i (y-h)} \tag{A.15}$$

where $y \geq h$.

3. Horizontal Source in the Ionosphere

The fields F_{ij} of the airspace or the ionosphere are related to their Fourier transforms $\bar{F}_{ij}$ by the integral

$$F_{ij}(x,y) = \frac{1}{2\pi} \int_{-\infty}^{\infty} \bar{F}_{ij}(u,y)\, e^{iux}\, du \tag{A.16}$$

where F = E or H, i = x,y or z, and where the subscript j denotes the region. The field component E_x is related to H_z by (A.5) and $\bar{H}_{zj}$ will be of the form

$$\bar{H}_{z1} = A_1 e^{iK_o y} + B_1 e^{-iK_o y} \quad \text{for } 0 \le y \le h \tag{A.17}$$

$$\bar{H}_{z2} = A_2 e^{iK_i (y-h)} + B_2 e^{-iK_i (y-h)} \quad \text{for } h \le y \le y_o \tag{A.18}$$

$$\bar{H}_{z3} = A_3 e^{iK_i (y-h)} \quad \text{for } y_o \le y \tag{A.19}$$

where $u = Sk_o$ should be substituted in the previous definitions of K_i and K_o. The boundary conditions $\bar{E}_{x1} = 0$ for $y = o$, $\bar{E}_{x2} = \bar{E}_{x1}$ and $\bar{H}_{z2} = \bar{H}_{z1}$ for $y = h$ together with $\bar{E}_{x3} = \bar{E}_{x2}$ and $\bar{H}_{z3} - \bar{H}_{z2} = \bar{J}_x = \int J_x e^{-iux} dx = J_{sex} dx$ for $y = y_o$ give 5 equations for determining the 5 coefficients A_1, B_1, A_2, B_2 and A_3. The vertical electric field at y=o follows as $\bar{E}_y = 2A_1 u/\omega e_o$. A lengthy calculation whows that

$$\bar{E}_y = -\eta u \Delta_e \frac{J_{sex}\, dx \quad \exp\left[i K_i (y_o - h) \right]}{k_o \Delta_e \cos K_o h - i K_o \sin K_o h} = \frac{N}{D} \tag{A.20}$$

Substituting (A.20) in (A.16), the residue contributions to the integral are evaluated as

$$E_y (o) = 2\pi i \sum_n \left. \frac{N}{\partial D / \partial u} \right|_{u = k_o S_n} \tag{A.21}$$

In line with the usual assumptions of mode theory the u-dependence of Δ_e is ignored in the evaluation of the derivative. * This results in

$$E_y (o) = \sum_n \frac{J_{sex}\, dx \eta \ \Delta_e \cos K_o h \quad \exp}{h \left[1 - \sin^2 K_o h + \frac{\cos K_o h \sin K_o h}{K_o h} (1 - ik_o h \ \Delta_e) \right]} \tag{A.22}$$

* This neglect does not imply an inaccuracy of the computed fields, because the calculation of the surface impedance Δ_e can be repeated with updated S values until the S and Δ_e sequences are found to converge.

with

$$\exp = \exp \left[i K_i (y_o - h) + i k_o S_n x \right] \tag{A.23}$$

The denominator of (A.22) is simplified applying (A.14). It is seen that the resulting equation is related by (A.15) to (A.1)

6. References

1. Bain, W. C., and B. R. May (1967), "D-region electron density distributions from propagation data," Proc. Inst. Elec. Engrs. (London) 114(11), 1593-1597.

2. Deeks, D. G. (1966), "D-region electron distributions in middle latitudes deduced from the reflection of long radio waves," Proc. Roy. Soc.291 (1426), 413-427.

3. Duff, G. L. and R. Mittra (1970), "Loop impedance in magnetoplasma: Theory and experiment," Radio Science 5 (1), 81-94.

4. Einaudi, F. and J. R. Wait (1970),"On the calculation of the launching efficiency in the earth-ionosphere waveguide for an ELF/VLF source at satellite height," Paper presented at the USNC/URSI Spring Meeting, Washington, D. C.

5. Galejs, J. (1965), "On the terrestrial propagation of ELF and VLF waves in the presence of radial magnetic field," Radio Science 69D(5), 705-720

6. Galejs, J. (1968), "Propagation of ELF and VLF waves below an anisotropic ionosphere with a dipping static magnetic field," J. Geophys. Res. 73 (1), 339-352.

7. Galejs, J. (1969a), "VLF modes below an idealized anisotropic ionosphere," Radio Science 4 (6), 491-516.

8. Galejs, J. (1969b), "Near fields and antipodal fields in the terrestrial earth-to-ionosphere wave guide," Proc. IEE 116 (7), 1150-1158.

9. Galejs, J. (1969c), Antennas in Inhomogeneous Media, Pergamon Press,Oxford.

10. Galejs, J. (1970), "F-layer reflections and ion effects in the propagation of terrestrial ELF waves," J. Geophys. Res. 75 (13), 2529-2539

11. GiaRusso, D. P., and J. E. Bergeson (1969), Studies of VLF radiation patterns of a dipole immersed in a lossy magnetoplasma, Boeing Sci. Res. Lab., Doc. D1-82-0797, Seattle, Wash.

12. Ginzburg, V. L. (1964), The Propagation of Electromagnetic Waves in Plasmas, Pergamon Press, Oxford.

13. J. P. Leiphart, R. W. Zeek, L. S. Bearce, and E. Toth (1962) "Penetration of the ionosphere by very-low-frequency radio signals - interim results of the LOFTI I experiment," Proc.IRE 50(1), 6-17.

14. Wang, T. N. C. and T. F. Bell (1969a), "Radiation resistance of a short dipole immersed in a cold magnetoionic medium," Radio Science 4 (2), 167-177

15. Wang, T. N. C. and T. F. Bell (1969b), "On VLF radiation fields along the static magnetic field from sources immersed in a magnetoplasma," IEEE Trans. on Ant. and Prop. AP-13 (6), 824-827.

16. Wang, T. N. C. and T. F. Bell (1970), "On VLF radiation resistance of an electric dipole in a cold magnetoplasma," Radio Science 5

AUTHOR INDEX

Security Classification

DOCUMENT CONTROL DATA - R & D

(Security classification of title, body of abstract and indexing annotation must be entered when the overall report is classified)

1. ORIGINATING ACTIVITY *(Corporate author)* Naval Research Laboratory Washington, D. C. 20390	2a. REPORT SECURITY CLASSIFICATION Unclassified 2b. GROUP

3. REPORT TITLE

PROCEEDINGS OF THE CONFERENCE ON ANTENNAS AND TRANSIONOSPHERIC PROPAGATION AS RELATED TO ELF/VLF DOWNLINK SATELLITE COMMUNICATIONS

4. DESCRIPTIVE NOTES *(Type of report and inclusive dates)*

Proceedings of a conference.

5. AUTHOR(S) *(First name, middle initial, last name)*

Loren S. Bearce (Conference Chairman)

6. REPORT DATE November 27, 1972	7a. TOTAL NO. OF PAGES 349	7b. NO. OF REFS 180
8a. CONTRACT OR GRANT NO. NRL Problem R01-44 b. PROJECT NO. AIRTASK NO. A3705381/625B/2F00222702 c. d.	9a. ORIGINATOR'S REPORT NUMBER(S) NRL Report 7462 9b. OTHER REPORT NO(S) *(Any other numbers that may be assigned this report)*	

10. DISTRIBUTION STATEMENT

Approved for public release; distribution unlimited.

11. SUPPLEMENTARY NOTES	12. SPONSORING MILITARY ACTIVITY Department of the Navy Naval Air Systems Command Washington, D.C. 20360

13. ABSTRACT

An initial conference on Antennas and Transionospheric Propagation as related to ELF/VLF Downlink Satellite Communications was held at the Naval Research Laboratory (NRL) on 8-10 June 1970 under the sponsorship of the Naval Air Systems Command and NRL for the purpose of providing a forum for interested people to review pertinent physical principles and data, recent theoretical and experimental results, and current thinking; to stimulate and focus attention on appropriate new activity for further studies; and to allow participants an opportunity to present and discuss recommendations for pertinent experimentation, related instrumentation, and studies considered to be most timely and meaningful for implementation in the '70's.

DD FORM 1 NOV 65 1473 (PAGE 1)

S/N 0101-807-6801

Security Classification

14. KEY WORDS	LINK A		LINK B		LINK C	
	ROLE	WT	ROLE	WT	ROLE	WT
Transionospheric propagation						
Satellite communications						
ELF/VLF communications						
Magnetoplasma						
Antenna impedance						
Antenna radiation						